MONTE CARLO INVESTIGATIONS OF RADIOTHERAPY BEAMS: STUDIES OF CONVENTIONAL, STEREOTACTIC AND UNFLATTENED BEAMS.

by

MOHAMED ARIFF JAAFAR SIDEK

UNIVERSITY OF
BIRMINGHAM

A thesis submitted to

The University of Birmingham

for the degree of

DOCTOR OF PHILOSOPHY

Department of Medical and Radiation Physics

School of Physics and Astronomy

The University of Birmingham

January 2010

Abstract

Monte Carlo modelling is a useful method of investigating the electron and photon transport in radiotherapy linear accelerators. Calculations made by Monte Carlo techniques have many roles including investigation of unusual situations where measurements are difficult and as a problem solver. The predictions made by a validated model can be used to confirm an assumption or prove a hypothesis.

This study is aimed to investigate the performance of the DOSI detector, a prototype detector which is position sensitive with submillimeter resolution. This solid-state detector is made of p-type diode and has silicon as its volume element. Work from other authors has shown that other silicon detectors overestimate the dose as field size and depth increase. To overcome this, a mechanism for correction has to be determined. For this reason, this investigation compares experimental data and calculated results using Monte Carlo method at 6 MV photon energy from a Varian linear accelerator. A small degree of perturbation has been found from this study, and work on improvement of the dose measurements has been carried out. Results have been presented and suggestion for a better dose meter is discussed.

In stereotactic beams, a reliable detector to measure the dose in small radiation fields is crucial for treatment planning. Not many detectors will show a correct dosimetry at the penumbra region due to lack of lateral electronic equilibrium. To overcome this, the solution is for the dosimeters to have small

active volumes and be tissue-equivalent. Since DOSI detector has most of these important criterion, it is one of the reasons for the performance of DOSI to be compared with 2 other detectors that could be used to measure the small beam. The stereotactic field has been modelled and Monte Carlo calculations have been compared with the experimental data. Results of the dose measurements and the simulations have been presented and discussed. The most superior detector is revealed in this research for small field measurements.

The next aim of this research is to gain more information on the filterless beam of the 6 MV Elekta linear accelerator. Flattening filter free beam has been discussed recently in several papers. The use of flattening filter removal linear accelerator is claimed beneficial in stereotactic technique and intensity-modulated radiation therapy. Yet, few simulations have been done with Elekta linear accelerator. Therefore, full Monte Carlo calculations are run to investigate the outcome of this filterless beam. Validation of the model has been done with good agreement with the standard measurements. Results are compared with measured data leading to valuable conclusions. Monte Carlo findings show excellent clinical characteristics for filterless beams in which there is reduced total scatter and lower leakage radiation.

I dedicate this work to my family;

my wife, my 4 daughters

and my son, who was born

during the course of this PhD programme,

who give me strength, unconditional love

and support throughout.

Acknowledgements

I would like to take this opportunity to thank my supervisors Dr Richard Hugtenburg and Dr Stuart Green for their thorough guidance, support and advice from day one of my placement in the university to the final stages of this thesis. I can not express enough, my thanks for their long hours and tireless efforts in helping me during computer breakdowns and problems including sacrificing their own weekends and family time, without whom the research and write-up could not have been completed.

I would also like to thank Mr Graham Chalmers, Dr Cecile Wojnecki and Dr Spyros Manolopoulos for their time and cooperation, helping me in many ways with information on the linear accelerators, commissioning data and the interesting experimental works with the DOSI. The exposure and the experience were invaluable.

For her efforts and assistance, a special thanks to Mrs Norma Simpson who has given me the support a student should have with university regulations and procedures. I am very grateful indeed.

Many thanks go to friends and colleagues, Adam Baker, Daniel Kirby, Zamir Ghani, Francesca Fiorini, and the newly graduated Dr Shane O'Hehir and Dr Margaret O'Hara with their special ways to get things going and support in the office. It has been nice to know you all.

I am indebted to my sponsor and employer, the government of Malaysia and Universiti Kebangsaan Malaysia (National University of Malaysia) for the scholarship and faith in me to pursue this doctorate study.

Finally, I would like to give thanks to those whose names are not mentioned here, for their direct or indirect assistance towards fulfilling this PhD programme.

To all of the above, I extend my deepest gratitude and appreciation. It is a pleasure to have all of you as a working team.

Table of Contents

Chapter 1 - Introduction **1**

1.1 Principle and Aims in Radiotherapy……. 1

1.1.1 Tumour Control Probability…… 4

1.1.2 Normal Tissue Complication Probability…….. 5

1.1.3 Therapeutic Ratio And Fractionation…… 5

1.1.4 Conformal Radiotherapy…… 8

1.1.5 Stereotactic Radiation Treatment…… 10

1.1.6 Intensity Modulated Radiation Therapy…….. 11

1.2 The Basics of Small Field Dosimetry…….. 13

1.3 Background of the Investigation…….. 14

1.4 The Scope of This Work……. 16

1.5 Layout of the Project…….. 19

Chapter 2 - Fundamentals of Radiotherapy Physics **22**

2.1 Interactions of Radiation with Matter…….. 22

2.1.1 Electron Interactions…… 23

2.1.1.1 Stopping power…….. 24

2.1.1.2 Soft collision interactions…… 25

2.1.1.3 Hard collision interactions……... 25

2.1.1.4 Radiative interactions…… 26

2.1.2 Photon Interactions…… 27

2.1.2.1 Rayleigh (Coherent) scattering……... 28

2.1.2.2 Photoelectric effect…… 29

2.1.2.3 Compton (Incoherent) scattering…… 30

2.1.2.4 Pair production…… 31

2.2 Quantities and Units in Radiotherapy…….. 32

2.2.1 Fluence…… 33

2.2.2 34

2.2.3 Percentage Depth Dose (PDD)…… 35

2.2.4 Off-Axis Ratio (OAR)…… 36

2.2.5 Relative Output Factor (ROF)…… 37

2.3 Electronic Equilibrium……. 38

2.3.1 Cavity Theory…… 39

2.3.1.1 Bragg-Gray cavity theory…… 40

2.3.1.2 Spencer-Attix cavity theory…… 41

2.3.1.3 Burlin cavity theory…….. 43

Chapter 3 - Detectors and Monte Carlo Methods **46**

3.1 Dose Detectors…….. 46

3.1.1 Ionisation Chamber…… 46

3.1.1.1 PinPoint ionisation chamber…….. 48

3.1.2 Solid State Detectors…….. 49

3.1.2.1 Diamond detector…… 50

3.1.2.2 DOSI detector…… 53

3.2 Radiotherapy Treatment Source……... 55

3.2.1 Radiotherapy Linear Accelerator (Linac)…….. 56

3.3 Monte Carlo Code…….. 58

3.4 The EGSnrc Code…….. 60

3.4.1 BEAMnrc…… 60
3.4.1.1 Component modules…… 61
3.4.2 DOSRZnrc…… 63
3.4.3 DOSXYZnrc…… 66
3.5 Variance Reduction…… 67
3.5.1 BlueBEAR Computer Cluster…… 68
3.5.2 Directional Bremsstrahlung Splitting…… 68
3.6 PEGS4 Data…… 69

Chapter 4 - Characterisation of the Model of the Linear Accelerator Head **70**
4.1 Introduction…… 70
4.2 The Process of Optimisation for Elekta…… 71
4.2.1 Methods…… 71
4.2.2 The Evolution Process of the Flattening Filter…… 76
4.2.3 Results…… 86
4.3 The Process of Optimisation for Varian…… 87
4.3.1 Methods…… 87
4.3.2 Results…… 97
4.4 Discussion…… 98

Chapter 5 - Investigation on DOSI Detector using Varian Linac **101**
5.1 Introduction…… 101
5.2 Methods…… 105
5.3 Results…… 113
5.4 Discussion…… 118

Chapter 6 - Investigation of the Performance of PinPoint Chamber, Diamond and DOSI Detector on Stereotactic Beams **122**
6.1 Introduction…… 122
6.2 Methods…… 124
6.3 Results…… 130
6.4 Discussion…… 141

Chapter 7 - Investigation on the Unflattened Beam using Elekta Linac **146**
7.1 Introduction…… 146
7.2 Methods…… 149
7.3 Results…… 156
7.4 Discussion…… 163

Chapter 8 - Conclusion **167**
8.1 Summary of Results…… 167
8.1.1 Investigation on DOSI Performance…… 168
8.1.2 Investigation on DOSI in Stereotactic Beams…… 169
8.1.3 Investigation on Filterless Beams in IMRT…… 171
8.2 Future Work…… 173

Appendix A - Calculation of the Percentage Difference for Various Flattening Filter Heights and Electron Energy for Elekta..... **176**

Appendix B - Calculation of the Percentage Difference for Various Flattening Filter Heights and Electron Energy for Varian..... **181**

Appendix C - Calibration on GafChromic Film using the 6 MV Varian Model..... **187**

Appendix D - Elekta Linac Specifications..... **192**

Appendix E - Varian Linac Specifications..... **193**

List of References..... **194**

List of Figures

Figure 1.1: Left, Wilhelm Conrad Roentgen and right, the x-ray image of the hand produced in 23 January 1896. [4 - 6].. 1
Figure 1.2: Left, a CT slice of the lung [7] and right, a CT reconstruction using a computer tool with a Siemens scanner [8]…..…….....…… 2
Figure 1.3: Relationship between the response of both tumour and normal tissue and radiation dose [14]…….. 7
Figure 1.4: A typical CTV and PTV delineated for Wilms' Tumour radiotherapy [22]…….. 9
Figure 1.5: A typical 2 field-beam showing the isodose curves in neuroblastoma treatment planning [22]……... 9
Figure 1.6: Top left, a stereotactic radiosurgery performed on a patient with 3D target image (top right) and 2D depictions of the target (bottom left and right) [24…… 11
Figure 1.7: An example of a 9 field IMRT technique dose distributions, where the grey levels indicate the intensity values of the beamlets [26]…… 12
Figure 2.1: Percentage depth dose curves in water for a 10 × 10 cm^2 field at 100 cm SSD for photon beams ranging from cobalt-60 gamma rays to 25 MV x-rays [77]…….…. 36
Figure 3.1: Left, the PTW Farmer thimble chamber and right, Markus plane-parallel ionisation chamber [101]……... 47
Figure 3.2: The PTW PinPoint ionisation chamber and its build-up cap [106]…….. 48
Figure 3.3: The diamond detector and its cross section [84, 3].....……... 50
Figure 3.4: Picture of the 128-channel detector and its associated electronics [57]…….…….. 54
Figure 3.5: A typical medical linac structure [126]…….. 57
Figure 3.6: Treatment head of a linac at a gantry angle of 90°…… 58
Figure 3.7: The modelled components of BEAMnrc module for Elekta (right) and Varian (left)…….…. 62
Figure 3.8: The schematic diagram for 15 MV 10 x 10 cm^2 field linac..... 63
Figure 3.9: The DOSRZnrc version 2006 GUI that was used for the project…… 65
Figure 3.10: The DOSRZnrc modelled phantom for calculating the depth doses…….. 65
Figure 4.1: Percentage depth doses for 10.0 cm and 30.0 cm square fields, 90 cm SSD for 15 MV Elekta linear accelerator..... 74
Figure 4.2: The PDDs for 10.0 cm and 30.0 cm square fields, 90 cm SSD for 10 MV Elekta…….…….. 74
Figure 4.3: The PDDs for 3.0 cm and 10.0 cm square fields, 90 cm SSD for 6 MV Elekta…….. 75
Figure 4.4: Output Factors for 6 MV, 10 MV and 15 MV Elekta…..…. 75

Figure 4.5: The off-axis ratios for 15 MV Elekta at 10 cm deep simulated with 2 flattening filters using the specification heights..... 76
Figure 4.6: 6 MV Percentage depth doses at 3, 10 and 30 cm square field, 90 cm SSD for Elekta model adjusted to 6.4 MeV electron energy……..……. 78
Figure 4.7: The OARs for 6 MV Elekta at various field sizes at 10 cm deep..... 79
Figure 4.8: 6.4 MeV Elekta off-axis ratio at 1.5 cm deep, 40 cm square field with various flattening filter heights…..... 80
Figure 4.9: 6.4 MeV Elekta off-axis ratio at 10.0 cm deep, 40 cm square field with various flattening filter height…….. 80
Figure 4.10: 6.4 MeV Elekta off-axis ratio at 1.5 cm deep, 40 cm square field 1.92 x flattening filter heights with increased number of histories..... 81
Figure 4.11: 6.4 MeV Elekta off-axis ratio at 10.0 cm deep, 40 cm square field 1.92 x flattening filter heights with increased number of histories……..… 81
Figure 4.12: 6.4 MeV Elekta PDDs, 1.92 x flattening filter original height at 10, 20 and 40 cm square field…….. 83
Figure 4.13: 15 MV Elekta, 40 x 40 cm^2 field, 2.7 cm deep, flattening filter heights from 1.0 to 2.0 x original height…….. 84
Figure 4.14: 15 MV Elekta, 40 x 40 cm^2 field, 10.0 cm deep, flattening filter heights from 1.0 to 2.0 x original height…….…..... 85
Figure 4.15: The 6 MV output factors for Elekta, 6.4 MeV, 1.92 x original height…….. 86
Figure 4.16: The PDDs for 10.0 and 30.0 cm square fields, 100 cm SSD for 6 MV Varian……..... 88
Figure 4.17: 6 MV Varian off-axis ratios for 40 x 40 cm^2 at 1.5 cm deep with various flattening filter heights……..…….. 88
Figure 4.18: 6 MV Varian off-axis ratios for 40 x 40 cm^2 at 10.0 cm deep with various flattening filter heights……..…….. 89
Figure 4.19: 6.0 MeV Varian off-axis ratios at 1.5 cm deep, 40 cm square field various flattening filter heights with increased number of histories..... 89
Figure 4.20: 6.0 MeV Varian off-axis ratios at 10.0 cm deep, 40 cm square field various flattening filter heights with increased number of histories..... 90
Figure 4.21: The 6 MV output factors for Varian, 6.0 MeV, 1.85 x original height…….. 91
Figure 4.22: The PDDs for 6 MV Varian for various field sizes.....… 92
Figure 4.23: Varian off-axis ratios, 5.3 MeV electron energy, various flattening filter heights at 1.5 cm deep……..... 94
Figure 4.24: Varian off-axis ratios, 5.3 MeV electron energy, various flattening filter heights at 10.0 cm deep……..... 95
Figure 4.25: The PDDs for Varian at 5.3 MeV electron energy and 1.4 x the original height of the flattening filter……..... 95
Figure 4.26: The Varian output factors, 5.3 MeV electron energy at 1.4 x original height…… 97

Figure 4.27: The process of achieving a validated Monte Carlo model for a radiotherapy linac…….. 99
Figure 5.1: A typical measurement of DOSI detector showing response versus position readout. Measurement was taken in Daresbury, where the detector was placed in parallel with a synchrotron beam collimator slit…….. 103
Figure 5.2: An example of a dynamic measurement obtained by DOSI detector where the sensitive array of the dosimeter placed 90° to a horizontal collimator slit moving vertically in a synchrotron beam……. 104
Figure 5.3: The Varian linac model in the Queen Elizabeth Hospital with the DOSI detector to be setup with water equivalent phantom surrounding the sensitive linear array……. 106
Figure 5.4: The Varian treatment head model using the BEAMnrc code…….. 107
Figure 5.5: Top left, a detail drawing of the DOSI pixel element in mm and top right, a structural drawing of the DOSI sensitive area and its guard ring. Bottom figure, the DOSI detector sensitive array on a PCB. *Courtesy of S. Manolopoulos*..... 108
Figure 5.6: The phantom used to model the DOSI detector in water medium using DOSXYZnrc…….. 109
Figure 5.7: The DOSI detector model that was used using DOSXYZnrc in a water phantom at 10 cm deep……... 109
Figure 5.8: The correction factor plots for different field sizes to convert the RW3 material to liquid water phantom for DOSI measurements. *Courtesy of S. Manolopoulos…….* 110
Figure 5.9: The DOSI profile across the 0.22 cm scoring width using Si voxels, 10 cm square field and 50 random number seeds……. 114
Figure 5.10: Comparing output factor results for MC Si voxels using 521 pegs4 data and DOSI measurements at 10 cm deep for 6 MV Varian…… 115
Figure 5.11: Comparing output factor results for MC thick and thin Si voxels at 10 cm deep for 6 MV Varian……..... 117
Figure 6.1: DOSI detector preparations for set-up with RW3 solid water slabs surrounding the sensitive volume…… 124
Figure 6.2: The Varian linear accelerator being mounted with a stereotactic collimator……..... 126
Figure 6.3: BEAMnrc linear accelerator head preview……..…… 128
Figure 6.4: Scoring voxels that were encoded using DOSXYZnrc….. 129
Figure 6.5: 6 MV Varian 10 mm stereotactic collimator at 7.5 cm deep…….. 131
Figure 6.6: 6 MV Varian 10 mm stereotactic collimator at 7.5 cm deep in log scale..... 131
Figure 6.7: 6 MV Varian 20 mm stereotactic collimator at 7.5 cm deep……..... 132
Figure 6.8: 6 MV Varian 20 mm stereotactic collimator at 7.5 cm deep in log scale..…….…… 132

Figure 6.9: 6 MV Varian 30 mm stereotactic collimator at 7.5 cm deep……. 133
Figure 6.10: 6 MV Varian 30 mm stereotactic collimator at 7.5 cm deep in log scale..…….. 133
Figure 6.11: 6 MV Varian 10 mm stereotactic collimator at 7.5 cm deep penumbra…….. 134
Figure 6.12: 6 MV Varian 20 mm stereotactic collimator at 7.5 cm deep penumbra…… 134
Figure 7.1: Elekta linear accelerator used in the Queen Elizabeth Hospital……. 150
Figure 7.2: 6 MV Elekta treatment head with no filter…….. 153
Figure 7.3: DOSXYZnrc scoring voxels used in the simulations…..... 154
Figure 7.4: 6 MV Elekta, Percentage Depth Dose, 100 cm SSD 10 x 10 cm^2 field..…….. 156
Figure 7.5: 6 MV Elekta unflattened beam off-axis ratios at 10 cm deep and 100 cm SSD……. 158
Figure 7.6: 6 MV Elekta unflattened beam using 6.0 MeV electron energy off-axis ratios…… 158
Figure 7.7: 6 MV Elekta flattened beam and unflattened beam at 10 cm deep and 100 cm SSD……. 159
Figure 7.8: 6 MV Elekta, output factors at 1.5 cm deep and 100 cm SSD…… 161
Figure C.1: FLURZnrc user code graphical user interface…….…….. 189
Figure C.2: The electron fluence plot using FLURZnrc for 6 MV Varian at 10 cm deep at 10 cm field width and 90 cm SSD..... 190
Figure C.3: Stopping power ratio for water to film for two different GafChromic films. *Courtesy of D. Kirby*……..…… 190
Figure D.1: Cross-sectional view of Elekta Precise treatment head. *Courtesy of Queen Elizabeth Hospital, Birmingham*..... 192
Figure E.1: Cross-sectional view of Varian 600C treatment head. *Courtesy of Queen Elizabeth Hospital, Birmingham*..... 193

List of Tables

Table 1.1: Some of the detectors that are used for measuring radiation dosimetry [55]…….…….. 15
Table 4.1: The best fit electron energy data for PDDs using original flattening filter height…… 78
Table 4.2: The discrepancies of the PDDs at the depth of 10, 20 and 28 cm……. 83
Table 4.3: The data that were used to plot the OF and the percentage errors…….. 86
Table 4.4: The result of the precision of the output factors at 6.0 MeV, 1.85 x original height…….…….. 91
Table 4.5: The result for the range of electron energy investigated….. 93
Table 4.6: The errors of the PDD at the depth of 10, 20 and 28 cm are demonstrated…… 96
Table 4.7: The deviations of the Monte Carlo result from the measured data…….. 98
Table 4.8: The summary of results for the linac machines…….. 99
Table 5.1: The correction factor used for DOSI measurements at depth of 1.5 and 10.0 cm. *Courtesy of S. Manolopoulos*….. 110
Table 5.2: The result for DOSI measurements of 9 voxels across the Si width……..……..… 114
Table 5.3: The result for DOSI measurements and the percentage differences……..…….. 115
Table 5.4: The result for MC and DOSI measurements and their percentage differences……..……. 116
Table 5.5: The result for MC thick and thin Si voxels and their percentage differences…… 117
Table 6.1: DOSXYZnrc parameters used in the GUI to define the water phantom.……...…….….. 129
Table 6.2: Penumbra broadening of the detectors used in stereotactic beams…… 135
Table 7.1: The summary of calculations made with the Monte Carlo code……..……..... 154
Table 7.2: The errors of the PDD at the depth of 10, 20 and 28 cm are demonstrated……...……. 156
Table 7.3: The largest percentage difference for the unflattened beam according to field sizes……..... 159
Table 7.4: The percentage difference for the output factors of the unfiltered beam at D_{max}……..…… 161
Table 7.5: The summary of results comparing between measured and calculated data……. 163
Table A.1: The best fit electron energy data for 6 MV Elekta from 6.0 to 6.5 MeV……. 176
Table A.2: The best match for flattening filter heights at 1.85 x, 1.9 x and 1.92 x specification…….. 177
Table B.1: The best match for flattening filter at 1.8 x, 1.83 x and 1.85 x original heights……..…… 181
Table B.2: The percentage differences for various electron energies… 183
Table B.3: The best match for flattening filter at 1.4 x original heights... 185

List of Abbreviations

% diff.	percentage difference
2D	two dimensional
3D	three dimensional
ADC	analogue-to-digital converter
BEAR	Birmingham Environment for Academic Research
C. D.	commissioning data
C. Data	commissioning data
CAX	central axis
CPU	central processing unit
CSDA	continuous slowing down approximation
CT	computed tomography
CTV	clinical target volume
CVD	compressed vapour-deposited
DBS	directional bremsstrahlung splitting
diff.	difference
DNA	deoxyribonucleic acid
EGSnrc	Electron Gamma Shower National Research Council of Canada
Eqn.	equation
ESTAR	Stopping Powers and Ranges for Electrons
FF	flattening filter
FPGA	fully programmable gate array
GTV	gross tumour volume
GUI	graphical user interface
IAEA	International Atomic Energy Agency
ICRU	International Commission on Radiation Units and Measurements
IMRT	Intensity modulated radiation therapy
linac	linear accelerator
M. Carlo	Monte Carlo
M. Data	measured data
MC	Monte Carlo
MLC	multileaf collimator
MOSFET	metal oxide semiconductor field effect transistor
MU	monitor unit
NIST	National Institute of Standards and Technology
NTCP	normal tissue complication probability
OAR	off-axis ratio
OF	output factor
PCB	printed circuit board
PDD	percentage depth dose
pixel	picture element
PMMA	polymethyl methacrylate
PTV	planning target volume
QA	quality assurance
ROF	relative output factor
S & H	sample and hold
SI	international system of units
SRS	stereotactic radiosurgery
SRT	stereotactic radiotherapy

SSD	source-to-surface distance
TCP	tumour control probability
TLD	thermoluminescent detectors
TRS	technical reports series
voxel	volume element

Chapter 1 - Introduction

1.1 Principle and Aims in Radiotherapy

From the discovery of x-rays by Wilhelm Conrad Roentgen in 1895, it had been realised soon afterwards that x-rays can be used as imaging and treatment modalities. In medical imaging, x-rays have been used to visualise the structure of tissues in living bodies including cancer cells (figure 1.1). This is achieved due to the x-ray properties which attenuate and interact differently in soft tissues and bones [1 - 3]. The outcome of this is x-ray radiography and computed tomography (CT). CT scans use x-rays to produce the modern day 2D slice images that can be stacked into 3D with an aid of computer tools as in figure 1.2.

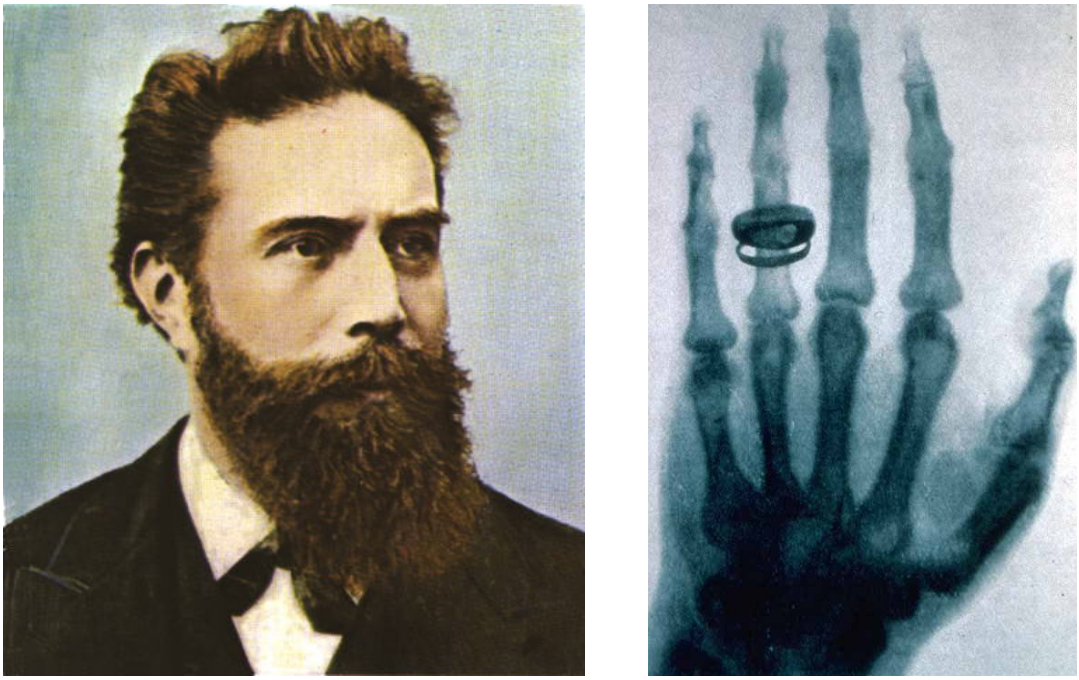

Figure 1.1: Left, Wilhelm Conrad Roentgen and right, the x-ray image of the hand produced in 23 January 1896. [4 - 6]

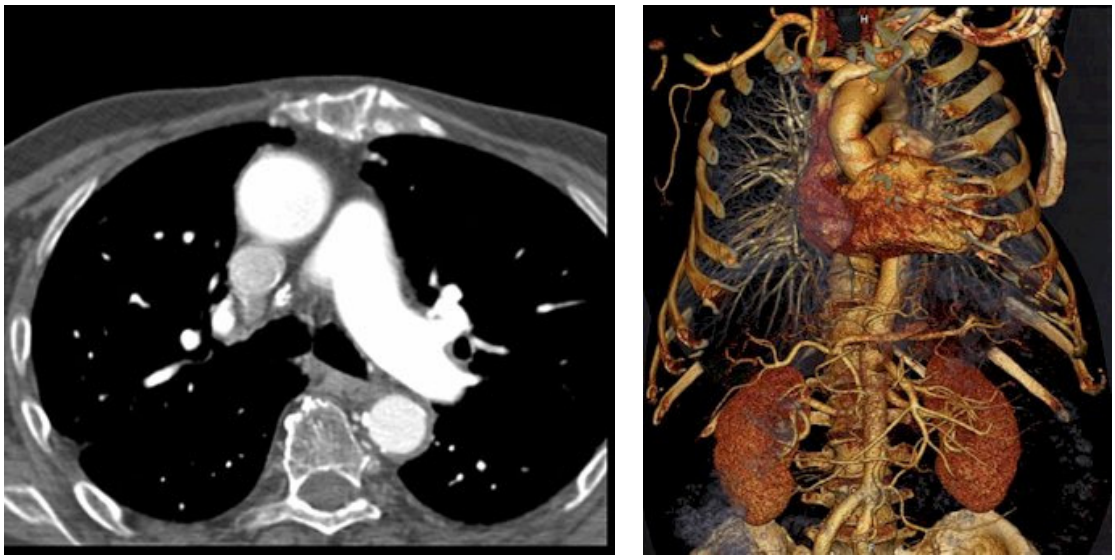

Figure 1.2: Left, a CT slice of the lung [7] and right, a CT reconstruction using a computer tool with a Siemens scanner [8].

In radiation therapy, high energy x-rays in the megavoltage range are used for cancer treatments. Today radiotherapy techniques have been improved with an aim to kill all cancer cells while preserving as many normal surrounding cells as possible. Wherever possible a cure for cancer is sought. If a cure is not possible, the aim is to relieve the symptoms of cancer (palliation), thereby improving the quality or extending the person's life. Radiotherapy can be used alone or with chemotherapy or surgery as a combined treatment [9].

Radiotherapy is used in treating growths such as various skin cancers; cancers of the mouth, nasal cavity, pharynx and larynx; brain tumours and many gynaecological cancers and lung cancers [9]. Photon radiation is also effective in treating leukaemia, breast, and prostate cancers and also for certain benign conditions such as arteriovenous malformation [9, 10].

Radiotherapy works by destroying the deoxyribonucleic acid (DNA), the nucleic acid that holds the genetic code in all living things. The DNA in cancer cells is damaged and thereby the radiation dose interferes with cell reproduction. When the irradiated cells fail to divide and reproduce themselves, they die in the attempt [9].

Normal cells are able to repair better from the damage caused by radiation exposure than the malignant and other abnormal cells. Thus, normal cells are able to recover if given the time to heal; usually a minimum of six hours is required, so in radiotherapy this is done by giving the dose in fractions. Fractionation involves repeating a smaller amount of dose throughout the total course of treatment. However, tumours with higher concentration of oxygen seem to be more responsive to radiotherapy than those with lower concentration of oxygen (hypoxic condition). Some types of tumour are more radioresistant, such as melanoma and sarcoma, whereas lymphoma is relatively very sensitive [9, 11].

If the dose and delivery of radiotherapy are well planned and the cancer is localised to the region of treatment, the cancer can be eliminated, and the normal tissues survive and the patient is cured. If not all of the cancer cells are killed, the cancer may revive. Since normal tissues cannot usually withstand the effects of further radiotherapy, treatment for cure is merely one chance for a patient and repeated treatments are for palliative purposes only. This is explained using probability curves [9, 12 - 15].

1.1.1 Tumour Control Probability (TCP)

When a small radiation dose, dD is irradiated independently on a population of N cancer cells, the number of cells eradicated, –dN, is proportional to N and dD, hence $\frac{dN}{dD} = -kN$ where $k = \frac{1}{D_0}$ [15]. The solution to this differential equation is the common exponential form,

$$N = N_0 e^{-D/D_0},$$

where, N_0 = the initial cell population and

D_0 = a dose characteristic of a large proportion of the population of cells being eradicated.

The tumour control probability (TCP) is the probability that all cells from a population of N_0 cells in a tumour are eradicated. The probability of any one cell surviving for a given dose, D, is just $\frac{N}{N_0} = e^{-D/D_0}$ and the probability of any one cell being eradicated is $1 - e^{-D/D_0}$, therefore the probability that all N_0 cells are eradicated during a given treatment regimen is a sigmoid-like function,

$$P(N_0 \text{ eradications}) = (1 - e^{-D/D_0})^{N_0}$$

1.1.2 Normal Tissue Complication Probability (NTCP)

The probability of radiation causing fatal damage to the healthy tissue which leads to serious complication arising from the treatment is called the normal tissue complication probability. This can be derived from similar grounds, where it is anticipated that, for a given treatment plan; normal tissue is less susceptible than tumour cells. As a result the probability of complication versus dose relation for normal tissue has the same form as that of tumour tissue although the rapid increase in probability occurs at a slightly higher characteristic dose [15].

1.1.3 Therapeutic Ratio and Fractionation

The ratio of TCP to NTCP probabilities gives the therapeutic ratio which is in clinical terms; maximal over a very small range of dose. This narrow range of effective therapeutic dose means that dosimetric accuracy is very important, defining the role of the physicist in radiotherapy practice. Spreading out the time in dose delivery usually improves the range of therapeutic dose. This gives healthy tissue a further advantage in which normal mechanisms of repair diminish the susceptibility of healthy tissue to radiation. A typical radiation dose delivered to a patient is 50 Gy, in which the total prescription dose would be spread over many weeks with a fraction of approximately 2 Gy per day [15].

The probability curves between cure and complication is in close proximity, as shown in figure 1.3 below. Therefore, other than geometrical accuracy and reproducibility of treatment, dosimetric precision is crucial to obtain a therapeutic gain [16, 17]. Since the effectiveness of the treatment depends on delivering the dose with an accuracy of 5% or better [18], a significant role for the physicist is to measure the dose to its prescribed amount [2].

In order to achieve this, the physicist is required to determine the best available dosimeter. Together with the aid of a computer and Monte Carlo codes, beam modelling has become valuable to provide a reference dose estimate for a planned treatment.

The role of the physicist in a radiotherapy department is to:-

1. perform commissioning and quality assurance, which is to measure the dose and demonstrate the reproducibility of the measurement of dose of the radiation source.

2. perform treatment planning which is to design patient treatments by determining the optimum positioning or targeting of the radiation source and time of exposure needed to deliver the dose prescribed by oncologists [15].

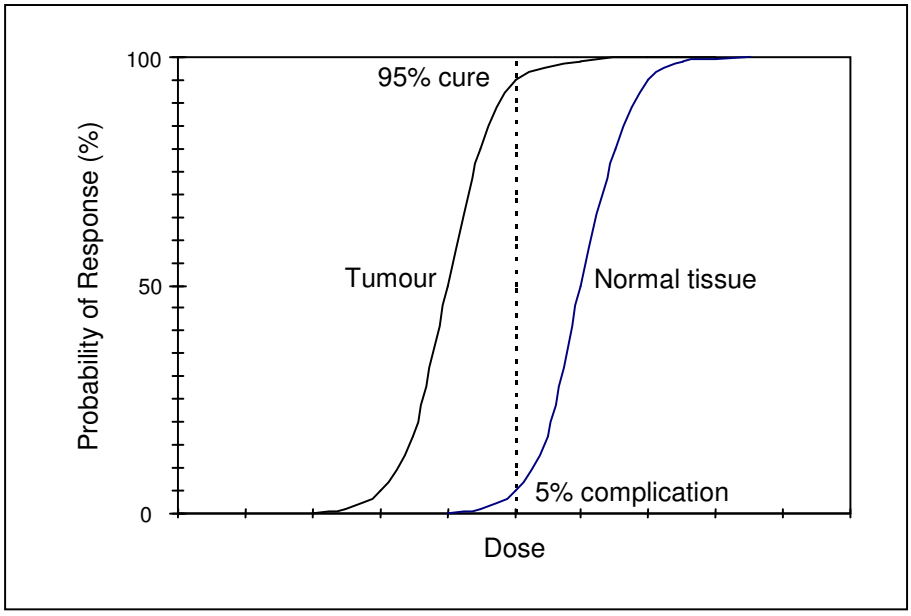

Figure 1.3: Relationship between the response of both tumour and normal tissue and radiation dose [14].

There are two types of radiation therapy. One is external beam radiation therapy, the other is internal radiation therapy known as brachytherapy, where the radioactive source is implanted. Some of the common sources are Cs-137, I-125 and Ir-192. These needles or interstitial seeds are typically used in cervical cancer, prostate cancer as well as head and neck cancer respectively [11, 15]. However, this subject is not part of the research, this study focusing on wholly external beam radiotherapy.

In external beam radiation therapy, a radiation beam is targeted at a particular part from outside the body using for instance a cobalt-60 teletherapy unit or more commonly a linear accelerator (linac) source explained in Chapter 3.2. Some of the techniques used in external beam radiotherapy include conformal radiotherapy, stereotactic treatment and intensity modulated radiation therapy [15]. These are now explained in greater detail.

1.1.4 Conformal Radiotherapy

The purpose of conformal radiotherapy is to tailor a dose envelope to a tumourous target volume and to deliver as low a radiation dose as possible to all normal cells. This means that the dose 'conforms' to the target volume and is achieved by using static multi-field coplanar or non-coplanar beams. The target volume is applied to the full extent of the tumour including any marginal spread of the disease plus a 'safety' margin extending to the so-called mobile target volume [14, 19, 20].

To maximise the chance of a successful local tumour control using 3-D conformal radiotherapy, the gross tumour volume (GTV) is defined by an appropriate tomographic scan. It is typical to add a 0.5 cm margin to ensure that microscopic tumour spread is adequately irradiated and controlled, to form the clinical target volume (CTV). Added to this is a further margin of normally 1.0 cm to account for patient setup variations and tumour movement between treatments, the resulting outline being the planning target volume (PTV). However, the margin could be reduced to 0.6 mm, for instance in prostate cancer to avoid critical organ such as the rectum [21]. An example of the margins is shown in figure 1.4.

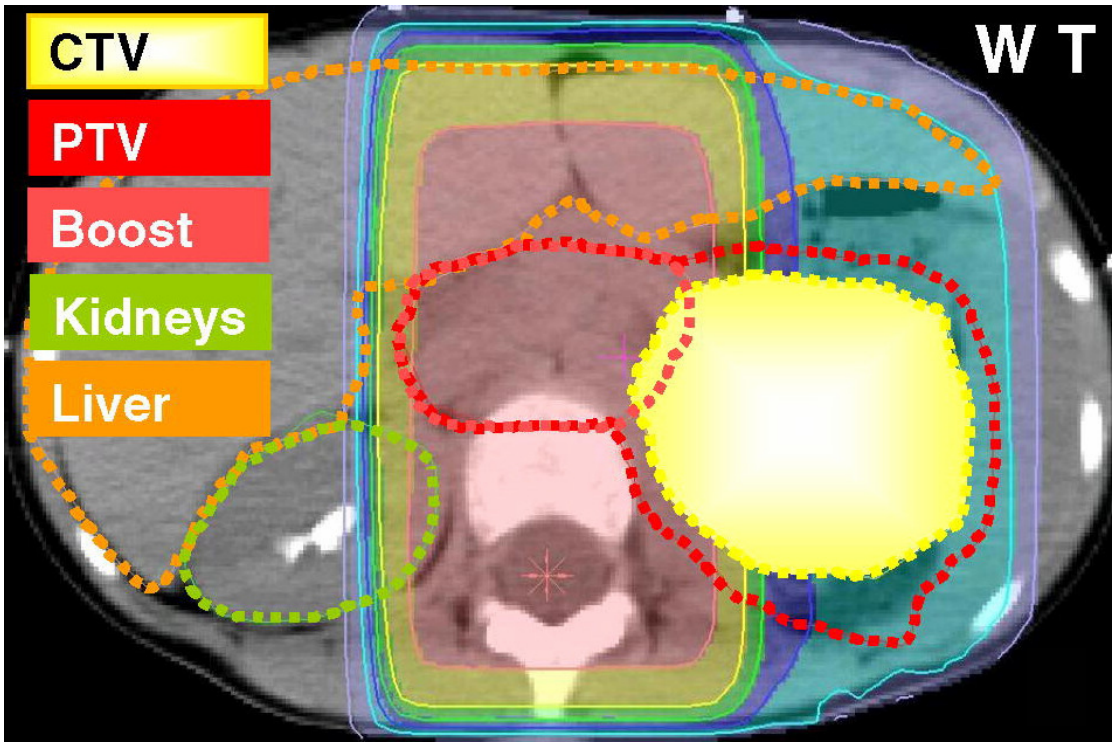

Figure 1.4: A typical CTV and PTV delineated for Wilms' Tumour radiotherapy [22].

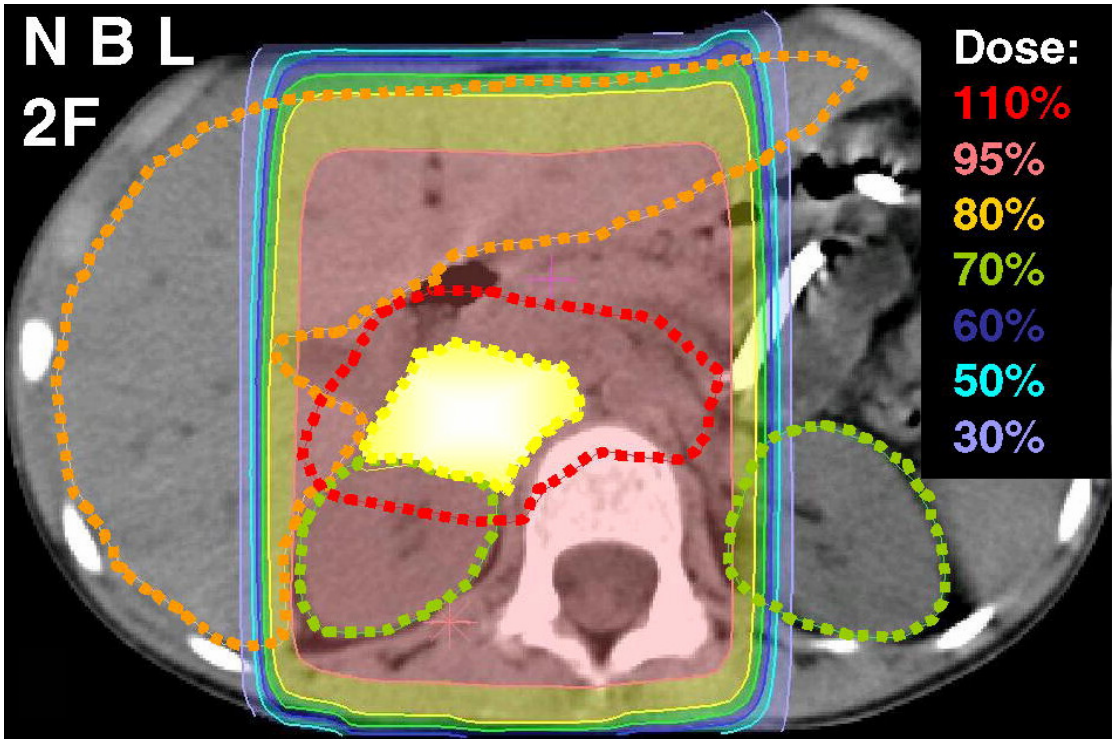

Figure 1.5: A typical 2 field-beam showing the isodose curves in neuroblastoma treatment planning [22].

An extra margin may be added to account for the distance between the 50% and 90% isodoses of the beam penumbra. Normally, the 50% isodose locates along the edge of the field shaping device, while the 90% isodose coincides with the PTV. This could be a margin of 0.5 to 1.0 cm circumference surrounding the PTV. In practice, production of the PTV from the GTV is performed in one step, without explicitly calculating the CTV. The CTV is implied by the size of the added margin [21, 23]. The isodose curves are displayed superimposed on CT image as an example in figure 1.5.

1.1.5 Stereotactic Radiation Treatment

Stereotactic radiosurgery (SRS) is a radiation therapy technique by which highly focused doses of radiation are delivered to a target through non-coplanar isocentric arcs in a single fraction irradiation. When the same procedure is being delivered in multiple fractions, it is called stereotactic radiotherapy (SRT). Both methods demand highly accurate and precise localisation of the treatment volume, since it is a treatment method for treating small lesions, generally less than 4 cm in diameter [14].

Stereotactic radiosurgery (figure 1.6) is considered when conventional surgery is not recommended due to excessive risk or non-operable lesions. Unlike conventional radiotherapy, the aim is that the target is to be destroyed rather than treated; therefore healthy cells are not preserved within the small volume. Irradiation for a single shot requires a high dose gradient and rigorous precision. Stereotactic radiosurgery eradicates tissues by inducing

gliosis or fibrosis within it. The most common application of radiosurgery is the treatment of benign arteriovenous malformations [14].

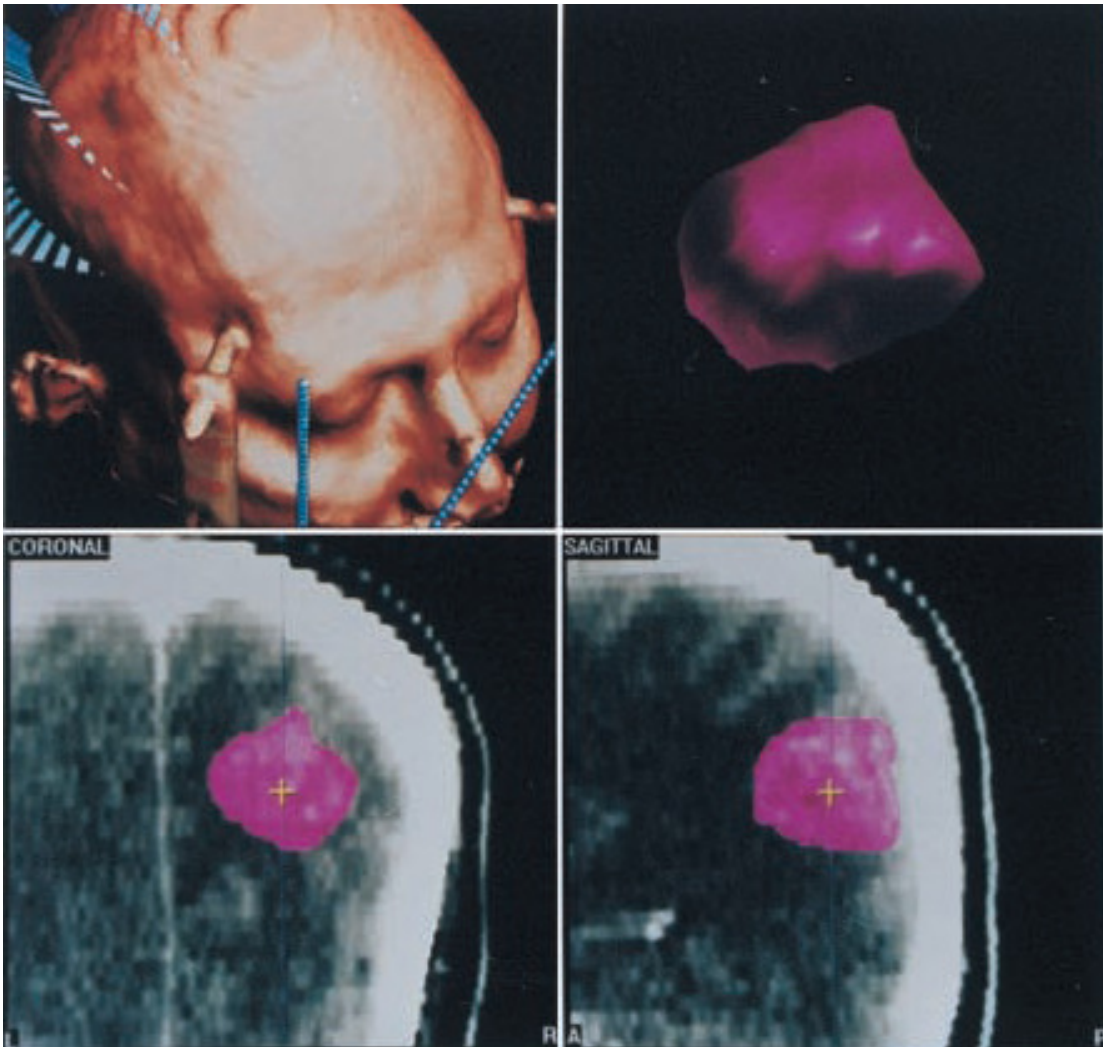

Figure 1.6: Top left, a stereotactic radiosurgery performed on a patient with 3D target image (top right) and 2D depictions of the target (bottom left and right) [24].

1.1.6 Intensity Modulated Radiation Therapy

Intensity modulated radiation therapy or IMRT is a type of conformal radiation therapy where the intensity of the radiation beam is modulated across the treatment field, therefore the field is not a uniform intensity. The treatment

planning algorithm is based on inverse planning where the algorithm starts with an ideal distribution and works backwards to find beam profiles to produce the treatment plan. Comparatively with conventional treatment, forward planning is used where a number of beams are directed from different directions and combined with different weights by trial and error to give acceptable dose distribution [25]. An example is given in figure 1.7 below.

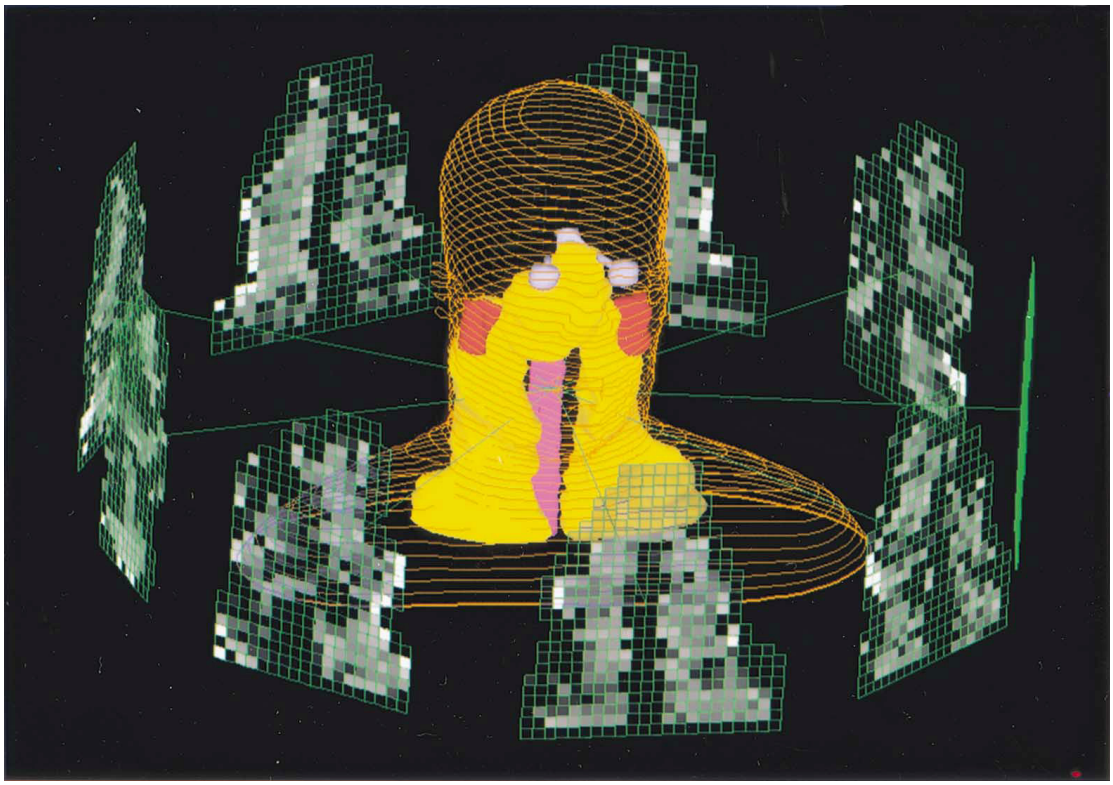

Figure 1.7: An example of a 9 field IMRT technique dose distributions, where the grey levels indicate the intensity values of the beamlets [26].

The efficacy of this treatment is still being disputed due to some of the reasons below:-

(i) There is only a small amount of clinical data to support its use.

(ii) There are too many inaccuracies associated with patient positioning.

(iii) Organ motion remains beyond the physicist's control.

(iv) The quality assurance procedures for IMRT are in their infancy.

(v) IMRT requires unusually long delivery times that are disruptive in a busy hospital environment.

(vi) IMRT involves patchwork of smaller fields; hence excessive transmission and leaf leakage radiation are generated during irradiation.

(vii) Fusion of CT and magnetic resonance imaging is inaccurate for IMRT.

(viii) IMRT start-up and maintenance costs are too expensive.

(ix) There is a costly learning curve for IMRT [27].

Criticisms concerned with IMRT are also cited in other literature [28 - 43].

1.2 The Basics of Small Field Dosimetry

Small field dosimetry relates to radiation field widths in the range from 0.4 to 4 cm, these being similar to typical secondary electron ranges. This small size of field is particularly used in stereotactic and IMRT modalities. The methods use high gradient fields which require higher beam accuracies and dose measurements. The dosimeters for appropriate measurements for these fields must be smaller than the size of the beam therefore some detectors are too large to be used with these techniques [44].

The difficulties in measuring small fields include the uncertainty and the complexity of dose normalisation; a large beam may contain a small beamlet

of various dose levels as in IMRT and lack of electron equilibrium (as explained in 2.3) at the field edge to be measured using conventionally available detectors in the radiotherapy department. Some of the detectors used for small fields are the diode detector, the PinPoint ionisation chamber and the diamond detector [44]. These detectors have their own advantages and disadvantages in their use. The detailed functions of these detectors will be discussed in chapter 3.

1.3 Background of the Investigation.

There are various dosimeters to measure radiotherapy output depending on the applications, for example ionisation chamber, chemical dosimetry, calorimeter and solid state detectors [45]. Solid state detectors have good spatial resolution, stability and robust construction [46 - 48]. These include diamond detectors and diode detectors which had increased use in radiotherapy [2]. Some of the application of the dosimeters are summarised in table 1.1.

Diamond detectors have near tissue equivalence and are suitable to be utilised for high energy electron and photon measurements in on-line applications [49 - 53]. However, the drawbacks are their non-linearity in dose and dose rate outputs [2]. The PinPoint ion chamber is an excellent ionisation chamber for small field measurements; its spatial resolution of around 0.2 cm is superior to that of larger ionisation chambers [54]. Nevertheless, despite its advantages the PinPoint chamber shows sensitivity to an absence of lateral

electronic equilibrium, which limits its fields of roughly 2 cm or larger for output factor measurements [54].

Table 1.1: Some of the detectors that are used for measuring radiation dosimetry [55].

DETECTOR	APPLICATION	VOLUME (cc)	RESOLUTION (mm)
Ion chamber (Farmer)	Radiotherapy & Calibration	0.6	7.0
Ion chamber (sealed)	Radiotherapy beam scanning	0.14	6.0
PinPoint chamber	Radiosurgery	0.015	2.0
Diamond	Radiotherapy beam scanning	1.8×10^{-3}	0.26
Diode	Radiotherapy beam scanning	0.3×10^{-3}	0.06
Film	Quality Assurance & Verification	10^{-6}	0.10

Another detector which is called DOSI [55 - 57], a prototype detector, has spatial resolution of 0.025 cm and is a position sensitive dosimeter which is capable of real-time measurement. However, its performance has never been compared in detail with Monte Carlo simulations; as a consequence, its limitations are not verified using computer calculations.

With the availability of computer speed and storage, dose calculation models have gradually evolved from simple scatter and inhomogeneity corrections to improved superposition/convolution models [58 - 61]. The next step which has already been available for many years is full Monte Carlo simulations which would result in the highest dose calculation accuracy. However, the limitations of computer power may still not always allow full MC simulations in practice.

Simplification and variance reduction techniques to speed up the calculations may still be necessary [62].

1.4 The Scope of This Work.

This research is primarily aimed at the improvement of our knowledge of dosimetry in IMRT and stereotactic radiation modalities which use small fields. This will be achieved by studying various dosimeters, especially the DOSI detector, and comparing them with Monte Carlo calculations. Small fields experience lack of electron equilibrium in the interfaces between entrance and exit dose which are typical non-homogeneous situations [3, 54, 63]. In such situations a lot of inaccuracies emerge in dose calculations and in detector measurements.

High resolution and accuracy are still needed at the beam edges in small field measurements to be used for treatment planning. Solid state detectors are useful in this situation where ionisation chambers cannot be utilised as a result of their physical size. These detectors give a reliable investigation of dose variation in non-equilibrium conditions. The construction of a sufficiently small mass of detector material does not perturb the radiation fluence much [3, 63, 64].

Hence, solid state detectors are particularly important for megavoltage energies because they offer sufficiently high spatial resolution to explore non-equilibrium regions as well as giving predictable response in a range of

scattered radiations. Therefore, the dose can be predicted on a basis of the response of the material and the relative energy absorption of the material and the medium [3, 64].

The Monte Carlo method represents the most precise method for dose calculations in three-dimensional heterogeneous media. The computer code simulates the transport of particles from first principles and takes into account the electronic disequilibrium at medium interfaces [65]. Comparisons of particle transport codes with standard experiments are very important to understand the underlying physics behind the outcome.

The EGSnrc Monte Carlo code has been used to examine changes in the output factors, in these circumstances enabling corrections to be devised to explain the perturbation caused by the detector in these fields. This is important for evaluating the accuracy of the dose delivered to patients undergoing treatment.

One of the aims of this project is to investigate a prototype of the DOSI detector, as a radiotherapy dosimeter for small field measurements. Different effects will be investigated; such as non-tissue equivalent response of low energy scattered photons and the detector size dependence due to electron equilibrium.

The radiation sensitive material of DOSI is silicon, which as it is not tissue equivalent, will give a perturbation to the dose measurement particularly at

low energies [64]. Essential corrections for parameters needed in radiotherapy and obtained with the DOSI detector such as off-axis ratios and output factors have to be validated with Monte Carlo calculations before clinical implementation can occur in every radiotherapy department.

This is a promising detector to be used in the study of small fields due to its small spatial resolution and dynamic responses. IMRT and stereotactic methods use small fields to treat highly conformal and localised cancer using multileaf collimators and small conical stereotactic collimators, respectively. Measurements for stereotactic beams have been performed in the penumbral regions using DOSI. A comparison between Monte Carlo calculations and direct measurements of the parameters will be helpful for a better evaluation of this detector.

Cavity theory is used to determine how to relate the detector measurement to the dose deposited in the surrounding medium. Bragg-Gray cavity theory assumes that the electron fluence in the cavity is not perturbed. Recent Monte Carlo findings have shown that this assumption in the small cavity theory is incorrect for solid state detectors. Although new theories have been proposed by some authors [66, 67], the Bragg-Gray theory is still relevant to be used in this project.

The use of unfiltered radiotherapy beam has been reported to be beneficial for IMRT [68, 69]. This project will also investigate the use of unfiltered beams using Monte Carlo approach to investigate the beam profiles and compare

these with beam measurements. Therefore, theoretical calculations and practical measurements have been compared in this study. It is hoped that this research will enable the development of generally acceptable filterless radiotherapy linac applications for clinical practice in IMRT.

1.5 Layout of the Project.

This thesis consists of 8 chapters altogether. In chapter 2, the fundamentals of radiotherapy physics is explained. This includes electron and photon interactions with matter, quantities that were used, the significance of percentage depth doses and output factors and cavity theory are also explained in this chapter.

Chapter 3 describes detectors mentioned in this research, the linear accelerator, the Monte Carlo method, its brief history and principles. The use of EGSnrc Monte Carlo code, the parameters and the variance reduction technique used in the simulations, the applications of DOSRZnrc and DOSXYZnrc.

In chapter 4, the characterisation of the linear accelerator head models are discussed. The chapter describes how the modelling process of the two linacs, Elekta and Varian were optimised, evolved and verified against benchmark data using megavoltage photon beams. Validated results are also illustrated and summarised.

In conjunction with the validation of MC results for 6 MV Varian machine, one investigation had been performed by another student to calibrate the correction factor for GafChromic films in proton beam measurements using electron spectra. The published work by Kirby et al. [70] is described briefly in Appendix C, while 3 other investigations using the validated models (Elekta and Varian) were conducted in this research and were described in the proceeding chapters.

Chapter 5 investigates the novel DOSI detector; its performance and its empirical measurement are examined. The effect of the high atomic number of silicon relative to water has been simulated and evaluated. The difference in output factors as measured by standard data has been compared. This chapter also discussed how the detector could be improved by using Bragg-Gray cavity theory. This work is unique because this is the first example of a Monte Carlo model developed for a thin (300 µm) and ultra-thin (25 µm) silicon strip-based dosimeter.

An investigation of the stereotactic beams using Monte Carlo methods is put forth in chapter 6. The performance of DOSI detector, PinPoint ion chamber and diamond dosimeter have been obtained. The results have been compared using empirical data against Monte Carlo code. The impact of lateral electronic disequilibrium in small fields has been discussed. Monte Carlo models have been used to analyse the use of the DOSI detector in a clinical situation where, due to the smallness of fields used, ideal solutions for routine dosimetry have still not been developed.

Chapter 7 reports the calculations of the unflattened beam of the linear accelerator. The flattening filter from the validated model was removed from the calculation. The simulated result has been compared with the measured data. This investigation reveals the effect of filterless beam in IMRT that relates to the dose reduction in cancer patients. Monte Carlo models, previously developed and validated for conventional flattened fields, are used to predict beam profiles for unflattened beams in comparison with measurements, which collectively have not been performed elsewhere for the Elekta therapeutic linear accelerator.

The final chapter is the summary of the results obtained from the project. It is the conclusion of the whole research. Suggestions for improvement and future work are also provided as a continuation from this study, mainly recommending using further computer simulations and comparing them with experimental results.

Chapter 2 - Fundamentals of Radiotherapy Physics

The fundamentals in radiotherapy physics are based on the theories of radiation interactions with matter, the quantities used in radiation measurements and the underlying principles and physics behind them, the detectors used for dosimetry and the sources of radiation suitable for treatment. These will be described in this chapter and the next in order for the terms used in this thesis to be adequately understood. All of these terms and definitions can be found in many literature sources and books including ICRU report 33 and authors such as Attix, Knoll and Khan [2, 71 - 74].

2.1 Interactions of Radiation with Matter

All living and non-living materials are composed of individual atoms which can be divided into smaller components, the nucleus, which is the central core of the atoms consisting of nucleons (protons and neutrons) and the electrons which surround the nucleus in orbital clouds [74].

In contrast to matter, radiation applies to the emission and propagation of energy in vacuum or in a medium. The dual nature of radiation is considered as particles known as photons and also as electromagnetic waves. Besides photons that travel at the speed of light; electrons, protons and neutrons can also travel with high speeds but never reach the speed of light in vacuum [74].

Electrons interact with matter in 3 different ways. One is through interactions with orbital electrons, the other through the electric fields of the atoms and another with the nuclei of the atoms. The primary interactions between photon radiation and matter could be possible in 5 ways which are coherent scattering, photoelectric effect, Compton scattering, pair production and photo disintegration. However the mechanism of photo disintegration where a nucleon is ejected from the nucleus is not discussed in this thesis since the threshold for the occurrence depending on the material used is about 8.5 MeV for heavy nuclei and 10.86 MeV for most isotopes with lower atomic number and is beyond the scope of this research [74, 75].

2.1.1 Electron Interactions

As an electron passes through matter, it interacts with the atoms mainly through Coulombic forces. Most of the photon interactions transfer small amounts of the incident kinetic energy of the electron. Hence, electrons lose their kinetic energy gradually and continuously as they go through medium. This process of energy loss is often referred to as the continuous slowing down approximation (CSDA). The energy loss by the electron depends on the electron energy, number of atomic electrons per unit volume and the ionisation energy of the atoms in the medium [2, 3, 76].

Through these collisions the electrons may lose their kinetic energy through collision and radiative losses or change their direction of travel via scattering. Hence, electrons interactions can be classified as energy loss interactions or

scattering interactions. However, it is important to note that energy deposition and scattering are not necessarily independent events. Interactions can be soft collisions with the atomic field, hard collisions with the orbital electron and radiative interaction with the nucleus [3, 77].

2.1.1.1 Stopping power

The average energy loss of a charged particle is described by the linear stopping power, S with a unit of $J.m^{-1}$ while the mass stopping power, $\frac{S}{\rho}$ is introduced to cancel out the density dependency. The change in direction of electrons is explained by the mass scattering power. The total mass stopping power of a material for charged particles is defined by the quotient $\frac{dE}{\rho dl}$, where dE is the total energy lost by the particle travelling a path length, dl in the material of density ρ. The typical unit for the quantity is $J.m^2.kg^{-1}$ or $MeV.cm^2.g^{-1}$ [2, 3, 71]. The total mass stopping power can be written as:-

$$\left(\frac{S}{\rho}\right)_{tot.} = \left(\frac{S}{\rho}\right)_{col.} + \left(\frac{S}{\rho}\right)_{rad.} \qquad \text{Eqn. 2.1}$$

where, $\left(\frac{S}{\rho}\right)_{col.}$ = the collisional mass stopping power and

$\left(\frac{S}{\rho}\right)_{rad.}$ = the radiation mass stopping power.

Stopping power is not used directly in this research, but a collaboration work with another PhD student is described in Appendix C where the mass stopping power was used to calibrate GafChromic films.

2.1.1.2 Soft collision interactions

An electron that passes close to an atom but does not directly hit an orbital electron will interact with the atom as a whole and experience soft collision. If an orbital electron absorbs enough energy, this interaction may leave the atom excited or ionised. A typical electron transfers approximately half of its total kinetic energy to the material through a large number of soft collisions [3, 77].

2.1.1.3 Hard collision interactions

An interaction when the incident electron collides with an orbital electron is referred to as a hard collision interaction. Part or all of the energy of the incident electron will be transferred to the orbital electron leading to the ejection of the bound electron. If the energy transferred exceeds the binding energy of the electron, the bound electron is ejected. The ejected electron, called a secondary electron or delta ray (δ-ray), occasionally has sufficient energy to cause subsequent ionisation. The vacancy in the orbital shell will be filled with the outer orbital electron followed by emission of characteristic x-rays or sometimes reabsorption of the characteristic x-rays and reemission of

the energy in the form of monoenergetic electrons called the Auger electrons [3, 74].

2.1.1.4 Radiative interactions

Radiative interactions are interactions between the incident electron and nuclei of the material atoms result in electron deflection and energy loss of the electron through production of x-ray photons known as bremsstrahlung. The incident electron will lose a small fraction of its energy in being deflected from its original path most of the time. As the electron decelerates, the electron suffers further deflections from its course and may encounter partial or complete energy losses throughout this process [3].

The outcome of the electron-nucleus interactions has a continuous x-ray spectrum up to the initial energy of the electron. The direction and the emission of bremsstrahlung is dependant on the energy of the incident electron. As the energy of the electron increases the direction of the bremsstrahlung x-ray is increasingly forward. Thus, transmission in the megavoltage range would create a beam of x-rays on the other side of the target [74]. For high energy electrons, ionisation can be ignored due to the fact energy loss by radiative interaction is much greater. Ionisation dominates once the energy of the electron drops below a critical energy, E_c. This can be estimated as:-

$$E_c \approx \frac{600}{Z} \text{ MeV} \qquad \text{Eqn. 2.2}$$

where, Z = the atomic number of the material [2, 78, 79].

2.1.2 Photon Interactions

In photon interactions, four types of events occur abundantly in radiotherapy. Three of these interactions, Rayleigh (coherent) scattering, photoelectric absorption and Compton (incoherent) scattering are predominant in the case when the energy of the photons does not exceed several MeV. While Rayleigh scattering is an elastic scattering where the incident photon is absorbed and reemitted without loss, photoelectric absorption and Compton scattering involve losses with the orbital electrons in the inner and outer shell of the absorbing medium respectively [2, 73, 74].

The fourth interaction is pair production and can happen only if the energy of the incident photons is at or above the energy threshold of 1.022 MeV which is equivalent to the rest mass of electron and positron (positive electron). The photon in the pair production mechanism involves interaction with the field of the nucleus of the absorbing medium [74].

Each of these interactions can be represented by its own cross-section which varies with photon energy and atomic number in a specific way [2, 74]. The total mass attenuation coefficient can be written as:-

$$\frac{\mu}{\rho} = \frac{N_A}{A}\sigma \qquad \text{Eqn. 2.3}$$

where, N_A = Avogadro's number,

A = the atomic mass number and

σ = the cross section of the material.

Hence, the sum of all the interactions yields the total mass attenuation coefficient given by the formula:-

$$\frac{\mu}{\rho} = \left(\frac{\mu}{\rho}\right)_{coh} + \left(\frac{\mu}{\rho}\right)_{pe} + \left(\frac{\mu}{\rho}\right)_{incoh} + \left(\frac{\mu}{\rho}\right)_{pair} \qquad \text{Eqn. 2.4}$$

where, $\left(\frac{\mu}{\rho}\right)_{coh}$ = the mass attenuation coefficient for coherent scattering,

$\left(\frac{\mu}{\rho}\right)_{pe}$ = the mass attenuation coefficient for photoelectric effect,

$\left(\frac{\mu}{\rho}\right)_{incoh}$ = the mass attenuation coefficient for Compton scattering and

$\left(\frac{\mu}{\rho}\right)_{pair}$ = the mass attenuation coefficient for pair production.

2.1.2.1 Rayleigh (Coherent) scattering

Rayleigh scattering, also known as coherent scattering is not of great importance in radiotherapy. It is negligible at energies above approximately 100 keV in soft tissues. Rayleigh scattering retains its original energy after changing its direction at low-energy photons. Furthermore, it is not directly

responsible for energy deposition [2, 74]. This process is usually neglected in x-ray interactions and computer simulations since no energy loss takes place but a complete model of the photon transport is sometimes vital in Monte Carlo code due to the change in x-ray directions [80].

Rayleigh scattering dominates over incoherent scattering for low photon energy and the probability is most prominent in high-Z absorbers. However the deflection angle decreases with increasing energy reducing the significance to low energies [73]. The cross section for coherent scattering is approximately described by:-

$$\sigma_{coh} \propto Z^{2.5} E_p^{-2} \qquad \text{Eqn. 2.5}$$

$$\Rightarrow \left(\frac{\mu}{\rho}\right)_{coh} \propto \frac{Z^{2.5}}{A} E_p^{-2} \qquad \text{Eqn. 2.6}$$

where, $\left(\frac{\mu}{\rho}\right)_{coh}$ = the mass attenuation coefficient for coherent scattering and

E_p = the incident photon energy.

2.1.2.2 Photoelectric effect.

Photoelectric effect occurs when the incident photon disappears after interactions with a tightly bound electron (electrons in the inner shells) whose binding energy is equal or less than the photon energy [2, 3, 74]. The kinetic energy of the ejected photoelectron, E_k is given by:-

$$E_k = E_p - E_b \qquad \text{Eqn. 2.7}$$

where, E_p = the incident photon energy and

E_b = the binding energy of the electron.

The photoelectron dissipates its energy in the absorbing medium mainly by excitation and ionisation. The photoelectric cross section, σ_{pe} approximately varies with incident photon energy and absorber atomic number which is proportional to the equation below:-

$$\sigma_{pe} \propto Z^4 E_p^{-3} \qquad \text{Eqn. 2.8}$$

$$\Rightarrow \left(\frac{\mu}{\rho}\right)_{pe} \propto \frac{Z^4}{A} E_p^{-3} \qquad \text{Eqn. 2.9}$$

Photoelectric absorption dominates at high atomic number, Z of the materials and at low photon energies, E_p [81, 82]. Since $\frac{Z}{A}$ is roughly equal to a constant, the mass attenuation coefficient for photoelectric absorption, $\left(\frac{\mu}{\rho}\right)_{pe}$ can be said to have a ~ Z^3 dependence [2, 3, 74].

2.1.2.3 Compton (Incoherent) scattering

Compton scattering or incoherent scattering is an inelastic collision interacting with free or bound electrons in the outer shells. The incident photon loses part

of its energy to the recoil electron and is scattered with the remaining energy. Because the scattered electrons transfer its energy to the absorbing medium by this interaction, it is a mechanism of great importance for dose measurements. In tissue-like media, the Compton interaction is the dominant energy deposition process in the therapeutic energy range in radiotherapy [3, 81, 83].

Compton scattering takes place mainly in the absorption of low atomic number of materials and high x-ray energy. The probability of the Compton scattering per atom is expressed as:-

$$\sigma_{incoh} \propto Z E_p^{-1/2} \qquad \text{Eqn. 2.10}$$

$$\Rightarrow \left(\frac{\mu}{\rho}\right)_{incoh} \propto \frac{Z}{A} E_p^{-1/2} \qquad \text{Eqn. 2.11}$$

Due to the constant property of $\frac{Z}{A}$, the Compton mass attenuation coefficient is not dependant on the atomic number [2].

2.1.2.4 Pair production

In pair production, the photon that interacts with the Coulomb field of the nucleus disappears and simultaneously an electron-positron pair appears. Energy at or in excess of the sum of the electron and positron rest masses is needed to provide kinetic energy of the pair. The electron and positron from

pair production lose their kinetic energy by excitation, ionisation and bremsstrahlung, just like any other secondary electrons. But, when the positron has exhausted all its kinetic energy, it recombines with an electron which annihilates into two photons each with energy of 0.511 MeV [3, 74].

The threshold energy required to create an electron-positron pair is their combined rest-mass energy of 1.022 MeV, which is possible only in the megavoltage range. Two annihilation photons of 511 keV energy are created later. The two annihilation radiations are ejected in opposite direction [3, 74]. The probability of pair production is given by:-

$$\sigma_{pair} \propto Z^2 \log E_p \qquad \text{Eqn. 2.12}$$

$$\Rightarrow \left(\frac{\mu}{\rho}\right)_{pair} \propto \frac{Z^2}{A} \log E_p \qquad \text{Eqn. 2.13}$$

From equation 2.7 above, considering $\frac{Z}{A}$ is a constant, interactions by pair production increase rapidly above 1.022 MeV with the atomic number, Z and the logarithm of the photon energy, E_p [2].

2.2 Quantities and Units in Radiotherapy

Many quantities and units are used in radiotherapy, but the ones described in these sections are merely those that have been used or mentioned in this research. These quantities are chosen according to importance and are summarised due to limited space.

2.2.1 Fluence

A beam of photons or charged particles can be described by many terms. One of which is the fluence that can be defined as:-

$$\Phi = \frac{dN}{dA} \qquad \text{Eqn. 2.14}$$

where, dN = the number of photons and

dA = the cross-sectional area of an imaginary sphere centred on the source.

The unit for fluence is m^{-2}. Meanwhile, the energy fluence is given by:-

$$\Psi = \frac{dE}{dA} \qquad \text{Eqn. 2.15}$$

where, dE = the incident energy and

dA = the cross-sectional area of a sphere, as above.

The unit for energy fluence is $J.m^{-2}$ [2, 74, 77].

2.2.2 Absorbed Dose

The term absorbed dose is referred to as the quantity of radiation energy that has been transferred to the medium which is applicable to any type of radiation and any medium [71]. Therefore, the absorbed dose is expressed by:-

$$D = \frac{d\bar{E}}{dm} \qquad \text{Eqn. 2.16}$$

where, $\frac{d\bar{E}}{dm}$ = the mean energy imparted by ionising radiation to a small mass of matter [74]. The international system of units (SI) for the absorbed dose is the gray, (Gy) defined as:-

$$1\ Gy = 1\ J.kg^{-1}$$

The dose deposition will be due to the electrons released by the photon beam, when a radiation beam passes through a medium. Furthermore, the released electrons move through the medium and deposit their energy along their paths. Therefore, the absorption of energy from electrons in megavoltage beams is deposited at a distance from the point of energy transferred by the photon. Hence, a non-electronic equilibrium or at best a quasi electronic equilibrium occurs [2, 3, 74].

2.2.3 Percentage Depth Dose (PDD)

The absorbed dose distribution in a phantom is the result of a statistical accumulation of energy deposition events that varies with depth. This variation relies on the beam quality or energy, field size and source to surface distance (SSD). The depth doses are usually measured in water media by using an ionisation chamber [2, 74]. The quantity percentage depth dose is expressed by:-

$$PDD = \frac{D_d}{D_{max}} \times 100\% \qquad \text{Eqn. 2.17}$$

where, D_d = the absorbed dose in any depth and

D_{max} = the maximum absorbed dose at depth on the central axis.

Several PDD curves for different photon energies are shown in figure 2.1. The depth of D_{max} increases with the increasing beam energy due to higher range of secondary electrons. The build-up region is between the surface and the maximum dose whereby a build up occurs of high speed electrons ejected from the surface and the subsequent layers of the medium. These electrons deposit their energy at a distance away from the sites where they originate [3, 74].

Due to this, the absorbed dose increases with depth until it reaches a maximum. This is useful clinically for skin sparing due to lower surface dose. As the photon fluence decreases due to attenuation with depth the secondary

electron production also decreases with depth beyond the maximum depth dose, D_{max}, hence the decrease in the depth dose curve beyond D_{max} [74].

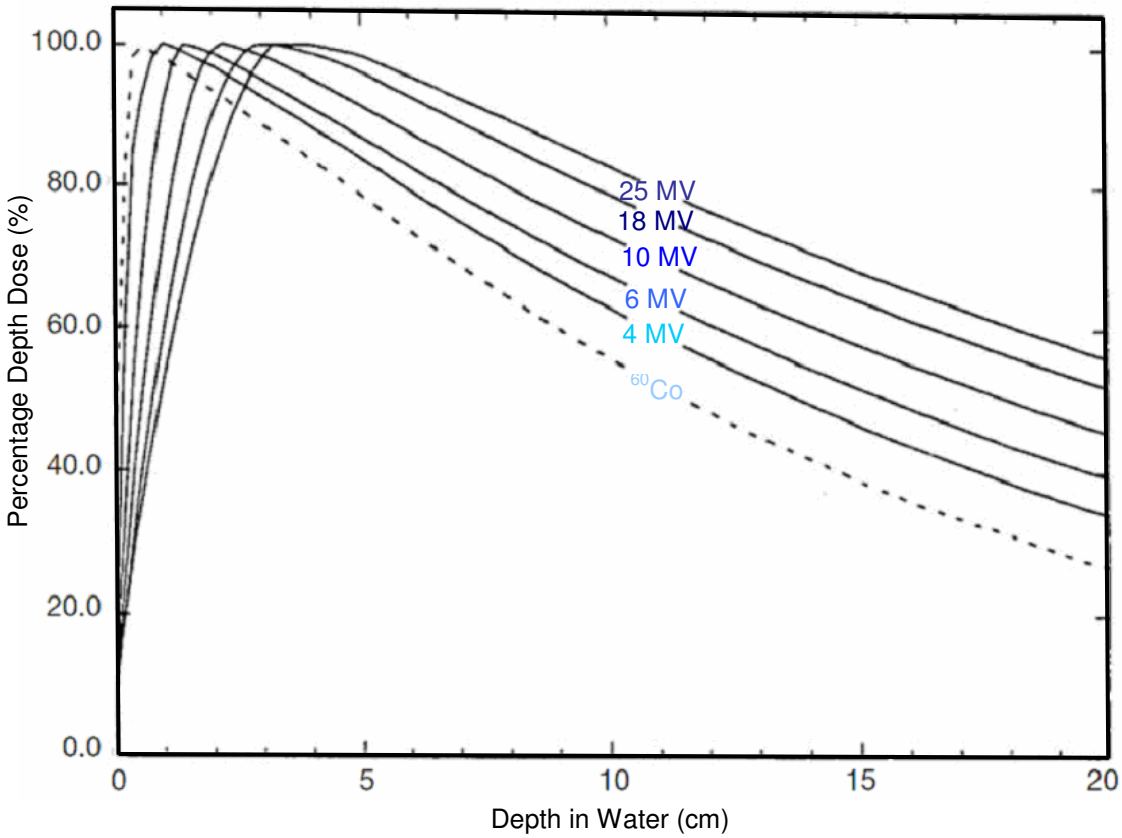

Figure 2.1: Percentage depth dose curves in water for a 10 × 10 cm^2 field at 100 cm SSD for photon beams ranging from cobalt-60 gamma rays to 25 MV x-rays [77].

2.2.4 Off-Axis Ratio (OAR)

The dose profile at depth, known as the off-axis ratio (OAR), is defined as the ratio of dose at an off-axis point to the dose on the central beam axis at the same depth in medium. This is required together with the PDD for the three-dimensional (3D) dose distributions in the medium. Usually, OARs are measured at various depths perpendicularly to the beam central axis [3, 74].

The beam profiles can be divided into three different regions which are the central, the penumbra and the umbra region. The central region is the flat region extended from the beam central axis before the field edge. The penumbra region is the fall off region at the beam edge whereas the umbra region is the region beyond the penumbra region or at the transmitted region of the collimated beam [3].

2.2.5 Relative Output Factor (ROF)

The dose at D_{max} in phantom, for a given photon energy at a given source to surface distance, depends on the collimator opening or the geometrical field size at the isocentre. The isocentre is the distance from the source to the rotation axis. The larger the field size, the larger the contribution of the scattered radiation to the absorbed dose [3, 74].

The relative output factor (ROF) is measured by the ratio of dose response of the field size at D_{max} relative to a reference field size of 10 × 10 cm^2 at the same SSD for the measured beam energy [3, 77]. This is obtained by the formula:-

$$ROF = \frac{D_{\text{max at open field size}}}{D_{\text{max at 10 cm x 10 cm open field}}} \text{ or} \qquad \text{Eqn. 2.18}$$

$$ROF_{\text{at depth,d}} = \frac{D_{\text{d at open field size}}}{D_{\text{d at 10 cm x 10 cm open field}}} \qquad \text{Eqn. 2.19}$$

2.3 Electronic Equilibrium

Electronic equilibrium is one of the fundamental requirements for accurate dosimetry in the megavoltage energy range. It is a requisite condition in order for electrons that would have been liberated by radiation in the occupied volume to be replaced by equal numbers of electrons from outside the volume of the detector [84].

For electronic equilibrium to occur, Fano [85] shows that two conditions must be met. First, the radiation field that generates primary electrons should be uniform throughout the volume of the detector. Second, the detector size should be significantly smaller than the average range of the electrons being generated. In these situations, the energy dependent response of a detector is governed by the ratio of the mass collision-stopping power of the detector material to that of the medium in which dose is required, for instance mass-collision stopping power of air to that of water for an ionisation chamber measurement [84].

These conditions are easily met for an ionisation chamber in a megavoltage beam due to the fact that the range of electrons in air is many times greater than the size of an air cavity. However in solid-state dosimeters, the range of electrons in the medium of the detector is very much less than that in air and as a consequence a more complicated analysis is required [84, 86].

Electrons from the primary photon beam can be regarded as having sufficiently long range to be considered with a cavity theory, while lower energy scattered photons and ionised electrons which are absorbed by the detector are generally produced within the detector, thus are in proportion to the photon mass-absorption coefficient. Exceptionally for energies below 100 keV, photoelectric effect which is highly Z-dependent begins to dominate [84, 86].

Electronic equilibrium particularly is not fully established in a number of situations; when radiation beams enter the body, for example in the interface between different density materials such as in lung and bone surface; also where the beam-size is smaller than the electron range as in stereotactic radiosurgery, for example when electrons generated from megavoltage beams travel several cm and significant numbers of electrons diffuse out of the field which are not replaced [64, 84].

2.3.1 Cavity Theory

For an absorbed dose to be measured at a point in a medium, a dosimeter is usually placed at that point. In general, this dosimeter differs from the medium in both atomic number and density, hence creates a discontinuity which can be thought as a cavity. If the material of the detector is the same or equivalent to the medium of interest then the dose to the medium D_{med} is equivalent to the measured dose D_{det} [2, 3]. Since this is generally unrealistic then:-

$$D_{med} = f.D_{det} \qquad \text{Eqn. 2.20}$$

where, f is a correction factor, which can be derived from a cavity theory to determine the absorbed dose in the medium, D_{med}. However, to determine f depends on several factors for instance the cavity size relative to the range of a secondary electrons, dose rate response, radiation damage history, ion recombination, temperature, pressure and humidity situations. This requires an approach known as cavity theories [2, 3, 87, 88].

2.3.1.1 Bragg-Gray cavity theory

The first theory developed to give a relationship between absorbed dose in a dosimeter and the absorbed dose in the medium containing the detector is the Bragg-Gray theory. Two conditions must be met for the Bragg-Gray theory to be applicable. They are firstly, the cavity must be small when compared with the range of charged particles incident on it so that its presence does not perturb the fluence of charged particles in the medium; and secondly, the absorbed dose in the cavity is deposited solely by charged particles crossing it and is not modified by the presence of the cavity, thus, photon interactions in the cavity are assumed negligible and therefore ignored [2, 3, 89 - 92].

Under these two conditions, according to the Bragg-Gray theory, the dose to the medium D_{med} is related to the dose in the cavity D_{cav} as follows:-

$$D_{med} = D_{cav}\left(\frac{S}{\rho}\right)_{cav}^{med} \qquad \text{Eqn. 2.21}$$

where, $\left(\frac{S}{\rho}\right)_{cav}^{med}$ = the ratio of the average unrestricted mass collisional stopping powers for the medium to that for the cavity. The application of unrestricted stopping powers eliminates the production of secondary charged particles (or δ electrons) in the cavity and the medium [2, 3, 89 - 92].

Combining equation 2.20 and 2.21, the factor f is equal to the ratio of the stopping power of the medium to cavity. Later, Laurence [93] made an assumption that electron energy loss continuously, due to the stopping power ratio for electrons in Bragg-Gray cavity theory is strictly dependent on their energy [2].

2.3.1.2 Spencer-Attix cavity theory

The Bragg-Gray cavity theory does not consider the production of secondary electrons generated as a consequence of the slowing down of the primary electrons in the sensitive volume of the detector. The Spencer-Attix cavity theory is a more general formulation that takes into account that these electrons can have sufficient energy taken away from the site to produce further ionisation. Some of these electrons released in the gas cavity would reduce the energy absorbed in the cavity and requires modification to the

stopping power of the gas [2, 3]. The dose delivered to the medium D_{med} is given by the expression:-

$$D_{med} = D_{cav}\left(\frac{\bar{L}}{\rho}\right)_{cav}^{med} = D_{cav}\frac{\int_{\Delta}^{E_{max}}\Phi_E\left(\frac{L(\Delta)}{\rho}\right)_{med}dE + \Phi_E(\Delta)\left(\frac{S(\Delta)}{\rho}\right)_{med}\Delta}{\int_{\Delta}^{E_{max}}\Phi_E\left(\frac{L(\Delta)}{\rho}\right)_{cav}dE + \Phi_E(\Delta)\left(\frac{S(\Delta)}{\rho}\right)_{cav}\Delta} \qquad \text{Eqn. 2.22}$$

where, $\left(\frac{\bar{L}}{\rho}\right)_{cav}^{med}$ = the ratio of the mean restricted mass collisional stopping powers from the medium to the cavity,

Φ_E = the fluence of particles with energy E,

$\left(\frac{L(\Delta)}{\rho}\right)$ = the restricted mass collision stopping power evaluated at energy $E = \Delta$,

$\left(\frac{S(\Delta)}{\rho}\right)$ = the unrestricted mass collision stopping power evaluated at energy $E = \Delta$ and

Δ = the lowest energy for which secondary electrons are considered part of the electron spectrum.

An assumption is made that all secondary electrons with energy below Δ are absorbed on the spot and is considered in the restricted stopping power, $\left(\frac{L(\Delta)}{\rho}\right)$. Meanwhile, the averaging extends from a minimum energy, Δ to the maximum electron energy in the spectrum and the two Bragg-Gray conditions still persist. Yet, these conditions are now applicable even to the fluence of the secondary particle; in addition to the fluence of the primary charged

particle. Spencer-Attix theory is used for ion chamber dose measurements over a wide range of energy [3, 94, 95].

In another study using Monte Carlo calculations [3, 66], Spencer-Attix cavity theory has been shown to be accurate within certain limits of depths and energy spectra. This is due to the decreasing number of lower energy electrons that can pass through a solid state detector hence depositing their dose in the cavity. The newly proposed cavity theory for solid state detectors irradiated in electron beams can be expressed as:-

$$D_{med}(p) = D_{det}(p).S^{S\text{-}A}{}_{med,det}.\gamma(p)^{e}.S^{T} \qquad \text{Eqn. 2.23}$$

where, $D_{med}(p)$ = the dose to the medium at point, p,

$D_{det}(p)$ = the average detector dose to the same point,

$S^{S\text{-}A}{}_{med,det}$ = the Spencer-Attix mass collision stopping power ratio of the medium to the detector material,

$\gamma(p)^{e}$ = electron fluence perturbation correction factor and

S^{T} = a stopper-to-crosser correction factor to correct for the dependence of the stopper-to-crosser ratio on depth and the effective cavity size.

2.3.1.3 Burlin cavity theory

For a cavity whose dimensions are many times larger than the range of the most energetic electrons, it can be said that the primary electrons generated

by the photons dissipate its energy at the site of the interaction [2, 96 - 98]. Unlike Bragg-Gray theory where the cavity is small, in large cavity the energy absorption in the surrounding medium will be proportional to the mass energy absorption coefficient of the medium and the equation 2.20 can be written as:-

$$D_{med} = \left(\frac{\bar{\mu}_E}{\rho} \right)_{det}^{med} D_{det} \qquad \text{Eqn. 2.24}$$

In this situation, the factor of f in equation 2.20 is equal to the mean ratio of mass energy absorption coefficient of the medium to detector material, $\left(\frac{\bar{\mu}_E}{\rho} \right)_{det}^{med}$. However, for the cavity that falls into neither small nor large cavity, Burlin (1966) [73] combined both conditions and gave the equation:-

$$D_{med} = \bar{D}_{det} [d \left(\bar{S} \right)_{det}^{med} + (1 - d) \left(\frac{\bar{\mu}_E}{\rho} \right)_{det}^{med}] \qquad \text{Eqn. 2.25}$$

where, $\bar{D}_{det}$ = the average dose delivered to the sensitive volume of detector,

d = a parameter related to the cavity size that approaches unity for small cavities and zero for large ones and

$\left(\bar{S} \right)_{det}^{med}$ = the mean ratio of mass collision stopping powers for the medium to detector.

This cavity model is the basis of the dose response of diode and diamond detectors on which relates to both Bragg-Gray and Burlin cavity proposed by Yin (2004) [64].

Chapter 3 - Detectors and Monte Carlo Methods

3.1 Dose Detectors

There are many types of dosimeters for example ion chambers, solid state detectors, thermoluminescent detectors (TLD) and films. Each of these detectors has different suitability in radiotherapy applications. Depending on the situation, one may require for instance a high response, high spatial and time resolution, very small dependence of response on photon or electron energy or good temperature and radiation stability. Some of the detectors used in this thesis are described in the next section.

3.1.1 Ionisation Chamber

An ionisation chamber (figure 3.1), one of the many detectors available, is responsible for absolute calibration and also for checking beam flatness and symmetry. It is a dosimeter which is available in a variety of designs such as free-air standard chamber for measuring of the exposure for primary calibrations, thimble air cavity chamber for measuring the absorbed dose and high-pressure ionisation chambers for measuring the low intensity γ radiation or cosmic radiation, etc. [2, 99].

One of the common types used as a standard meter is the cavity ionisation chamber where a known volume of air is contained between two electrodes, having a potential difference across them. Under normal conditions, no

electrical current flows between the electrodes. When radiation is incident, free ion pairs are produced causing an electrical current to pass between the electrodes. The amount of current produced is proportional to the amount of radiation exposed [2, 99, 100].

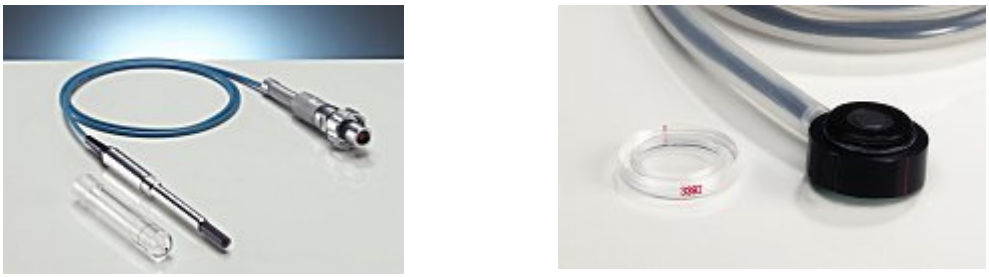

Figure 3.1: Left, the PTW Farmer thimble chamber and right, Markus plane-parallel ionisation chamber [101].

One of the common ionisation chambers used in radiation therapy, the thimble ionisation chamber, can be calibrated based on the standard dosimeter. This air-filled ionisation chamber has a solid wall of different thicknesses for different photon energies as required. The wall can be thought of as representing compressed air for the detector, since its effective atomic number is the same as that of air. This volume of the air-filled cavity can be made minimal for high photon energies [2, 74, 102, 103]. The absorbed dose in a medium, D_m can be determined by the formula:-

$$D_m = X_g S_{m,g} p_{m,g} \frac{\overline{W}}{e} \qquad \text{Eqn. 3.1}$$

where, X_g = exposure reading of a cavity chamber, is given by the

ratio of the absolute value of the total charge of the ions of one sign produced in air, dQ when all the electrons and positrons liberated by photons in mass of air, dm are completely stopped in air,

$S_{m,g}$ = the stopping power ratio of medium to air,

$p_{m,g}$ = the electron fluence perturbation correction factor,

$\overline{W}$ = the mean energy expended in air per ion pair formed and

e = the charge of an electron.

The details for determining the absorbed dose can be referred to the protocols in ICRU 1969, 1972, 1984 [104, 105, 45].

3.1.1.1 PinPoint ionisation chamber

Figure 3.2: The PTW PinPoint ionisation chamber and its build-up cap [106].

The PinPoint ionisation chamber (figure 3.2) is a small size ionisation chamber which has a sensitive volume of only 0.015 cm^3, a 2 mm diameter and a length of 5 mm. It has a rigid stem of 3.6 cm for mounting. It is vented to air through its cable and connector and has a wall material of 0.09 mm graphite with a protective 0.57 mm polymethyl methacrylate (PMMA) cover and an aluminum central electrode. Due to its small volume it has a very high spatial resolution when used by scanning perpendicularly to the chamber axis. It is an ideal device for dose measurements in small fields as in IMRT and stereotactic beams. The waterproof ion chamber can be used in air, solid state phantoms and in water [107, 108].

3.1.2 Solid State Detectors

The collecting volume of an ionisation chamber is designed to be considerably larger than solid state dosimeters since the density of the charge collection volume is much smaller than that of any solid state material. Solid state detectors are used increasingly because of their high spatial resolution and good stability [2, 67].

Based on measuring principles, there are two types of solid state detectors. One type of detectors is the integrating or passive type dosimeter; one example being the thermoluminescent dosimeter (TLD). The other type of detector is the electrical conductivity detector or the active type, for example the diamond detector and DOSI detector which will be explained in this

chapter. All of the detectors must be calibrated with a standard dosimeter before they can be used to measure the absorbed dose [2].

3.1.2.1 Diamond detector

The use of diamond as detecting material is favourable due to its atomic number, Z = 6 which is close to that of normal tissue. Another reason is that its density is similar to that of soft tissue; therefore the local electron spectrum is relatively unperturbed in the detector's vicinity [84]. A diamond detector (figure 3.3) can also be used as a thermoluminescence dosimeter. Thermoluminescence is the emission of light during heating after the absorption of radiation exposure. The amount of light that the material gives out is proportional to the amount of exposure it has absorbed.

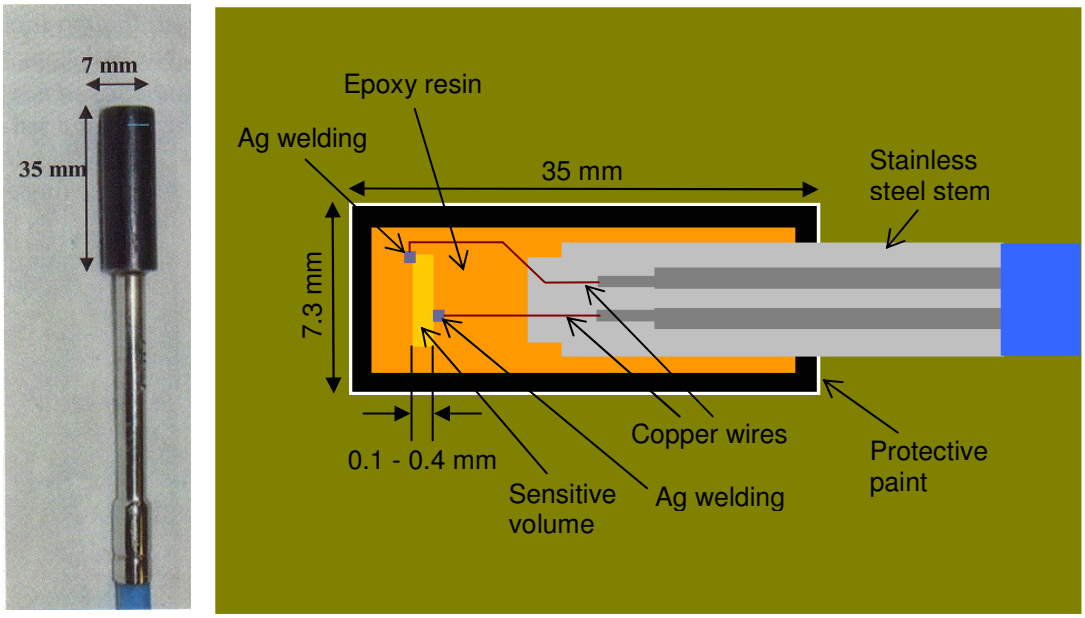

Figure 3.3: The diamond detector and its cross section [84, 3].

However, a more practical way in radiotherapy is to measure the induced electrical conductivity in the presence of radiation with an electric field applied through contact with the surface of the diamond crystal [109]. It is connected to an electrometer via a tri-axial lead which carries a 100 V bias and is shielded to earth. This gives the diamond detector a high sensitivity, stability and reproducibility over long time periods. The active volume of a diamond detector is roughly 4 mm in diameter and 0.4 mm in thickness [84].

Diamond detector can be manufactured from a natural diamond (PTW, Freiburg) or from a compressed vapour-deposited (CVD) diamond. For a good dosimeter, a high purity is not required. As a matter of fact, a significant nitrogen component is required to obtain reasonable dose-rate linearity [110]. Work on radiation induced conduction in a diamond detector by J. F. Fowler [111] shows that the current flow, R, produced by a perfect diamond is given by:-

$$R = D^{½} \qquad \text{Eqn. 3.2}$$

where D is the dose rate. The current induced is related to the radiation intensity but it is also inversely proportional to the recombination rate. If a perfect diamond is irradiated, an equal number of conducting electrons and hole-carriers are generated so the recombination rate is proportional to the number of electrons. Hence, if the radiation intensity is increased by four times the current will be increased by a factor of two. Fowler's work shows that if an impurity such as nitrogen exists then electrons will be caught in

longer-lived traps, a larger reservoir of hole-carriers will then be generated with an increased amount of exposure. The dose rate is then given by:-

$$R = D^{\Delta} \qquad \text{Eqn. 3.3}$$

where Δ varies between 0.5 and 1. In practice, Δ is found to be varying between 0.95 and 0.99 for a natural diamond, which is independent of the energy and radiation type. This theory explains why a diamond detector requires a priming exposure of several Gray prior to normal usage to reach an equilibrium number of hole-carriers [52, 84].

As compared to a gas-filled ionisation chamber, a diamond detector and other solid-state dosimeters can be used to achieve superb spatial accuracy and are more sensitive than the ionisation chamber. The amount of energy required to create free ion-pairs by a diamond detector is smaller than that of the ionisation chamber, in addition the density of charge is also several orders of magnitude higher [84].

For a solid-state material, diamond in fact has one of the highest band gaps which is 5.6 eV [112], however, it is approximately six times smaller than the average energy required to form free charge in air which is 34 eV. Other examples of the usage of the detector are in the application of a collimator designed to generate a high-dose gradient beam in retinoblastoma, in a non-divergent beam application and in high dose-rate brachytherapy [84, 113, 114]. Another advantage of the diamond detector is its fast electrical response

which is in the nanosecond range. This means that the detector is not affected by modern radiotherapy methods which are much slower pulse-rate [84, 115].

For the sake of completeness, other than radiotherapy another usage of the diamond detector is for measuring monochromatic beams produced by a synchrotron. This is due to its high sensitivity and high reproducibility, and furthermore, not forgetting its submillimeter resolution [84, 116]. The detector is sufficiently small and has a Z value which is close to water that can be of use in a synchrotron beam [84, 117]. However, the future of the diamond detector as a suitable dosimeter for synchrotron based medicine is not the subject of this project.

3.1.2.2 DOSI detector

Dosimeters capable of measuring dose distributions on-line with submillimeter spatial resolution are crucial for commissioning and quality assurance of small radiation fields. High spatial resolution dosimeters based on silicon microstrip technology have recently been designed to characterise small radiotherapy and radiosurgery fields, aimed to provide relative dosimetric measurement with film-like spatial resolution and capable of resolving the temporal changes in radiation intensity [56].

The detectors, n-type silicon dosimeters, are 300 μm thick on which linear arrays of p-type diodes are fabricated by ion implantation. The pitches of the detectors' diodes are in a variety of lengths. They are 25, 100 and 250 μm

pitch detectors, promising submillimeter resolutions. The read-out sensors use an XDAS data acquisition system consisting of a front-end read-out application-specific integrated circuit. There are 128 channels to each detector with preamplifier “sample and hold” (S & H) circuitry. Each detector has dual S & H circuits for every channel which allows the chip to be active even during read-out. Depending on speed of the analog-to-digital converter (ADC), the dead time is minimised to be around 110 µs. The system’s dimensions are merely 268 mm x 101 mm [57].

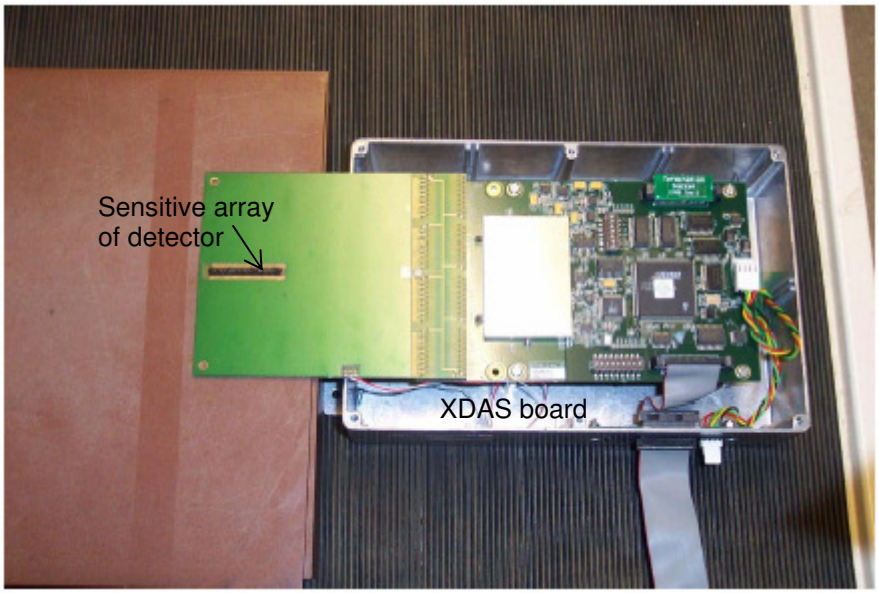

Figure 3.4: Picture of the 128-channel detector and its associated electronics [57].

Other features of the detector comprise of simultaneous double sampling for noise reduction, a single tap output stage using a 14-bit ADC, fully programmable gate array (FPGA) for memory storage and image processing. This includes background subtraction, gain normalisation and signal averaging [57].

The data can be sent to a computer via a cable for storage and further processing. The integration time for the system is between 10 µs to 50 µs. The maximum read-out rate is 5 Mbs^{-1}. Only small charge is stored but the maximum that can be held in every channel is 15 pC [57].

The detector's gadgetry is shown in figure 3.4 above. The sensitive array of the detector is located on the left of the image interconnected on its printed circuit board (PCB). All of the system, except the sensor, is housed inside a metallic box; this is to provide a precaution from accidental radiation damage [57]. The other circuitry components together with the FPGA are also visible from the illustration in figure 3.4.

3.2 Radiotherapy Treatment Source

The most commonly used source of gamma teletherapy radiation before 1966, was cobalt-60. It was confined in a lead shell, but can be adjusted with movable jaws (collimators) into the desired shape and size. Such machines have been replaced by linear accelerators which do not have the problems of radioactive source disposal, in addition can provide faster treatments and higher energy therapies [11].

The Co-60 machine produces γ rays of two predominant energies of 1.17 MeV and 1.33 MeV. The other energy beams which contribute less than 10% to the total intensity of the beam are lower energy γ rays scattered by the source itself and the surroundings, plus a lesser component of electron contamination [2, 118].

3.2.1 Radiotherapy Linear Accelerator (Linac)

The linear accelerator (linac) uses microwave technology to accelerate electron emissions from a cathode (figure 3.5). The frequency of 3000 MHz is typically applied to the electrons in an evacuated cylindrical wave-guide [74, 119, 120]. The high energy electrons are focussed to strike a target positioned just after a bending magnet to produce megavoltage x-rays [11].

Typical energies of 6, 10 and 15 MV photons are in use in radiotherapy. Maximum depth doses of more than 1 cm below the skin surface are achieved, resulting in skin sparing and the ability to treat deep-seated tumours. The primary target can be removed from the beam with a rotating carousel, as a consequence of which high-energy electrons can be made available for treatments. In contrast to photons, electrons travel a fixed distance depending on the beam energy and can be used directly for treating superficial tumours [11].

The linac beam exits from the component of the accelerator called a gantry, which swivels around a moveable couch. The patient lies on the couch where lasers are aligned at the isocentre to ensure proper positioning during treatment and planning. Radiation fields can be delivered to the tumour from any angle by rotating the gantry and moving the treatment couch, according to position, size and shape of the tumour (figure 3.6). The beam profile of a linac measured at the isocentre in air varies with field size [2, 121 - 125].

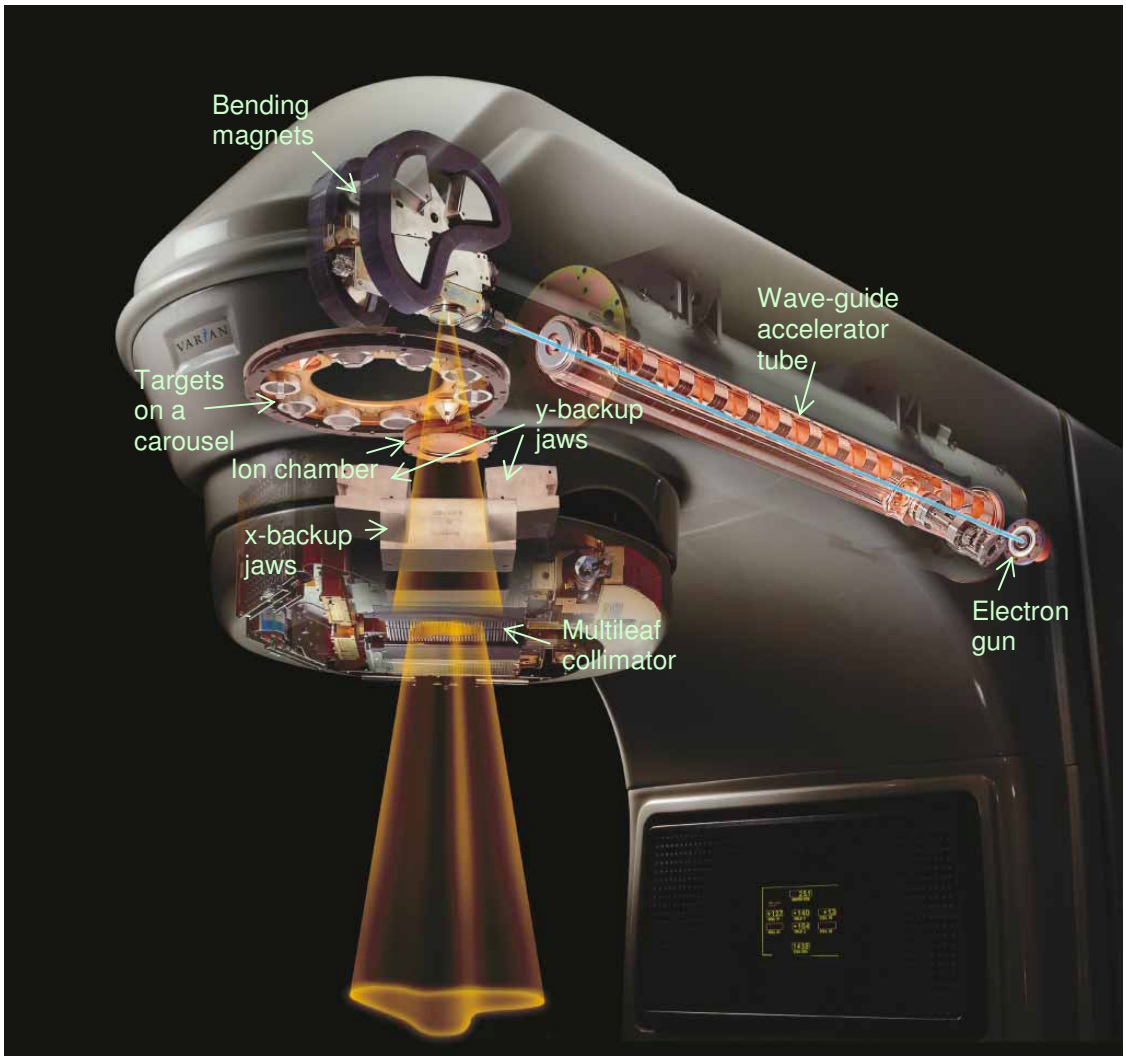

Figure 3.5: A typical medical linac structure [126].

Linac x-ray beams have a sharper dose fall-off at the penumbra than cobalt beams due to a smaller virtual source size, generally of about 2 mm in diameter [127]. Usually, multiple electron and photon energies are available to conform to the required treatment depth. For example, an Elekta Precise linac is capable of producing two different photon energies (6 and 15 MV) and five different electron energies (4, 6, 8, 12 and 18 MeV). In addition, the dose rates of 1 to 10 Gy per minute are higher than those of cobalt units, allowing shorter treatment times [2, 119].

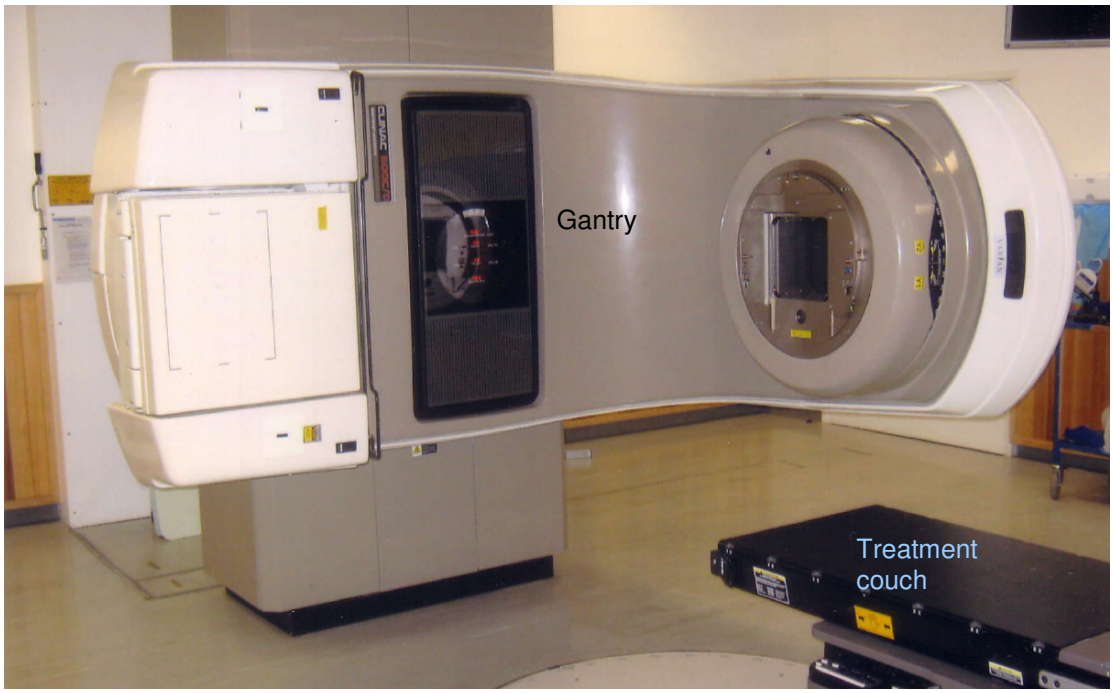

Figure 3.6: Treatment head of a linac at a gantry angle of 90°.

3.3 Monte Carlo Code

The Monte Carlo (MC) simulation can be applied to many scientific fields of interest however discussion will be only based on radiation dosimetry. Initially it was a method to solve for neutron diffusion in a fission material. Due to the reliance on random numbers to the probability distributions the term Monte Carlo method was coined by von Newmann and Ulam in 1947 which refers to a casino in Monaco [128, 129].

It is a computational method that is based on probabilities of radiation and particle interactions over a wide range of energies, simulated in a defined geometry of source and medium. The newly emitted electrons or photons are

followed and recorded until all particles are absorbed or leave the geometry under consideration [2, 129].

Because of the repetitive task of mimicking complex interactions of particle transport to calculate radiation doses, a powerful computer is essential. When a particle, let it be a photon, collides with an atom, the particle undergoes one of a series of interactions, namely photoelectric effect, Compton scattering, pair production and bremsstrahlung radiation. These are random processes described by probability distribution functions taken from the atomic cross sections. The distance travelled by a particle before interaction is simulated by the Monte Carlo code, and so is the interaction thereafter including its initial energy, the change in energy and direction, the type of interaction, the angle of emission of the secondary particles and so forth [130].

A large number of events called histories (usually more than 10 million) must be simulated since it is a statistical process. The accuracy of the result will depend on the detailed specification of the geometry and other factors such as the accuracy in the cross section libraries and the number of histories simulated [131].

For instance, work pertaining to MC has been used to commission a multileaf collimator model in dose calculations for IMRT, in which measured data are within acceptable criteria. Other work computes the in-vivo dose given to patients during conventional treatments and IMRT from portal images. It can be concluded that novel dose reconstruction using MC simulations is reliable

in homogeneous and heterogeneous phantoms. Another example is a MC code hybrid method to determine the fluence delivery of a dynamic IMRT whose results are accurately reproduced [132 - 134].

3.4 The EGSnrc Code

There are many algorithms that can be used in dose measurements some of which are MCNP, FLUKA and PENELOPE. The significance of using the MC method is that it can offer precise prediction of radiation dosimetry situations. Many an article has been published to support this [135 - 149], due to its precise algorithms for radiation transport purposes and to play the role as a high-resolution detector [150]. However in this research the EGSnrc system is used for modelling the linac treatment head due to its suitability, and ease of use to obtain results. The EGSnrc (Electron Gamma Shower nrc) system comprises of BEAMnrc, DOSXYZnrc, DOSRZnrc, FLURZnrc and other simulation codes that come as a package under license to the National Research Council of Canada (nrc) [151].

3.4.1 BEAMnrc

Of the many MC codes available, BEAMnrc is highly suitable to be used for modelling a linear accelerator (linac). It is able to accurately model all aspects of a linac including the details of target, flattening filter and in particular it is capable of modelling the multileaf collimator (MLC) rounded ends [152 - 156]. Therefore, leaf effect and leakage can be fully taken into account.

An accurate estimation of the leakage radiation through the air gap between adjacent leaves can be calculated, giving a result of the order of 1 - 3% [157, 158] depending on the MLC design. This effect may yield the outcome of low doses to sensitive organs which are shielded by the MLC. This is an important contribution to the normal tissue absorbed dose.

3.4.1.1 Component modules

The Monte Carlo modelling was based on the technical drawings supplied by Elekta Oncology Systems from the SL Series Linac Physics Manual. Most of the components media and dimensions are available for replication. However, for the Varian machine the dimensions of the flattening filter is not given, thus this was initially assumed to be similar to the Elekta. The dimensions for both linacs can be seen in Appendices D and E.

The linacs were modelled almost completely with the EGSnrc-based Monte Carlo code using the BEAMnrc version 2005. The Elekta radiation transport for 6 MV, 10 MV and 15 MV photons were simulated with eight different component modules. They were the tungsten target, the primary collimator with the flattening filter inside, another flattening filter for 10 MV and 15 MV beam hardening, the chamber with a column of air gap in between, the multileaf collimator in the y-axis, the y-axis back-up jaws, the x-axis second back-up jaws and another column of air before the 100 cm scoring plane as in figure 3.7.

For the Varian 6 MV linac there were extra components to be modelled for instance the conical collimator for stereotactic modelling, if not in use it is replaced with an air gap. The scoring plane was placed at 90.0 cm and 92.5 cm similar to the experiment measurements for 90 cm SSD and stereotactic dosimetry respectively. For both machines, the ion chamber, mirror and wedge were not modelled because they did not cause significant effects on the beam. The schematic geometry showing the component modules are shown in figure 3.8 and also in chapter 6 and 7 for illustration purposes in accordance with the simulated arrangement of the experiment set-ups.

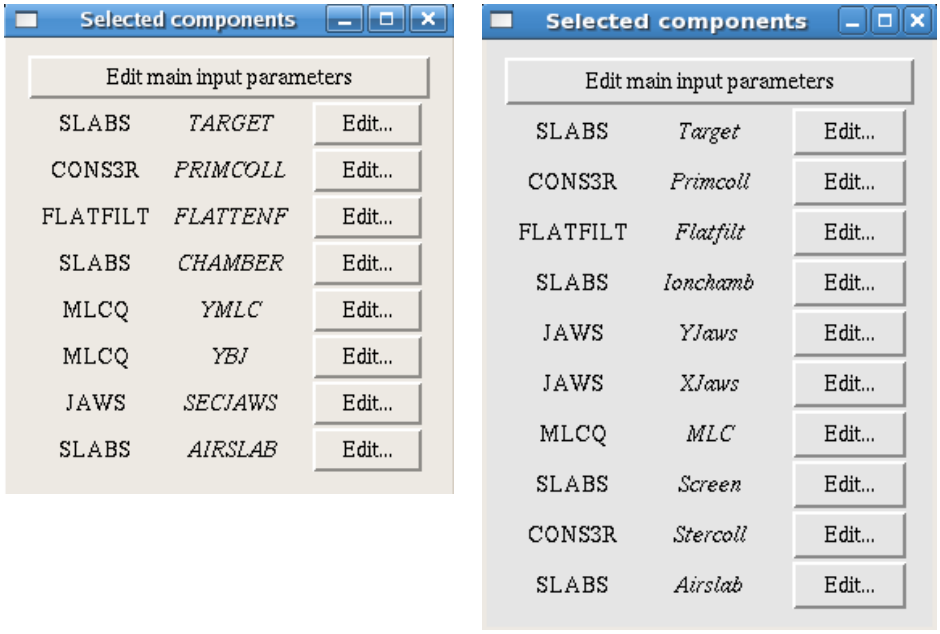

Figure 3.7: The modelled components of BEAMnrc module for Elekta (right) and Varian (left).

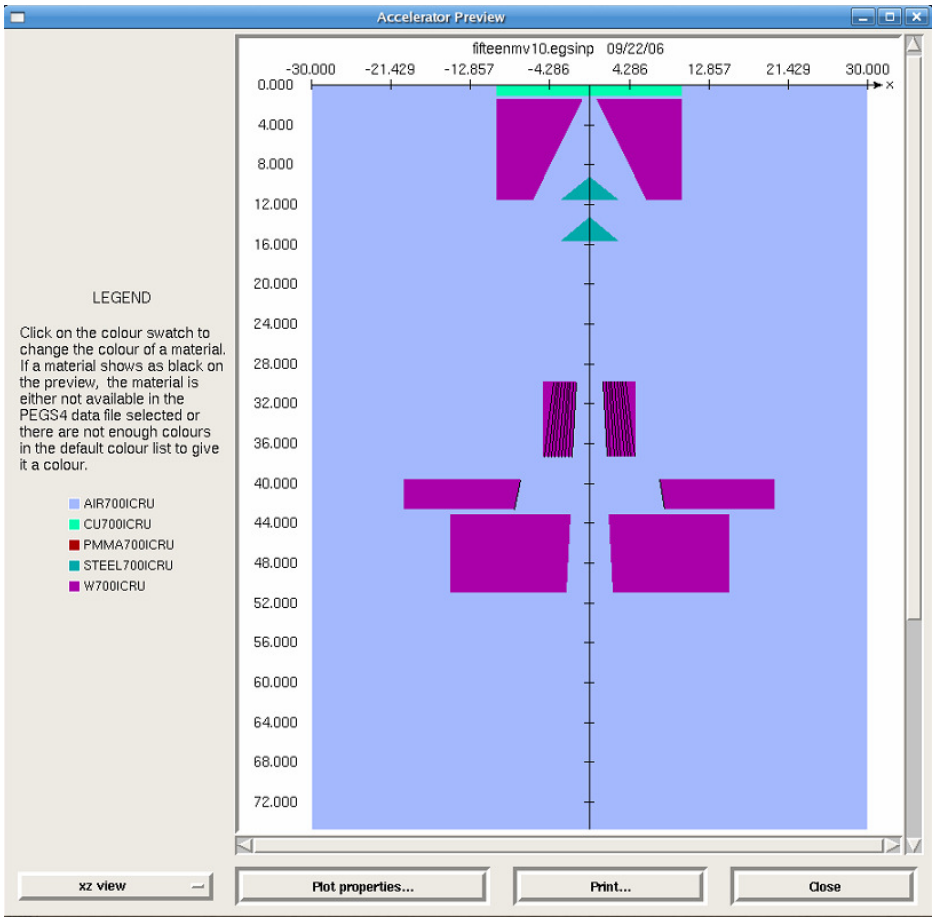

Figure 3.8: The schematic diagram for 15 MV 10 x 10 cm^2 field linac.

For the calculations of the doses, other EGSnrc packages, DOSRZnrc and DOSXYZnrc were used. The calculated data were utilised to determine the percentage depth doses, off-axis ratios and the output factors.

3.4.2 DOSRZnrc

DOSRZnrc is the code to simulate the passage of an electron or photon beam in a phantom of a finite cylindrical geometry. It tallies the dose distributions in an arbitrary volume made up of any number of regions. The energy deposited within various defined regions was scored and analysed statistically following

from the BEAMnrc generated phase space files that was simulated in the scoring plane [159].

The user can perform optimisation as in figure 3.9, on the General Information tab. There is a target radio button group box, where one can choose the type of compilation desired. By default, it is set to optimisation. This uses the active configuration file generated in the EGSnrc graphical user interface (GUI) environments. All GUIs were provided by the vendor to minimise typing error and to facilitate inputs that relate with specific parameters. The other available options are no optimization, debug and clean, whereas optimization is suggested for production runs on conditions that the user-code and the input file have been thoroughly tested on [160].

As an example, the geometry given in figure 3.10 has 15 slabs with thicknesses of 0.25 cm and 1 slab with a thickness of 5 cm in water phantom. The radius of the water phantom varies towards the centre outwards due to the importance of the dose measurement at the central axis. The radius has 0.25 cm increments near the centre and bigger increments away from it. The chosen radii are 0.25, 0.50, 1.00, 1.50, 5.00, 6.00, 7.00, 8.00, 9.00, 10.00 and 20.00 cm as in figure 3.10 below.

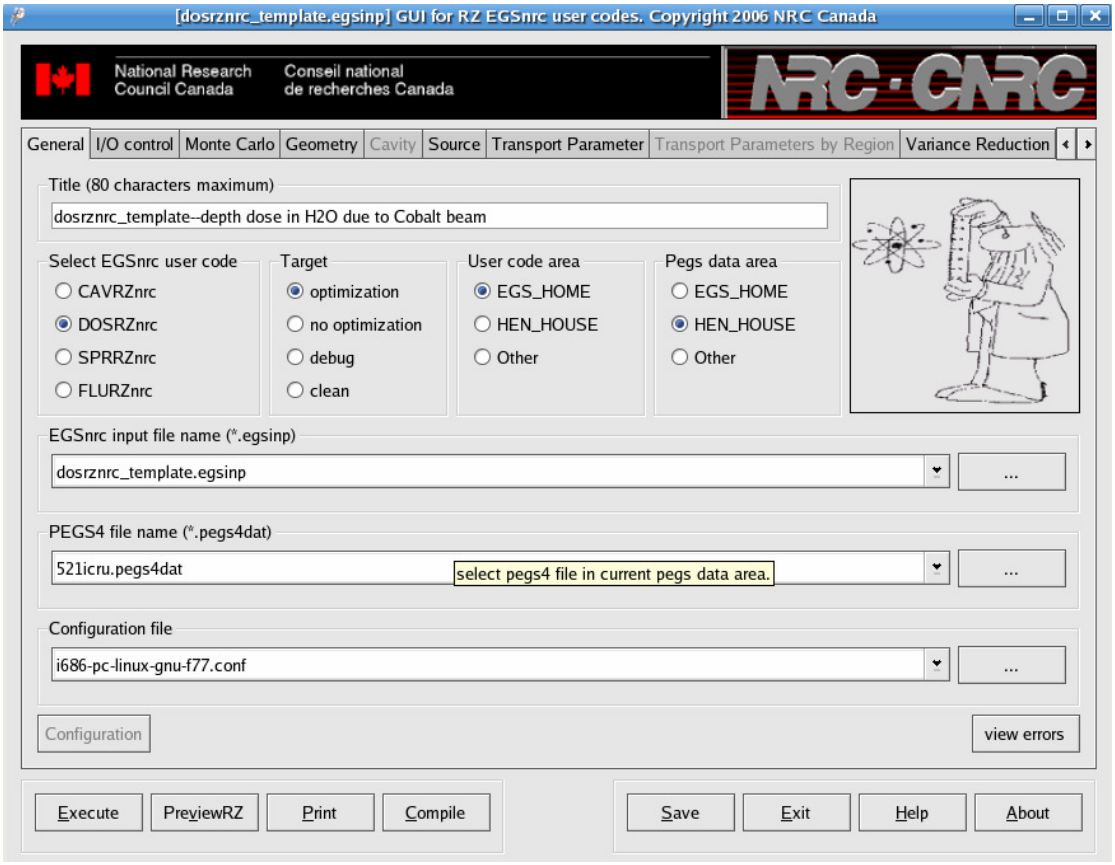

Figure 3.9: The DOSRZnrc version 2006 GUI that was used for the project.

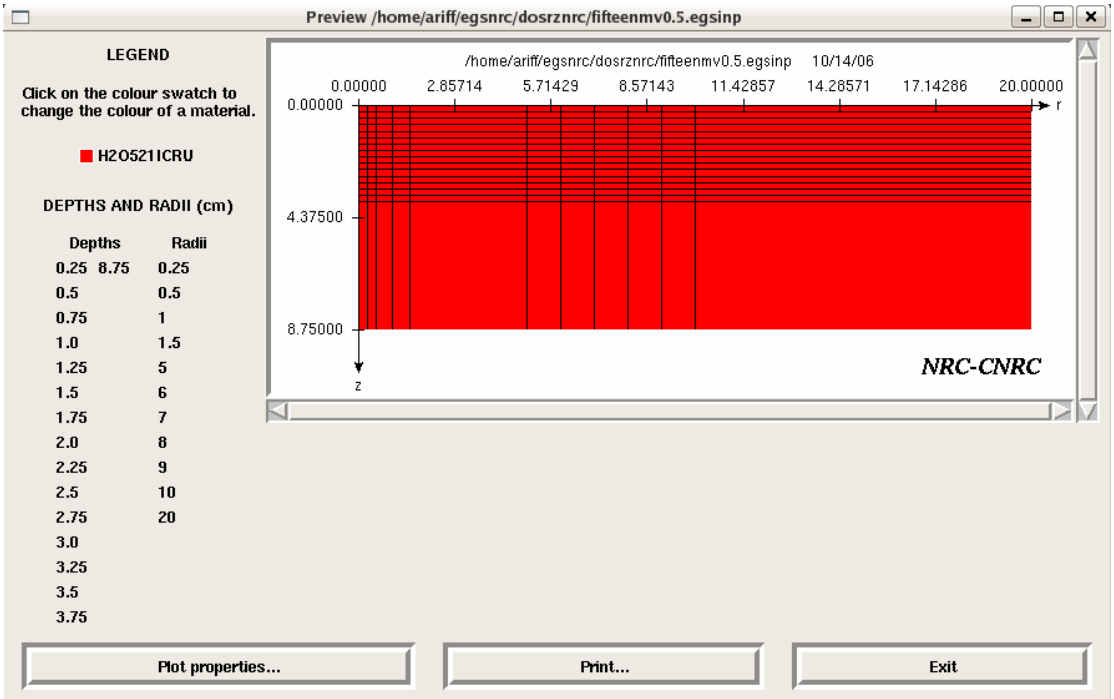

Figure 3.10: The DOSRZnrc modelled phantom for calculating the depth doses.

It can be comprehended that the depth doses were calculated with a 0.25 cm radius and 0.25 cm thick. The number of histories used was as high as 10 billion and as low as 1 million. The lower number of histories was used for the bigger field sizes. This results from the use of larger volume elements (voxels) for larger fields and the fact that most source photons are stopped in the linac jaws or MLC for small fields. Results were produced after each compilation and run of every file as saved in the ".egslst" files. Not all doses were calculated from this configuration, the above parameters are for illustration only.

3.4.3 DOSXYZnrc

The DOSXYZnrc is a general-purpose EGSnrc code for 3-dimensional absorbed dose calculations. It simulates the transport of photons and electrons in a rectilinear geometry and scores the energy deposition in the designated volume elements (voxels). The geometry is a Cartesian coordinate with the x-y plane on the page, x to the right, y down the page and the z-axis into the page. Dimensions are completely variable in all three directions where every voxel can have different materials and varying densities [161].

The code allows sources such as a phase-space data generated by a BEAMnrc simulation. DOSXYZnrc was run using the ".egsinp" file extension while the results can be found in the ".egslst" file extension with the same given filename. Much of the information using the GUI is in the EGSnrc manual which is available online [161].

3.5 Variance Reduction

The variance reduction technique was used in the BEAMnrc code results to reduce the error in result. Since the dose calculation is one form of normal distribution from a sample, the standard deviation can be obtained from the square root of the sample variance, given by:-

$$s = \sqrt{\frac{\sum_{i=1}^{N}(x_i - \bar{x})^2}{(N-1)}} \qquad \text{Eqn. 3.4}$$

where, x_i = the sample score of the integer, i in the set,

$\bar{x}$ = the sample mean and

N = the total sample size [73].

Hence, the standard error of the mean can be obtained from the formula:-

$$\sigma = \frac{s}{\sqrt{N}} \qquad \text{Eqn. 3.5}$$

To obtain a smaller uncertainty, the number of samples used was increased to as many as 300 different random number seeds to achieve less than 2% error. These were calculated in parallel by sending job submissions to a computer cluster. The time involved depends on computer processors, job specifications and statistical needs.

3.5.1 BlueBEAR Computer Cluster

The BlueBEAR computer cluster is provided for students and researchers to run computer codes in parallel. Coined from the terms Birmingham Environment for Academic Research (BEAR), the environment has many partners one of which is IBM. The BlueBEAR cluster consists of 1,536 processing cores and 144 TeraBytes of user disk space [162]. This is an advantage for a student to submit more than one job at a time, however the walltime limit is 10 days and storage space of 50 GB is allocated. Nevertheless, requests for extra space and longer walltime can be made.

3.5.2 Directional Bremsstrahlung Splitting

Directional bremsstrahlung splitting (DBS) is an option in the BEAMnrc code where the photons are split at the time of creation, whereby those aimed away from the field of interest are not. If a charged particle undergoes a bremsstrahlung or annihilation event then the DBS splits the event with the bremsstrahlung splitting number, NBRSPL. The resultant photons are given weight which is reduced by a factor of $NBRSPL^{-1}$ [163].

DBS then computes through these photons to determine whether they are aimed in the region of interest specified. If it is, then the photon is kept and considered low-weighted. If not, Russian Roulette is played on the photon to decide its survival where the threshold is compared by a random number and

$NBRSPL^{-1}$. If the random number is smaller, then the photon is kept and its weight is multiplied by NBRSPL and becomes a high-weighted photon. The high weighted photon will be split again when it undergoes interactions and Russian Roulette will be played again for photons that were not aimed into the field of interest. As a result, DBS will eliminate all but many low weight photons inside the field and few high weight photons outside the field [163].

3.6 PEGS4 Data

The BEAMnrc, DOSRZnrc and DOSXYZnrc codes run using the cross-section data of the material in the pegs4 folder in the directory on area EGSnrc/pegs4/data. This default cross-section data that is stored in the folder uses Storm and Israel compilation set [164]. The files 700icru.pegs4dat and 521icru.pegs4dat contain a large number of commonly used materials. The numbers in the file identifiers correspond to electron energy of 521 and 700 keV, relating to thresholds for secondary electron production of 10 and 189 keV kinetic energy respectively. These data sets go up to 55 MeV in both cases. Both files contain data for the photon energy from 0.01 MeV to the upper energy of 55 MeV [163].

Chapter 4 - Characterisation of the Model of the Linear Accelerator Head

4.1 Introduction

The modelling of a linear accelerator treatment head is an important research topic. The verified model can be used to predict a multitude of parameters. However, construction of a complete model of the linac head is not an easy task due to its complexity and the necessary detailed modelling approach to obtain a dose-calculation that gives 2% or 2 mm accuracy or better [65].

One approach is to perform a full MC simulation through the linac head to obtain the phase-space files and to adjust a few critical parameters of the component modules until a sufficiently good match with the standard data is obtained. This method is however quite time consuming and involves trial and error. Nevertheless, the effort is worthwhile because the MC simulation, once validated will provide the most accurate prediction of dose in situations which have material inhomogeneity and irregular geometry, such as patients [165]. However, this needs high computer calculation speed and large amounts of storage [62, 166].

In this chapter, 2 linac machines, manufactured by Elekta and Varian were modelled. The models have been validated with the commissioning data with most of the discrepancies minimised through an optimisation process. Some ideas to hasten the process and to optimise the dose calculations involved

were considered to achieve the goal of having two validated models that match with the standard measurements.

4.2 The process of optimization for Elekta

4.2.1 Methods

Modelling of the Elekta Precise Linear Accelerator (Linac) was performed from the specification obtained from the Linac Physics Manual supplied by the manufacturer, Elekta Oncology Systems. The main components were mimicked using the dimensions specified. These were the tungsten-rhenium target, primary collimator, flattening filter or filters depending on the energy, multileaf collimators, y-backup jaws, x-backup jaws and PMMA screen.

However, not every component of the linac was mimicked in full detail. When there was a choice between simplified and detailed dimensions, a simplified model was chosen. For instance, the monitor chamber was not modelled to keep the simulation as simple as possible. Another instance was that the flattening filter has a many faceted disk but the model was based on a simple cone.

These were due to the fact that a simple linac model was easier to produce and to understand the underlying physics of the photon transport than a detailed model, which is also time consuming and blurred out the physical aspects of the modelling. The detailed modelling was not as important as

acquiring a result which is consistent with the measured data but also care should be taken so that time was not wasted to achieve such a goal.

Also to minimise the simulation time, directional bremsstrahlung splitting was used in order to consider only the photon and electron transports that fall within the specified area of 50 x 50 cm^2 at 100 cm SSD, while others were discarded.

The first 15 MV Elekta model was not very successful. It had the correct percentage depth doses (PDD) as in figure 4.1 but incorrect output factors (OF). The PDD from the commissioning data do not have values in between 0 and the maximum dose, D_{max}. Measurements in the build-up region using a cavity ionisation chamber are not considered to be accurate because of a lack of electron equilibrium.

The methods for 10 MV and 6 MV Elekta were the same. The output factor results were incorrect although the correct PDDs were obtained as in figure 4.2 and 4.3. The discrepancies were revealed in the relative output factors for the Monte Carlo simulations where the output factors for the bigger field sizes approached a plateau. The same trends were seen for 15 MV, 10 MV and 6 MV output factors for Elekta as illustrated in figure 4.4.

The puzzling findings for output factors at first were thought to be due to the collimators in the linac head that scattered some of the radiation back to the monitor chamber. As a result the ionisation chamber would measure the dose

as specified and stop at a lower true beam output. Due to normalisation at 10 cm field width, the smaller dose would increase the output factors at larger field sizes. Hence, the simulation results show a lower reading at increasing field sizes due to the simulation was independent of the dose read out in the monitor chamber. Although Liu et al. (2000) [167] have reported that the backscatter dose variation in the ion chamber increase the relative output by about 2% to 3% for 3 to 40 cm^2 fields, surprisingly, these discrepancies were later found to be due to the incorrect Off-Axis Ratios (OAR), despite the fact that the correct dimensions of the component modules were modelled as in the specification.

Even though the PDD curves for 15 MV, 10 MV and 6 MV show good agreement, the OARs for these simulations were not promising. Figure 4.5 shows data at 15 MV and the profiles of the OAR were not flat like a typical radiotherapy beam should be. This was an indication of the flattening filters which were too thin in the middle. It is hoped that after the modifications were made, the calculated output factor variation with field size would be validated with the measured data.

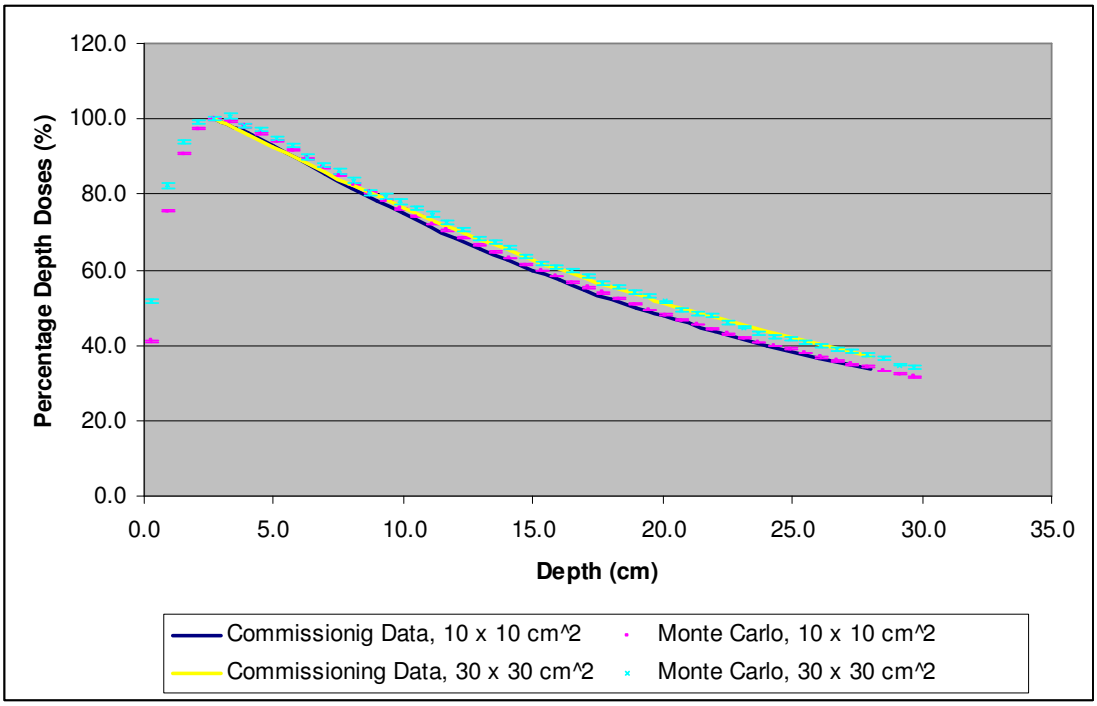

Figure 4.1: Percentage depth doses for 10.0 cm and 30.0 cm square fields, 90 cm SSD for 15 MV Elekta linear accelerator.

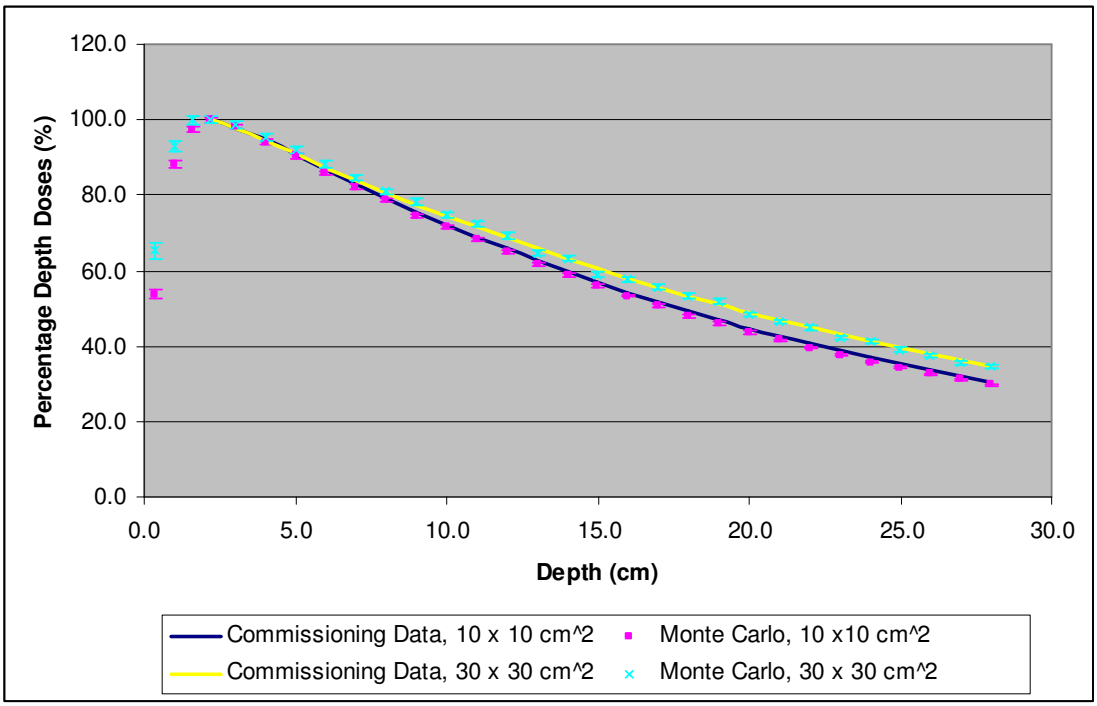

Figure 4.2: The PDDs for 10.0 cm and 30.0 cm square fields, 90 cm SSD for 10 MV Elekta.

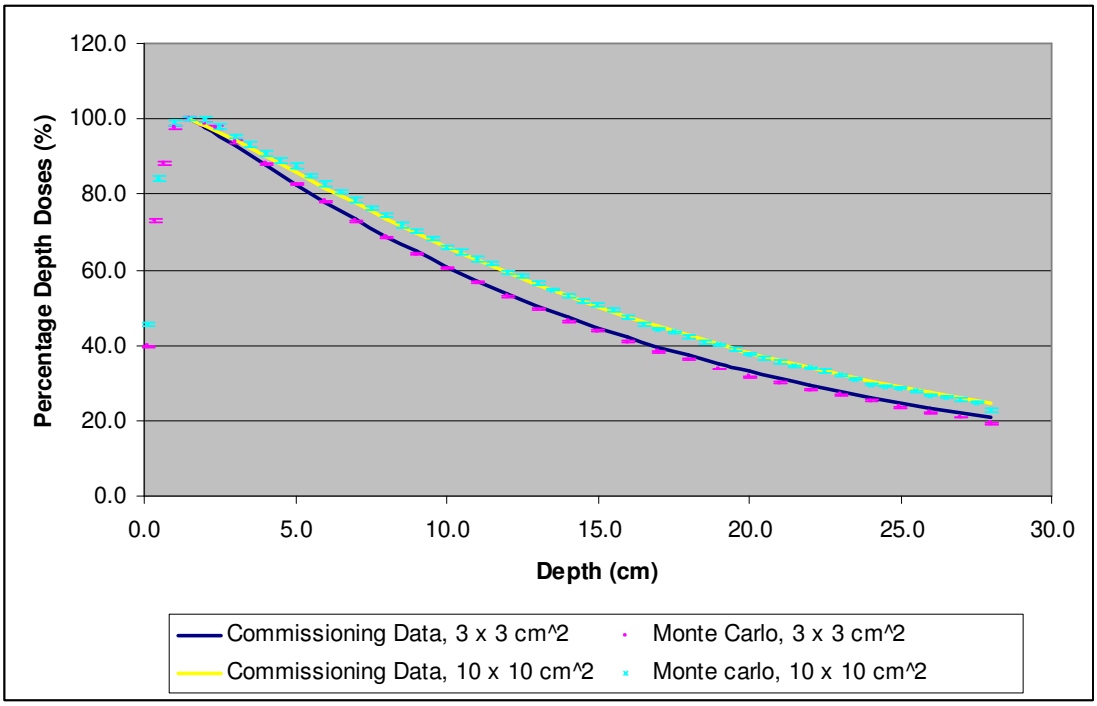

Figure 4.3: The PDDs for 3.0 cm and 10.0 cm square fields, 90 cm SSD for 6 MV Elekta.

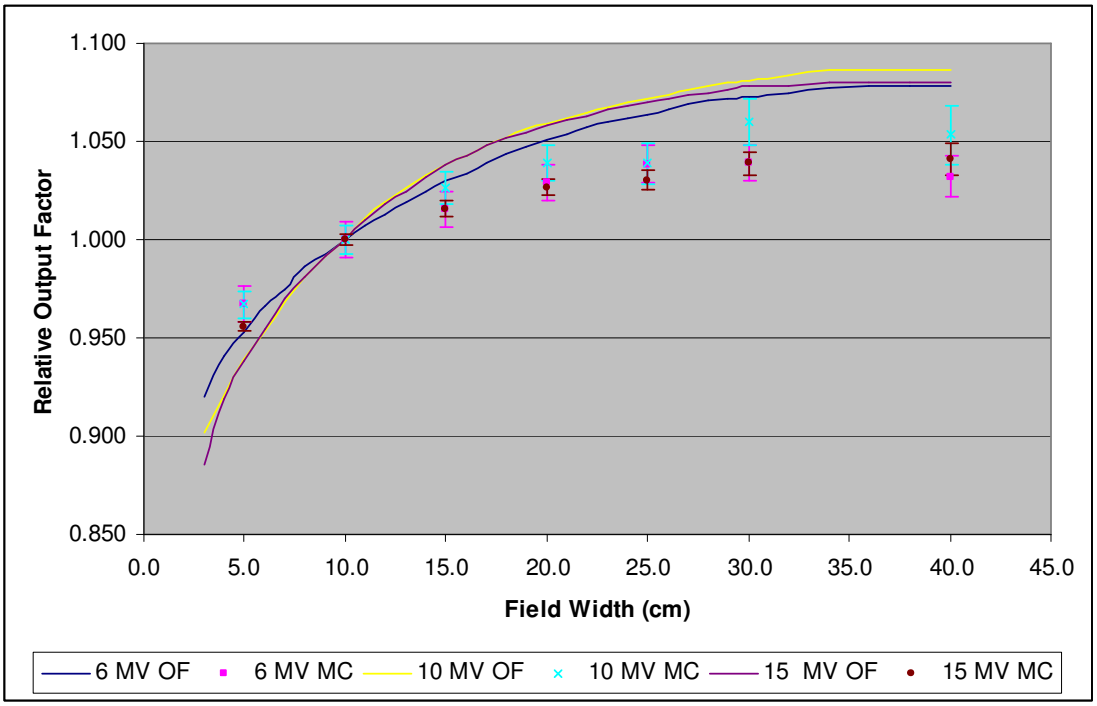

Figure 4.4: Output Factors for 6 MV, 10 MV and 15 MV Elekta.

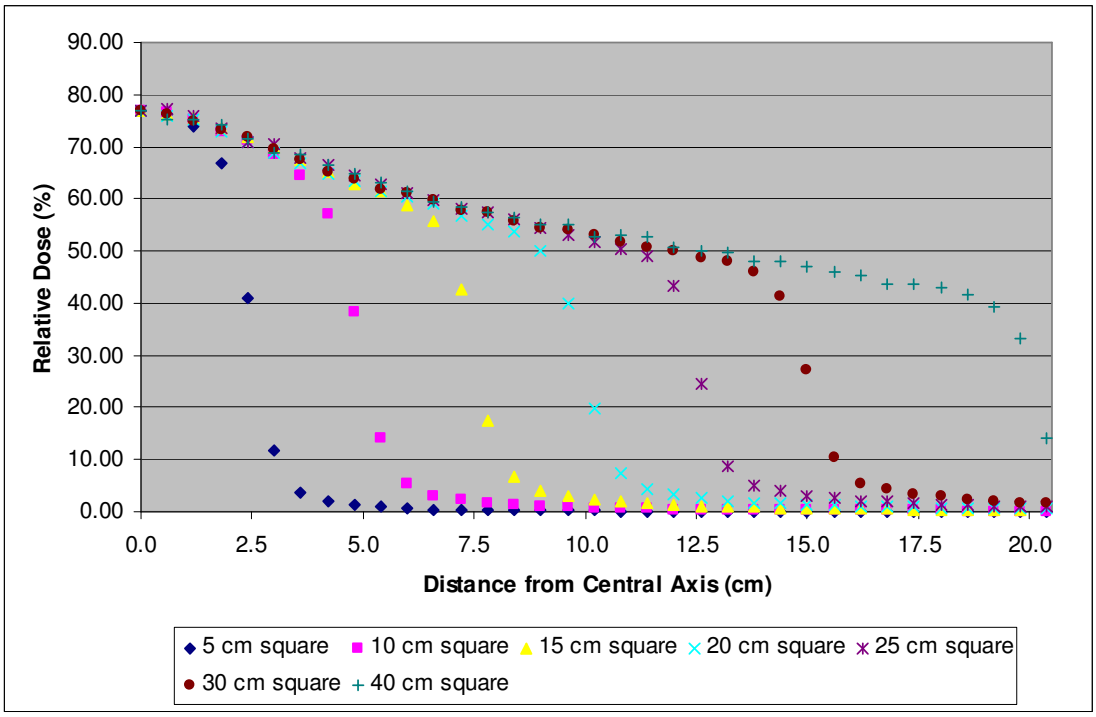

Figure 4.5: The off-axis ratios for 15 MV Elekta at 10 cm deep simulated with 2 flattening filters using the specification heights.

4.2.2 The Evolution Process of the Flattening Filter

The 15 MV and 10 MV Elekta linac energies use 2 flattening filters but the 6 MV uses only 1. Hence, the modelling should start with 1 flattening filter rather than 2 which was most appropriately for 6 MV Elekta and Varian. Since the 15 MV and 10 MV Elekta Linac involve a second flattening filter, hopefully when the adjustment of the 6 MV flattening filter had been verified with the commissioning data the addition of the high energy filter would made the beam continue to stay flat. Otherwise the thickness of the flattening filters for the 15 and 10 MV were needed to be altered, until a flat beam was obtained. Therefore, the Monte Carlo simulations were carried forward to model the 6

MV Elekta and Varian machine from this time onwards. Descriptions of the Varian modelling are contained in the next section.

The 6 MV Elekta simulations were run with a number of electron energies, from 6.0 to 6.5 MeV. Out of these, the best percentage depth dose would be chosen as a suitable electron energy. Results of the PDDs are given in table 4.1. The simulation points were compared with the measured data to see which of the electron energies best match with the measured data. This analysis was performed for the smallest field size (3 x 3 cm^2) since here the accuracy of the modelling of in-phantom photon scatter is least important.

The smallest average number of the points deviated from the PDD curves should give the least deviated points from the measured data as shown in Appendix A. Table 4.1 below summarizes which one of the electron energies gives the best result.

More of the 6.4 MeV electron energies were run at different field sizes to see whether the PDDs still agree with the commissioning data. They seemed to agree well as shown in figure 4.6. After the right electron energy has been achieved, the off-axis ratio profile was plotted to check for consistency. The OAR profile for this electron energy seemed to be displaced away from the flat radiotherapy beam, as shown below in figure 4.7.

Table 4.1: The best fit electron energy data for PDDs using original flattening filter height.

Field Size (3.0 cm)
e^- Energy (6.0 MeV)

Depth (cm)	Monte Carlo	M. Data	Local % Diff.	PDD Diff.
10	60.3	60.8	-0.76	-0.5
20	31.7	33.1	-4.22	-1.4
Total % difference			-4.97	-1.9

Field Size (3.0 cm)
e^- Energy (6.1 MeV)

Depth (cm)	Monte Carlo	M. Data	Local % Diff.	PDD Diff.
10	60.7	60.8	-0.16	-0.1
20	32.3	33.1	-2.51	-0.8
Total % difference			-2.67	-0.9

Field Size (3.0 cm)
e^- Energy (6.2 MeV)

Depth (cm)	Monte Carlo	M. Data	Local % Diff.	PDD Diff.
10	60.2	60.8	-0.93	-0.6
20	32.4	33.1	-2.02	-0.7
Total % difference			-2.95	-1.2

Field Size (3.0 cm)
e^- Energy (6.3 MeV)

Depth (cm)	Monte Carlo	M. Data	Local % Diff.	PDD Diff.
10	60.3	60.8	-0.79	-0.5
20	32.5	33.1	-1.93	-0.6
Total % difference			-2.72	-1.1

Field Size (3.0 cm)
e^- Energy (6.4 MeV)

Depth (cm)	Monte Carlo	M. Data	Local % Diff.	PDD Diff.
10	60.9	60.8	0.21	0.1
20	32.6	33.1	-1.58	-0.5
Total % difference			-1.36	-0.4

Field Size (3.0 cm)
e^- Energy (6.5 MeV)

Depth (cm)	Monte Carlo	M. Data	Local % Diff.	PDD Diff.
10	61.4	60.8	1.01	0.6
20	33.3	33.1	0.61	0.2
Total % difference			1.62	0.8

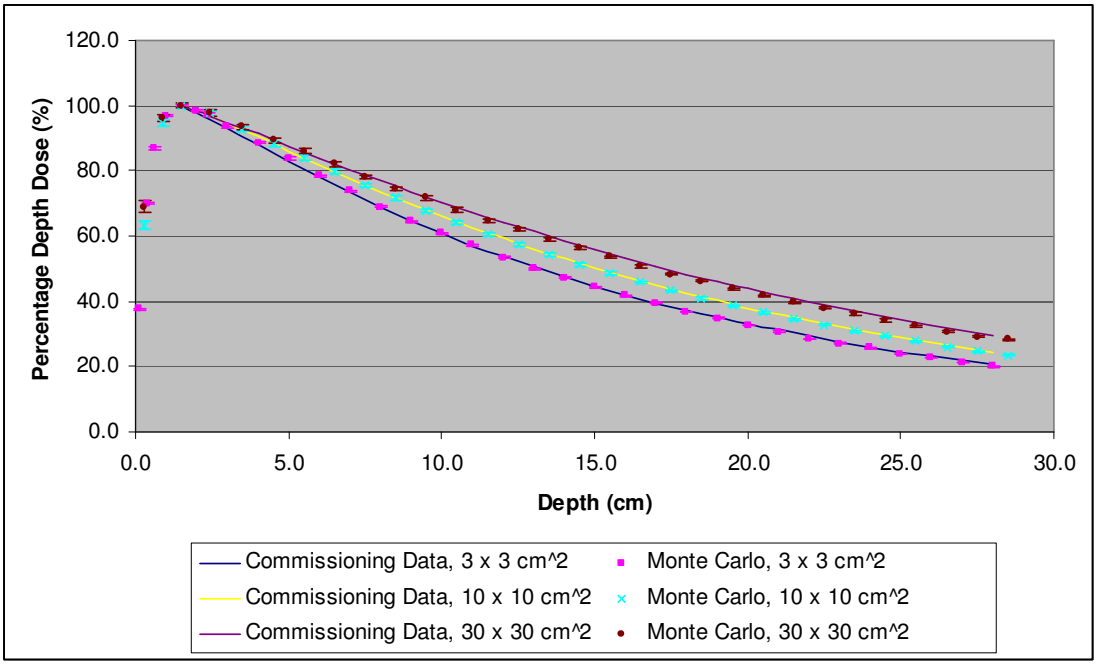

Figure 4.6: 6 MV Percentage depth doses at 3, 10 and 30 cm square field, 90 cm SSD for Elekta model adjusted to 6.4 MeV electron energy.

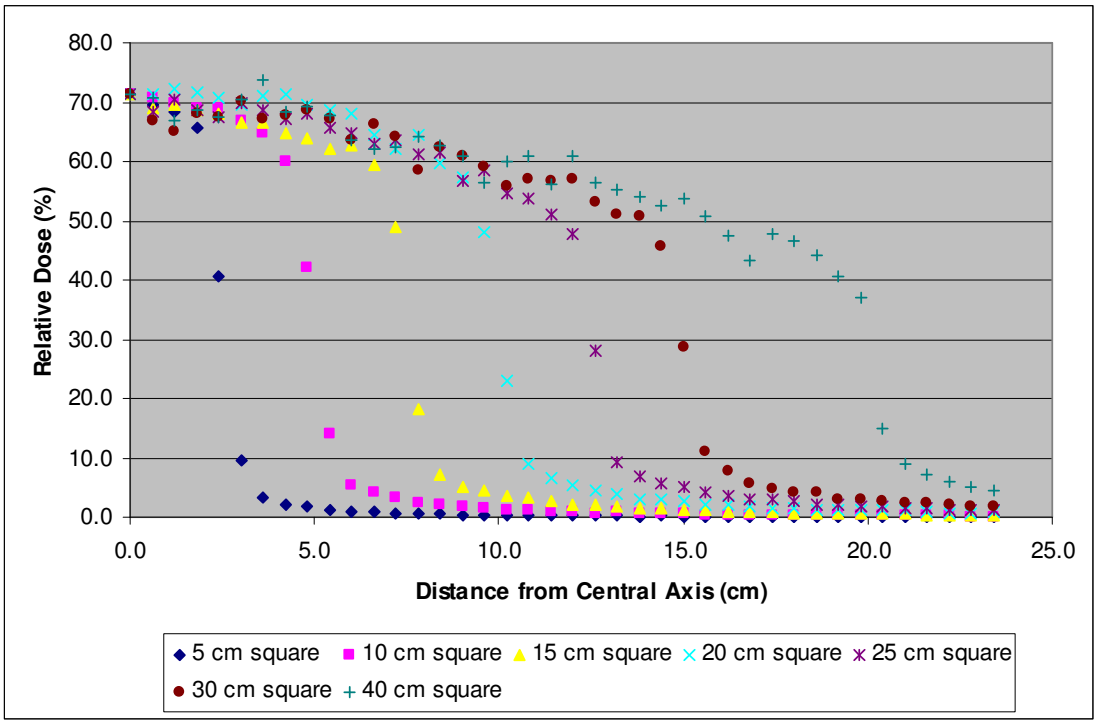

Figure 4.7: The OARs for 6 MV Elekta at various field sizes at 10 cm deep.

Further modification of the flattening filter was needed in order to obtain a validated model. Due to this, various heights of the flattening filter were simulated from the original specification to twice the original height using the Monte Carlo code to produce results that can be chosen as best fit to the commissioning data. Further runs for 6.4 MeV electron energy and the adjusted flattening filter heights were performed from an increment of 0.5 cm to twice the height of the original filter.

From figure 4.8 and 4.9, it has been shown that the best match for the Monte Carlo simulations should be around 1.85 to 1.92 x the original height of the flattening filter. To find out the most accurate one, the simulations at this range were run at longer calculations with increased number of histories from 10^8 to 10^9 to get better uncertainties.

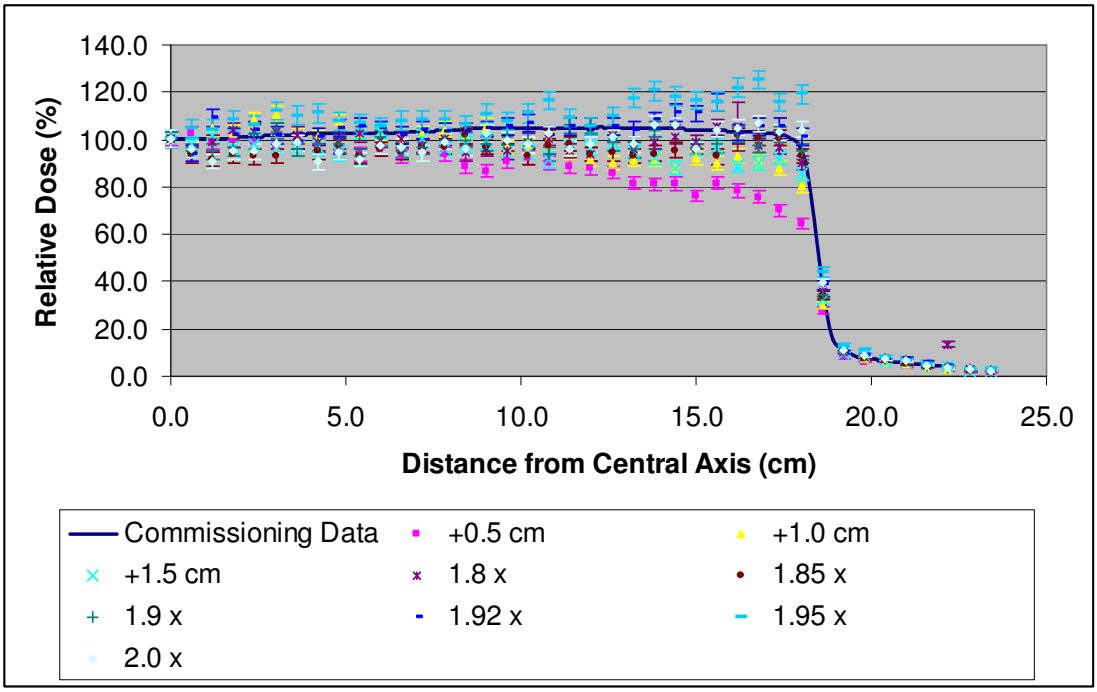

Figure 4.8: 6.4 MeV Elekta off-axis ratio at 1.5 cm deep, 40 cm square field with various flattening filter heights.

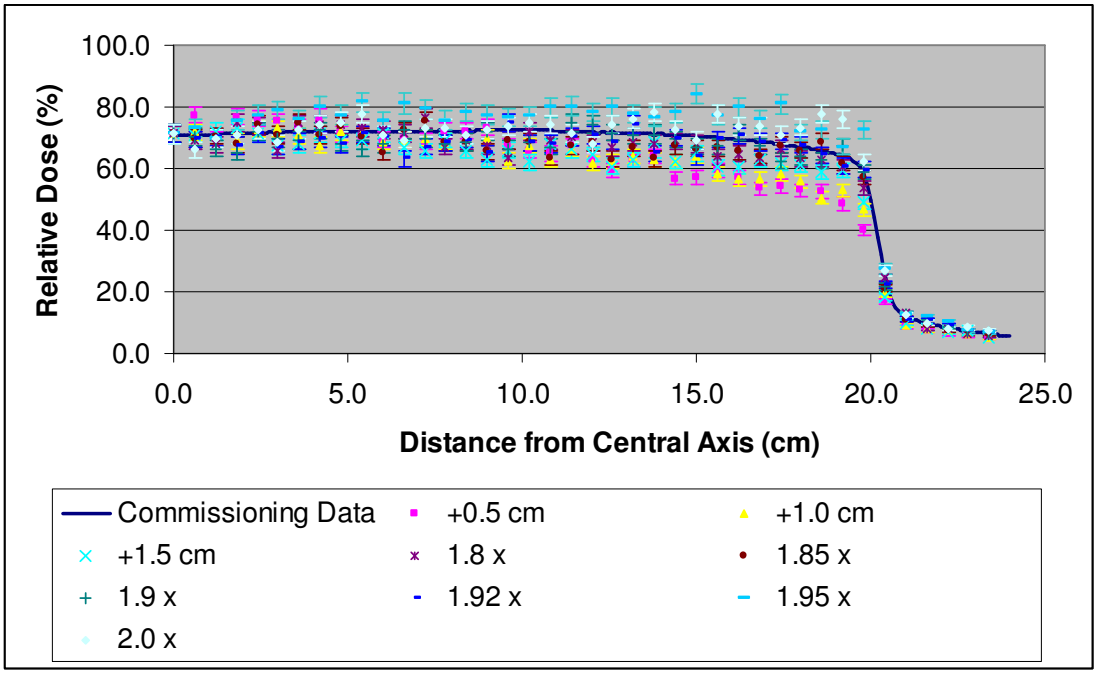

Figure 4.9: 6.4 MeV Elekta off-axis ratio at 10.0 cm deep, 40 cm square field with various flattening filter height.

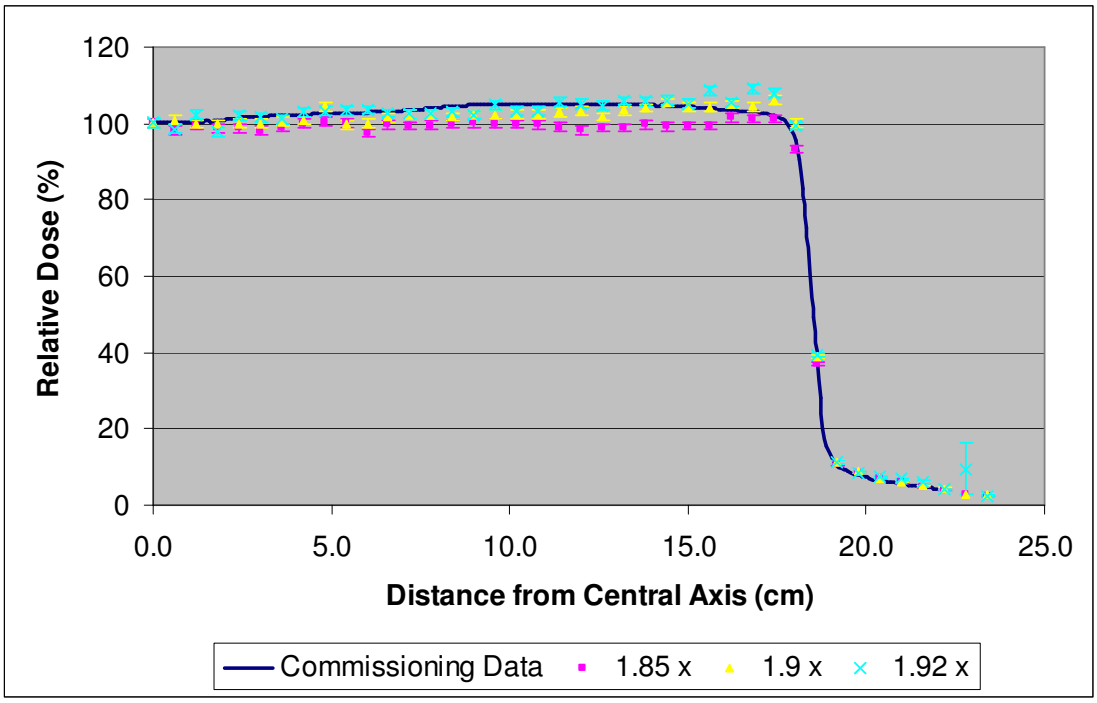

Figure 4.10: 6.4 MeV Elekta off-axis ratio at 1.5 cm deep, 40 cm square field 1.92 x flattening filter heights with increased number of histories.

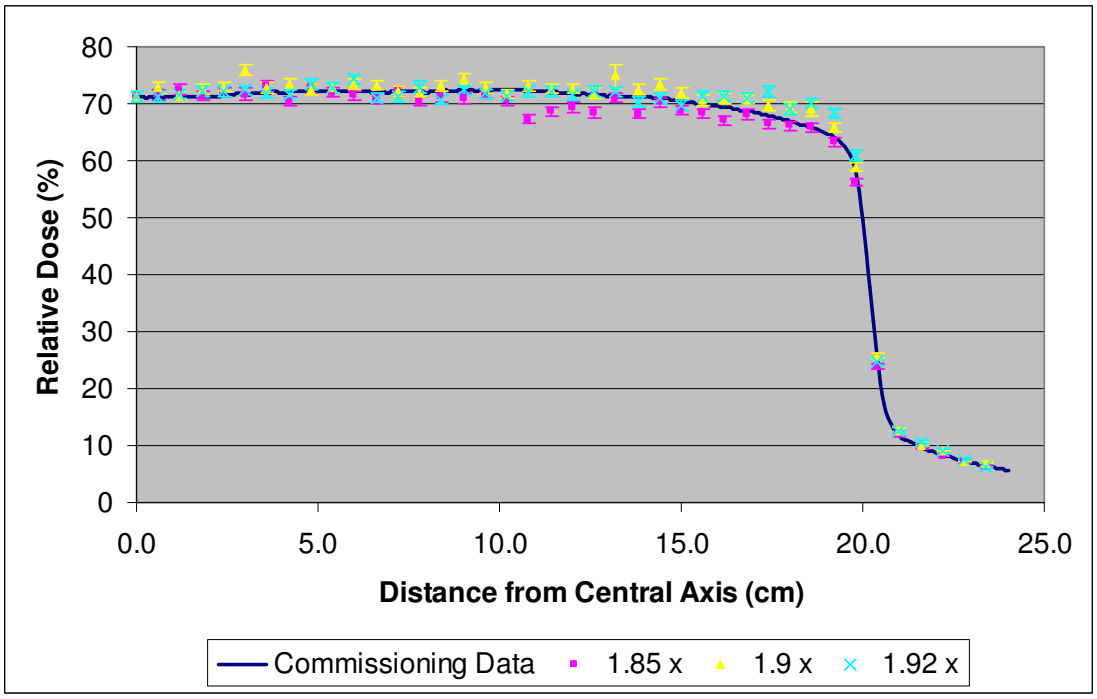

Figure 4.11: 6.4 MeV Elekta off-axis ratio at 10.0 cm deep, 40 cm square field 1.92 x flattening filter heights with increased number of histories.

The decision on the most appropriate flattening filter height was made on the basis of the minimum sum of the deviations between the MC calculated and the measured beam profile. The analyses of these are in Appendix A. These converged to an optimum flattening filter thickness of 1.92 x the original height and the final profiles as shown in the preceding page in figure 4.10 and 4.11.

For the three different heights (1.85 x, 1.9 x and 1.92 x) from Appendix A, it has been shown that the smallest total average displacement is when the flattening filter height was adjusted to 1.9 x the original dimension, where the average of all the points lie above the profile data at 1.5%. But the 1.92 x original height profile gave a better performance at 10 cm deep at 1.42% average difference as compared to 2.24% for 1.9 x; therefore, it was hope that this would give a better output factor and overall result in the long run.

From figure 4.12, the Monte Carlo simulations show slight higher curves than the PDD from the commissioning measurement. This could indicate that the MC calculations generate slightly more scattered dose than measured in the standard values as a result of increasing the flattening filter height. However, this should be stopped or else the process would continue endlessly and would take so much time to complete. Furthermore, to achieve the target value of 2% PDD difference or better was already accomplished.

Although the PDD curves from the Monte Carlo calculations are in disagreement within less than 4% at 10 x 10 cm^2 field for local percentage

difference, but for the larger field sizes some smaller discrepancies are shown but with less than 3% difference as in table 4.2 below. In terms of Percentage Depth Dose, in all cases differences are more or less 1%.

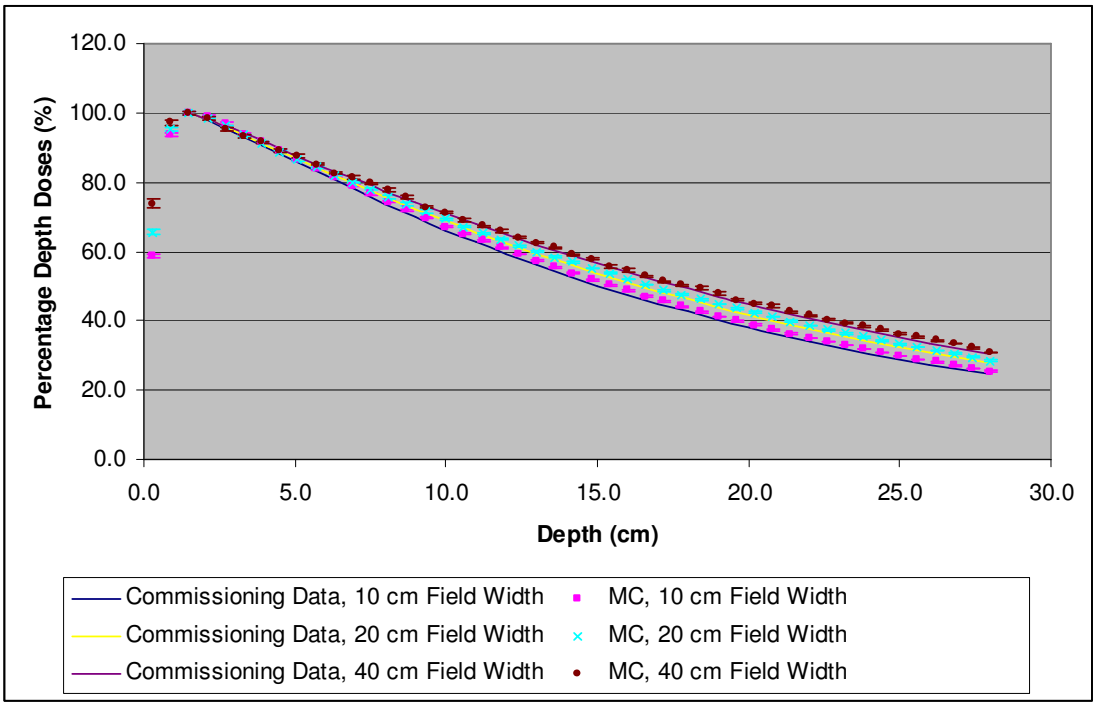

Figure 4.12: 6.4 MeV Elekta PDDs, 1.92 x flattening filter original height at 10, 20 and 40 cm square field.

Table 4.2: The discrepancies of the PDDs at the depth of 10, 20 and 28 cm.

Field Size (10 cm)

e^- Energy (6.4 MeV), 1.92 x FF height

Depth (cm)	M. Carlo	M. Data	Local % Diff.	PDD Diff.
10	67.19	66.1	1.65	1.1
20	39.14	38.0	3.00	1.1
28	25.42	24.5	3.76	0.9

Field Size (20 cm)

e^- Energy (6.4 MeV), 1.92 x FF height

Depth (cm)	M. Carlo	M. Data	Local % Diff.	PDD Diff.
10	69.31	68.8	0.74	0.5
20	42.82	41.7	2.69	1.1
28	28.51	27.8	2.56	0.7

Field Size (40 cm)

e^- Energy (6.4 MeV), 1.92 x FF height

Depth (cm)	M. Carlo	M. Data	Local % Diff.	PDD Diff.
10	71.25	71.0	0.35	0.2
20	45.33	44.8	1.18	0.5
28	30.93	30.6	1.07	0.3

For the 15 MV Elekta model, the 6 MV flattening filter was used in addition to a second flattening filter. The thickness of the steel cone from the energy difference filter was changed to various heights from the original to twice the height. The off-axis ratios of the various thicknesses are shown below.

From all the off-axis ratio profiles in figure 4.13 and 4.14, there were some changes to the simulated beam at D_{max} and at 10 cm deep in the water phantom. None can be seen to be in good agreement when the height of the flattening filter was raised. All of the profiles tend to curve downwards and the shoulder started to increase in the relative dose output after about 1.5 x the original height of the flattening filter. This would not create a flat beam and the modelling of the flattening filter became harder to finalise.

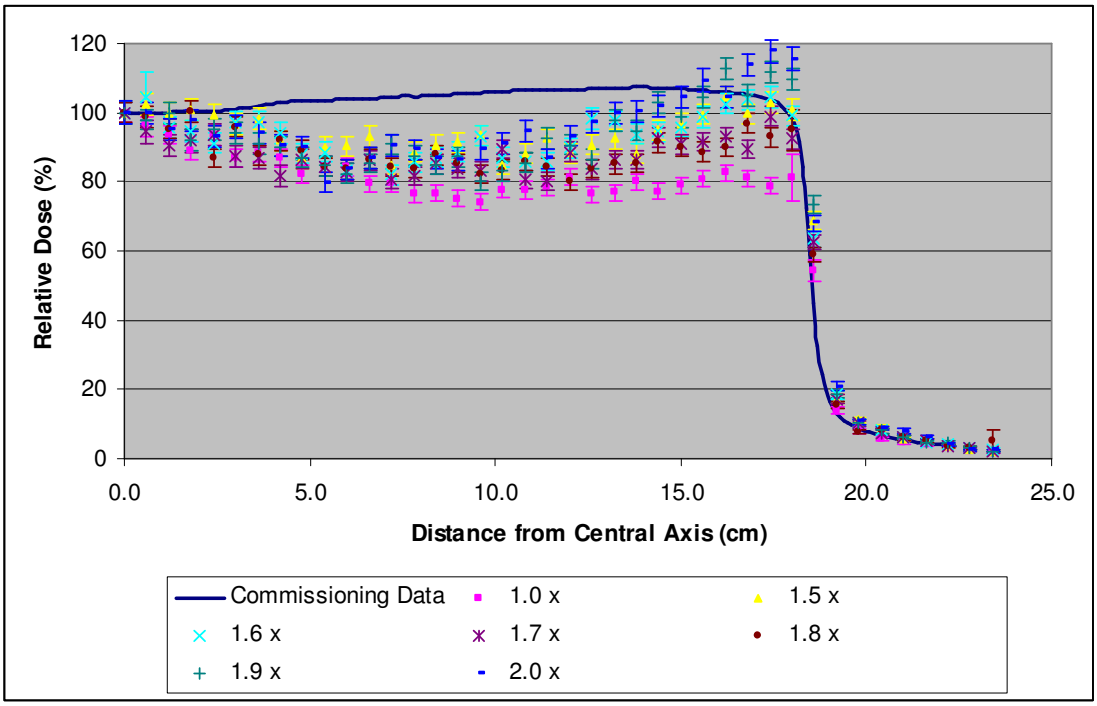

Figure 4.13: 15 MV Elekta, 40 x 40 cm^2 field, 2.7 cm deep, flattening filter heights from 1.0 to 2.0 x original height.

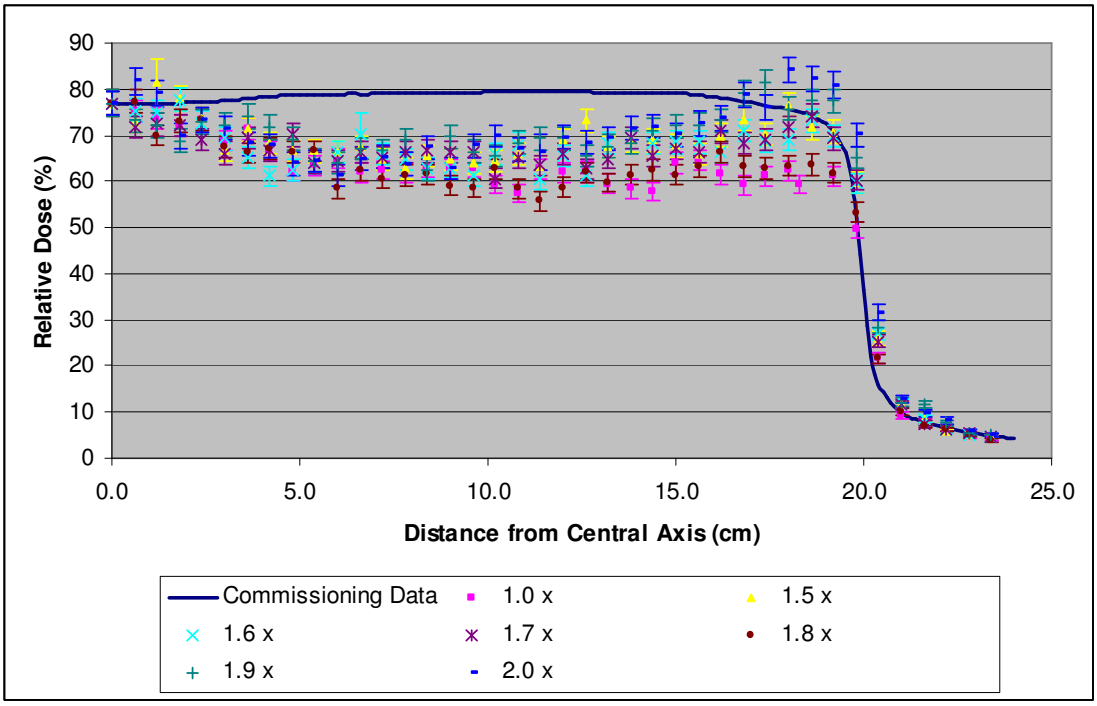

Figure 4.14: 15 MV Elekta, 40 x 40 cm^2 field, 10.0 cm deep, flattening filter heights from 1.0 to 2.0 x original height.

The best of these profiles, by comparison with experimental data is when the height of one of the flattening filter was modified to 1.5 x the manufacturer's specification. This was due to the simulated shoulder just at par with the central axis although the profile was curving inwards which made it the most reliable for the second flattening filter height for a 15 MV radiotherapy beam.

But in doing the adjustments for the 15 MV and 10 MV so that the OAR profiles would be entirely flat, would take too long for this PhD programme to complete. Further investigation using the 6 MV validated model would be more appropriate research to work with.

4.2.3 Results

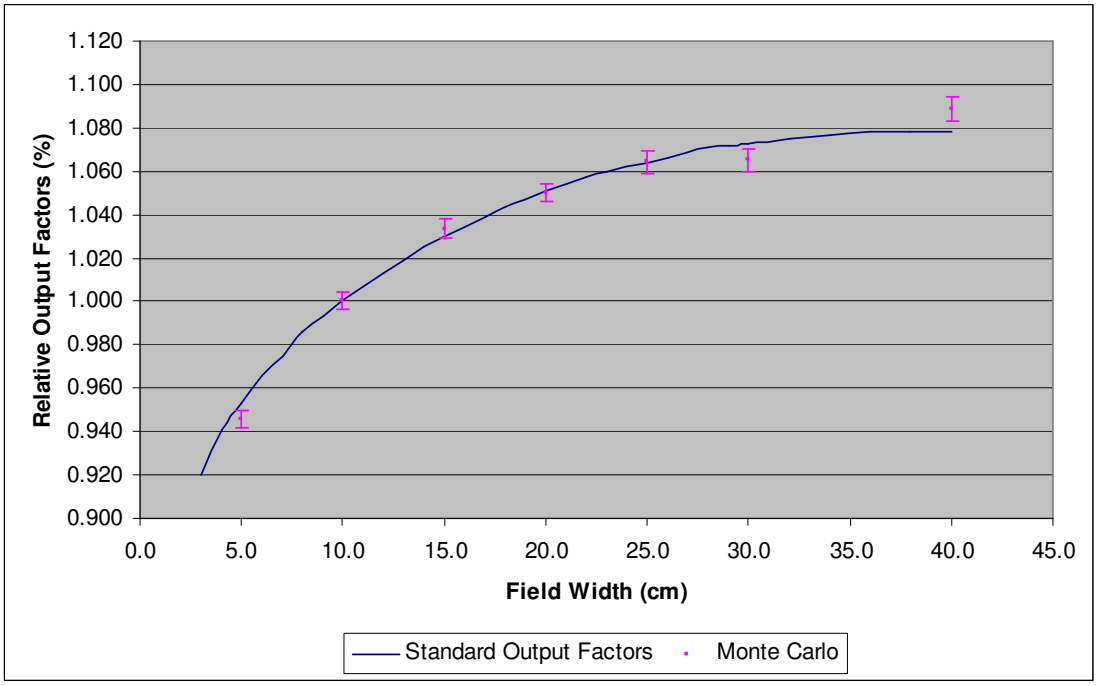

Figure 4.15: The 6 MV output factors for Elekta, 6.4 MeV, 1.92 x original height.

Table 4.3: The data that were used to plot the OF and the percentage errors.

Field Width (cm)	Measured Data	MC Normalised Dose	MC Percentage Error (%)	MC Uncertainties (±)	Percentage Diff. from M. Data (%)
5	0.953	0.9458	0.4	0.0038	-0.76
10	1.000	1.0000	0.4	0.0040	0.00
15	1.030	1.0336	0.4	0.0041	0.35
20	1.051	1.0500	0.4	0.0042	-0.09
25	1.064	1.0643	0.5	0.0053	0.02
30	1.073	1.0652	0.5	0.0053	-0.72
40	1.078	1.0888	0.5	0.0054	1.00

The finalised output factors for 6 MV Elekta were displayed above in figure 4.15 after many runs with adjusted electron energy to 6.4 MeV and flattening filter height of 1.92 x the original. Table 4.3 has shown that the output factors do not out lie from the measured data too much which is less than or equal to

within 1% error. Hopefully this would be a useful result as a valid modelling for Elekta at 6 MV.

4.3 The process of optimization for Varian

4.3.1 Methods

The components that were modelled for the Varian linac were the tungsten-rhenium target, primary collimator, flattening filter, y-jaws, x-jaws, multileaf collimator, PMMA screen and the stereotactic collimator if applicable. The Varian linear accelerator has little information to most of its components. Therefore, the flattening filter was based on the Elekta linac dimension. But by using this information, the percentage depth dose did not seem to be in agreement with the measured data as can be seen in figure 4.16 on the next page. This was especially true for 30 cm square field.

The result for the PDD at 30 cm field size was too low for the 6 MV energy with respect to the measured data; therefore, the off-axis ratios were checked to see whether the beam output was flat at 10 cm deep. It can be seen from the profiles below that the beam was not flat at the initial dimension of the flattening filter. To choose the best height, the flattening filter was adjusted from its initial state to twice its original height to find optimum values. At optimum, the resulting OAR, PDD and output factor plots are shown below in figure 4.17 and 4.18.

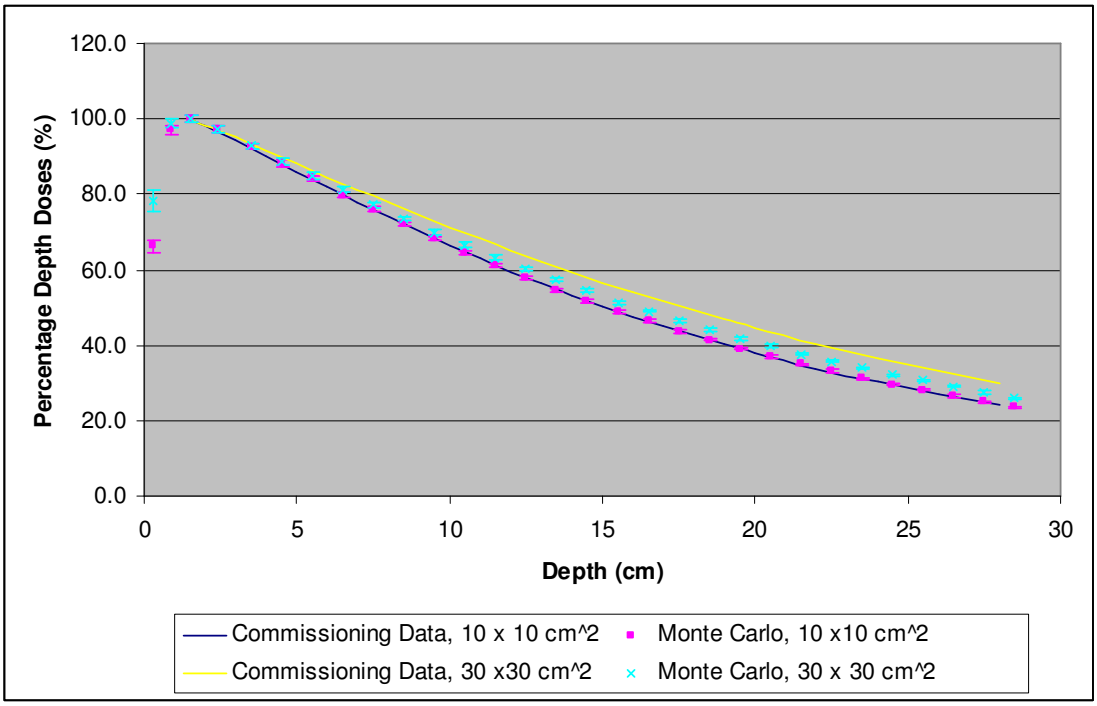

Figure 4.16: The PDDs for 10.0 and 30.0 cm square fields, 100 cm SSD for 6 MV Varian.

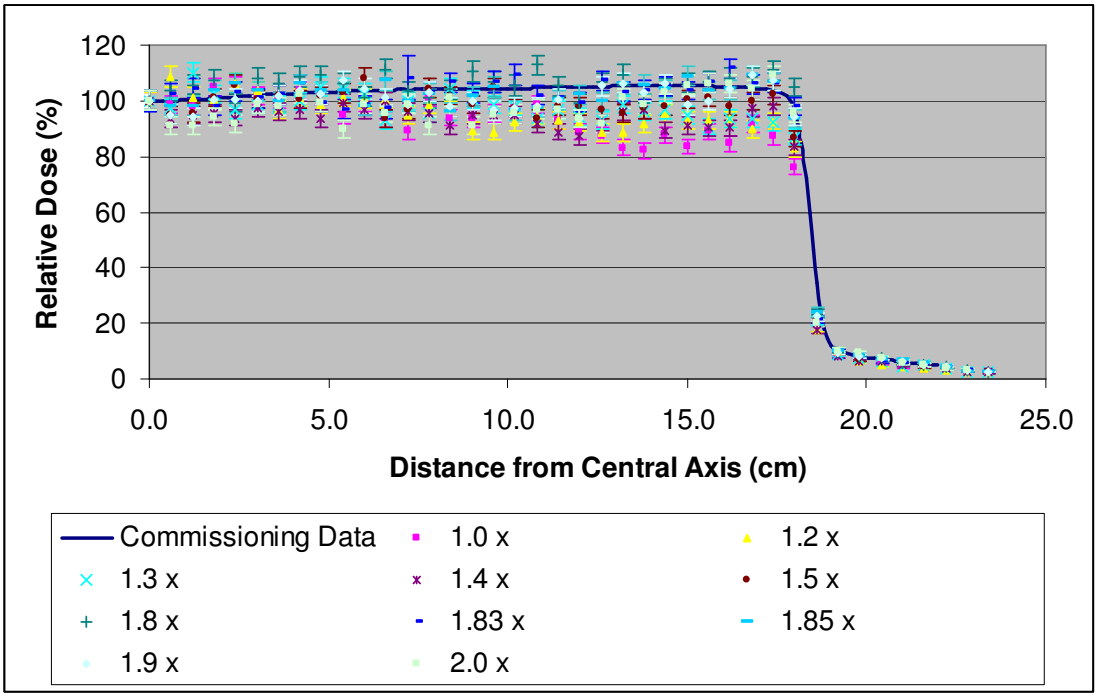

Figure 4.17: 6 MV Varian off-axis ratios for 40 x 40 cm^2 at 1.5 cm deep with various flattening filter heights.

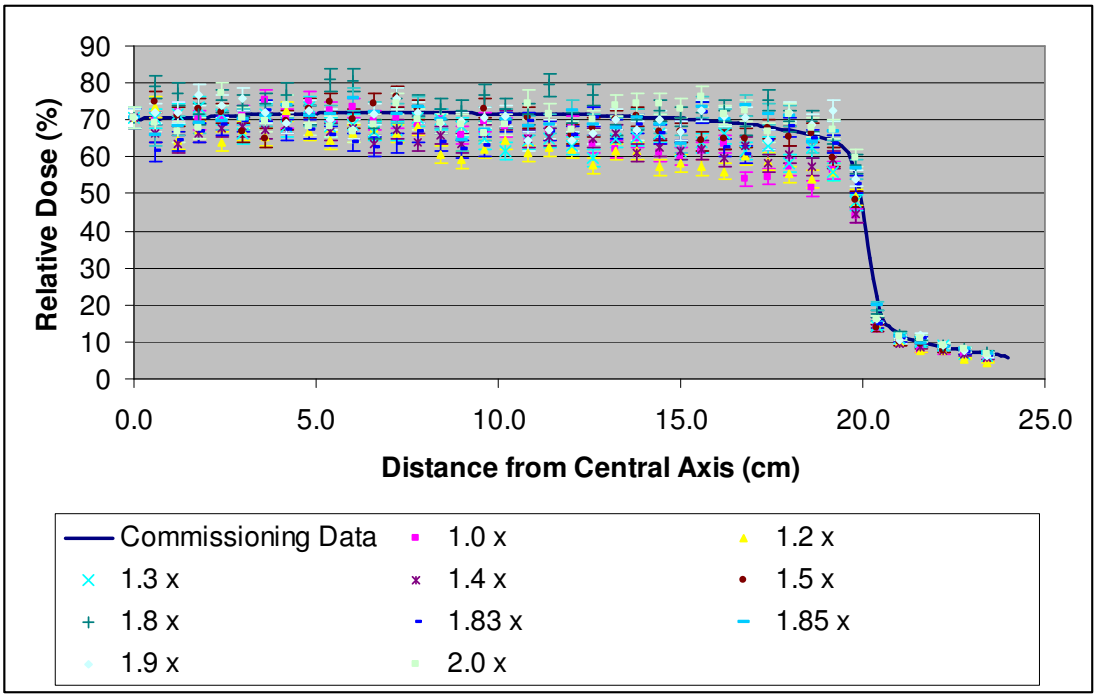

Figure 4.18: 6 MV Varian off-axis ratios for 40 x 40 cm^2 at 10.0 cm deep with various flattening filter heights.

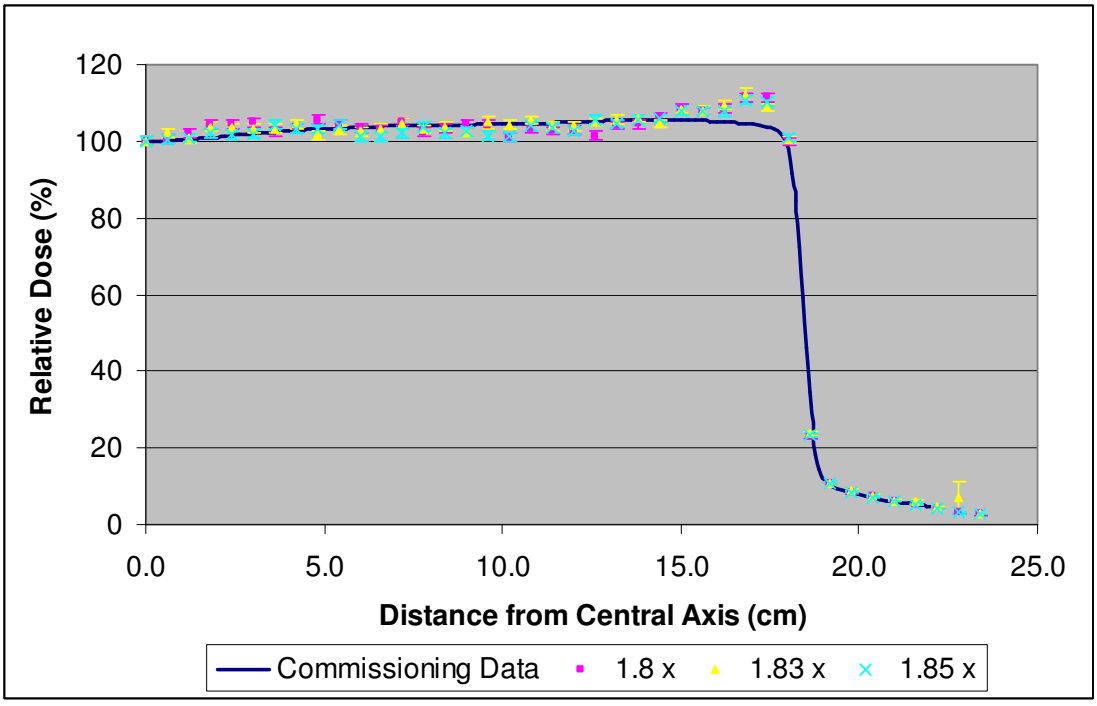

Figure 4.19: 6.0 MeV Varian off-axis ratios at 1.5 cm deep, 40 cm square field various flattening filter heights with increased number of histories.

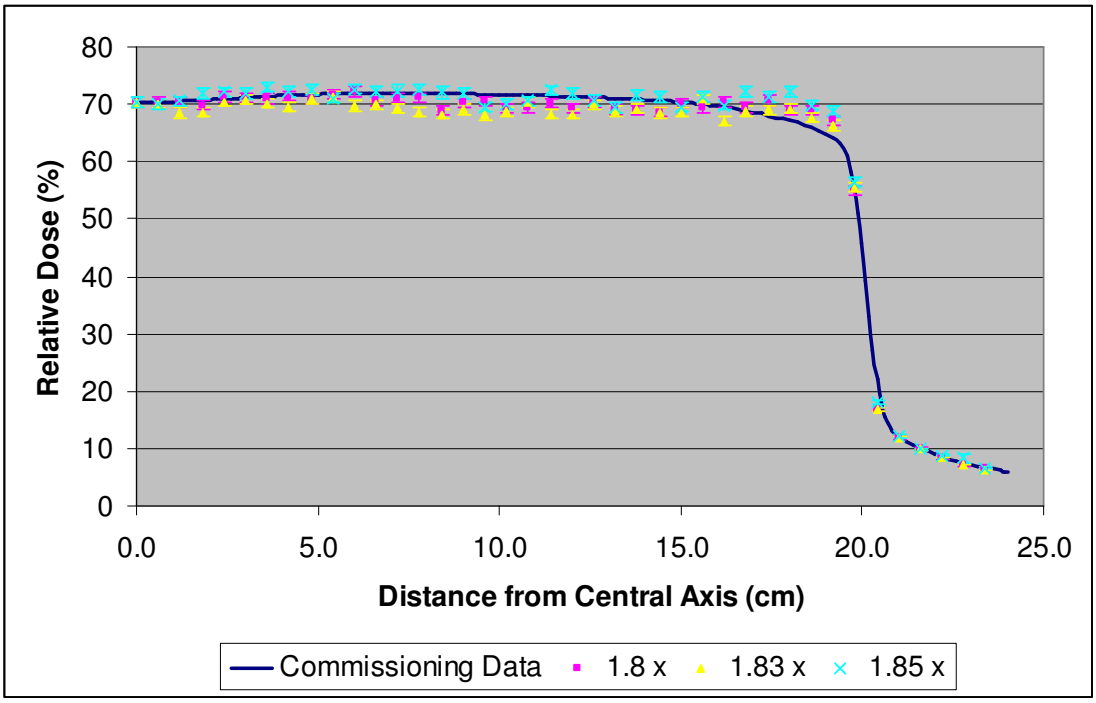

Figure 4.20: 6.0 MeV Varian off-axis ratios at 10.0 cm deep, 40 cm square field various flattening filter heights with increased number of histories.

From the results above it could be seen that the best agreement should be, when the height of the flattening filter was between 1.8 to 1.9 times the initial height. In order to obtain which one would be the best result the simulations should be run at higher number of histories. Results from further runs were shown above in figure 4.19 and 4.20.

To know the increased height that agrees well with the measured data, the percentage errors were tabulated in Appendix B. It is hoped that the smallest error would give a valid result that can be used to predict the result of experiments using the Varian machine.

The result above has shown that 1.8 x the original height would be the best match but 1.85 x also shows a promising result. Since the 1.8 x did not show

a better result at 1.5 cm deep, therefore the 1.85 x were taken for plotting the output factor. The output factor result shown in figure 4.21 below does agree with the measured data. It seemed that the percentage difference gave a precision less than 0.6% error as in table 4.4. However, if this is a valid result the PDDs should give an agreeable result for this height.

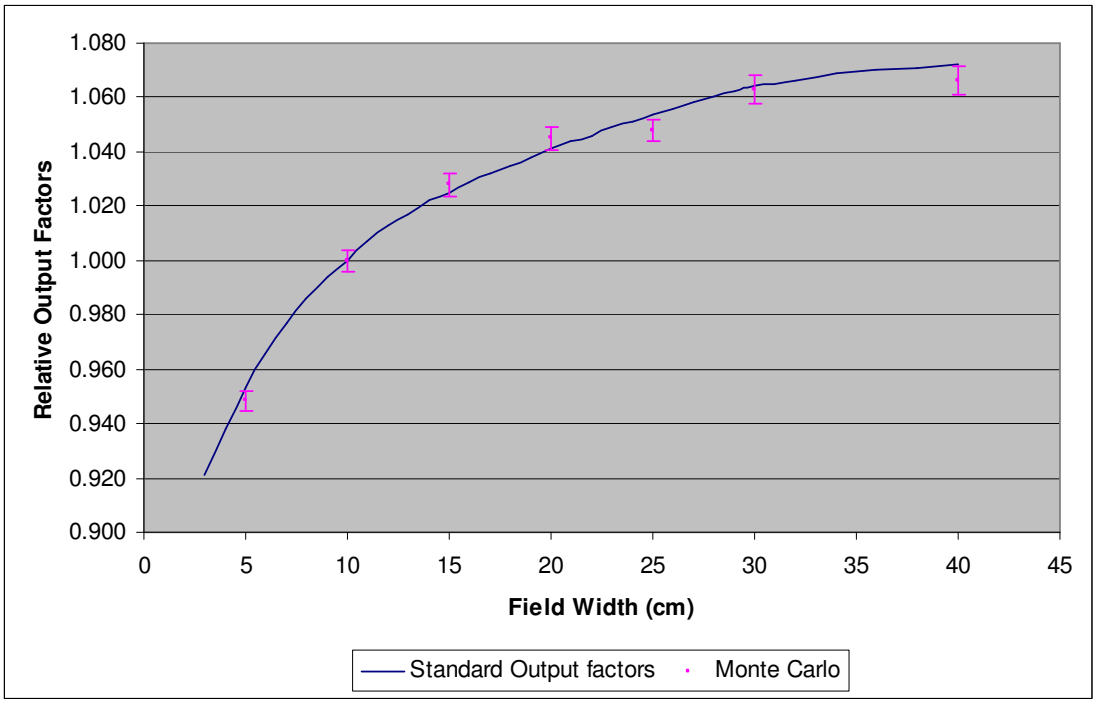

Figure 4.21: The 6 MV output factors for Varian, 6.0 MeV, 1.85 x original height.

Table 4.4: The result of the precision of the output factors at 6.0 MeV, 1.85 x original height.

Field Width (cm)	Measured Data	MC Normalised Dose	MC Percentage Error (%)	MC Uncertainties ±	Percentage Diff. from M. Data (%)
5	0.953	0.9483	0.4	0.0038	-0.49
10	1.000	1.0000	0.4	0.0040	0.00
15	1.025	1.0279	0.4	0.0041	0.28
20	1.041	1.0449	0.4	0.0042	0.37
25	1.054	1.0478	0.4	0.0042	-0.59
30	1.064	1.0627	0.5	0.0053	-0.12
40	1.072	1.0660	0.5	0.0053	-0.56

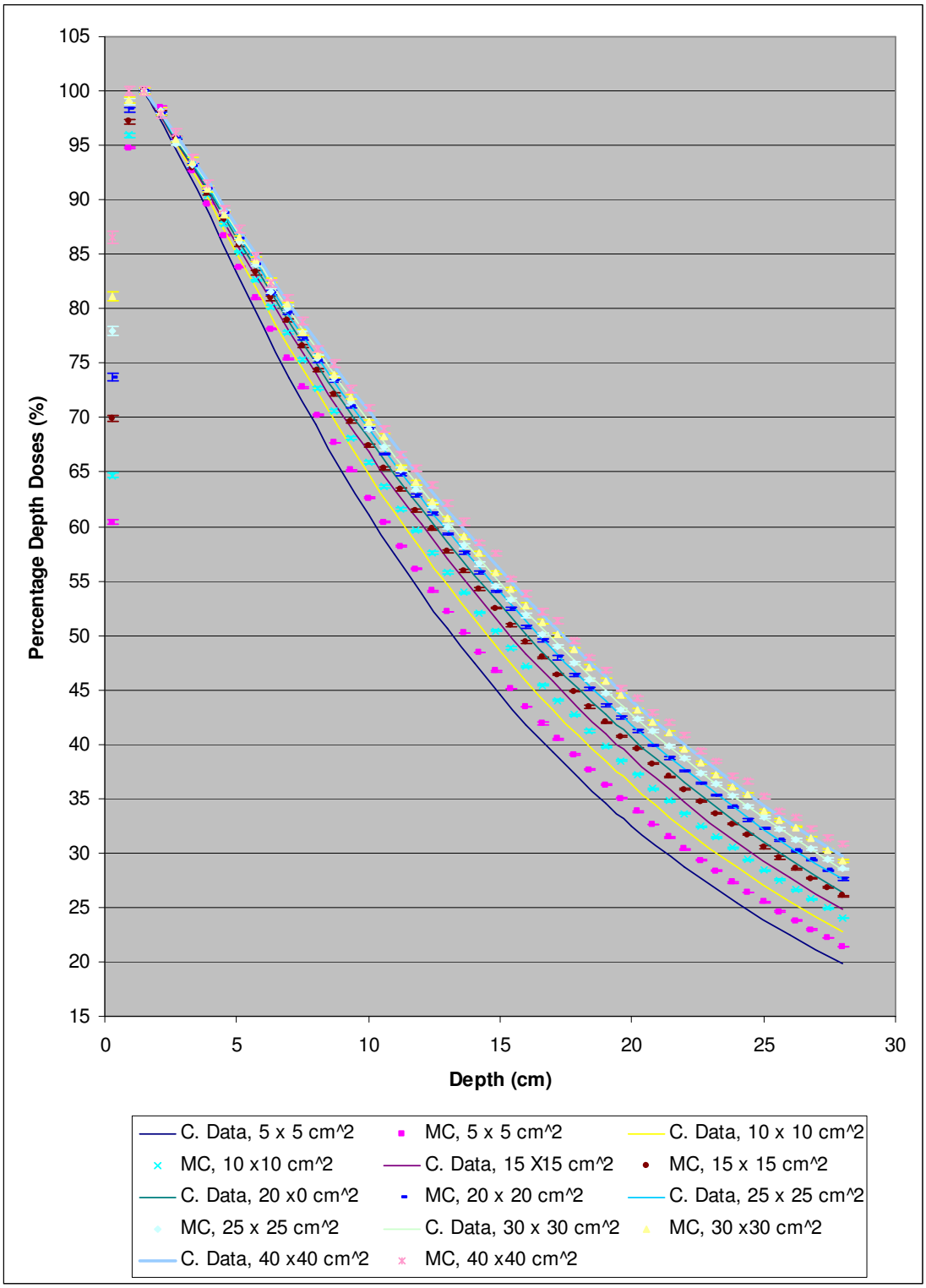

Figure 4.22: The PDDs for 6 MV Varian for various field sizes.

Although the Varian output factors were in agreement with the measured data and also the difference for the points was less than 1% but the results were

unable to show that the modelling was in agreement with the percentage depth doses at different field sizes. Almost all of the values of the MC simulations were higher than the commissioning data as in figure 4.22 and the local percentage error was as big as 7.5%.

Due to the mismatch of the PDDs, the electron energy of the linac machine needed to be redone with lower energy until it matches and after that the flattening filter has to be run with numerous heights to obtain the right OAR. Again, the PDD has to be compared with the measured data until it agrees. If not the process has to go on in cycle until the Monte Carlo Output Factor (OF) simulations simply match with the measured data or within 2% error or better.

To get validated data, the electron energy was simulated with energy reducing from its original value of 6.0 MeV to 5.0 MeV. The PDDs were compared with the standard data. To find out the best fit electron energy, the sum of the differences of the points and the standard data should give the lowest value. The analyses are displayed in Appendix B.

Table 4.5: The result for the range of electron energy investigated.

e^- Energy (MeV)	Differences in 10 x 10 cm^2 (%)	Differences in 20 x 20 cm^2 (%)	Total Differences (%)
5.0	-4.681	-1.851	-6.532
5.1	-2.430	0.147	-2.283
5.2	-0.905	-1.135	-2.041
5.3	1.218	-0.294	0.924
5.4	2.408	0.359	2.767
5.5	4.683	3.010	7.693
5.6	5.875	8.018	13.893
5.7	7.686	6.103	13.789
5.8	9.805	5.790	15.595
5.9	10.426	6.567	16.993

From table 4.5 above, it has been shown that the best fit electron energy for the Varian linac is 5.3 MeV which has less than 1% error comparing with all of the energies that has been done using the MC simulations. The next step was to investigate whether the height of the flattening filter used was able to give a consistent result with the commissioning data. Starting from the initial height, the flattening filter was modified until the best OAR conformed to the commissioning data. The profiles of the OAR are shown below in figure 4.23 and 4.24.

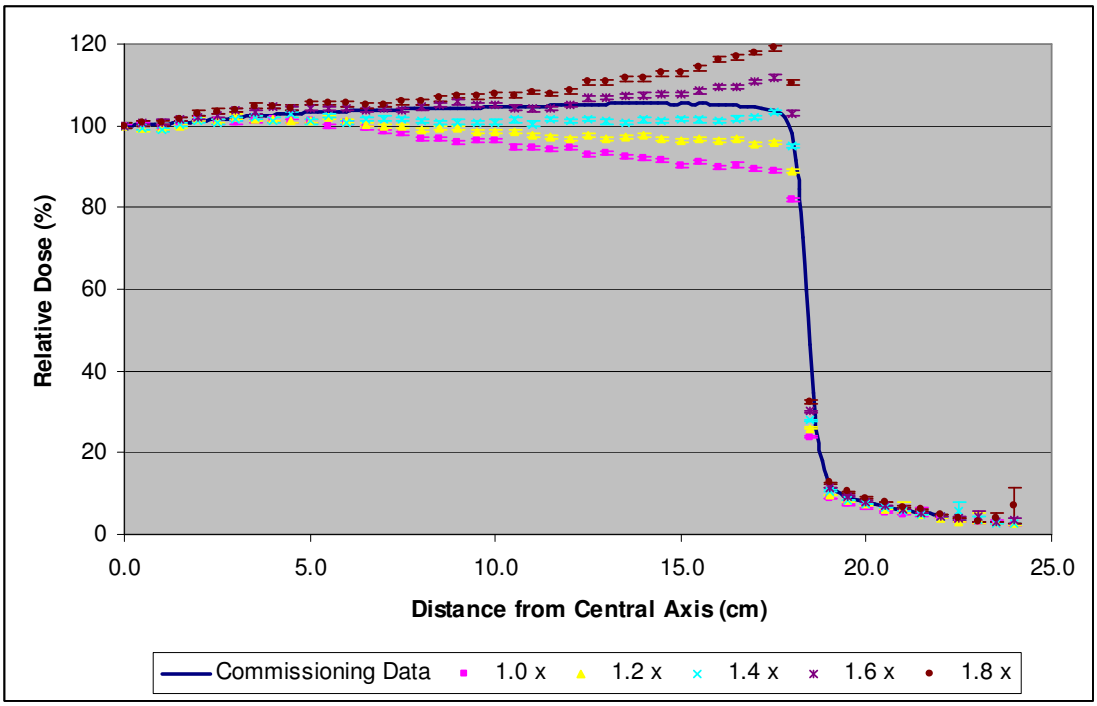

Figure 4.23: Varian off-axis ratios, 5.3 MeV electron energy, various flattening filter heights at 1.5 cm deep.

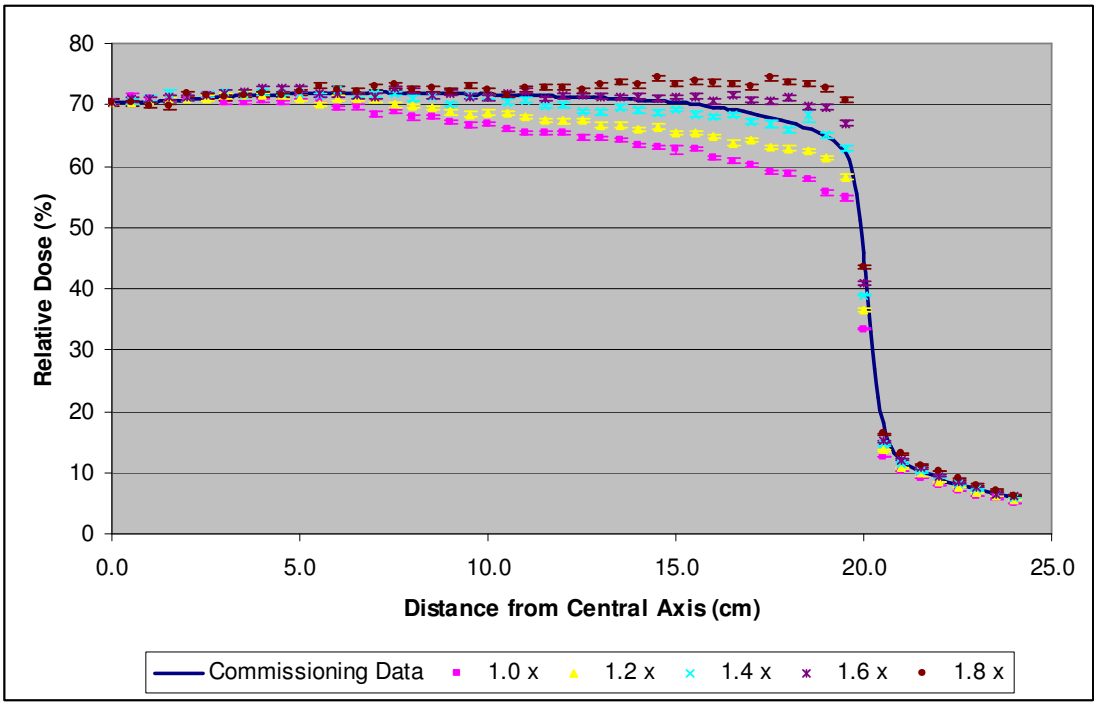

Figure 4.24: Varian off-axis ratios, 5.3 MeV electron energy, various flattening filter heights at 10.0 cm deep.

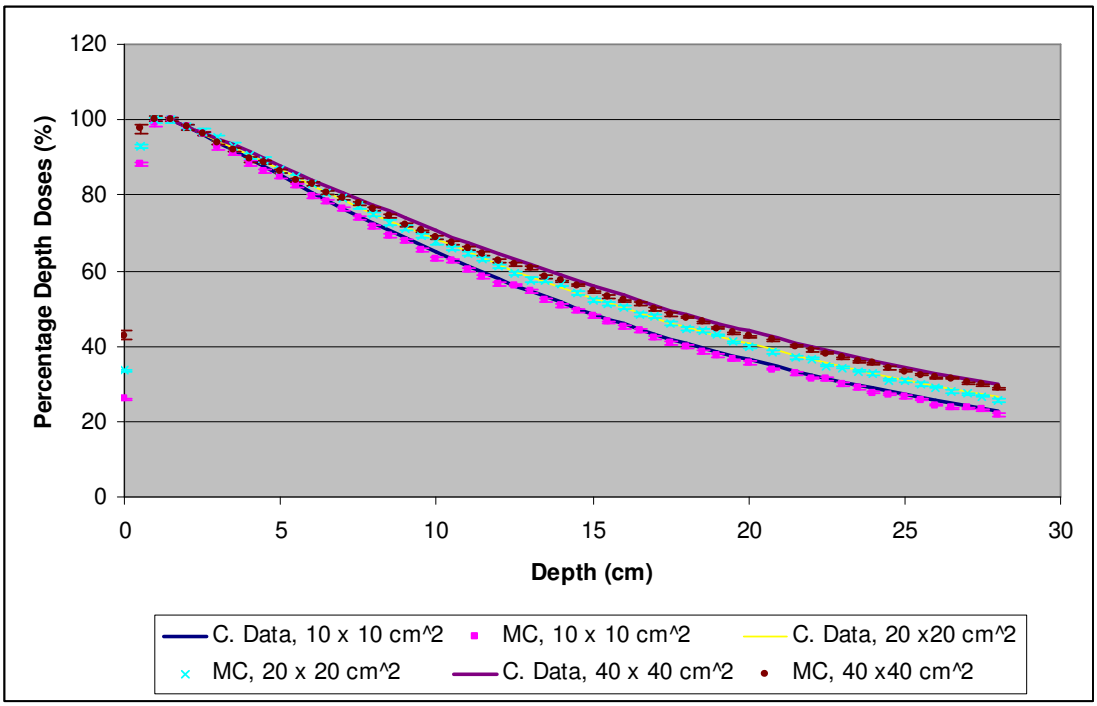

Figure 4.25: The PDDs for Varian at 5.3 MeV electron energy and 1.4 x the original height of the flattening filter.

Table 4.6: The errors of the PDD at the depth of 10, 20 and 28 cm are demonstrated.

Field Size (10 cm)

e^- Energy (5.3 MeV), 1.4 x FF height

Depth (cm)	M. Carlo	M. Data	Local % Diff.	PDD Diff.
10	63.20	64.8	-2.46	-1.6
20	35.58	36.3	-1.98	-0.7
28	21.81	22.7	-3.94	-0.9

Field Size (20 cm)

e^- Energy (5.3 MeV), 1.4 x FF height

Depth (cm)	M. Carlo	M. Data	Local % Diff.	PDD Diff.
10	67.60	68.1	-0.74	-0.5
20	39.77	40.6	-2.04	-0.8
28	25.68	26.4	-2.74	-0.7

Field Size (40 cm)

e^- Energy (5.3 MeV), 1.4 x FF height

Depth (cm)	M. Carlo	M. Data	Local % Diff.	PDD Diff.
10	68.67	70.6	-2.74	-1.9
20	42.56	44.0	-3.27	-1.4
28	28.76	29.7	-3.15	-0.9

From the profiles in figure 4.23 and 4.24 above, it can be seen that the best adjustment for the flattening filter height was at 1.4 x the initial height of the Varian linac. To check whether this specification was valid the PDDs were plotted to see whether they were still agreeable.

The PDDs of the MC simulation were slightly lower than the measured data as in figure 4.25. The overall points at 10 cm and 20 cm deep were < 2.5% local percentage error for 10 and 20 cm field sizes as in table 4.6. In general, most of the points were slightly lower and greater deviations from the commissioning data can be seen at 40 cm field size and deeper depths at 28 cm. However, the PDD differences for all points are better than 2% accuracy.

But to increase the electron energy and to redo the height of the flattening filter seemed to be never ending, therefore if the OAR profile is within acceptable consistency, it could be said that the modelling agrees reasonably well.

4.3.2 Results

The output factors for these specifications are plotted in figure 4.26 below. The points do not deviate by greater than 2% from the commissioning data. From table 4.7 that follows, the deviation from the standard values was less than 1.8%, which is satisfying enough for a radiotherapy measurement.

Since the differences were small, it is suggested that the Varian linac model by means of the Monte Carlo code could be used for predicting results with all the necessary alteration made that mimic the environment encompassing the experimental research.

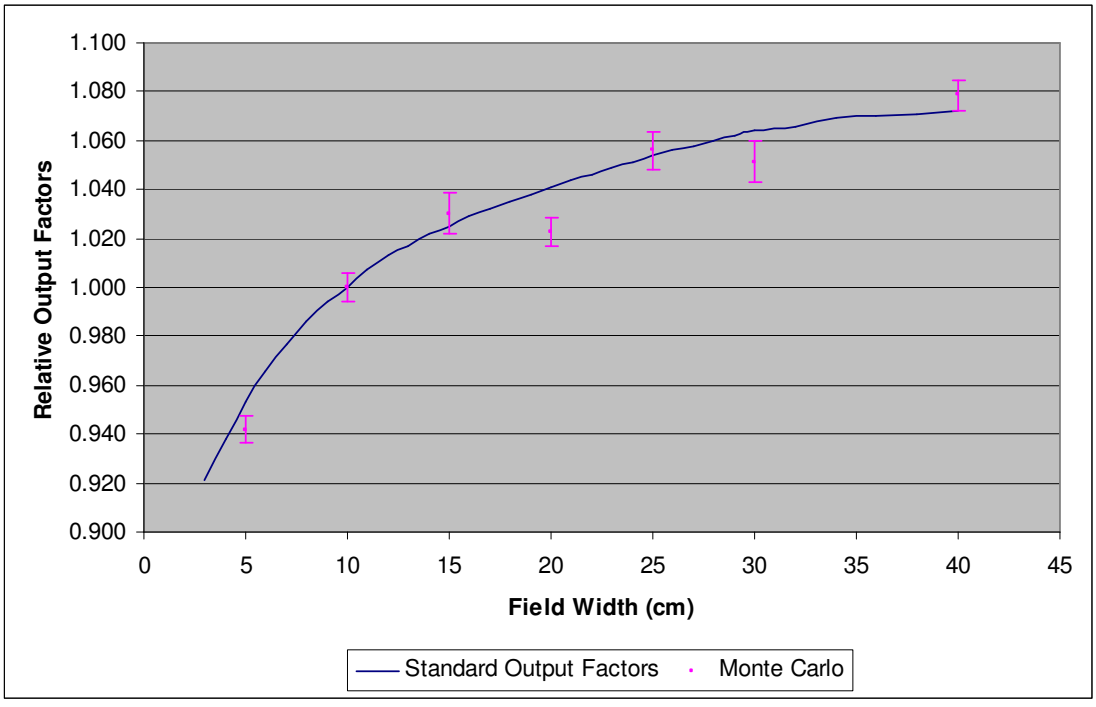

Figure 4.26: The Varian output factors, 5.3 MeV electron energy at 1.4 x original height.

Table 4.7: The deviations of the Monte Carlo result from the measured data.

Field Width (cm)	Measured Data	MC Normalised Dose	MC Percentage Error (%)	MC Uncertainties ±	Percentage Diff. from M. Data (%)
5	0.953	0.9418	0.6	0.0057	-1.17
10	1.000	1.0000	0.6	0.0060	0.00
15	1.025	1.0302	0.8	0.0082	0.50
20	1.041	1.0227	0.6	0.0061	-1.76
25	1.054	1.0558	0.7	0.0074	0.17
30	1.064	1.0513	0.8	0.0084	-1.19
40	1.072	1.0785	0.6	0.0065	0.61

4.4 Discussion

In this work, a generalised model for the treatment head for 6 MV Elekta and Varian Linacs were completed to be used for further investigations in radiotherapy. Simulated output factors that fall within 2% range were obtained, which were validated against the commissioning data. However, the 10 MV and 15 MV Elekta linac were not completed due to time constraints and involving a second flattening filter to be adjusted.

The process of optimization for both machines took slightly more than a year to complete, including the implementation of directional bremsstrahlung splitting, in order for the simulation running more efficiently. Most of the runs were sent to the Bluebear computer cluster for running the simulations in parallel with 10^9 number of histories. The MC percentage errors for PDDs and OARs were better than 1% accuracy on the idea that the final output factors would be < 2% accuracies. The summary of the process are shown in the diagram below (figure 4.27).

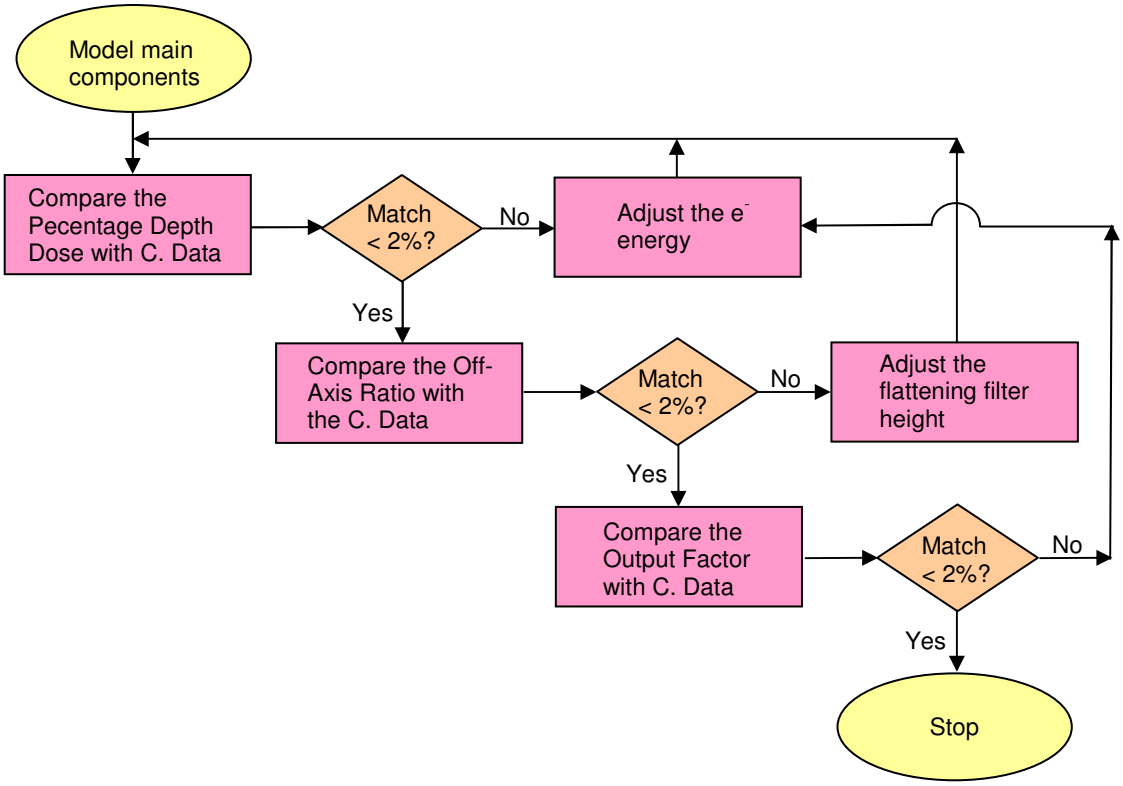

Figure 4.27: The process of achieving a validated Monte Carlo model for a radiotherapy linac.

The final 6 MV output factor for Elekta was ≤ 1.0%; however, the final output factor for Varian was < 1.8% due to great difficulty to match the PDDs and OARs and to adjust between the height of the flattening filter and the electron energy of the linac. Table 4.8 below shows the adjustments that were made in the process.

Table 4.8: The summary of results for the linac machines.

	6 MV Elekta	**6 MV Varian**
Electron energy	6.4 MeV	5.3 MeV
Flattening filter height	1.92 x specification height	1.4 x original height
Off-axis ratio local average difference	≤ 2.6% at 1.5 cm deep	≤ -4.0% at 1.5 cm deep
Percentage depth dose difference	≤ 1.1% at depth of 20 cm, 10 cm field width	≤ -1.9% at depth of 10 cm, 40 cm field width
Output factor accuracy	≤ 1.0% at 40 cm field width	≤ -1.8% at 20 cm field width

To conclude, both Elekta and Varian machines were modelled, and parameters adjusted to give a sufficiently close agreement between the simulator and the measured machine data (PDD, OAR and Output Factors). The final level of agreement was not perfect, but the residual deviations shown in table 4.8 were considered to be sufficiently small that the model could be used as a basis for further predictions. These predictions are shown in the following chapters.

Chapter 5 - Investigation on DOSI Detector using Varian Linac

5.1 Introduction

This investigation aims to predict the performance of the DOSI detector, a position sensitive detector based on the silicon strip detector technology [56, 57]. One of its main characteristics is the thin sensitive layer, as described in section 3.1.2.2. It is discussed in Yin et al. (2004) [64] and references therein that solid-state detectors such as diodes and MOSFETs will give a perturbation to the dose measurement so that a correction is needed before the results can be used in radiotherapy. For example, a correction to output factor measurements of up to 8% at 30 x 30 cm square field, and 12% at 40 x 40 cm square field are predicted [64, 67].

The response difference is as a consequence of Compton scatter which generates lower energy photons and therefore influences the photon energy spectrum as field size and depth increase. Compton scattering increases the proportion of low energy photons, and the interaction of these via the highly Z-dependent photoelectric effect becomes significant. The difference with DOSI is that it has a fine substrate of 0.3 mm [57] whereas diode detector has a silicon substrate of 0.5 mm [64] and other metal contacts are at greater distance from the sensitive volume, although they are perhaps somewhat larger.

Yin et al. [64] has described the modification of the Burlin cavity theory to correct for the 6 MV diode measurements by dealing with the primary and scatter photon spectra separately. However the need for such correction to be made would hamper the time involved as well as the accuracy of clinical measurements.

An ideal dosimeter would be a detector that has a tissue equivalent atomic number and density which is roughly equal to that of water. For a silicon dosimeter, such as diode and DOSI detectors, on the other hand, have effective atomic number and density which are roughly 3.89 and 2.33 times to that of water respectively.

However, solid-state detectors have other advantages over ionisation chambers due to high sensitivity, high resolution and small physical dimension, making them suitable for small field dosimetry. In fact, diode detectors are frequently used in the megavoltage range despite the fact that there are significant discrepancies in response with field size and depth compared with ionisation chambers [67].

DOSI, which is a proto-type detector, has more or less the same advantages as diodes but is superior to diodes in its position sensitivity, fast read-out electronics and capability for dynamic real time measurements. Examples for the output of the DOSI detector regarding position sensitivity and dynamic scanning are illustrated in figure 5.1 and 5.2. These are measurements taken with synchrotron beams showing static and dynamic responses with regard to

position and time using a collimated slit. Due to these beneficial capabilities it is a worthwhile to examine its performance further with Monte Carlo calculations so that investigations on, whether or not the difference in measurements are needed for correction beforehand or whether there is a possibility that the detector capability could be improved.

A 6 MV Varian linear accelerator beam has been used to measure the response of the DOSI detector as a function of field size. This investigation with Monte Carlo code will give some insights whether DOSI should be included in the category of detectors that require corrections for greater sensitivity to scattered radiation.

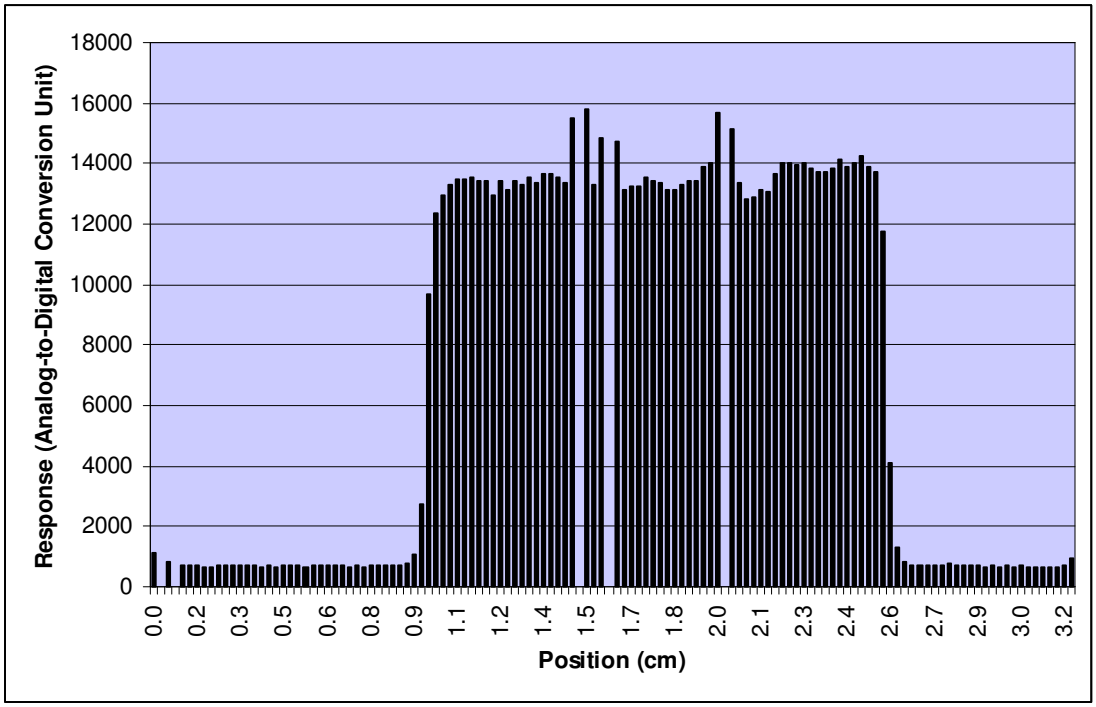

Figure 5.1: A typical measurement of DOSI detector showing response versus position readout. Measurement was taken in Daresbury, where the detector was placed in parallel with a synchrotron beam collimator slit.

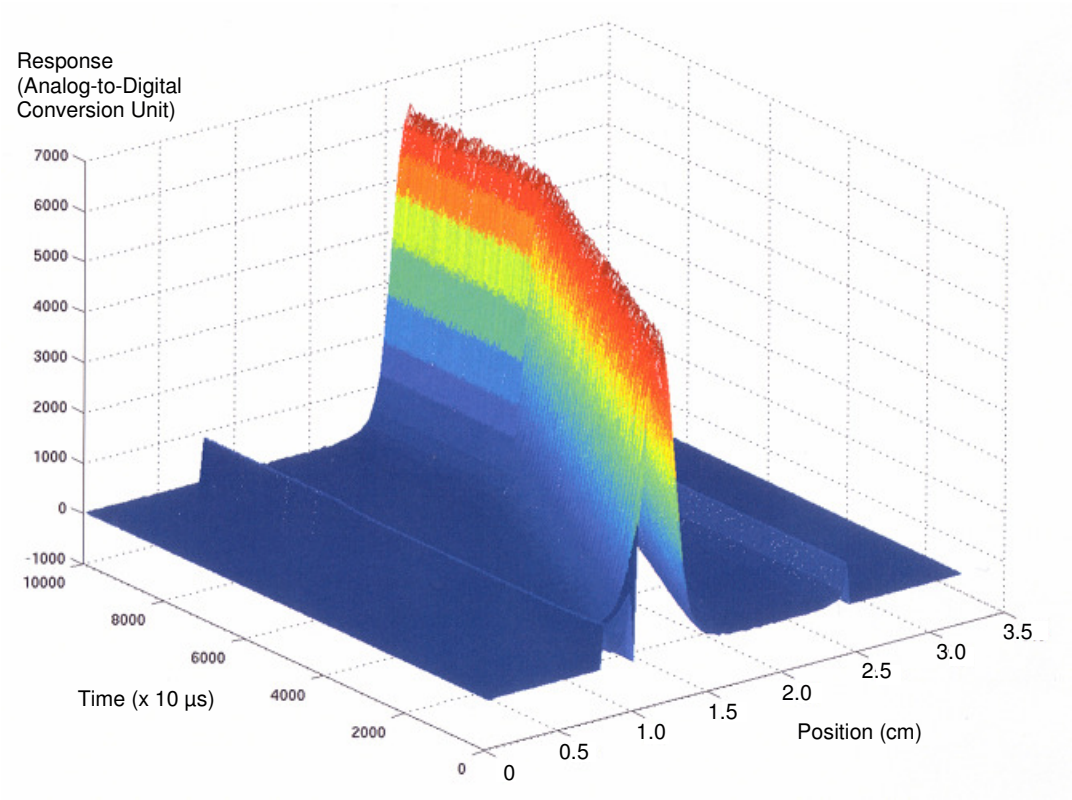

Figure 5.2: An example of a dynamic measurement obtained by DOSI detector where the sensitive array of the dosimeter placed 90° to a horizontal collimator slit moving vertically in a synchrotron beam.

It is anticipated that the DOSI detector may require much smaller corrections than measured in diodes and predicted in the method used by Yin et al. [64]. This is because scattered secondary electrons have a range that is greater than the thickness of the substrate, for example, a 500 keV scattered photon would have a range of roughly 0.9 mm in silicon. In addition, an electron with a continuous slowing down range of 25 µm has an energy of approximately 50 keV in Si [168].

5.2 Methods

The Varian Clinac model 600C/D (figure 5.3) was modelled using the BEAMnrc code as described in chapter 4. By using the validated 6 MV Varian linac model, the BEAMnrc code was setup at 90 cm SSD with a range of field sizes at 5, 10, 15, 20, 25 and 30 cm width. These were achieved by adjusting the x and the y-jaws with the help of the BEAMnrc graphical user interface as in figure 5.4. Note the single flattening filter in this model. However, the MLC was kept wide open as it did not play an important role in the experiment. The 40 x 40 cm^2 field was not part of the setup owing to DOSI experimental work was done with the largest available water equivalent phantom using 30 x 30 cm^2 slabs of RW3. DOSI detail drawings and sensitive array can be seen in figure 5.5.

The BEAMnrc code was compiled as a shared library and using its own input and pegs data files which is the 700ICRU material data set. This is an option where the phase space file was not stored, using isource = 9 source type in the DOSXYZnrc code. The source was sampled as soon as the particles crossed the scoring plane without the need to store the data, saving huge disk space in MBytes sometimes in GBytes sizes depending on usage. Apart from that, the variance reduction technique such as directional bremsstrahlung splitting was also being used to obtain the best efficiency in CPU time and statistical error discussed in section 3.5.

Figure 5.3: The Varian linac model in the Queen Elizabeth Hospital with the DOSI detector to be setup with water equivalent phantom surrounding the sensitive linear array.

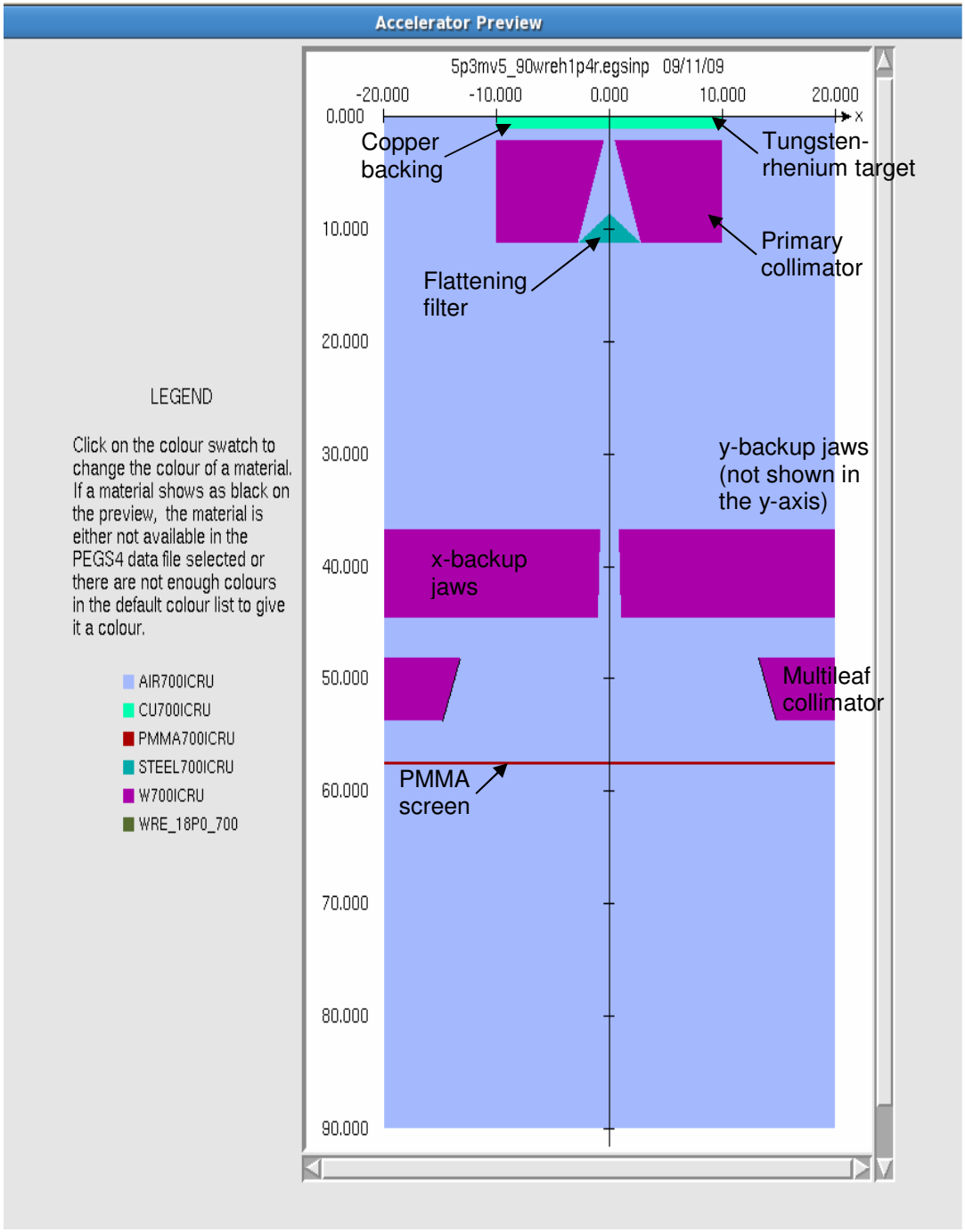

Figure 5.4: The Varian treatment head model using the BEAMnrc code.

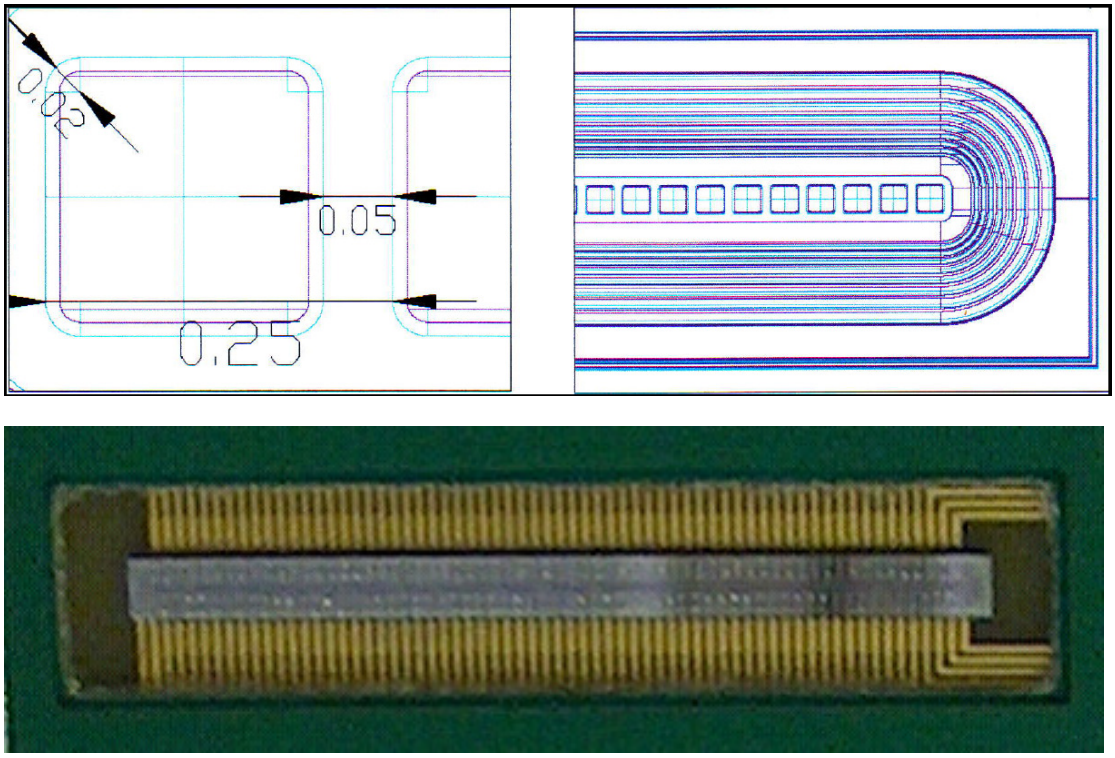

Figure 5.5: Top left, a detail drawing of the DOSI pixel element in mm and top right, a structural drawing of the DOSI sensitive area and its guard ring. Bottom figure, the DOSI detector sensitive array on a PCB. *Courtesy of S. Manolopoulos.*

The dose simulations were run in a water phantom using DOSXYZnrc code. The water phantom has a dimension of 30 cm x 30 cm x 30 cm to match the dimension of the available RW3 slabs, and was surrounded by air with thickness of 50 cm at all sides. A model of the DOSI detector was imbedded in the water phantom placed at 10 cm deep with a silicon strip of 3.3 cm x 0.22 cm x 0.03 cm in dimension as in figure 5.6 and 5.7. The size of the water phantom used mimicked the experiment with DOSI using water equivalent phantom of RW3 material. Note DOSI detector is not waterproof. Hence, this limits the range of the experimental and the simulated field size to the largest size slabs which is the 30 x 30 cm^2 field at the isocentre. DOSI data were later

corrected to liquid water measurements using the plots in figure 5.8 and table 5.1.

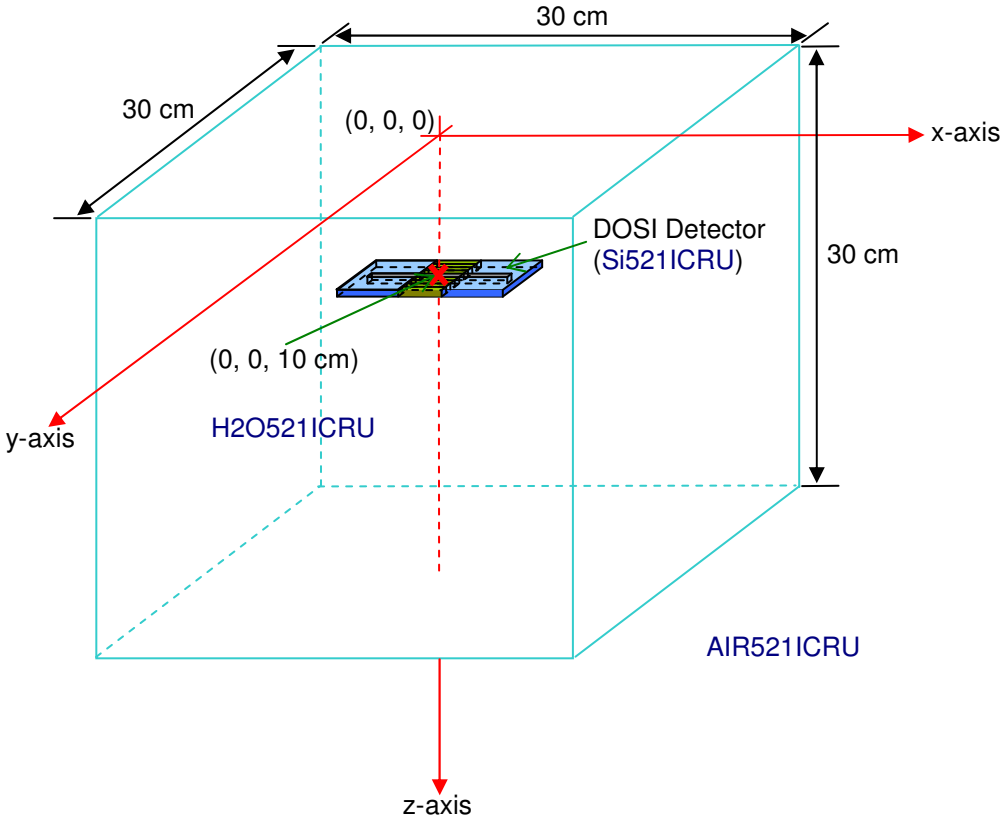

Figure 5.6: The phantom used to model the DOSI detector in water medium using DOSXYZnrc.

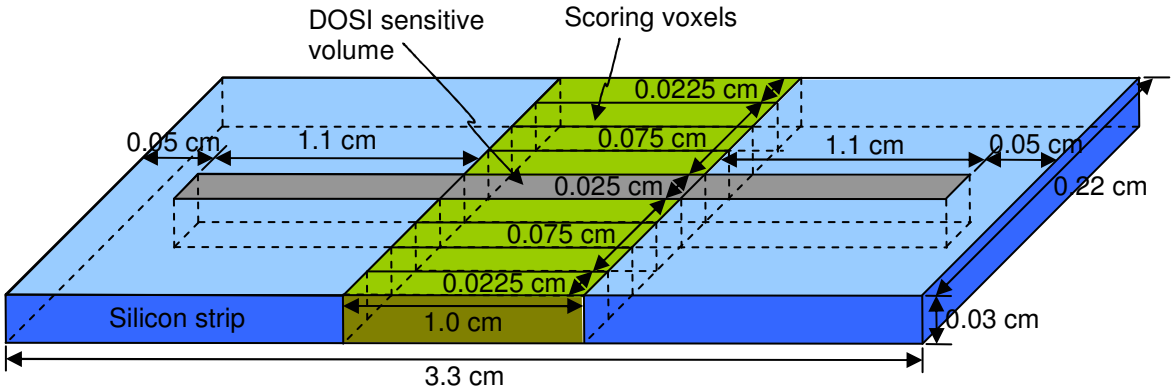

Figure 5.7: The DOSI detector model that was used using DOSXYZnrc in a water phantom at 10 cm deep.

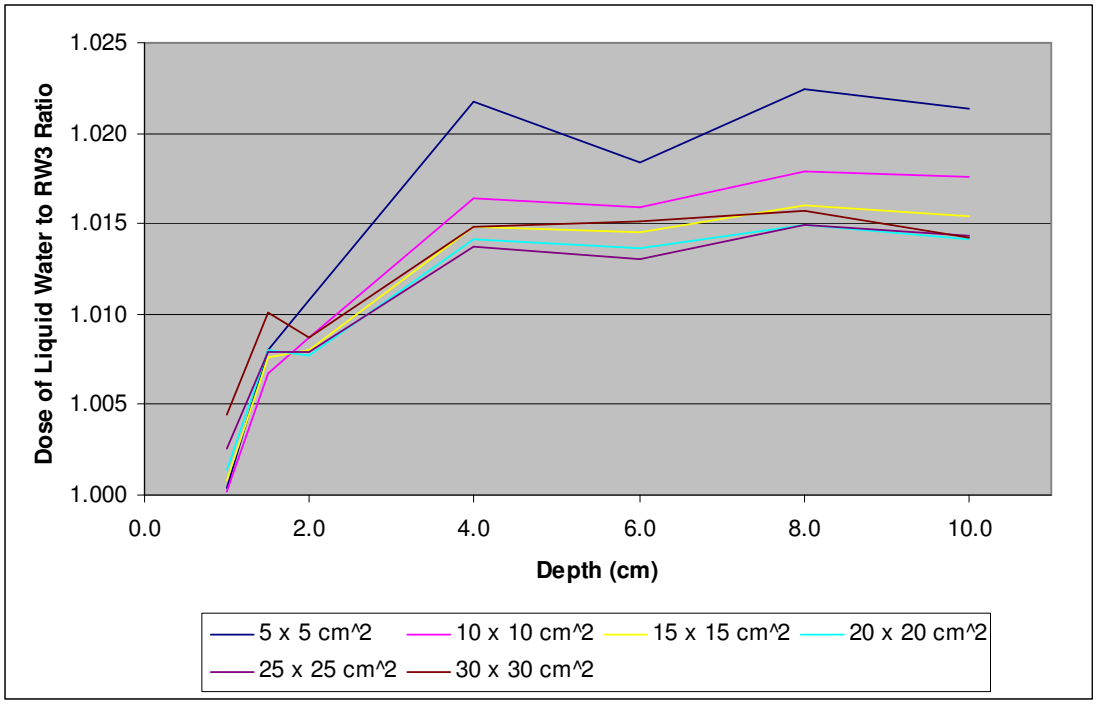

Figure 5.8: The correction factor plots for different field sizes to convert the RW3 material to liquid water phantom for DOSI measurements. *Courtesy of S. Manolopoulos.*

Table 5.1: The correction factor used for DOSI measurements at depth of 1.5 and 10.0 cm. *Courtesy of S. Manolopoulos.*

Depth (cm)	Field Width (cm)					
	5	10	15	20	25	30
1.5	1.008	1.007	1.008	1.008	1.008	1.010
10.0	1.021	1.018	1.015	1.014	1.014	1.014

Due to the fact that the width of the sensitive region was 250 μm, the cut off electron energy used was reduced to the total energy of 521 keV. This is done in order for electron transport in the small scoring region to be performed correctly, in which if ignored leading to an incorrect distribution of dose in the scoring voxels. The electron slowing down range in silicon is approximately the length of the scoring width at 700 keV cut off total energy, hence the lower 521 ICRU cross section data were used. The numbers 521 ICRU and 700

ICRU in the pegs4 data files correspond to secondary electron production at 10 and 189 keV cut off kinetic energy respectively.

For example, for an interaction after producing a pair production, an electron that has an energy of 511 keV will have a difference of 189 keV kinetic energy from the cut of 700 keV total energy, similarly an electron that is created after a pair production will have 10 keV kinetic energy less from the 521 keV cut off total energy. These two cross section data will give significant difference of the lower energy thresholds to be followed through for the slowing down range of the secondary electrons.

For instance, for a 10 keV electron the range is 2.515×10^{-4} cm in water and 1.485×10^{-4} cm in silicon whereas electrons with a kinetic energy of 189 keV have a range of 4.488×10^{-2} cm in water and 2.423×10^{-2} cm in silicon [168]. These data were obtained from the NIST Scientific Databases, ESTAR. The cut off total energy at 700 keV would be quite high to compensate for the electrons that just made it to the 250 µm width scoring voxels at the higher 189 keV cut off kinetic energy. The consequence of choosing the 700ICRU media data would be a reduced accuracy of the results.

The scoring volume was chosen to be 1 cm along the strip which is smaller than the total length of the sensitive array. The widths of nine 250 µm voxels were aligned side by side, all with 300 µm thickness, which corresponds to the actual Si substrate. Although the DOSI sensitive layer is 250 µm wide, the Si substrate is 2.2 mm across. The response was calculated across the full width

of substrate in order to see if there was a changing response across the PCB mounting material. The DOSI strip with the 9 scoring voxels that were modelled in the calculations is illustrated on the previous page in figure 5.7. However, for output factor calculations only the central voxel was used in MC computations, since the uncertainty of the results were within 1% error after many parallel runs.

For the uncertainties to be acceptable, parallel computation on the BlueBEAR cluster with 50 different random number seeds were required. The aim is to achieve the uncertainties to better than 1% after 50 calculations. The number of histories used varies from 10^8 to 10^9 and the run time calculations took between 28.4 to 173.9 hours. The output factors were obtained from the chosen field sizes and were plotted and normalised at 10 x 10 cm^2 field.

At a later stage, the DOSI model was rerun with a thinner substrate with DOSXYZnrc code at 25 µm to analyse its performance while other parameters remained the same. These also include the same BEAMnrc code models that were used and unchanged dimensions of the water phantom. These later calculations were run with a larger number of random number seeds, a total of 100 to 300 depending on field size to ensure results with an uncertainty of ~1%. The same variance reduction technique was also used and the output factors was normalised at 10 x 10 cm^2 field. These calculations would hopefully show the performance of the detector at a theoretically thinner sensitive voxel.

5.3 Results

The dose tallies for DOSI measurements at the 9 scoring voxels are given in figure 5.9. It could be seen that the 5 voxels at the centre could be used as scoring bins that can be combined to calculate the dose results. These voxels are within 1.0% error from the scoring voxel at the central axis which is the DOSI sensitive array as in table 5.2. The scoring voxels at the two extremes however, are shown to be perturbed by the edges of the Si strip and their smaller volumes.

Results for DOSI detector data and the Monte Carlo calculated output factors are shown in figure 5.10. The variation in the output factor for DOSI can be seen here and from table 5.3 below. Although the relative error for DOSI detector is 0.3%, the total error in the experimental setup including the variations in the monitor units (MU) recorded by the accelerator, as well as the correction factors for converting the results in the solid water equivalent material to liquid water phantom, all in all would contribute to around 1% overall uncertainty.

The detector has a 3.0% difference at 5 x 5 cm^2 field the largest discrepancy obtained from the DOSI measurement. On the other hand, DOSI measurements do not show much difference at 30 x 30 cm^2 field which is within 0.9% error. As for the Monte Carlo simulations, all points are in good agreement with the DOSI results by within 1.8% error. However, Monte Carlo calculations show a disagreement to the commissioning data at 30 x 30 cm^2

field by almost 3.0% difference which is as predicted by Yin et al. [64] for Si detector at larger field sizes. While at other points, Monte Carlo calculations show good agreement by within 1.8% to the commissioning data.

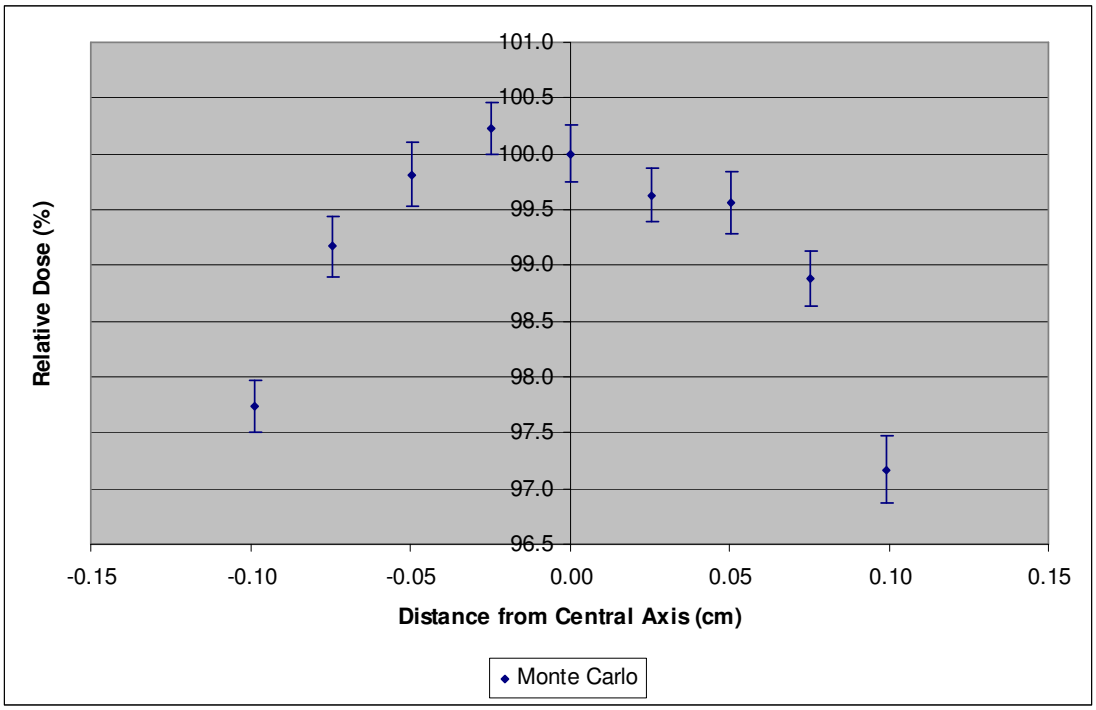

Figure 5.9: The DOSI profile across the 0.22 cm scoring width using Si voxels, 10 cm square field and 50 random number seeds.

Table 5.2: The result for DOSI measurements of 9 voxels across the Si width.

Distance from CAX (cm)	Percentage Error (%)	Normalised Dose	Error Bar ±	Dose Difference from CAX (%)
-0.098	0.236	97.73	0.231	-2.27
-0.075	0.274	99.17	0.272	-0.83
-0.050	0.288	99.81	0.288	-0.19
-0.025	0.236	100.23	0.236	0.23
0.000	0.254	100.00	0.254	0.00
0.025	0.245	99.63	0.244	-0.37
0.050	0.280	99.56	0.279	-0.44
0.075	0.250	98.88	0.247	-1.12
0.098	0.309	97.17	0.300	-2.83

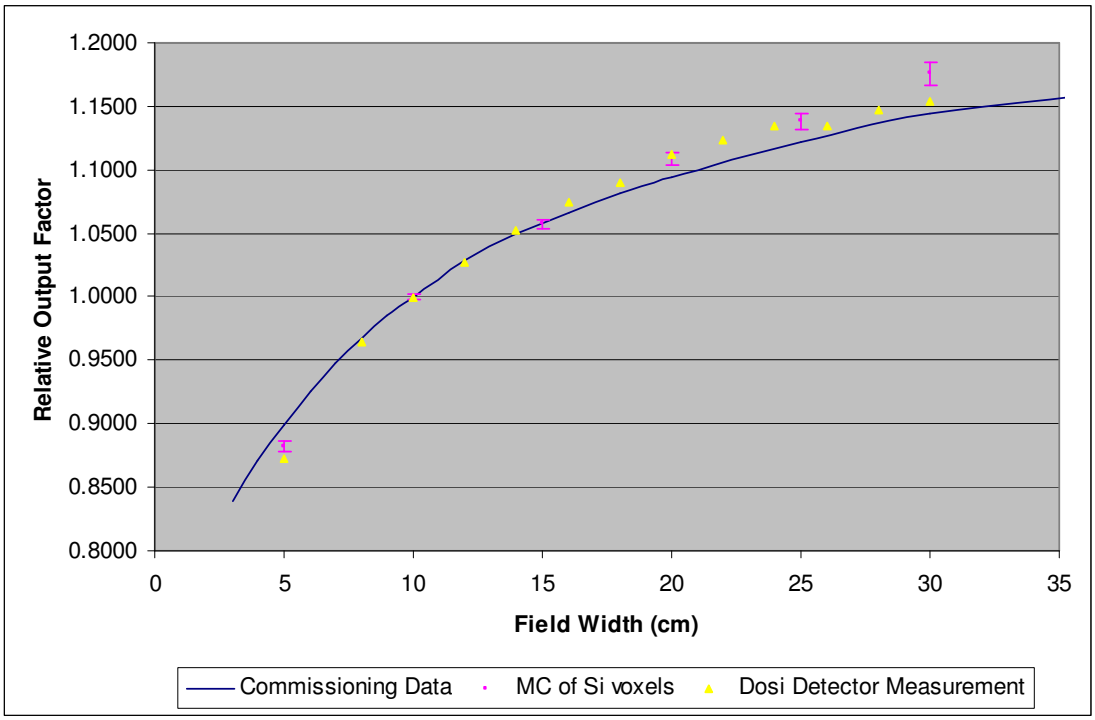

Figure 5.10: Comparing output factor results for MC Si voxels using 521 pegs4 data and DOSI measurements at 10 cm deep for 6 MV Varian.

Table 5.3: The result for DOSI measurements and the percentage differences.

Field Width (cm)	Relative Output Factor	DOSI Error Bar ±	Commissioning Data	DOSI Percentage Difference from C. Data (%)
5	0.87202	0.0026161	0.8986	-2.96
8	0.96406	0.0028922	0.9677	-0.38
10	1.00000	0.0030000	1.0000	0.00
12	1.02695	0.0030809	1.0286	-0.16
14	1.05189	0.0031557	1.0488	0.29
16	1.07499	0.0032250	1.0655	0.89
18	1.08948	0.0032684	1.0813	0.75
20	1.11221	0.0033366	1.0940	1.66
22	1.12303	0.0033691	1.1051*	1.62
24	1.13476	0.0034043	1.1162*	1.66
26	1.13440	0.0034032	1.1267*	0.68
28	1.14705	0.0034412	1.1356*	1.01
30	1.15457	0.0034637	1.1445	0.88

(*) estimated value

This work has shown that the Monte Carlo calculations agree with the DOSI measurements within 2% whilst predicting the observable difference with the

commissioning data as the field size increases as in table 5.4. Whereas, the DOSI measurements have some disagreement with the commissioning data with up to 3% discrepancies (table 5.3), hence it has been established that the DOSI can be used as a dosimeter in radiotherapy but which will need some correction to its readings for 30 x 30 cm square field and for bigger fields. However, these errors are much smaller than predicted in Yin et al. [64].

Table 5.4: The result for MC and DOSI measurements and their percentage differences.

Field Width (cm)	Normalised Dose from Monte Carlo	M. Carlo Percentage Error (%)	Commiss-ioning Data	M. C. Percentage Difference from C. D. (%)	DOSI Data	M. C. Percentage Difference from DOSI (%)
5	0.8826	0.4916	0.8986	-1.78	0.87202	1.21
10	1.0000	0.2678	1.0000	0.00	1.00000	0.00
15	1.0572	0.3659	1.0634*	-0.59	1.06344*	-0.59
20	1.1089	0.4697	1.0940	1.36	1.11221	-0.29
25	1.1382	0.5799	1.1223	1.41	1.13458*	0.32
30	1.1758	0.7374	1.1445	2.74	1.15457	1.84

(*) estimated value

As a continuation work from this experiment, a thinner Si strip was modelled. This would predict the performance of a DOSI detector possessing a thinner substrate. The Si scoring voxels was remodelled with a dimension of 1 cm x 0.025 cm and 0.0025 cm thick which is more than 10 times thinner than the original DOSI detector. The rest of the parameters were the same while the simulations were run with 100 to 300 different random number seeds to attain adequate statistics, in which the percentage errors of the results were calculated using sample standard deviation. The results are given in figure 5.11 and table 5.5.

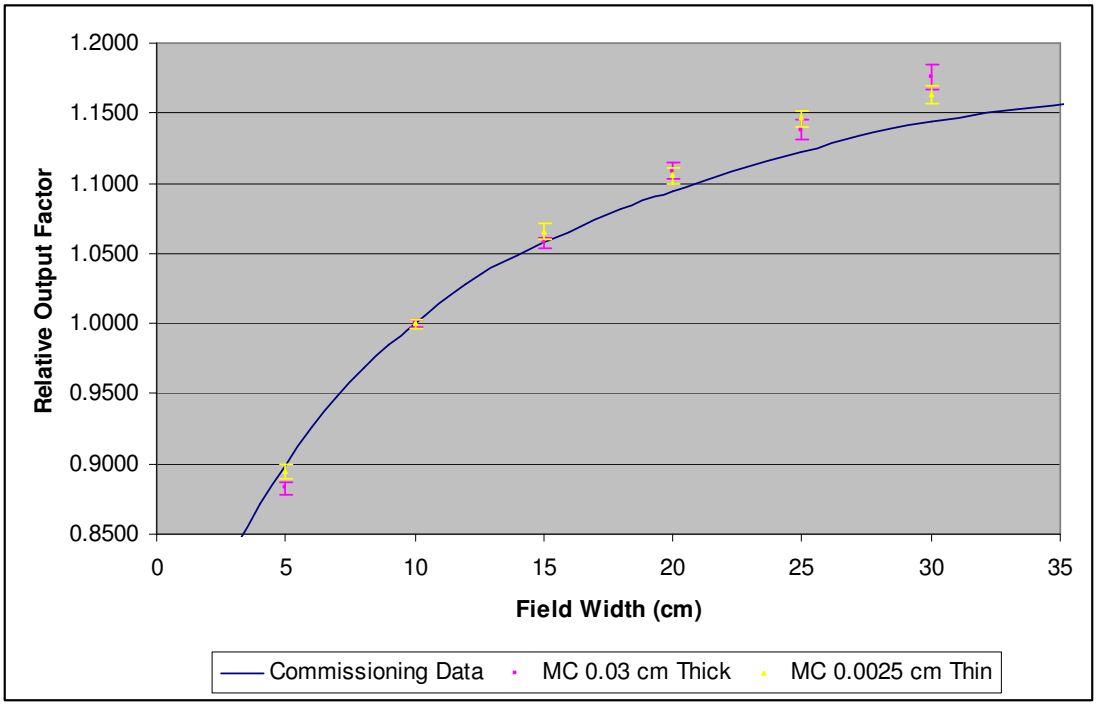

Figure 5.11: Comparing output factor results for MC thick and thin Si voxels at 10 cm deep for 6 MV Varian.

Table 5.5: The result for MC thick and thin Si voxels and their percentage differences.

Field Width (cm)	Commissioning Data	Normalised Dose for 0.03 cm Thick Si	Percentage Difference from C. D. (%)	Normalised Dose for 0.0025 cm Thin Si	Percentage Difference from C. D. (%)
5	0.8986	0.8826	-1.78	0.8946	-0.45
10	1.0000	1.0000	0.00	1.0000	0.00
15	1.0634*	1.0572	-0.59	1.0657*	0.21
20	1.0940	1.1089	1.36	1.1054	1.04
25	1.1223	1.1382	1.41	1.1463	2.13
30	1.1445	1.1758	2.74	1.1635	1.66

(*) estimated value

The result in figure 5.11 has shown that the thinner Si model gives a slightly better agreement in the response as a function of field size compared with an ionisation chamber than the original DOSI model. In table 5.5, the observable difference for the 5 and 30 cm widths indicates better agreement, reducing the discrepancy to 0.4% and 1.7% respectively, as compared to 1.8% and 2.7%

previously. This suggests that a DOSI built with a thinner (25 μm thick) substrate would give improved tissue equivalent response.

Although, the results have shown that there are improvement to the 5 cm and 30 cm field widths when the Si substrate is thinner, there are also some exceptions, for instance at 25 x 25 cm^2 field, the Monte Carlo calculations out lie by 2.1% greater than the previous calculation of 1.4%. This should be addressed since the validation model for 6 MV Varian has an inherent error of ≤ 1.8%. Hence the simulations here for thin Si voxels are at the limits of the accuracy achievable with the model.

5.4 Discussion

Although DOSI detector measured the dose in a one-dimensional linear array, the Monte Carlo calculations has been used to exploit the model of the dosimeter in the x, y and z directions of the whole volume of the Si strip. In the x-direction, the Monte Carlo calculations have been used to investigate DOSI sensitive volume using 1 cm of the total scoring length of 3.2 cm. This has been shown to be in agreement with the DOSI measurement to better than a 2% error.

In the y-direction the central scoring voxel has been aligned on both sides of the dimension to observe the response of the Si detector and has been found to be accurate better than 1%. Monte Carlo shows that neither the size nor the x or y-directions of the strip becomes the factors to perturb the

calculations during radiation transport although DOSI sensitive pixel has a size of approximately 250 µm x 250 µm. If the DOSI detector could be manufactured to evolve into two dimensional arrays with its original pixels, Monte Carlo calculations have been shown to be capable reproducing the dosimetry.

However, the elemental semiconductor of silicon has caused some effect on the measurement made by this detector. The effect is due to the low energy scattered photons and secondary electrons. The mean path length of a secondary electron in a solid-state detector is considerably shorter compared with an air cavity ionisation chamber therefore the absorbed dose measured by this range of detectors may not be accurate [169].

To make this point clearer, the thickness in the z-direction of the Si substrate of the DOSI detector in this research is 300 µm, which relate to the continuous slowing down range of an electron of energy roughly 230 keV in silicon. The low energy scattered photons generate short range secondary electrons characteristics for which it is more difficult to satisfy the requirements of Bragg-Gray cavity theory. Nonetheless the difference between the Monte Carlo calculations to the DOSI data suggest that the silicon material in the detector could become a factor in the discrepancies at 30 x 30 cm^2 field size and above.

In the z-direction, the silicon strip has been exploited further using reduced thickness of the substrate. This is an investigation into how the DOSI detector

might work theoretically at a thinner dimension. For a 25 µm silicon strip, this would accommodate the lower energy of scattered photon than the thicker 300 µm DOSI; hence the shorter range of secondary electrons. The continuous slowing down range for an electron at this level is approximately 51 keV [168]. This has a greater advantage to the lower energy electrons that would satisfy the electron equilibrium within a thinner substrate, equivalent to a smaller cavity. The discrepancy found at this stage is 1.7% difference with the commissioning from ionisation chamber at 30 x 30 cm^2 field. This in turn is considered to be a good agreement with the standard detector.

In conclusion, since the DOSI response compares well to the validated beam measurements performed with an ionisation chamber and has been accurately modelled with a MC code that incorporates the silicon substrate and no other effects, it can be said that the detector is acting as a Bragg-Gray cavity for the dose measurements. The electron equilibrium is obtained from the secondary electrons that have been produced during the photon interactions in the water phantom material. However at 30 x 30 cm^2 and larger field sizes some corrections to the measurements are suggested.

As the Si substrate becoming thinner (as in the 25 µm strip) the accuracy becomes better at larger field size which is lower than the accuracy of the validated model of 1.8%. In this case, it can be said, that the mean secondary electron range is larger than the silicon substrate and smaller cavity means far more lower energy electrons would satisfy the principle, therefore no significant perturbation of the electron fluence could be seen from these

simulations. The DOSI system at this point does not require the separation of primary and secondary components as suggested for silicon diodes by Yin et al. [64].

Furthermore, a silicon detector such as the DOSI detector which is made from a thin silicon layer could be made a useful detector in radiotherapy that would give no observable perturbation to the dose response if the substrate is thin enough in the same way as in the Monte Carlo calculations, which is as thin as 25 µm thick. This would give the detector, like DOSI to be beneficial because it can cut out commissioning and QA time; it could measure the dose with no discrepancies and act as a tissue equivalent detector.

Chapter 6 - Investigation of the Performance of PinPoint Chamber, Diamond and DOSI Detector on Stereotactic Beams

6.1 Introduction

Manolopoulos et al. [44] described the DOSI detector as a position sensitive detector that has been used for measurements of a stereotactic collimator-beam system and which is useful in reducing time and acquiring accuracy in radiation dosimetry. In their work, the DOSI detector was used to measure stereotactic beams that pass through various sized collimators. The full set of measurements took 45 minutes including time to change collimators due to fast read-out electronics in the DOSI. In addition to the DOSI detector, a diamond detector and a PinPoint chamber were also been used for comparisons [44].

Stereotactic beams are used to treat brain tumours and pituitary adenomas and the like [170]. The size of the beam can be as small as 4 mm and up to 4 cm in diameter. Due to this small field and the close adjacency of critical normal structures, the treatment planning and dose delivery system must be highly accurate to irradiate the tumour while the patient is immobilised with bolted frames [44, 171, 172].

This demanding precision needs a high resolution detector to measure the dose, since as the radiation field becomes smaller the dose gradient of the beam becoming steeper. The less extended penumbra leads to many

detectors not correctly resolving the smaller field width [173, 174]. Conventional dosimetry uses films, gels, thermoluminiscence dosimeter (TLD), diodes or diamond detectors that give high spatial resolution measurements.

However, film, gel and TLD are not real time dosimeters and in need of other devices to produce the measurements, using densitometer, magnetic resonance imaging (MRI) and TLD reader, respectively. On the other hand, diodes have been shown to have energy and dose rate dependence [172, 175]. As for diamond, which is nearly tissue equivalent (and consequently largely energy independent) its dose rate dependence needs to be corrected empirically [44, 176 - 178].

All these conventional dosimeters do not have the capability for dynamic measurements in real time, as the DOSI detector has. The DOSI detector's small pixels have a dimension of 250 µm pitch, so theoretically, it can measure with high spatial resolution. It has been shown to accurately measure stereotactic beam penumbras. The agreement in field size was better than 3% for all collimators [44]. The dose performance obtained from DOSI is compared with measurements made by the standard detectors. However, the dosimetric performance of the DOSI has never been investigated with Monte Carlo simulations.

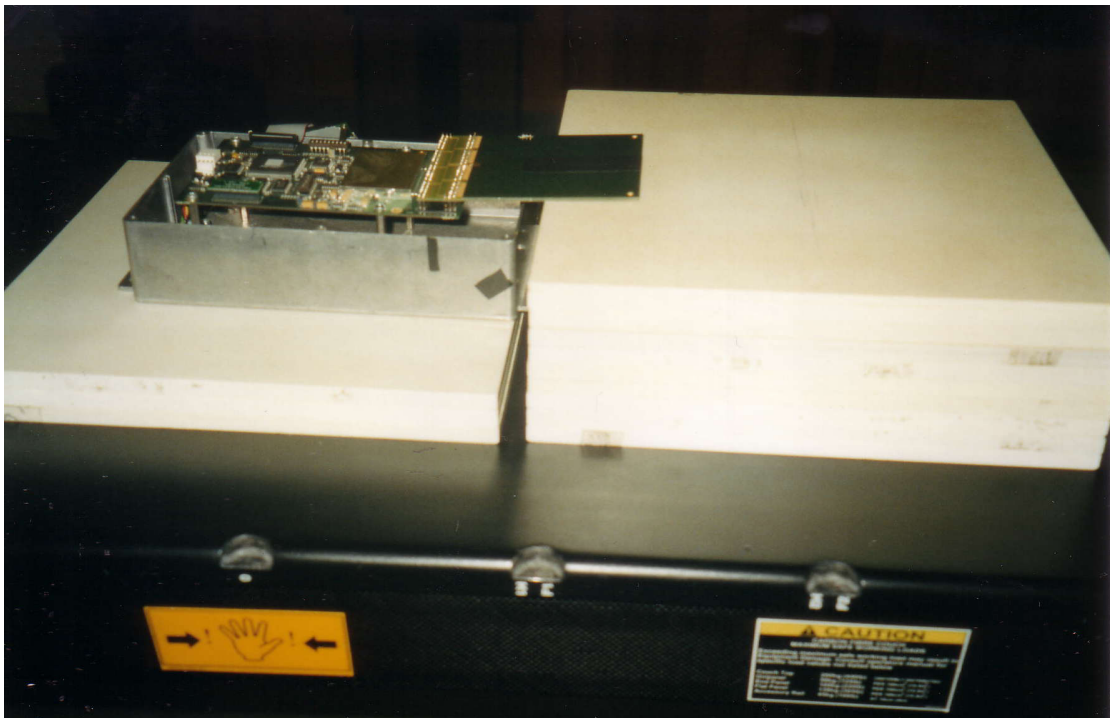

Figure 6.1: DOSI detector preparations for set-up with RW3 solid water slabs surrounding the sensitive volume.

In this chapter, Monte Carlo dosimetry results have been included for comparison with measurements made from different detectors such as diamond, PinPoint and DOSI detectors. Confirmation of the experimental performance of DOSI in measuring stereotactic beams will give greater confidence in the performance of DOSI in this and other measurement situations.

6.2 Methods

All detector measurements were obtained from the experimental work performed using 6 MV stereotactic beams from a Varian Clinac 600C linear accelerator. The PinPoint chamber and the diamond detector used in the

experiment are described fully as in Chapter 3 and the prototype DOSI detector is explained in detail in Chapters 3 and 5 of the thesis.

The diamond and PinPoint detectors measurements were done in a large water tank to provide full scatter conditions and for the non-waterproof DOSI, RW3 solid water slabs of various thicknesses were used. The solid water phantom was placed in such a way that the DOSI detector was surrounded by this material at all sides top and bottom with minimal air-gaps. The linac field size was setup to 5 x 5 cm^2 field with a gantry angle at 0°, collimator angle at 90° and a dose rate of 600 $MU.min^{-1}$ for 10 x 10 cm^2 field defined at 100 cm from the source.

The diamond detector was positioned with its stem perpendicular to the stereotactic beams, whilst the orientation of the stem of the PinPoint chamber was in parallel to the beam central axis. The diamond detector had to be corrected empirically as a function of dose rate, as suggested by Fowler (1966) [111] and was pre-irradiated with 20 Gy before the off-axis ratios (OAR) measurements were made. All beam profiles were measured with 92.5 cm SSD and at depth of 7.5 cm at the isocentre for 10, 20 and 30 mm stereotactic collimators. For each detector, dose rates were between 1 and 10 $Gy.min^{-1}$.

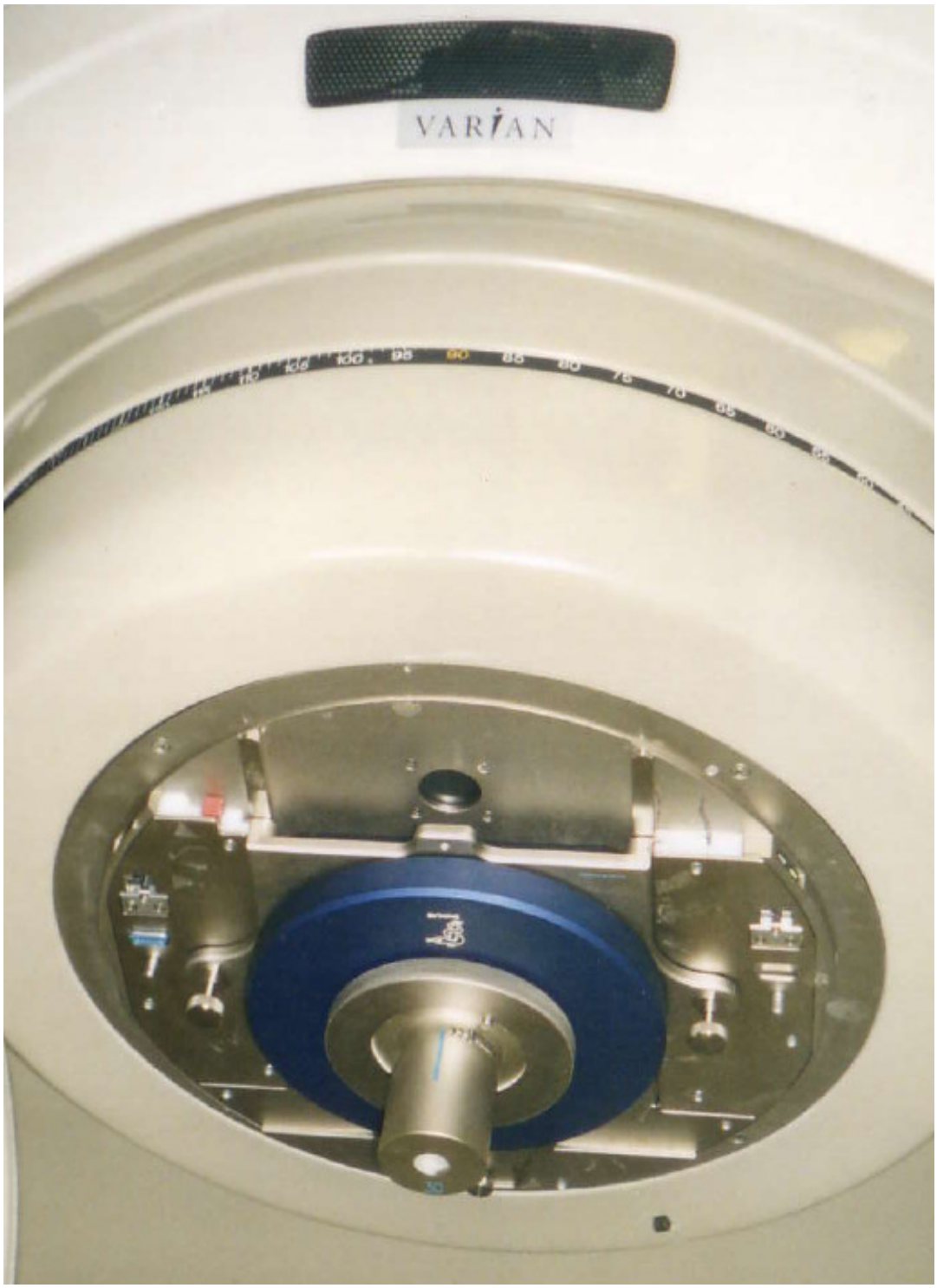

Figure 6.2: The Varian linear accelerator being mounted with a stereotactic collimator.

The BEAMnrc model from a previous validated Varian 6 MV beam was used to predict the outcome of stereotactic beams with addition of 3 circular lead collimators designed to give beam diameters of 10 mm, 20 mm and 30 mm at

100 cm SSD. These were placed one after another to model the stereotactic collimator head. Figure 6.2 shows one of the collimators being mounted on the treatment head.

To model the experimental set-up using the BEAMnrc code in addition to the stereotactic conical collimator system supplied by BrainLab, a 5 x 5 cm square field obtained from the x and y-jaws were used as the source model. This was done by adjusting the validated model to accommodate the required field. The multileaf collimators were open wide as they were not in use during this procedure.

The phase-space scoring plane was tallied at 92.5 cm where the water phantom was positioned to mimic the experimental set-up. The linac treatment head and the stereotactic collimator can be seen from the illustration below in figure 6.3. The diagram however is not drawn to scale.

Whilst the DOSXYZnrc code was used to represent a large water tank with 50 cm uniform thickness of H_2O at each side, the position of the scoring voxels were laid out at depth of 7.5 cm in water 700ICRU medium. The size of the voxels is 1 mm x 1 mm x 5 mm each to deduce the penumbra effect from the collimator beam. In table 6.1 some of the parameters that were assigned to the Monte Carlo code were shown using the DOSXYZnrc graphical user interface.

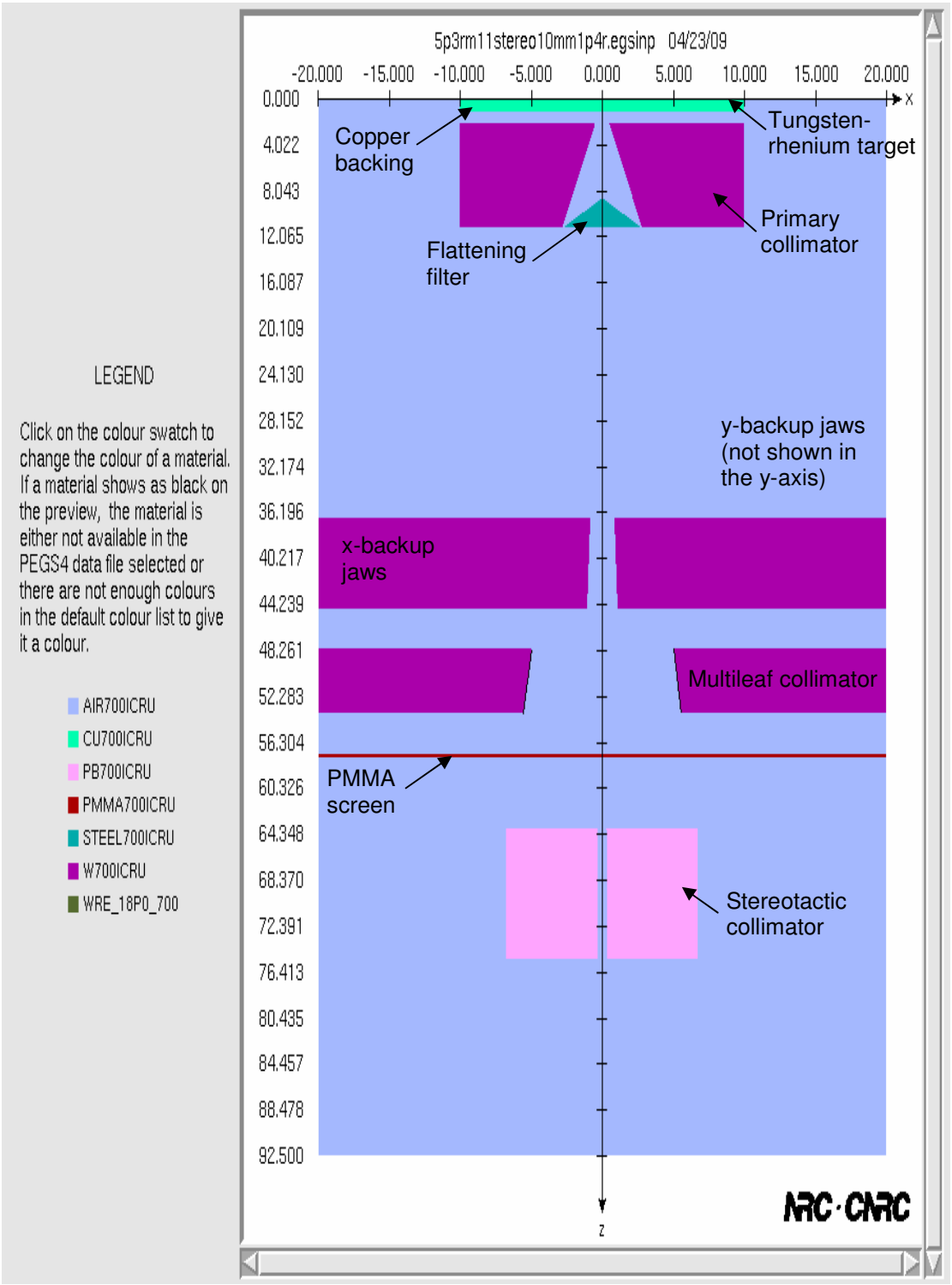

Figure 6.3: BEAMnrc linear accelerator head preview.

Table 6.1: DOSXYZnrc parameters used in the GUI to define the water phantom.

Define Phantom								
Step 1: Voxels Dimensions								
Define x voxels: as groups			Define y voxels: as groups			Define z voxels: as groups		
Number of x voxels or groups of voxels: 1			Number of y voxels or groups of voxels: 1			Number of z voxels or groups of voxels: 1		
Define x voxels			Define y voxels			Define z voxels		
Minimum x-boundary (cm): -0.05			Minimum y-boundary (cm): -0.05			Minimum z-boundary (cm): -0.25		
	x-width (cm)	Number in group		y-width (cm)	Number in group		z-width (cm)	Number in group
Group 1	0.1	49	Group 1	0.1	1	Group 1	0.5	41
						Group 2	1.0	1
						Group 3	0.5	14
Step 2: Define Media (include medium for region surrounding phantom)								
Number of media: 1								
Media								
					Medium			
1					H2O700ICRU			
Step 3: Output								
Select the voxels for which to list the dose…								
IZSCAN of voxels								
from x	to x	from y	to y	from z	to z	scan		
1	49	1	1	16	16	x-scan per page		

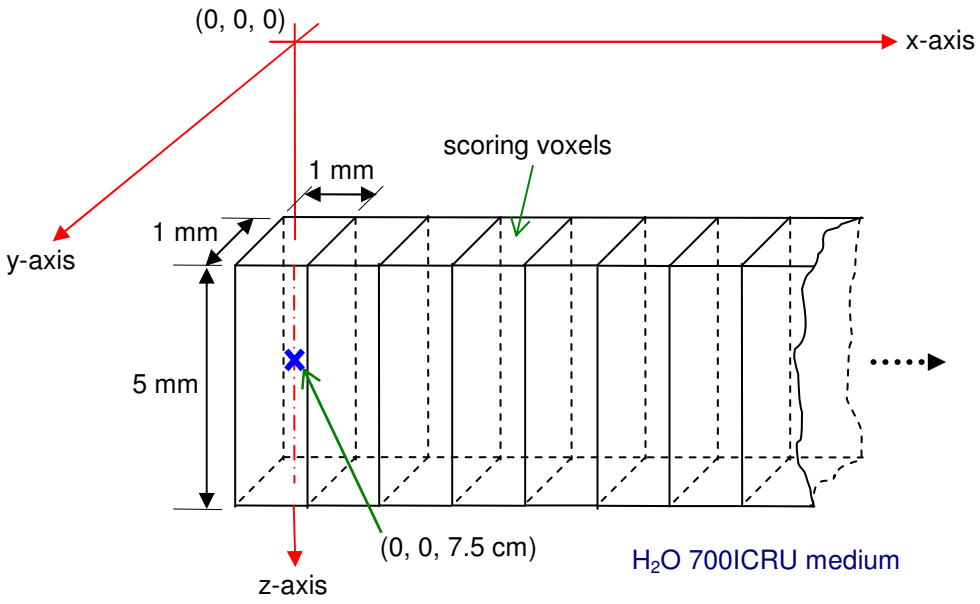

Figure 6.4: Scoring voxels that were encoded using DOSXYZnrc.

The image of the water phantom used during the calculations is shown in figure 6.4. The illustration however is not drawn to scale. To get good statistics the code was run with 10 different random number seeds for each collimator using isource = 9, a full BEAMnrc treatment head simulation source type. The results of the calculations are given in the next section.

6.3 Results

The plots for the stereotactic collimators for 6 MV Varian at 92.5 cm SSD and 7.5 cm deep for the Monte Carlo calculations and measurements from detectors are given below. As a reminder, the DOSI sensitive array is only 3.2 cm, therefore only half of the beam profile is shown here.

From the penumbra curves (figure 6.5) below, it could be seen that all 4 measurements are in good agreement with one another. To get better information on the results the graphs were plotted in logarithmic-linear scale and are shown below in figure 6.6.

It can be seen from figure 6.6 that the DOSI trend follows the PinPoint chamber whereas the Monte Carlo calculations follow the diamond output. The trend is less obvious in the 20 mm collimator data (figure 6.7 and 6.8) and cannot be seen in the 30 mm collimator results (figure 6.9 and 6.10) because of the small size of the DOSI available to us. However in all cases the Monte Carlo dosimetry is in good agreement with the diamond detector.

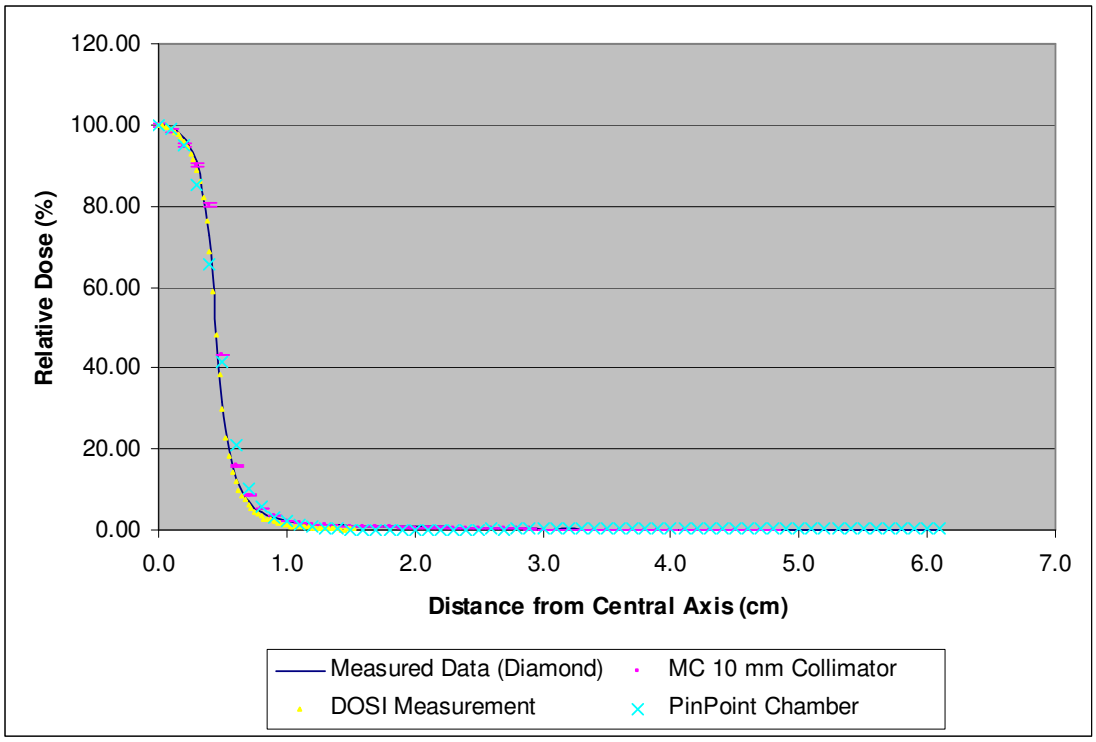

Figure 6.5: 6 MV Varian 10 mm stereotactic collimator at 7.5 cm deep.

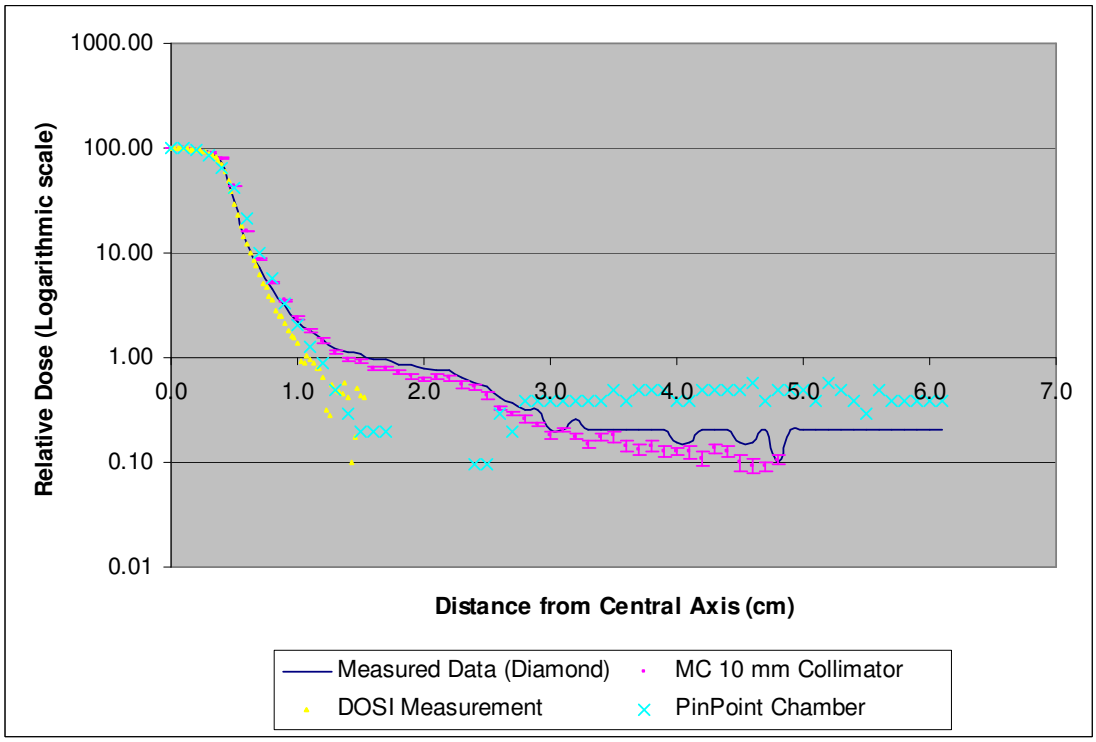

Figure 6.6: 6 MV Varian 10 mm stereotactic collimator at 7.5 cm deep in log scale.

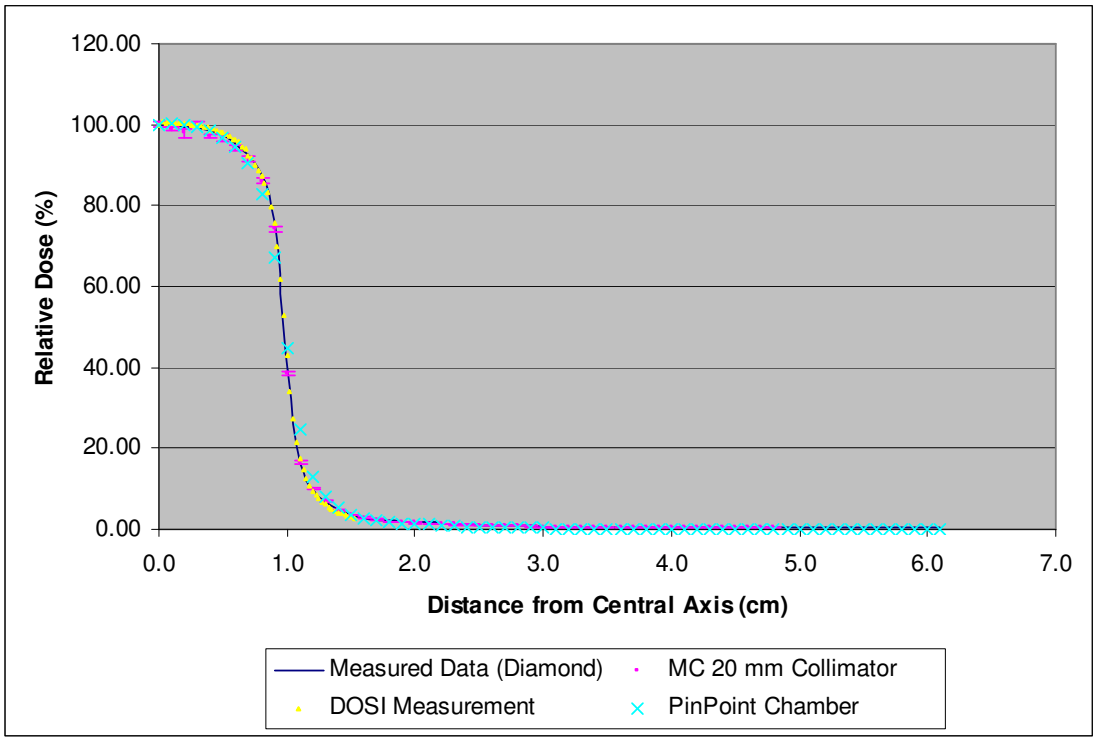

Figure 6.7: 6 MV Varian 20 mm stereotactic collimator at 7.5 cm deep.

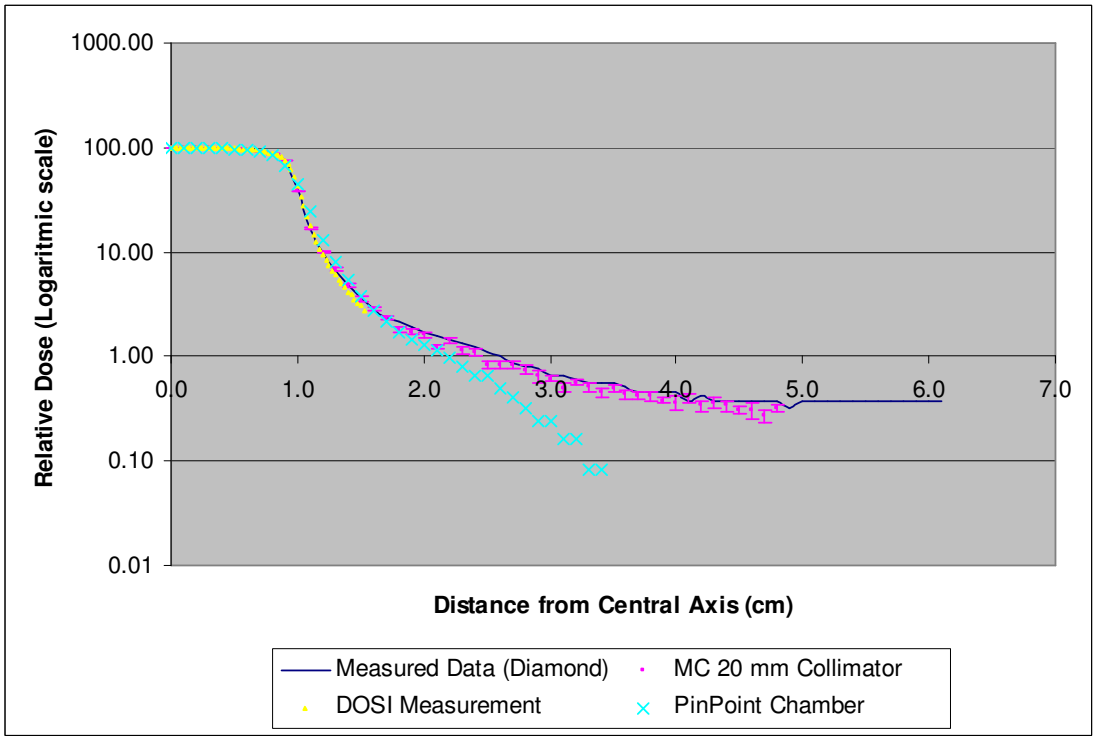

Figure 6.8: 6 MV Varian 20 mm stereotactic collimator at 7.5 cm deep in log scale.

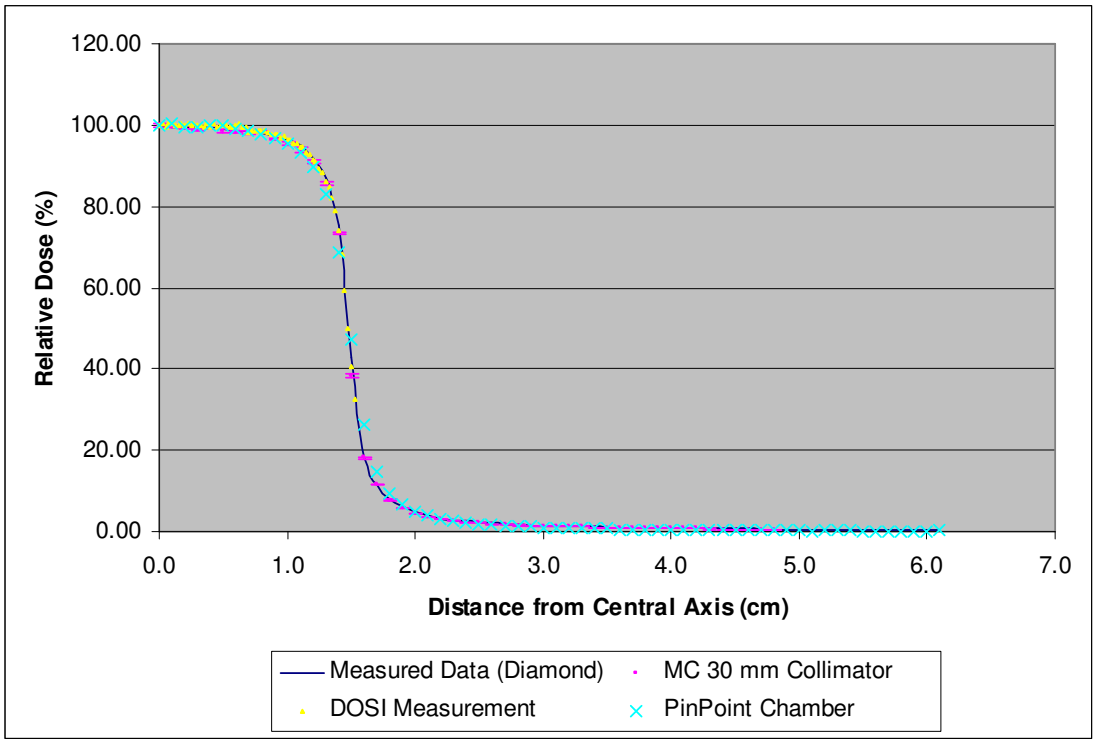

Figure 6.9: 6 MV Varian 30 mm stereotactic collimator at 7.5 cm deep.

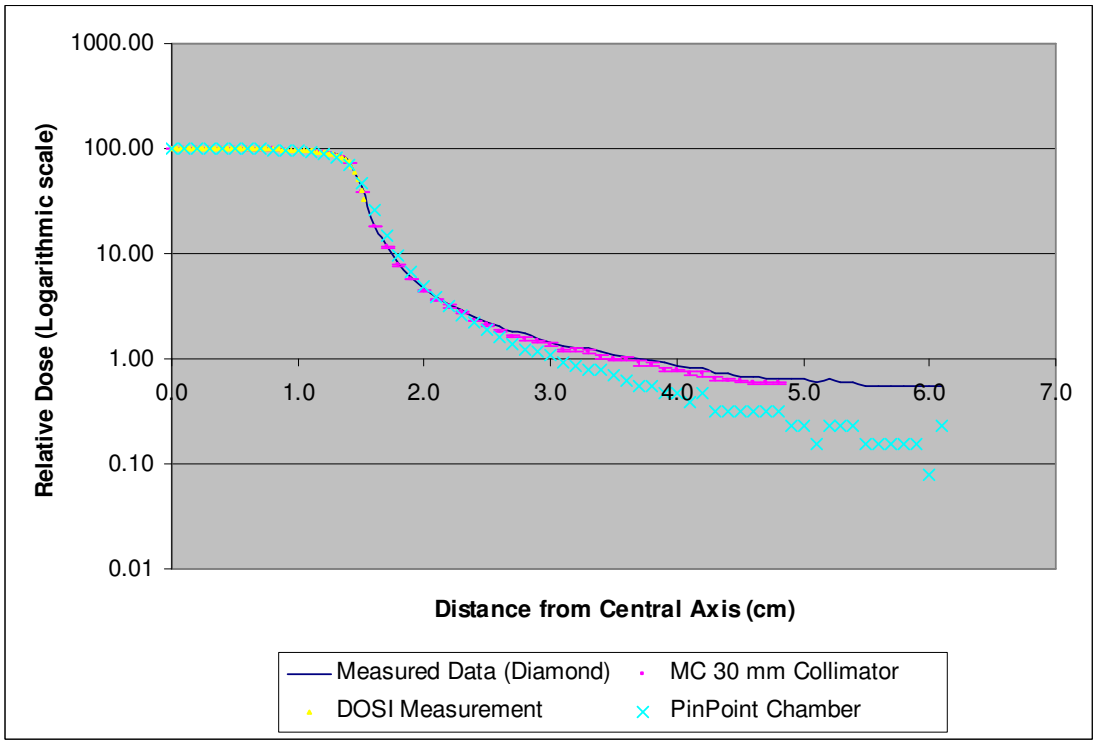

Figure 6.10: 6 MV Varian 30 mm stereotactic collimator at 7.5 cm deep in log scale.

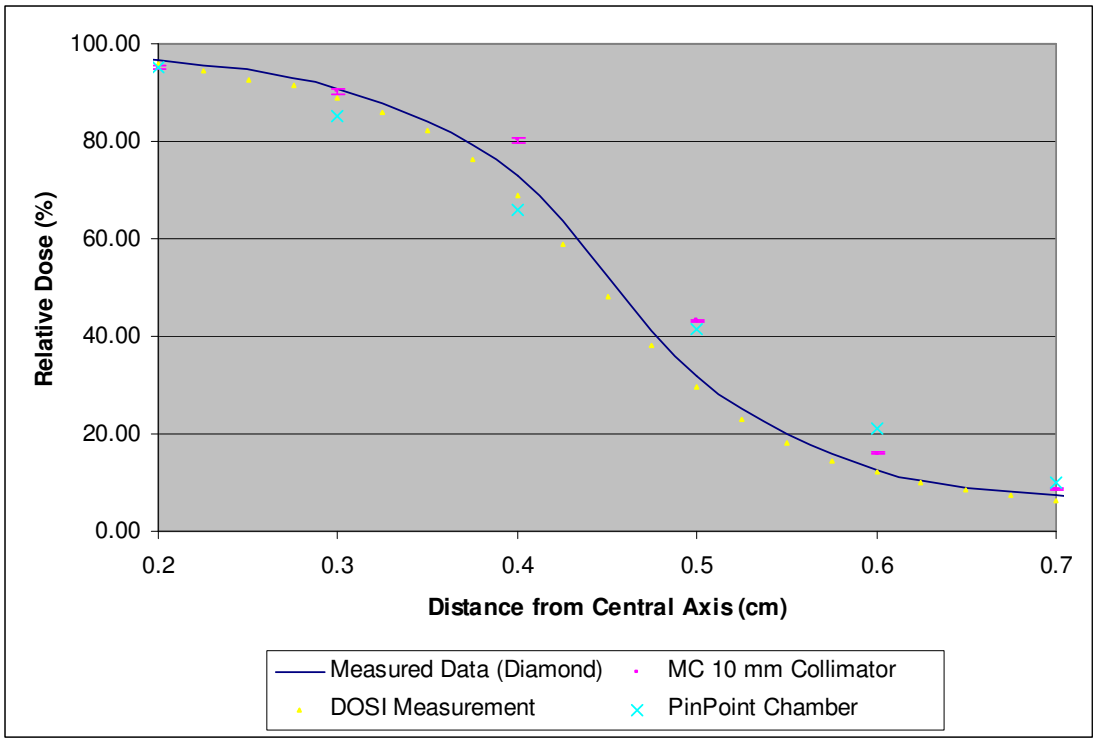

Figure 6.11: 6 MV Varian 10 mm stereotactic collimator at 7.5 cm deep penumbra.

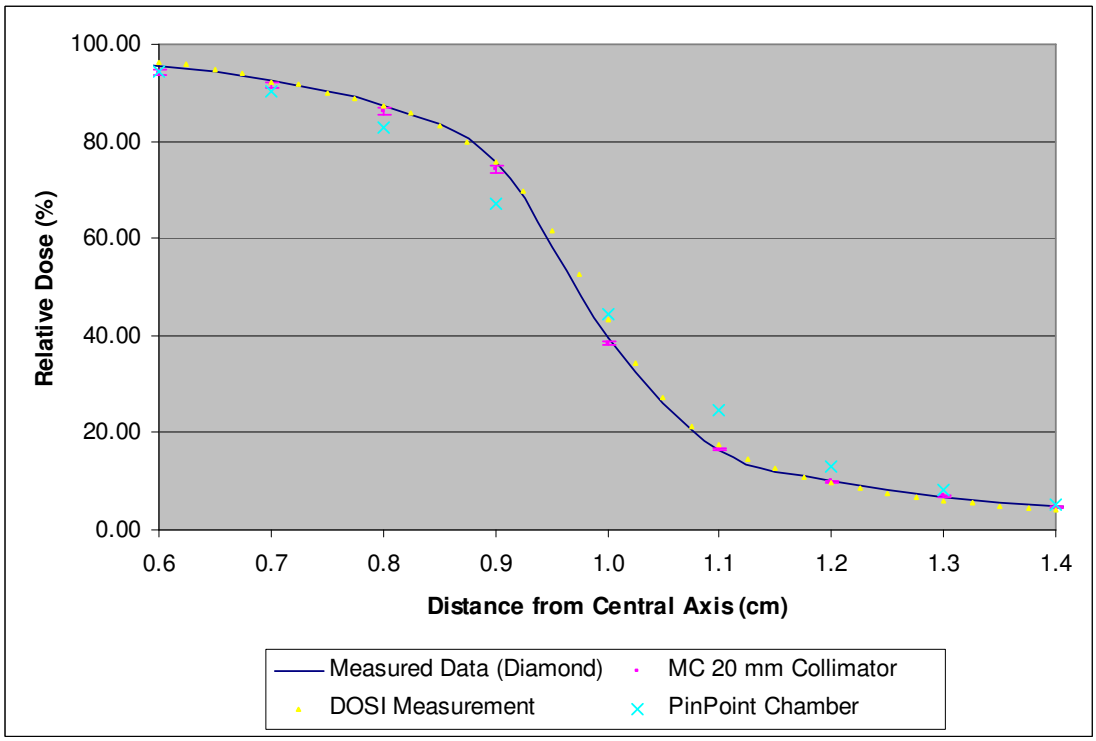

Figure 6.12: 6 MV Varian 20 mm stereotactic collimator at 7.5 cm deep penumbra.

Table 6.2: Penumbra broadening of the detectors used in stereotactic beams.

Detectors	10 mm Collimator Penumbra Width (cm)		20 mm Collimator Penumbra Width (cm)		Average Penumbra Width (cm)	
	80 - 20%	90 - 10%	80 - 20%	90 - 10%	80 - 20%	90 - 10%
PinPoint	0.2832	0.4494	0.3213	0.5575	0.30	0.50
DOSI	0.1817	0.3366	0.2112	0.4420	0.20	0.39
Diamond	0.2000	0.3426	0.2206	0.4513	0.21	0.40
M. Carlo	0.1846	0.3791	0.2326	0.4692	0.21	0.42

It has been suggested by McKerracher and Thwaites, 1999, Higgin et al.,1995 and Bjarngard et al., 1990 [179 - 181] that for a measurement made for stereotactic beams the maximum inner diameter of a detector should be smaller than the beam radius. This is as a result of the sharp edge of the beam at the penumbra region which is difficult for a large detector to give a correct reading.

The error in the measurement is as a consequence of the fact that lateral equilibrium of the secondary particle fluence is not obtained in the sensitive volume of the detector at the beam boundary. For instance, for a 7.5 - 35 mm range of beam diameter at the isocentre used in the Queen Elizabeth University Hospital Birmingham, the required sensitive width for a detector should be less than 3.75 mm according to McKerracher and Thwaites, Higgin et al. and Bjarngard et al. [179 - 181].

Since all 4 measurement tools used here have achieved the required width, the result should help determine which detector is in reality more reliable for stereotactic measurements. The need to have a reliable detector is important in achieving the right dose to the planning target volume (PTV) and so the healthy tissue surrounding it is not being over irradiated.

The PinPoint chamber underestimates the dose at the penumbral tail and broadens the penumbra as in figure 6.5 to 6.12 and due to volume averaging and non-water equivalence of an air ionisation chamber within its 2 mm active diameter. This sensitive width is the biggest of all the detectors used in this research, hence the largest average penumbra width of 0.3 cm at 80 - 20% and 0.5 cm at 90 - 10% as in table 6.2.

Whereas, outside the field boundary the dose is mainly due to photon scatter and transmission through the leaves, the PinPoint chamber seems to under respond significantly in this region (as compared with the diamond and the MC simulation).

Results obtained show that the PinPoint chamber is not capable of measuring the dose outside the field edge as in figure 6.6, 6.8 and 6.10. In the penumbral region its performance is inferior to DOSI or a diamond detector due to penumbra broadening (figure 6.11 and 6.12).

It is possible that the small volume of the ionisation chamber means that it does not have sufficient sensitivity for accurate measurements in the tail of the beam penumbra, and that these measurements are therefore compromised by detector and other leakage currents.

To calculate the average current in the ionisation chamber (i.e. $\frac{\text{charge}}{\text{time}}$) being measured at the lowest value of the PinPoint chamber in figure 6.8, from the

definition of dose, D which equals to the energy absorbed, E per unit mass of the irradiated material, m.

$$D = \frac{E}{m} \qquad \text{Eqn. 6.1}$$

But,
$$\frac{E}{m} = \frac{Q}{m}\overline{W}_g \qquad \text{Eqn. 6.2}$$

where, Q = the total charge of ions of one sign produced in air liberated by photons,

m = the mass of air and

$\overline{W}_g$ = the average energy absorbed per unit charge of ionisation produced in air.

Since 1 MU = 1 cGy, the dose rate of 600 MU.min^{-1} at centre of field is equivalent to:-

$$600 \text{ MU.min}^{-1} = 600 \text{ MU.min}^{-1} \times \frac{1 \text{cGy}}{1 \text{MU}}$$

$$= 600 \text{ cGy.min}^{-1}$$

$$= 6 \text{ Gy.min}^{-1}$$

Hence, in 1 min the dose received by the ionisation chamber is 6 Gy. From Eqn. 6.1 and 6.2,

$$D = \frac{Q}{m}\overline{W}_g$$

$$6\ \text{Gy} = \frac{Q}{m}\,\overline{W}_g$$

$$Q = 6\ \text{Gy} \times \frac{m}{\overline{W}_g} \qquad \text{Eqn. 6.3}$$

The volume of the PinPoint chamber, V = 0.015 cm^3 and the density of dry air at 0℃ and 100 kPa, ρ_{air} = 1.2754 $kg.m^{-3}$. Therefore, the mass of air in the PinPoint chamber,

$$m = \rho_{air} \times V$$

$$= 1.2754\ \text{kg.m}^{-3} \times 0.015\ \text{cm}^3 \times \frac{1\,\text{m}^3}{10^6\ \text{cm}^3}$$

$$= 1.9131 \times 10^{-8}\ \text{kg}$$

Since, the value of the average energy absorbed per unit charge of ionisation produced in air, $\overline{W}_g$ = 33.85 $J.C^{-1}$. From Eqn. 6.3, the total charge in the ionisation chamber per min at centre of field,

$$\frac{Q}{t} = 6\ \text{Gy.min}^{-1} \times \frac{1.9131 \times 10^{-8}\ \text{kg}}{33.85\ \text{J.C}^{-1}}$$

$$= 3.3910 \times 10^{-9}\ \text{C.min}^{-1}$$

Then, the total charge in the ionisation chamber per second at centre of field or the current,

$$I = 3.3910 \times 10^{-9}\ \text{C.min}^{-1} \times \frac{1\,\text{min}}{60\ \text{s}}$$

$$= 5.6517 \times 10^{-11} \text{ A}$$

Thus, the current at 1% of CAX dose,

$$I = 5.6517 \times 10^{-11} \text{ A} \times 0.01$$
$$= 5.6517 \times 10^{-13} \text{ A}$$

This value is large compared to the manufacturer chamber leakage value of 4 x 10^{-15} A. Beyond this, the current in the chamber would have some output perturbation. At the lowest PinPoint value in figure 6.7, the detector receives 0.08% of the dose from the central axis which is a 100% dose. Hence, the current in the chamber,

$$I = 5.6517 \times 10^{-11} \text{ A} \times 0.0008$$
$$= 4.5214 \times 10^{-14} \text{ A}$$

It can be said that the PinPoint chamber is at the limit of detection to give a good reading since the manufacturer leakage current in the chamber of the PinPoint chamber is 4 x 10^{-15} A, due to the dose measurement at penumbral tail could be less than 0.08% of the dose at the central axis. Moreover, the manufacturer leakage in the cable is 10^{-12} $C.Gy^{-1}.cm^{-1}$ can be considered as the current multiply by the exposure time per absorbed dose per length of cable in which for 6 Gy radiation, 100th min exposure time and assuming 1 cm of cable being irradiate, the cable leakage:-

$$L_c = 4.5214 \times 10^{-14}\ A \times \frac{0.6\ s}{6\ Gy \times 1\ cm}$$

$$= 4.5214 \times 10^{-15}\ C.\ Gy^{-1}.cm^{-1}$$

It has been shown that the leakage of the cable from the PinPoint is less than the manufacturer leakage cable. Hence, this might give some perturbation to the PinPoint ionisation chamber values. It is shown that below 1% of the central axis dose the current in the ion chamber is too low to give reliable readings.

Diamond detector performance shown in the result was found to be reliable as it matches nicely with the Monte Carlo simulations. This is due to its non-directional dependence and near tissue-equivalence of carbon [182]. Diamond detector shows good reproducibility as a result of its small thickness of 0.4 mm layer and a desirable tool to have for its accuracy, even though dose rate dependence can sometimes affect this solid-state detector when used with particular electrometers [183]. Nevertheless, pre-irradiation of the detector before taking measurements is a must but it is shown to benefit from this procedure.

The DOSI detector on the other hand has a pitch of 0.25 mm for its sensitive voxel, and 0.3 mm thick, which is the smallest sensitive volume of all the detectors. This, however, is not the only criteria that would make this prototype detector the most accurate to measure stereotactic beams. A silicon detector which has a high-Z component might affect the measurement in various ways.

Not only energy dependence, dose rate and directional dependence of response are significant factors to be a dosimeter of choice. Here, in this research DOSI detector does not show much of the broadening of the penumbra due to its small active voxels (table 6.2) but shows a significant fall in dose measurement outside the beam edge as in figure 6.6.

The main DOSI detector drawback would be over-response to low energy Compton scattering from its silicon element, and this would tend to show higher measurement at the penumbral tail as result of normalisation at the central axis. This is not what was observed.

Monte Carlo simulation techniques that were included for comparison has shown the performances of different detectors being considered and their responses on the impact using collimators of 10, 20 and 30 mm diameter at 100 SSD for stereotactic beam sizes. Here, MC has been found useful where correction factor for a diamond detector as well as energy and dose rate dependence from PinPoint chamber and DOSI detector can cause errors.

6.4 Discussion

This study has pointed out that the reliability of the detectors used in this research against Monte Carlo calculations in radiosurgery beams. The OAR measurements are affected by the finite size of the detector, the change in the electron transport including the surrounding envelope in the detector, variation

in the detector directional response, detector energy dependence and dose rate dependence [184].

The findings written here are similar to other results from Dawson et al., 1984 and Beddar et al., 1994 [185, 178]. The penumbra broadening due to the finite size of the sensitive volume of the detector is the most important feature. The presence of lateral electron disequilibrium still persists in the penumbral measurements, yet the small sensitive area of a detector is the key to achieving the right dose read-out to overcome this difficulty.

The bigger detector with the sensitive area gives a slight broadening of the beam edge as shown by using the PinPoint chamber due to the averaging of the dose across detector. The introduction of the air cavity into the field (as in the ion chamber active volume) causes an increase in the lateral electronic disequilibrium and hence a lower dose to the air in the cavity that would exist in tissue at that position.

Also, the lateral electronic disequilibrium affects measurements when the detector is not tissue equivalent, hence any change in photon or electron spectrum causes a change in response relative to a tissue equivalent detector.

The change in the electron transport for the silicon element found in the DOSI detector and the surrounding envelope, which both being high density and high-Z material also corresponds to the final output of the detector. The

electron range in this case is less than the range in water and so the lateral electron transport in the penumbra region is reduced.

This has also been reported in other detectors using silicon as in diode detectors by Beddar et al. 1994 [178]. However, the sharpening of the measured penumbral beam in a symmetrical effect in DOSI was not seen due to the lower dose measurement outside the field boundary. This under-estimation in the penumbral tail suggesting a significantly reduced electron range in the detector's sensitive array generated by lower energy Compton scattering photons.

It is important to have accurate dosimetry in the penumbral region due to the rigid conformance of the high dose region to the target volume and the sparing of the surrounding tissues. Therefore, the corrections made to minimise the error in the detector is important as in the pre-irradiation of a diamond detector and the dose rate correction factor for diamond.

Profile measurements with the diamond detector were performed with the stem of the detector placed perpendicular with the stereotactic beams which is necessary to give a sharper penumbra due to the small thickness of less than 0.4 mm of the diamond sensitive disk.

To conclude, the study of the work using Monte Carlo simulations indicate that the lack of lateral electronic equilibrium in the detector response could cause

errors in dose calculations. This would occur in the outcome of the tissue non-equivalence detector and would be worse as the detector size increases.

It has been shown that Monte Carlo simulation with 1 mm x 1 mm x 5 mm thick sensitive volume could be used as a reliable reference for dosimetry with stereotactic measurements, particularly where lateral electronic equilibrium does not exist. It is also important to note that the MC calculations have limitations to how small the size of the voxels should be used due to longer computer time, as a result of using an increased number of histories or increased number of random number seeds to achieve acceptably small statistical errors.

From the above result it can be said that the DOSI detector is a good dosimeter, comparable to a standard detector such as the PinPoint chamber. Unfortunately, the DOSI detector like the PinPoint ionisation chamber is not as reliable a tool for measuring the dose in the tail region and at the penumbra.

However, much confidence comes from the diamond detector due to its tissue equivalent advantage. This has been shown by the Monte Carlo simulations theoretically by using water equivalent voxels and practically by DOSI experimental measurements with its silicon sensitive array and PinPoint air cavity chamber results.

It has been shown that MC techniques could be used as reliable references for dosimetry to compare the performances of other detectors using practical measurements. Monte Carlo calculations with the validated photon and electron transport have shown that diamond detectors, if corrected for dose rate dependence and pre-irradiation, produce better results with superior determination of the actual treatment volume than the prototype DOSI detector or the PinPoint ionisation chamber.

Chapter 7 - Investigation on Elekta Linac with Unflattened Beam using Monte Carlo Simulation

7.1 Introduction

Intensity modulated radiation therapy (IMRT) in radiotherapy uses a patchwork of small beamlets to irradiate the target volume. As a consequence of this, IMRT does not rely on initially flat beams. This opens the possibility to use the beam from a conventional linac with the flattening filter removed. In addition, the use of an unfiltered beam would lower the dose to the non-targeted area. Previous research has shown that the filterless beam is more stable and has many other advantages such as reduction in head scatter, reduced leakage radiation and lowering of the whole body dose [186].

Highly conformal treatments are achieved using IMRT in which high doses are delivered to targeted volumes while the surrounding tissues are spared. In IMRT, treatment time and monitor units (MU) are increased to generate the appropriate leaf and intensity sequence of the treatment delivery [68].

Modern linear accelerators use high energy electron beams that bombard the target in the linac head to produce high energy bremsstrahlung photons. The photons created through this process are forward-peaked and the photon fluence is only approximately uniform with angle. Therefore, flattening filters are introduced in the path of the beam by attenuating the radiation so that the dose becomes relatively flat and uniform at a given depth in the patient,

usually at 10 cm deep. The flattening filter provides a flat beam for a field area as large as 40 x 40 cm^2 at the isocentre [68].

The photon beam is further modified using x and y-jaws and multileaf collimators (MLC) to create the desired fields which usually are irregular in shape. Since the MLC produces inhomogeneous maps of photon beams to the targets, the MLC is the key element in the implementation of an IMRT program [68]. By manipulating the MLC, the initially uniform photon beam fluence is adjusted to create areas of high and low intensity according to the treatment plan. Since the beam intensity is based on the optimisation of elemental areas, it is not necessary to start with a uniform beam. The benefits of a flattening filter-free beam have been reported by several authors [69, 186 - 190].

One of the benefits of the unflattened beam is the increase in output. It has been shown that the filterless beam increases the output of a linear accelerator on the central axis by a factor of 2 or more [68, 69, 187, 188, 191 - 193]. In an EGSnrc Monte Carlo study on flattening filter free beams, dose rates increase by a factor of 2.31 for 6 MV and 5.45 for 18 MV and out-of-field dose reductions were also reported using Varian linear accelerators [68, 187, 191].

A significant improvement in out-of-field dose was also reported by Titt et al. in 2006 [190, 194] for small field sizes. Other works have shown that the effect of filterless beam on some dosimetric properties including photon

energy spectra and central axis absorbed dose but were limited to 10 x 10 cm^2 field size and was not completely studied for the other field sizes [187, 190 - 192].

In a study by Mesbahi in 2007 [187], a Varian linac was simulated using MCNP4C Monte Carlo code and the effect of removing flattening filter on photon energy spectra, dose rate and percentage depth dose (PDD) values and beam profile were evaluated for different field sizes. His results also showed that an increase in the dose rate and a lower out-of-field dose were observed for a 6 MV filterless beam.

Although the benefit of the increased output has been shown to be of greater advantage to radiosurgical procedures due to the high doses delivered and small output factors [69], nevertheless, it is beneficial in IMRT to decrease the beam-on time hence reducing the therapy time.

Furthermore, flattening filter free with nominal energies above 15 MeV have been shown to produce fewer neutrons and hence require potentially less shielding [68, 193, 195]. As technology advances, the use of a flattening filter free in IMRT may become available clinically as the problems arise from utilising it are being addressed. Complex design in treatment planning and dose delivery will be made possible in the future as research in IMRT is progressing.

However, none of this research has been performed on Elekta machines using Monte Carlo techniques. The study reported by Cashmore [186] with an unflattened photon beam is entirely experimental and uses a Farmer chamber, parallel plate chamber and films for dosimetric evaluation. Measurements and commissioning data have been obtained using an Elekta Precise linear accelerator for a 6 MV photon energy with and without a flattening filter. These results have not yet been confirmed with computer simulations. The purpose of this investigation is to draw some conclusions on the filterless beam results using the EGSnrc code.

7.2 Methods

The validated BEAMnrc model for Elekta was modified without the flattening filter in the accelerator head to compare with the Cashmore [186] experimental study. The Monte Carlo code was run without a phase space file for 6.0 MeV and 6.4 MeV electron energies with the ISOURCE = 9 option. This source type option was to run the BEAMnrc and the DOSXYZnrc concurrently so that huge phase space files were not stored in the computer hard disk. However the BEAMnrc code has to be compiled as a shared library for this option to be functioning.

Figure 7.1: Elekta linear accelerator used in the Queen Elizabeth Hospital.

When the flattening filter was not used in the linac head the validated Elekta model was adjusted with the medium of the flattening filter being replaced by air. The reasons of using two electron energies are firstly, because 6.4 MeV was the original validated value, and secondly 6.0 MeV electron energy was an attempt to avoid the high intensity dose at the central axis. The actual linac is shown in figure 7.1 and the model is portrayed below in figure 7.2.

The initial electron energy is not clearly supplied by the manufacturer and usually adjusted by the engineer during commissioning and varies among the linacs even within the same model. The validated electron beam model was selected by comparing the measured and calculated PDDs, OARs and OFs data as mentioned in great detail in chapter 4. The tuning of the electron energy by comparing the calculated and measured PDD curves for 10 x 10 cm^2 field size is an approach to determine the primary energy within 0.2 MeV that has been reported by Sheikh-Bagheri and Rogers, 2002 and Mesbahi, 2007 [147, 187].

A scoring plane at 100 cm SSD was tallied in the BEAMnrc code with no phase space file. By running the DOSXYZnrc using ISOURCE = 9 option, the absorbed dose was sampled from what would be the source particle at the scoring plane during a normal run of the BEAM accelerator at D_{max} and 10 cm deep in the water phantom. The phantom model as shown in figure 7.2 has scoring voxels of 6 x 6 x 6 mm^3 in size and 50 cm in all external dimensions. The DOSXYZnrc code was used to score absolute absorbed dose per incident particle in the scoring voxels.

For PDD calculations in the water phantom, the 6 x 6 x 6 mm^3 cubic voxels were used to score along the central axis of the beam. By running the DOSXYZnrc code, the dose was calculated in each scoring voxel in the H2O700ICRU medium. The same approach was used for the beam profiles, except that the central axis of the scoring voxels was vertical to the central axis of the beam as in figure 7.3. The depth of the scoring voxels was measured at D_{max} (1.5 cm) for output factors and 10 cm deep for OAR beam profiles. The lateral resolution for beam profiles does not have to be very small due to the smallest field width is 5 cm therefore 6 mm in length is adequate.

For the intention of comparing between calculated and measured data, the PDDs were normalised at D_{max}, the OAR values of each voxel were normalised to the maximum value of energy deposited in the central axis while the output factors were normalised at the 10 x 10 cm^2 field. These parameters are similar to the experimental work in order to calculate the doses and to compare directly with the measurements reported by Cashmore [186].

For dose calculations in the water phantom, the numbers of histories generated were 10^7 and 10^9 depending on the field sizes, computational time and statistical error obtained using DOSXYZnrc code. Photon and electron cut-off energies of 10 and 189 keV were used which is common in the EGSnrc code. The run time was between 16.3 to 211.7 hours using the Bluebear computer cluster.

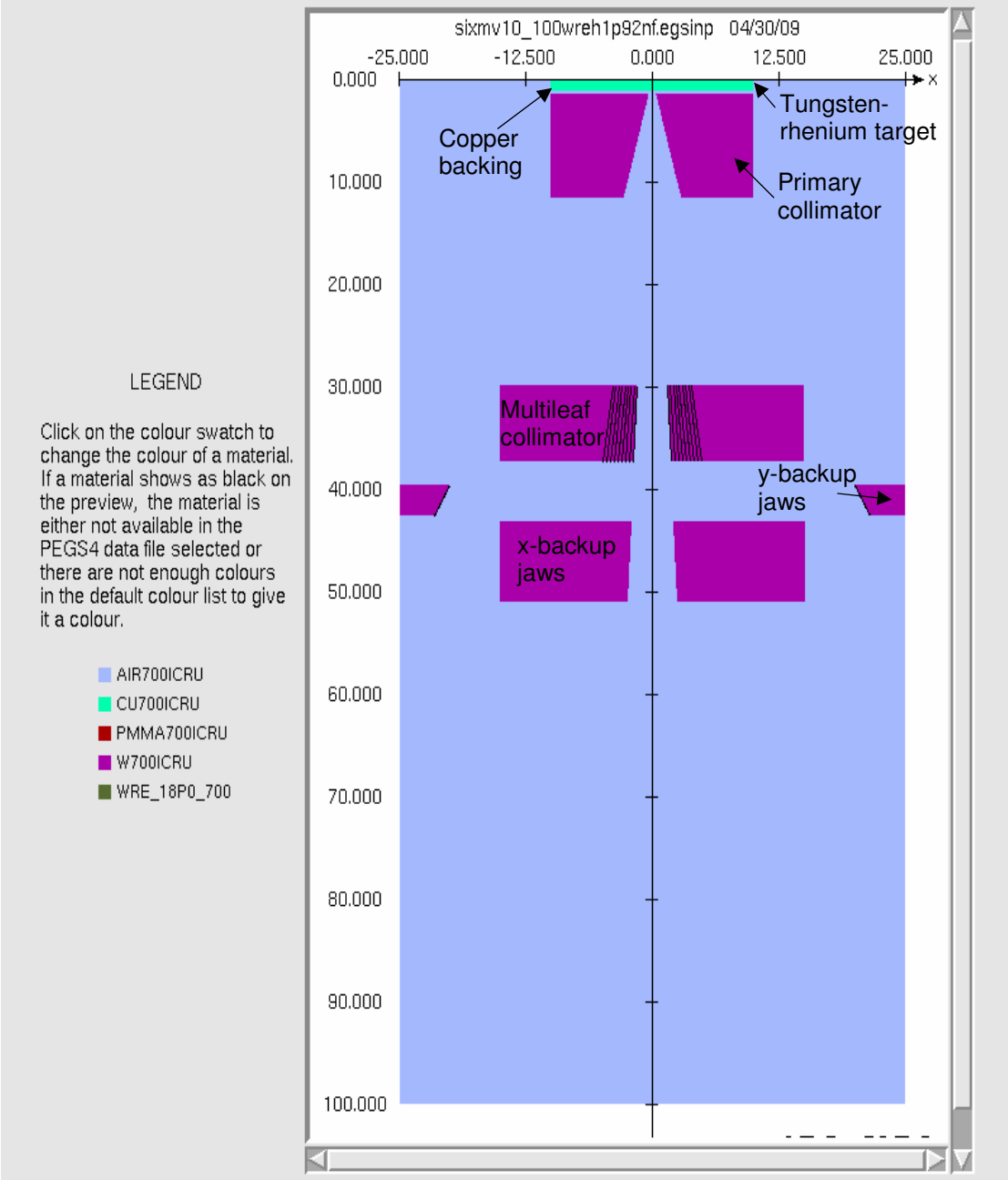

Figure 7.2: 6 MV Elekta treatment head with no filter.

Measurements for field sizes collected for this study including 5 x 5, 10 x 10, 15 x 15, 20 x 20, 25 x 25, 30 x 30 and 40 x 40 cm^2 defined by the jaws and multileaf collimator. Machine total scatter factors were calculated and

compared with the experimental data. The summary of the simulations are provided in table 7.1.

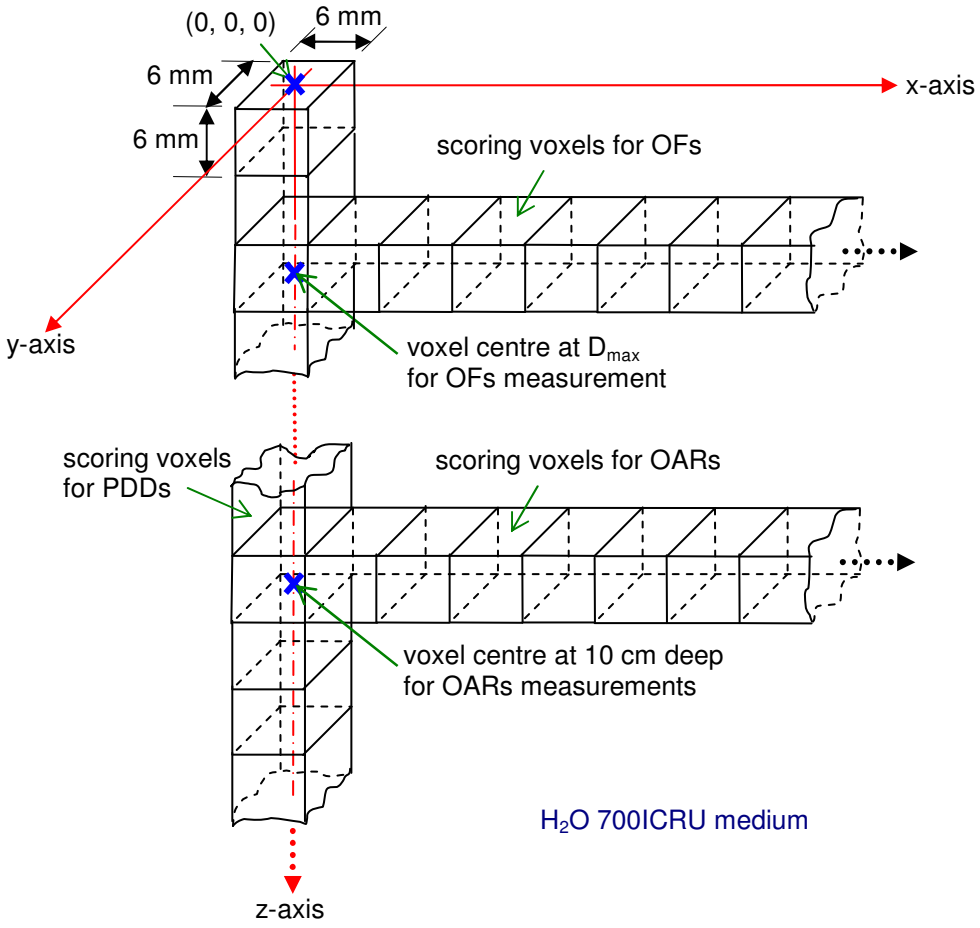

Figure 7.3: DOSXYZnrc scoring voxels used in the simulations.

Table 7.1: The summary of calculations made with the Monte Carlo code.

Depth Doses	Open beam (Filtered and unfiltered beam)	10 x 10 cm^2 field at 100 cm SSD
Off-axis ratios	Open beam (Unfiltered beam)	5 x 5, 10 x 10, 15 x 15, 20 x 20 and 30 x 30 cm^2 at 10 cm deep and 100 cm SSD for 6.4 MeV electron energy (validated model) and 6.0 MeV electron energy.
Output Factors	Open beam (Filtered and unfiltered beam)	5 x 5, 10 x 10, 15 x 15, 20 x 20, 25 x 25, 30 x 30, 40 x 40 cm^2 at 1.5 cm deep and 100 cm SSD

Statistical uncertainty of MC results was around 1% at peak intensity for PDD, OAR and OF calculations. For the sampling of bremsstrahlung photons, EGSnrc relies on the 700icru.pegs4dat that have been converted to tables including bremsstrahlung production probabilities, photon energy distributions and photon angular distributions. The sampling of bremsstrahlung photons are performed at each electron sub-step and the table of production probabilities are used to determine whether a bremsstrahlung photon will be created using the default Storm-Israel cross-sections data [161, 187].

In order to increase the number of photons crossing the phase space scoring plane per initial electron and reducing the run time, directional bremsstrahlung splitting (DBS) was used. The number of bremsstrahlung photons generated per incident electron on the target is increased and also the photons not aimed at the splitting field are rejected. The splitting field must be bigger than the largest field size in the calculations used which was chosen to be 50 x 50 cm^2 [163, 187]. Further variance reduction techniques used are discussed in section 3.5.

Local dose differences between two points were calculated by using the formula below:-

$$\text{Local percentage difference} = \frac{(\text{Dose}_{\text{MC Calculations}} - \text{Dose}_{\text{Measured Data}})}{\text{Dose}_{\text{Measured Data}}} \times 100\%$$

7.3 Results

For percentage depth dose, (for a 10 x 10 cm^2 field) the plots in figure 7.4 show that the Monte Carlo results agree well with experimental data for the filtered beam but slightly disagrees with the unfiltered beam.

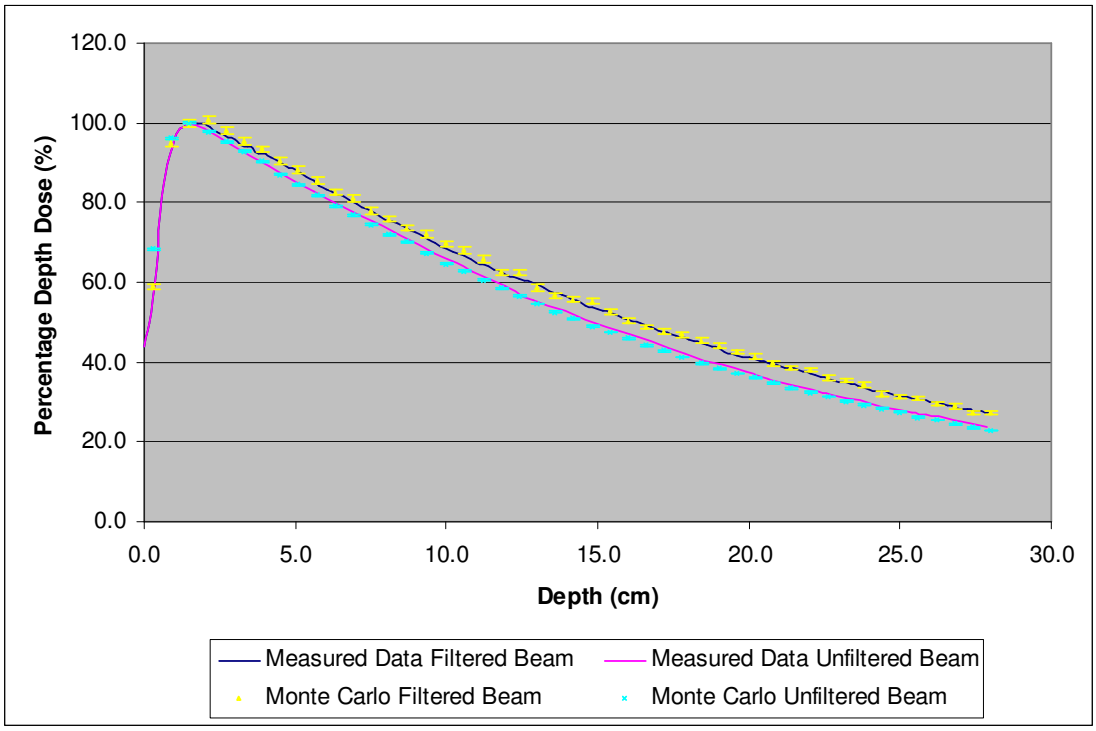

Figure 7.4: 6 MV Elekta, Percentage Depth Dose, 100 cm SSD 10 x 10 cm^2 field.

Table 7.2: The errors of the PDD at the depth of 10, 20 and 28 cm are demonstrated.

Field Size (10 cm)
Flattened Beam
e^- Energy (6.4 MeV)

Depth (cm)	M. Data	Monte Carlo	Local % Diff.	PDD Diff. (%)
10	68.38	69.63	1.83	1.25
20	40.69	41.31	1.52	0.62
28	27.09	27.19	0.38	0.10

Field Size (10 cm)
Unflattened Beam
e^- Energy (6.4 MeV)

Depth (cm)	M. Data	Monte Carlo	Local % Diff.	PDD Diff. (%)
10	65.91	64.58	-2.01	-1.33
20	37.50	36.65	-2.28	-0.85
28	23.86	22.78	-4.54	-1.08

Although the flattened beams from the Monte Carlo calculations are in good agreement within less than 2% (local percentage difference), but for the unflattened beam some larger discrepancies are shown but still with less than 5% difference as in table 7.2 above. In terms of Percentage Depth Dose, in all cases differences are at less than 2%.

From figure 7.4 the Monte Carlo simulations shows a slight lower curve than the PDD from Cashmore's [186] experiment. This could indicate that the MC calculations generate less scattered dose than measured in the experimental values as a result of removing the flattening filter. It could however be due to some other cause.

In figure 7.5 below, the off-axis ratios were plotted and compared with the experimental work. The result showed the same general effect which is reducing the off-axis beam up to the penumbra region. The shapes of the Monte Carlo simulations are in broad accordance with the experimental measurements but with a greater decrease in the beam dose at the field edges, becoming more apparent at the larger field sizes.

Since the validated MC simulations were run with the original 6.4 MeV electron energy, it is possible that the dose at the central axis was more intense as a consequence of the greater electron energy. Therefore, a reduction in the electron energy of 6.0 MeV was rerun for the unfiltered beam and the result was plotted in figure 7.6.

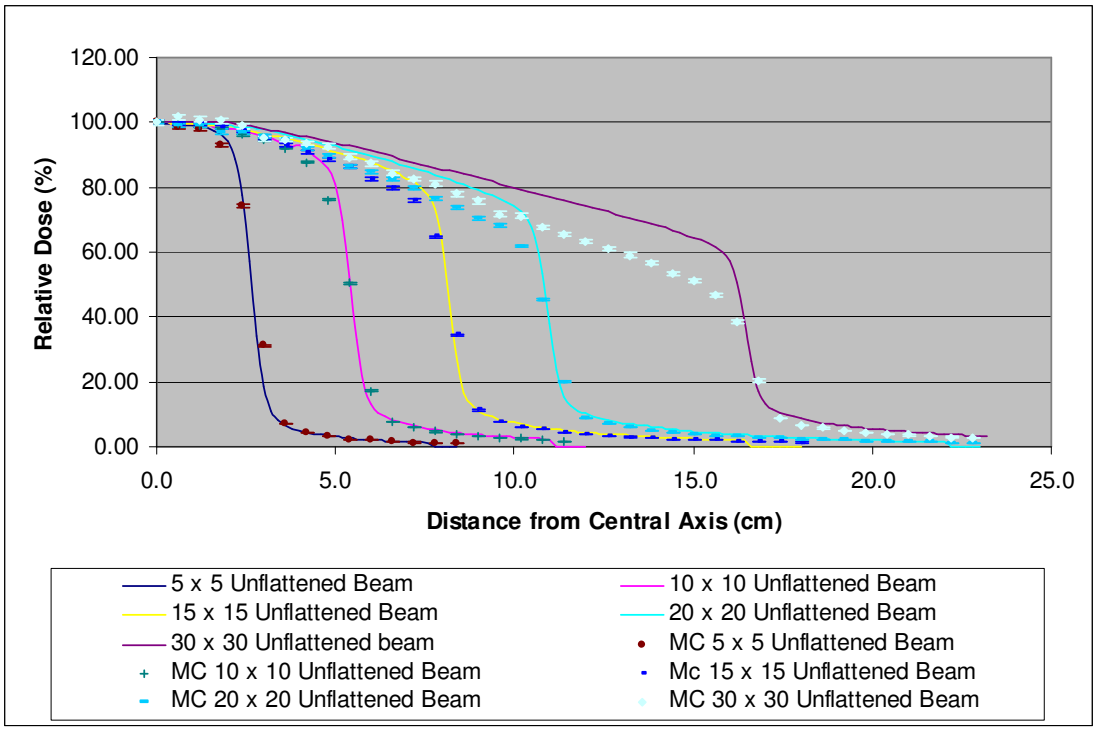

Figure 7.5: 6 MV Elekta unflattened beam off-axis ratios at 10 cm deep and 100 cm SSD.

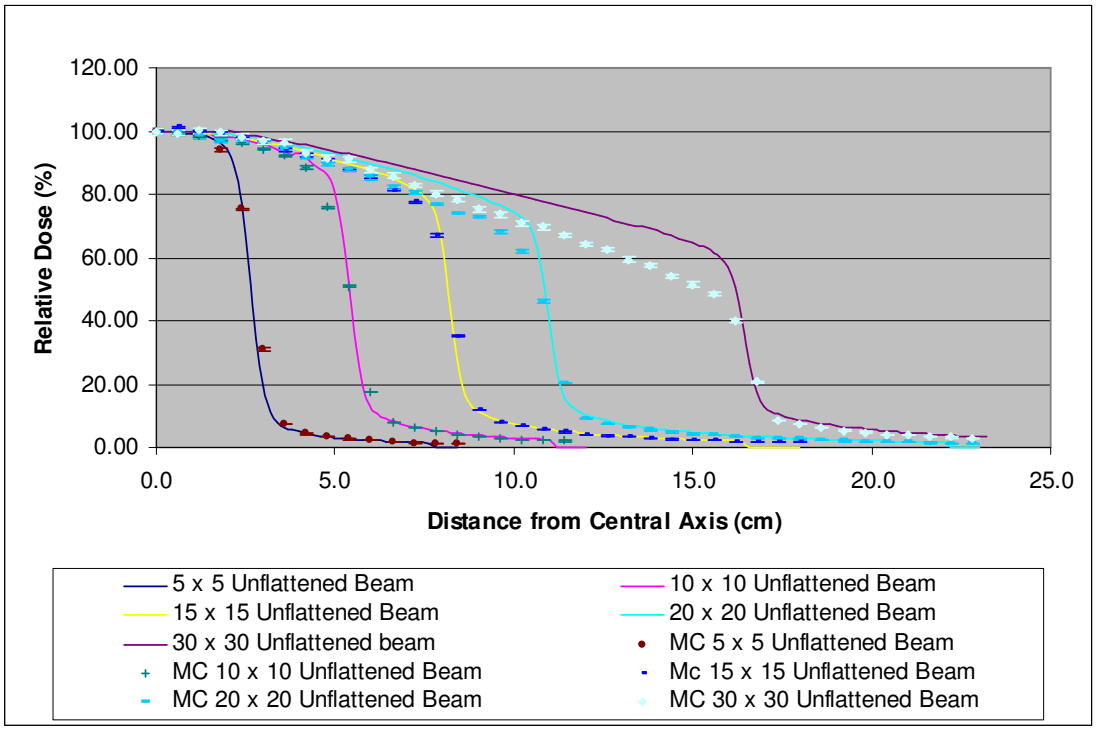

Figure 7.6: 6 MV Elekta unflattened beam using 6.0 MeV electron energy off-axis ratios.

Table 7.3: The largest percentage difference for the unflattened beam according to field sizes.

Field Size (cm^2)	Distance from Central Axis (cm)	Monte Carlo Data (%)	Measurement by Cashmore [186] (%)	Percentage Difference (%)
5 x 5	3.0	31.112	18.882	12.230
10 x 10	4.8	76.126	86.025	-9.899
15 x 15	7.8	64.835	73.292	-8.457
20 x 20	10.2	61.905	72.474	-10.569
30 x 30	15.6	46.873	61.577	-14.704

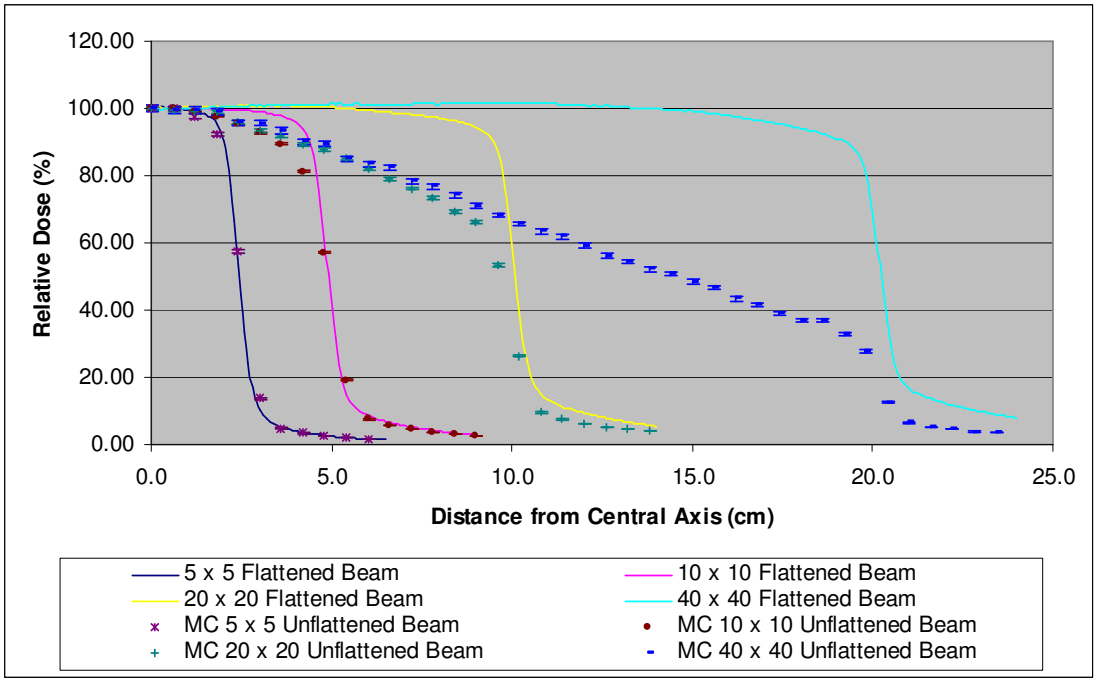

Figure 7.7: 6 MV Elekta flattened beam and unflattened beam at 10 cm deep and 100 cm SSD.

From the above profiles there were no significant differences shown in the Monte Carlo calculations after normalised to 100% at the central axis in figure 7.5 and 7.6. The discrepancies of the Monte Carlo simulations have been shown to be due to other factors, perhaps a lack of optimisation of the modelling of the linac head, or perhaps due to inaccuracies in the modelling of the Bremsstrahlung source angular distribution. The biggest percentage

difference is shown to be at 30 x 30 cm^2 field size of roughly 14.7% at the field boundary of 15.6 cm from the central axis as in table 7.3.

The above open beam profiles (figure 7.5 to 7.7) show the forward-peaked nature of the fluence with no filter. In figure 7.7, the smaller field OAR of the filterless beam shows minor differences in shape compared to the flattened beam. Larger fields show larger effects. That is, the 5 x 5 cm^2 field shows little change in profile as compared to the filtered beam, while the 30 x 30 cm^2 field shows a large difference. This is in good agreement with Cashmore's [186] measurements. Moreover the 5 x 5 cm^2 field also show not much difference in shape and boundary edge to those measured with flattening filter at larger field sizes.

The larger field sizes show enhanced central axis with rounding of the profiles which are also reported by Vassiliev et al. 2006 [191] using a Varian linac machine. The dose outside the peak edge is found to be lower using the MC calculations. This is as a result of a reduction in the scattered dose.

At 100 cm SSD for a 10 x 10 cm square field, the dose 2 cm away from the geometrical field edge at the tail of the penumbra is reduced from 7.9% to 6.7% at 10 cm deep. This is 15.7% relative change in the dose outside the field boundary about 4% more than that found by Cashmore [186], who reported an 11.3% relative change. Both results acknowledge the benefit of using a filterless beam to lower the dose for the tissue outside the field edge.

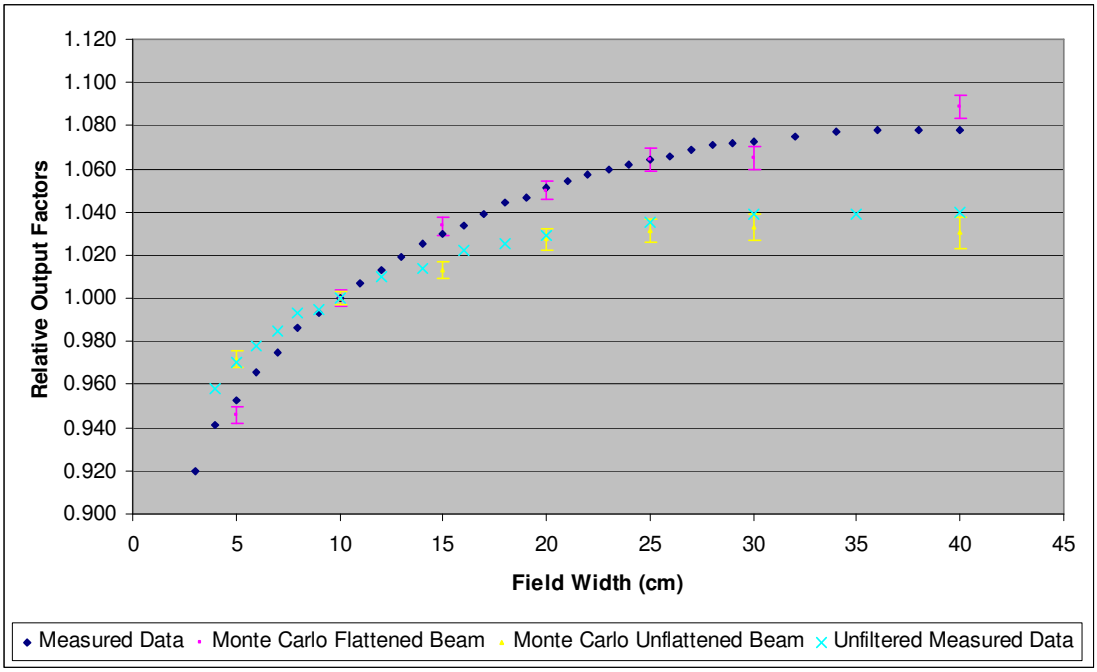

Figure 7.8: 6 MV Elekta, output factors at 1.5 cm deep and 100 cm SSD.

Table 7.4: The percentage difference for the output factors of the unfiltered beam at D_{max}.

Field Size	Measured Data	MC Normalised Dose	MC Percentage Error (%)	MC Uncertainties	Percentage difference from experiment (%)
5	0.970	0.972	0.4	± 0.004	0.21
10	1.000	1.000	0.3	± 0.003	0.00
15	1.018	1.013	0.4	± 0.004	-0.49
20	1.029	1.027	0.5	± 0.005	-0.16
25	1.035	1.032	0.5	± 0.005	-0.33
30	1.039	1.033	0.6	± 0.006	-0.56
40	1.040	1.030	0.7	± 0.007	-0.94

To investigate further, the output factor was plotted in figure 7.8. In general terms the simulated results show a very similar shape to the experimental data. However there is some possible reduction in the Monte Carlo data at large field size. This is an indication of a greater reduction of scattered doses than the experimental measurements show.

From table 7.4, the percentage difference from the work of Cashmore [186] and the MC simulations is less than 1% error therefore the MC data can be used to analyse the total scatter of the unfiltered beam. From figure 7.8 the total scatter factors measured at 100 cm SSD and at D_{max} also show a reduced range against the field width in agreement with the work from Cashmore [186]. The curve from the MC result confirms the reduction of head scatter as the phantom scatter remains more or less the same, depending on the field sizes at the surface.

The ratio of 40 x 40 to 5 x 5 cm^2 fields from the flattened beam OF curve is 1.131 while the ratio of 40 x 40 to 5 x 5 cm^2 fields for the MC unflattened beam is 1.060. This is a significant decrease seen in the filtered beam and the unfiltered beam over the range of 40 x 40 to 5 x 5 cm^2 from 13.2% to 5.99% respectively. The total scatter factor has been reduced by 54.31%, an approximate match with the measurement made by Cashmore [186] of about 50% reduction.

The summary of the results are shown in the table 7.5 below. Most of the MC calculations are in agreement with measurements made by Cashmore [186]. However, there are some results that do not agree within a 2% difference. This might be due to the simple model of the Elekta linac used in these calculations or some other causes.

Table 7.5: The summary of results comparing between measured and calculated data [186].

Investigation on Elekta Linac	**Results**		**Percentage Difference**
Percentage Depth Doses	Flattened beam		1.25% at 10 cm deep
	Unflattened beam		- 1.33% at 10 cm deep
Off-Axis Ratios	Result from Cashmore 61.6%	Monte Carlo Results 46.9%	-14.7% at 30 x 30 cm^2 field, 15.6 cm from CAX
Out-of-Field Dose	Result from Cashmore 11.3% relative change	Monte Carlo Results 15.7% relative change	3.4% at 2 cm outside 10 x 10 cm^2 field
Output Factors	Flattened beam		1.00% at 40 x 40 cm^2 field
	Unflattened beam		- 0.94% at 40 x 40 cm^2 field
Total Scatter Factors	Result from Cashmore 50% reduction	Monte Carlo Results 54.31% reduction	4.31%

7.4 Discussion

The validated model of the Elekta linac head used in this research was based on the specification provided by the manufacturer. However the accuracy of the information cannot be guaranteed. It is important to note that during the optimisation process the height of the flattening filter was increased to 1.92 x the original height supplied by Elekta Oncology Systems whilst the primary electron energy was raised to 6.4 MeV. These changes were required to match the simulated and measured data for PDD, OAR and OF.

The unflattened beam for the PDD using Monte Carlo technique agrees well with the measured data from Cashmore [186] to better than 2%. The use of the flattening filter has hardened the radiation beam on the central axis by

attenuating the low energy component of the spectrum. This increases the apparent energy of the beam.

When the unflattened beam was used, additional soft x-rays were added to the beam and so a lower observed energy was obtained. The MC result is slightly lower than that reported by Cashmore [186] by approximately 1%. Nevertheless, this study has confirmed that the filterless beam energy approximated that of 5 MV flattened beam as found by Cashmore [186] using BJR25 data.

In the OARs result, the Monte Carlo calculations has shown that the use of filterless beam has reduced the dose at a distance away from the central axis. The shape of the unflattened beam profiles are in rough agreement with these of Cashmore [186] but with much greater reduction in dose near the beam boundary of as much as approximately 15% for 30 x 30 cm^2 field. Otherwise, similar results are obtained.

Other than that, the 5 x 5 cm^2 unflattened beam shows almost no change, enhanced central dose and the rounding of the profiles for larger field sizes have also been observed using Monte Carlo techniques. The dose outside treatment field is reduced by 15.7%, more than that found by Cashmore [186] but reaffirming that the dose are lower to the surrounding tissues using unflattened beam.

The output factors of the filterless beam are shown to be slightly lower by around 1% using Monte Carlo calculations as compared to measurements made by Cashmore [186]. However the results are consistent with those from Cashmore [186], who showed a reduction in total scatter factor of 50%. It can be said that the scatter from the treatment head is reduced substantially since phantom scatter remains unchanged.

Although the unfiltered beam from the Monte Carlo calculations have shown that the PDD (figure 7.4), Off-Axis Ratios (figure 7.5 and 7.6) and the Output Factors (figure 7.8) of the simulations do not match perfectly the results of Cashmore [186], the calculations obtained can still be used for comparisons. In fact, considering that these simulations use a very simple model for the Elekta machine, the agreement with experimental measurement is manageable for further investigations.

It is likely that the discrepancies shown in the shape of the OARs (figure 7.5 and 7.6) could originate in the physics of the Bremsstrahlung model used in EGSnrc or some other factors. In simulations of the flattened beam it is quite possible that inaccuracies of the Bremsstrahlung model are removed by empirical optimisation of the thickness and geometry of the flattening filter as performed earlier in this thesis.

This study has shown that the Monte Carlo simulations have not been fully optimised for the unfiltered beam. The Monte Carlo results for the unfiltered beam showed a lower reduction in scattered radiation than the measured

beam. However, the discrepancies of the beam profiles from the measured data, which can be as high as 15% for larger field size, remain unexplained. Also, to optimise the linac head to its fullest would take longer than the time available; therefore the research has to stop here.

Nevertheless, it can be said the aim of using an unfiltered beam for IMRT using Elekta Precise linac has been verified by the Monte Carlo calculations. The major benefits are confirmed, for instance reduced total scatter, out-of field dose and leakage radiation. Hence the filterless beam could be use for clinical purposes to decrease the total dose to patients with improved dose distribution and faster delivery.

Chapter 8 - Conclusion

8.1 Summary of Results

In this work, the Monte Carlo method was used to simulate two linear accelerators, one Elekta machine and the other Varian. The simulated linacs were validated and tuned to match the commissioning data within acceptable agreement. Both data used 6 MV photon energy that were compared with experimental results.

Two other linac energies, 10 and 15 MV have not been completed due to difficulty in adjusting two flattening filters at the same time. The completion of 2 validated models has been compared with measured results and has been used to predict the performance of solid-state detectors and a filterless beam. It has been shown that Monte Carlo modelling could be used to understand the basic mechanism of the dose measurements in question. It can provide a useful prediction and verify assumptions that are otherwise difficult to solve mathematically.

One additional project that benefited from the development of these models was the dose calibration of GafChromic film in the Varian linear accelerator beam. Electron spectra for the calculation of stopping-power corrections were calculated with the code FLURZnrc utilising the model developed in BEAMnrc presented in this thesis in Appendix C. The other 3 investigations pertaining to the 6 MV Elekta and Varian models were summarised in the next section.

8.1.1 Investigation on DOSI Performance

Although DOSI detector is position sensitive and capable of fast readout, it is still a solid-state detector made of silicon as a sensitive volume. The p-type semiconductor is not a tissue equivalent material. As a result, a perturbation in dosimetry exists due to the higher Z medium than water, producing more secondary electrons from low energy photons. The measurements in experimental set-ups have shown that the detector produces data with an error of within 3%. This has been predicted by authors such as Yin et al. (2004) [64] at large field size and depth.

MC simulations have shown that either parts of the sensitive array or the whole area of the Si strip (except for the edges) can be used with acceptable discrepancies for small field sizes. This indicates a positive future for DOSI to become a 2-dimensional detector capable of reproducing dose measurements with acceptable results.

However, to establish an improved detector, DOSI sensitive layer would have to be thinner to take into account the shorter range of secondary electrons for electronic equilibrium to be established. In this research MC model has been used to predict the improvement of 1.7% at 30 x 30 cm^2 from the originally 2.7% error. To further study this would require a DOSI manufactured to 25 μm thick. This has not yet been produced.

8.1.2 Investigation on DOSI in Stereotactic Beams

In this investigation, DOSI detector and 2 other dosimeters, diamond and PinPoint detector were compared with MC calculations to observe their performances in stereotactic beams. These beams are small being less than 4 cm in diameter. Therefore some detectors such as the thimble ion chamber are not suitable to measure the dose in the penumbral region.

As a reference calculation, the Monte Carlo method has shown that the PinPoint chamber broadens the penumbra and underestimates the dose in the penumbral tail. Moreover, unwanted signal can be obtained from the measurements due to amplification factor as discovered by other authors [181].

Meanwhile, the DOSI detector with its smallest voxels, 0.25 mm pixel size and 0.3 mm thick, does not appear to be the best dosimeter to measure all aspects of stereotactic beams. DOSI detector does not show much of the broadening of the penumbra due to its small active volume but shows a significant fall in dose measurement outside the beam edge. This perturbation remains to be resolved for this novel detector.

Overestimation to low dose Compton scattering would show higher measurement at the penumbral tail as result of normalisation at the central axis. This suggests a reduced continuous slowing down approximation of electrons in the detector sensitive array as a result of lower energy Compton

scattering photons. Recommendation for reduced thickness in the Si strip would be beneficial for the DOSI detector as previous results have suggested.

Diamond detector performance result is found to be superior as it matches with the Monte Carlo simulations. This is due to its near tissue-equivalence and its non-directional dependence [182]. Diamond detector shows good reproducibility and an advantageous tool to have for its accuracy. Profile measurements with the diamond detector are highly accurate with the stem of the detector placed perpendicularly to give a sharper penumbra.

The findings written here are similar to other results based on Dawson et al. (1984), Beddar et al., (1994) [185, 178]. The finite size of the sensitive volume of the detector, the change in the electron transport including the surrounding envelope in the detector, variation in the detector directional response, detector energy dependence and dose rate dependence are important factors to consider. The presence of lateral electron disequilibrium still persists in the penumbral measurements and the key to overcome this is a small sensitive volume and a tissue-equivalent material.

It is paramount to have an accurate dosimetry in the penumbral region due to the rigid conformance of the high dose region to the target volume and the sparing of the surrounding tissues. Therefore, the corrections made to minimise the error in the detector measurements are important. The study of this work using Monte Carlo simulations indicates that the lack of lateral electronic equilibrium in the detector response could cause errors in some

detectors. This occurs in the results of the tissue non-equivalence detector and is worse as the detector size increases.

Monte Carlo has been shown to be a reliable reference for dosimetry with stereotactic measurements, particularly where lateral electronic equilibrium does not exist. Suggestions for the size of the voxels to be used depend on the profile to be measured, the computational processing time and accuracy. For penumbra measurement, the sensitive area of the voxel should be 1 mm x 1 mm. The uncertainties can be reduced by increasing number of histories or increasing the number of random number seeds to achieve better than 2% errors.

Monte Carlo calculations with the validated photon and electron transport have shown that diamond detectors, if corrected for dose rate dependence and pre-irradiation, produce better results with superior actual treatment volume than the prototype DOSI detector or the PinPoint ionisation chamber.

8.1.3 Investigation on Filterless Beams in IMRT

In this research the flattening filter has been removed from Elekta linac for IMRT study. The MC filterless beam output factor matches within tolerable discrepancies with the measured data. The differences between measurements and the MC calculations could be as a result of reduced scattered dose or other factors.

The 5 x 5 cm^2 field shows little change in profile as compared to the filtered beam with little difference in shape and boundary edge. The larger field sizes show enhanced central axis with rounding of the profiles which are in accord with experimental measurements.

However, the dose outside the main beam is found to be lower using the MC calculations as a result of a reduction in the scattered dose. The largest discrepancies of the MC off-axis ratios have been shown to be 14.7% less than the measured data for 30 x 30 cm^2 field at the field boundary of 15.6 cm from the central axis. These inaccuracies might be due to a lack of optimisation of the modelling of the linac head or perhaps due to other factors.

Moreover, the benefit of using a filterless beam to lower the dose for the tissue outside the field edge using Monte Carlo calculation has been established although it has found to be 15.7% relative change, 4.4% more than practical measurements. The overall variability of the MC total scatter factors measured at 100 cm SSD and at D_{max} have been reduced by 54.31% also confirm the reduction of head scatter as the phantom scatter remains more or less the same, depending on the field sizes at the surface.

Although the filterless beam from the Monte Carlo calculations have shown that the PDD, off-axis ratios and the output factors of the simulations do not match perfectly with the experimental results, the calculations obtained can still be used for comparisons. Nonetheless, it can be said the Monte Carlo calculations have verified the benefits of filterless beam for IMRT resulting in

reduced total scatter, less out-of-field dose and leakage radiation. This would as a consequence decrease the total dose to patients with improved dose distribution and would reduce the treatment time for IMRT sessions.

8.2 Future Work

Some ideas for future work in Monte Carlo modelling would be to further investigate the 10 and 15 MV energy beams from the Elekta linac. Since the adjustment of 2 flattening filters for these energies is hard to manage, one simple suggestion would be to have a simplified model of one filter with adjusted height tuned to the PDDs, OARs and OFs commissioning data with the respective energies. This could be easier or harder to achieve than to use the validated 6 MV filter and to add another filter which would complicate the beam profile as in the previous result in this thesis. This one flattening filter adjustment would be another trial and error process.

As for the DOSI model, a continuation for better performance of the detector would be recommended since the theoretical 25 μm thin DOSI still gives about 2.1% largest error. It would beneficial to know by using the MC technique what value of thickness would give better than 2% accuracy.

As a continuation from this theoretical thin Si substrate, further investigation could be used to calculate the stereotactic beams. This finding would indicate whether it could be improved in the performance of penumbral measurement to be a detector as reliable as the diamond detector in tissue-equivalence

dosimetry. This could show whether DOSI would be the favourite detector in the future.

Finally in the IMRT filterless beam, research can be done using the Monte Carlo model to investigate the energy sensitivity in the Elekta machine. With flattening filter removed, the machine could not operate correctly under all circumstances and further study is required. Measurements in the build-up region show an increase in surface dose due to flattening filter removal [186]. This is due to the number of electrons reaching the monitor chamber is too low for the machine to operate correctly.

Electron contamination in the linac beam provides a dose in the phantom at build-up region of the percentage depth dose curve. It is as a result of the interaction in the treatment head and air column of the radiation beam rather than a contribution from low energy scattered photon. Electron contaminants are produced at places where the principal beam passes through. These are mainly from the flattening filter, collimator jaws and also the volume of air which becomes higher for extended SSD [196]. It has been reported that the electron contamination from 4 to 25 MV from various linac machines can contribute between 6 to 11% of maximum dose at the surface for 10 x 10 cm^2 field [142].

Electron contamination in filtered beam is used to control the beam properly. The use of Cu or Al sheets with various thicknesses in MC study will show whether the surface dose could be reduced. To boost a certain amount of

contamination of electrons in the monitor chamber, it is necessary to make the machine run in clinical mode by using the correct thickness of metal sheets; hopefully this will reduce the surface dose in the build-up region during flattening filter-free beam therapy.

Appendix A - Calculation of the Percentage Difference for Various Flattening Filter Heights and Electron Energy for Elekta

Elekta Precise Data Analyses

Table A.1: The best fit electron energy data for 6 MV Elekta from 6.0 to 6.5 MeV.

6 MV Percentage Depth Dose 90 cm SSD Commissioning Data (%)		**Monte Carlo runs**	**6.0 MeV**		**6.1 MeV**	
Field Width 3.0 cm			Field Width 3.0 cm		Field Width 3.0 cm	
Depth (cm)	N. Dose (%)	Depth (cm)	N. Dose (%)	Loc. Percentage Diff. (%)	N. Dose (%)	Loc. Percentage Diff. (%)
1.5	100.0	1.5	100.0	0.00	100.0	0.00
2.0	97.7	2.0	98.6	0.88	98.8	-1.13
3.0	93.0	3.0	93.9	0.92	93.3	-0.29
4.0	87.9	4.0	88.0	0.10	88.2	-0.34
5.0	82.7	5.0	82.7	0.02	83.6	-1.15
6.0	78.0	6.0	78.1	0.07	77.9	0.16
7.0	73.4	7.0	72.8	-0.79	73.5	-0.17
8.0	69.0	8.0	68.6	-0.58	68.6	0.62
9.0	64.8	9.0	64.1	-1.04	64.1	1.04
10.0	60.8	10.0	60.3	-0.76	60.7	0.16
11.0	57.1	11.0	56.5	-1.06	56.4	1.27
12.0	53.7	12.0	53.0	-1.37	53.1	1.03
13.0	50.5	13.0	49.5	-2.07	49.8	1.44
14.0	47.5	14.0	46.4	-2.27	47.0	1.00
15.0	44.7	15.0	43.7	-2.29	44.0	1.53
16.0	42.1	16.0	40.9	-2.96	41.6	1.27
17.0	39.5	17.0	38.3	-2.98	38.9	1.43
18.0	37.3	18.0	36.2	-2.95	36.5	2.25
19.0	35.2	19.0	33.6	-4.47	34.3	2.68
20.0	33.1	20.0	31.7	-4.22	32.3	2.51
22.0	29.4	22.0	28.2	-4.06	28.4	3.52
24.0	26.1	24.0	25.2	-3.33	25.4	2.85
26.0	23.2	26.0	22.1	-4.62	22.5	3.02
28.0	20.7	28.0	19.3	-6.73	19.3	6.71
			Average	-1.94	Average	1.31

6.2 MeV		**6.3 MeV**		**6.4 MeV**		**6.5 MeV**	
Field Width 3.0 cm		Field Width 3.0 cm		Field Width 3.0 cm		Field Width 3.0 cm	
N. Dose (%)	Loc. Percentage Diff. (%)	N. Dose (%)	Loc. Percentage Diff. (%)	N. Dose (%)	Loc. Percentage Diff. (%)	N. Dose (%)	Loc. Percentage Diff. (%)
100.0	0.00	100.0	0.00	100.0	0.00	100.0	0.00
98.9	-1.20	98.0	-0.35	98.4	-0.72	100.1	-2.46
93.5	-0.53	93.6	-0.62	93.6	-0.62	94.7	-1.86
87.6	0.33	88.2	-0.38	88.5	-0.70	88.9	-1.13
82.7	0.03	83.1	-0.50	83.8	-1.30	84.0	-1.54
77.9	0.14	77.5	0.68	78.4	-0.51	79.0	-1.29
73.2	0.25	72.9	0.71	74.0	-0.76	74.4	-1.41
68.9	0.19	68.3	0.96	68.9	0.12	69.6	-0.88
64.2	0.88	64.5	0.54	64.5	0.46	65.9	-1.68

60.2	0.93	60.3	0.79	60.9	-0.21	61.4	-1.01
56.7	0.73	56.8	0.54	57.2	-0.24	57.7	-1.00
53.4	0.50	53.3	0.70	53.4	0.52	53.8	-0.12
49.7	1.51	50.0	0.97	50.0	0.93	50.7	-0.44
47.1	0.87	46.8	1.52	47.2	0.74	47.7	-0.33
44.2	1.07	44.0	1.49	44.2	1.05	45.0	-0.74
41.4	1.65	41.2	2.07	41.7	0.88	42.1	0.02
38.8	1.79	38.8	1.65	39.4	0.27	39.4	0.23
36.6	2.00	36.5	2.19	36.7	1.59	37.3	-0.08
34.8	1.22	34.5	1.97	34.9	0.97	35.5	-0.94
32.4	2.02	32.5	1.93	32.6	1.58	33.3	-0.61
28.6	2.85	28.7	2.24	28.5	3.08	29.6	-0.76
25.5	2.15	25.4	2.51	25.6	1.83	26.0	0.35
22.5	2.86	22.6	2.45	22.8	1.73	23.2	-0.03
19.8	4.31	20.0	3.36	20.0	3.26	20.2	2.60
Average	1.10	Average	1.14	Average	0.58	Average	-0.63

Table A.2: The best match for flattening filter heights at 1.85 x, 1.9 x and 1.92 x specification.

6.4 MeV Electron Energy, 1.85 x Original Height of the Flattening Filter					
1.5 cm Deep			10 cm Deep		
Normalised to 100.2 %	Measured Data (%)	Local Percentage Diff. (%)	Normalised to 71.2 %	Measured Data (%)	Local Percentage Diff. (%)
100.200	100.2	0.000	71.200	71.2	0.000
98.208	100.2	-1.988	71.582	71.2	0.537
99.532	100.6	-1.062	72.446	71.2	1.750
98.755	100.8	-2.029	71.336	71.3	0.050
98.682	101.3	-2.584	72.051	71.5	0.771
98.136	101.9	-3.694	71.706	71.8	-0.131
98.949	102.1	-3.086	73.173	71.9	1.771
99.921	102.4	-2.421	70.411	72.0	-2.207
100.394	102.5	-2.054	72.705	72.1	0.839
100.127	102.6	-2.410	71.989	72.1	-0.153
97.443	102.8	-5.211	71.471	72.1	-0.872
99.751	103.1	-3.249	70.904	72.1	-1.659
99.398	103.5	-3.963	72.174	72.1	0.103
99.471	103.9	-4.262	70.460	72.2	-2.410
99.799	104.5	-4.498	71.175	72.3	-1.556
100.164	104.9	-4.515	70.916	72.3	-1.914
100.054	105.0	-4.710	71.681	72.4	-0.993
100.006	105.0	-4.756	70.546	72.4	-2.560
99.690	104.8	-4.876	67.241	72.3	-6.997
99.095	104.9	-5.534	68.659	72.0	-4.640
98.221	104.3	-5.829	69.449	71.8	-3.275
98.755	105.0	-5.948	68.462	71.8	-4.649
98.913	105.0	-5.797	71.052	71.4	-0.487
99.666	104.9	-4.990	68.240	71.1	-4.022
99.180	104.7	-5.272	70.226	70.9	-0.951
99.508	104.3	-4.595	68.807	70.5	-2.401
99.544	103.9	-4.192	68.363	70.0	-2.338
101.512	103.5	-1.921	67.068	69.4	-3.360
101.208	103.1	-1.835	68.129	68.7	-0.831
101.281	102.0	-0.705	66.513	67.9	-2.042

93.412	95.6	-2.289	66.230	67.0	-1.150
36.954	38.0	-2.752	65.810	65.8	0.016
10.726	10.5	2.148	63.368	64.1	-1.141
8.497	7.8	8.938	56.264	58.1	-3.159
7.158	6.6	8.449	23.890	25.9	-7.762
5.975	5.6	6.694	11.907	12.0	-0.779
4.909	4.8	2.262	9.566	9.7	-1.385
Average Difference		-2.285	8.242	8.3	-0.695
			7.037	7.3	-3.598
			6.260	6.3	-0.629
			Average Difference		-1.623
Total Average Difference			-1.941		

6.4 MeV Electron Energy, 1.9 x Original Height of the Flattening Filter					
1.5 cm Deep			10 cm Deep		
Normalised to 100.2 %	Measured Data (%)	Local Percentage Diff. (%)	Normalised to 71.2 %	Measured Data (%)	Local Percentage Diff. (%)
100.200	100.2	0.000	71.200	71.2	0.000
100.992	100.2	0.791	72.844	71.2	2.309
99.868	100.6	-0.728	71.422	71.2	0.311
99.791	100.8	-1.001	72.518	71.3	1.708
100.008	101.3	-1.275	72.909	71.5	1.970
99.932	101.9	-1.932	76.040	71.8	5.905
100.456	102.1	-1.611	72.765	71.9	1.204
100.737	102.4	-1.624	73.483	72.0	2.060
104.339	102.5	1.794	72.557	72.1	0.633
99.702	102.6	-2.825	72.818	72.1	0.995
100.047	102.8	-2.678	73.379	72.1	1.773
101.567	103.1	-1.487	73.261	72.1	1.610
102.372	103.5	-1.090	72.231	72.1	0.181
102.385	103.9	-1.458	71.996	72.2	-0.283
101.708	104.5	-2.672	73.065	72.3	1.059
102.180	104.9	-2.593	74.318	72.3	2.791
102.334	105.0	-2.539	72.778	72.4	0.523
102.346	105.0	-2.527	71.774	72.4	-0.865
102.282	104.8	-2.402	73.131	72.3	1.149
102.960	104.9	-1.850	72.648	72.0	0.900
103.317	104.3	-0.942	72.596	71.8	1.108
101.669	105.0	-3.172	71.839	71.8	0.055
103.368	105.0	-1.554	74.957	71.4	4.982
103.956	104.9	-0.900	72.465	71.1	1.920
105.489	104.7	0.754	73.470	70.9	3.625
104.339	104.3	0.038	71.957	70.5	2.066
104.275	103.9	0.361	70.561	70.0	0.801
104.927	103.5	1.379	70.926	69.4	2.199
104.365	103.1	1.227	70.809	68.7	3.069
106.115	102.0	4.034	69.674	67.9	2.612
99.919	95.6	4.518	69.361	67.0	3.523
38.825	38.0	2.172	69.061	65.8	4.955
11.225	10.5	6.902	65.812	64.1	2.671
8.755	7.8	12.246	58.898	58.1	1.374

7.262	6.6	10.026	25.764	25.9	-0.525
6.255	5.6	11.696	12.655	12.0	5.459
5.096	4.8	6.172	10.144	9.7	4.576
Average Difference		0.682	8.989	8.3	8.306
			7.316	7.3	0.215
			6.974	6.3	10.697
			Average Difference		2.241
Total Average Difference			1.492		

6.4 MeV Electron Energy, 1.92 x Original Height of the Flattening Filter					
1.5 cm Deep			10 cm Deep		
Normalised to 100.2 %	Measured Data (%)	Local Percentage Diff. (%)	Normalised to 71.2 %	Measured Data (%)	Local Percentage Diff. (%)
100.200	100.2	0.000	71.200	71.2	0.000
98.552	100.2	-1.645	71.304	71.2	0.146
102.319	100.6	1.709	71.642	71.2	0.621
97.832	100.8	-2.944	72.189	71.3	1.246
101.966	101.3	0.658	72.072	71.5	0.799
101.521	101.9	-0.372	72.397	71.8	0.831
101.116	102.1	-0.964	71.955	71.9	0.076
103.000	102.4	0.586	71.668	72.0	-0.461
103.183	102.5	0.666	73.412	72.1	1.819
103.510	102.6	0.887	72.748	72.1	0.899
103.615	102.8	0.792	74.231	72.1	2.956
102.686	103.1	-0.402	71.018	72.1	-1.501
102.503	103.5	-0.964	71.278	72.1	-1.140
102.476	103.9	-1.370	72.956	72.2	1.047
102.960	104.5	-1.473	70.719	72.3	-2.187
102.215	104.9	-2.560	72.345	72.3	0.062
104.766	105.0	-0.223	71.720	72.4	-0.939
103.274	105.0	-1.643	71.343	72.4	-1.460
103.196	104.8	-1.531	72.228	72.3	-0.100
105.512	104.9	0.583	72.306	72.0	0.425
105.224	104.3	0.886	71.499	71.8	-0.419
104.635	105.0	-0.348	72.254	71.8	0.632
105.839	105.0	0.799	72.059	71.4	0.922
105.852	104.9	0.907	70.289	71.1	-1.140
106.087	104.7	1.325	71.005	70.9	0.148
105.198	104.3	0.861	69.678	70.5	-1.166
108.547	103.9	4.472	71.226	70.0	1.751
105.538	103.5	1.969	71.330	69.4	2.781
109.057	103.1	5.778	71.057	68.7	3.431
107.932	102.0	5.816	72.228	67.9	6.374
99.206	95.6	3.772	69.079	67.0	3.104
39.444	38.0	3.800	70.068	65.8	6.487
11.256	10.5	7.203	68.299	64.1	6.551
8.594	7.8	10.179	60.936	58.1	4.881
7.299	6.6	10.588	24.601	25.9	-5.017
6.876	5.6	22.790	12.363	12.0	3.023
5.941	4.8	23.767	10.592	9.7	9.198
Average Difference		2.550	9.092	8.3	9.545

	7.601	7.3	4.128
	6.207	6.3	-1.480
	Average Difference		1.422
Total Average Difference	1.964		

Appendix B - Calculation of the Percentage Difference for Various Flattening Filter Heights and Electron Energy for Varian

Varian Clinac 600C/D Data Analyses

Table B.1: The best match for flattening filter at 1.8 x, 1.83 x and 1.85 x original heights.

6.0 MeV Electron Energy, 1.8 x the Original height of the Flattening Filter					
1.5 cm Deep			10.0 cm Deep		
Normalised to 100%	Measured Data (%)	Local Percentage Diff. (%)	Normalised to 70.4%	Measured Data (%)	Local Percentage Diff. (%)
100.000	100.0	0.000	70.400	70.4	0.000
100.532	100.1	0.431	70.279	70.3	-0.029
102.161	100.4	1.754	70.400	70.5	-0.142
104.266	100.9	3.336	69.841	70.7	-1.215
104.377	101.4	2.936	71.342	71.0	0.482
104.987	101.9	3.029	71.134	71.2	-0.093
102.682	102.4	0.275	71.003	71.4	-0.557
103.446	102.8	0.629	71.419	71.6	-0.253
105.618	103.1	2.443	70.937	71.7	-1.064
104.311	103.4	0.881	71.748	71.8	-0.073
103.491	103.5	-0.009	72.142	71.8	0.476
103.214	103.8	-0.565	70.531	71.9	-1.903
105.053	103.9	1.110	71.057	72.0	-1.309
102.405	104.1	-1.629	71.200	71.9	-0.974
103.435	104.2	-0.734	68.855	71.9	-4.235
104.599	104.2	0.383	70.279	71.8	-2.118
104.311	104.4	-0.086	70.510	71.6	-1.523
101.020	104.5	-3.331	69.359	71.6	-3.130
103.336	104.7	-1.303	69.425	71.5	-2.902
102.748	104.8	-1.958	70.126	71.4	-1.784
102.926	105.1	-2.069	69.293	71.3	-2.814
101.407	105.2	-3.605	70.389	71.2	-1.139
104.200	105.4	-1.139	69.118	71.0	-2.650
104.366	105.5	-1.075	68.998	70.9	-2.683
106.294	105.5	0.753	68.636	70.6	-2.782
108.500	105.4	2.941	70.159	70.4	-0.342
107.835	105.4	2.310	69.414	70.0	-0.837
108.411	105.1	3.150	70.301	69.5	1.153
111.370	104.6	6.472	69.447	68.8	0.940
111.480	103.8	7.399	70.597	68.0	3.819
99.889	97.9	2.032	69.009	67.2	2.691
22.784	34.4	-33.768	69.031	65.9	4.750
10.895	10.3	5.780	67.091	64.2	4.504
8.246	8.2	0.558	54.953	55.5	-0.986
7.295	7.0	4.214	16.762	22.1	-24.154
6.074	6.0	1.230	11.854	12.0	-1.218
5.045	5.2	-2.972	9.999	10.0	-0.009
Average Difference		-0.005	8.409	8.6	-2.216
			7.176	7.6	-5.581
			6.454	6.7	-3.673
			Average Difference		-1.389

Total Average Difference	-0.724

6.0 MeV Electron Energy, 1.83 x the Original height of the Flattening Filter					
1.5 cm Deep			10.0 cm Deep		
Normalised to 100%	Measured Data (%)	Local Percentage Diff. (%)	Normalised to 70.4%	Measured Data (%)	Local Percentage Diff. (%)
100.000	100.0	0.000	70.400	70.4	0.000
102.094	100.1	1.992	70.138	70.3	-0.230
100.664	100.4	0.263	68.525	70.5	-2.801
103.772	100.9	2.846	68.634	70.7	-2.922
103.670	101.4	2.239	70.465	71.0	-0.753
103.299	101.9	1.373	70.803	71.2	-0.557
103.344	102.4	0.922	70.117	71.4	-1.797
104.447	102.8	1.602	69.550	71.6	-2.863
101.700	103.1	-1.358	71.010	71.7	-0.962
103.096	103.4	-0.294	71.359	71.8	-0.614
102.511	103.5	-0.956	69.779	71.8	-2.815
103.411	103.8	-0.374	69.920	71.9	-2.753
104.729	103.9	0.798	69.277	72.0	-3.781
103.220	104.1	-0.845	68.580	71.9	-4.618
103.738	104.2	-0.443	68.220	71.9	-5.118
102.376	104.2	-1.751	69.070	71.8	-3.802
104.853	104.4	0.433	68.046	71.6	-4.964
104.290	104.5	-0.201	68.732	71.6	-4.005
105.618	104.7	0.877	70.313	71.5	-1.660
103.918	104.8	-0.842	68.318	71.4	-4.316
103.918	105.1	-1.125	68.285	71.3	-4.228
105.111	105.2	-0.084	69.910	71.2	-1.812
105.719	105.4	0.303	68.820	71.0	-3.071
106.012	105.5	0.485	69.234	70.9	-2.350
104.560	105.5	-0.891	68.525	70.6	-2.939
108.309	105.4	2.760	68.623	70.4	-2.524
107.971	105.4	2.439	70.847	70.0	1.210
109.356	105.1	4.049	66.956	69.5	-3.661
112.002	104.6	7.076	68.776	68.8	-0.035
108.872	103.8	4.886	68.972	68.0	1.430
100.417	97.9	2.571	69.179	67.2	2.945
23.857	34.4	-30.648	67.632	65.9	2.627
10.807	10.3	4.925	66.302	64.2	3.274
8.964	8.2	9.319	55.435	55.5	-0.117
7.619	7.0	8.840	16.894	22.1	-23.555
6.255	6.0	4.256	11.946	12.0	-0.451
5.981	5.2	15.012	9.855	10.0	-1.447
Average Difference		1.093	8.501	8.6	-1.157
			7.258	7.6	-4.500
			6.253	6.7	-6.671
			Average Difference		-2.459
Total Average Difference			-0.752		

6.0 MeV Electron Energy, 1.85 x the Original height of the Flattening Filter	
1.5 cm Deep	10.0 cm Deep

Normalised to 100%	Measured Data (%)	Local Percentage Diff. (%)	Normalised to 70.4%	Measured Data (%)	Local Percentage Diff. (%)
100.000	100.0	0.000	70.400	70.4	0.000
100.485	100.1	0.385	70.048	70.3	-0.358
100.857	100.4	0.455	70.514	70.5	0.019
102.177	100.9	1.266	71.967	70.7	1.792
101.681	101.4	0.277	72.069	71.0	1.505
101.873	101.9	-0.027	71.921	71.2	1.013
104.185	102.4	1.743	72.954	71.4	2.177
103.407	102.8	0.590	72.251	71.6	0.909
103.170	103.1	0.068	72.602	71.7	1.259
104.309	103.4	0.879	71.070	71.8	-1.017
101.105	103.5	-2.314	72.682	71.8	1.228
101.241	103.8	-2.465	72.307	71.9	0.566
102.098	103.9	-1.734	72.330	72.0	0.458
103.689	104.1	-0.395	72.512	71.9	0.851
102.211	104.2	-1.909	72.114	71.9	0.298
102.583	104.2	-1.552	71.933	71.8	0.185
101.545	104.4	-2.734	69.560	71.6	-2.849
101.218	104.5	-3.140	70.048	71.6	-2.168
103.948	104.7	-0.718	70.570	71.5	-1.300
103.440	104.8	-1.297	72.398	71.4	1.398
102.685	105.1	-2.298	71.830	71.3	0.744
105.730	105.2	0.504	70.672	71.2	-0.741
104.546	105.4	-0.810	69.469	71.0	-2.156
105.742	105.5	0.229	71.581	70.9	0.960
105.979	105.5	0.454	71.320	70.6	1.019
108.077	105.4	2.540	69.480	70.4	-1.306
107.817	105.4	2.293	71.297	70.0	1.853
107.716	105.1	2.489	69.787	69.5	0.413
110.829	104.6	5.955	72.182	68.8	4.916
110.412	103.8	6.370	71.331	68.0	4.898
100.846	97.9	3.009	72.251	67.2	7.516
23.429	34.4	-31.892	69.866	65.9	6.019
10.842	10.3	5.257	68.708	64.2	7.022
8.613	8.2	5.031	56.390	55.5	1.604
7.172	7.0	2.457	18.074	22.1	-18.217
6.098	6.0	1.636	12.250	12.0	2.082
5.227	5.2	0.525	9.873	10.0	-1.274
Average Difference		-0.240	8.866	8.6	3.088
			8.283	7.6	8.989
			6.586	6.7	-1.703
			Average Difference		0.792
Total Average Difference			0.296		

Table B.2: The percentage differences for various electron energies.

Field Width (10 cm)

Depth (cm)	10	22	28
Measured Data	64.8	32.2	22.7
Electron Energy (MeV)	Monte Carlo Values		
5.0	64.2	31.7	22.2
5.1	64.4	31.9	22.5

5.2	64.7	32.1	22.6
5.3	64.7	32.5	22.8
5.4	64.9	32.5	23.0
5.5	65.2	32.8	23.2
5.6	65.2	32.9	23.4
5.7	65.4	33.1	23.6
5.8	65.8	33.3	23.8
5.9	65.8	33.5	23.8

e^- Energy (MeV)	Local Percentage Difference at Depth (%)			Summation of Differences (%)
	10 cm	22 cm	28 cm	
5.0	-0.926	-1.553	-2.203	-4.681
5.1	-0.617	-0.932	-0.881	-2.430
5.2	-0.154	-0.311	-0.441	-0.905
5.3	-0.154	0.932	0.441	1.218
5.4	0.154	0.932	1.322	2.408
5.5	0.617	1.863	2.203	4.683
5.6	0.617	2.174	3.084	5.875
5.7	0.926	2.795	3.965	7.686
5.8	1.543	3.416	4.846	9.805
5.9	1.543	4.037	4.846	10.426

Field Width (20 cm)

Depth (cm)	10	22	28
Measured Data	68.1	36.5	26.4
Electron Energy (MeV)	Monte Carlo Values		
5.0	67.8	36.4	26.1
5.1	68.2	36.5	26.4
5.2	67.7	36.3	26.4
5.3	67.9	36.5	26.4
5.4	67.9	36.6	26.5
5.5	68.3	36.8	26.9
5.6	68.5	37.0	28.0
5.7	68.7	37.3	27.2
5.8	68.3	37.4	27.2
5.9	68.5	37.3	27.4

e^- Energy (MeV)	Local Percentage Difference at Depth (%)			Summation of Differences (%)
	10 cm	22 cm	28 cm	
5.0	-0.441	-0.274	-1.136	-1.851
5.1	0.147	0.000	0.000	0.147
5.2	-0.587	-0.548	0.000	-1.135
5.3	-0.294	0.000	0.000	-0.294
5.4	-0.294	0.274	0.379	0.359
5.5	0.294	0.822	1.894	3.010
5.6	0.587	1.370	6.061	8.018
5.7	0.881	2.192	3.030	6.103
5.8	0.294	2.466	3.030	5.790
5.9	0.587	2.192	3.788	6.567

Table B.3: The best match for flattening filter at 1.4 x original heights.

5.3 MeV Electron Energy, 1.4 x the Original height of the Flattening Filter					
1.5 cm Deep			10.0 cm Deep		
Normalised to 100%	Measured Data (%)	Local Percentage Diff. (%)	Normalised to 70.4%	Measured Data (%)	Local Percentage Diff. (%)
100.000	100.00	0.000	70.400	70.40	0.000
99.291	100.05	-0.759	70.608	70.35	0.366
98.848	100.30	-1.448	71.023	70.50	0.742
100.342	100.65	-0.306	71.841	70.65	1.685
101.266	101.00	0.263	71.127	70.80	0.462
100.899	101.30	-0.396	71.607	71.00	0.855
101.481	101.90	-0.411	71.983	71.20	1.100
102.165	102.35	-0.181	71.607	71.40	0.290
101.367	102.60	-1.201	72.087	71.50	0.821
102.735	102.95	-0.209	71.854	71.60	0.354
100.987	103.20	-2.144	71.815	71.70	0.160
102.519	103.40	-0.852	71.529	71.85	-0.446
100.658	103.50	-2.746	72.464	71.80	0.924
101.519	103.75	-2.150	71.555	71.90	-0.480
101.810	104.00	-2.105	71.711	72.00	-0.402
101.747	104.05	-2.213	71.763	71.90	-0.191
101.152	104.10	-2.832	71.075	71.90	-1.148
100.823	104.20	-3.241	71.360	71.85	-0.681
100.937	104.20	-3.132	70.088	71.80	-2.384
100.684	104.40	-3.560	71.399	71.65	-0.350
100.937	104.50	-3.410	71.166	71.70	-0.745
101.456	104.55	-2.959	70.452	71.60	-1.603
100.468	104.80	-4.133	70.763	71.50	-1.030
101.671	104.85	-3.032	69.712	71.40	-2.364
101.228	105.10	-3.684	69.959	71.30	-1.881
101.582	105.15	-3.393	68.894	71.25	-3.306
100.962	105.30	-4.120	68.804	71.10	-3.230
100.747	105.40	-4.415	69.608	71.00	-1.960
101.443	105.40	-3.754	69.167	70.80	-2.307
101.203	105.50	-4.073	68.700	70.60	-2.692
101.722	105.40	-3.490	69.206	70.40	-1.696
101.418	105.35	-3.732	68.362	70.05	-2.409
101.291	105.10	-3.624	68.051	69.60	-2.226
101.785	104.80	-2.877	68.336	69.20	-1.248
102.026	104.50	-2.368	67.194	68.50	-1.906
103.241	103.55	-0.298	66.831	67.55	-1.065
94.860	97.90	-3.105	65.935	67.20	-1.882
27.826	46.30	-39.900	68.206	66.15	3.109
10.686	12.20	-12.409	65.027	64.90	0.195
8.353	9.00	-7.189	62.885	62.15	1.183
7.402	7.80	-5.100	38.964	45.90	-15.111
6.601	6.80	-2.929	14.459	18.20	-20.555
5.573	6.00	-7.119	11.527	12.00	-3.942
4.777	5.30	-9.876	10.091	10.25	-1.547
4.282	4.80	-10.801	9.201	9.00	2.234
Average Difference		-4.031	8.063	8.05	0.159

	7.275	7.30	-0.343
	6.488	6.55	-0.941
	5.895	5.90	-0.081
	Average Difference		-1.378
Total Average Difference	-2.648		

Appendix C - Calibration on GafChromic Film using the 6 MV Varian Model

(i) Introduction

The use of a validated model Linac was not limited only to x-ray radiotherapy, it was also used for calibration of GafChromic films that were being employed for proton therapy. This chapter describes the use of the validated Monte Carlo model to derive a beam quality correction factor use in the dosimetry of proton beams. From the IAEA 2000 [197], the formalism in TRS-398 the beam quality correction factor for absorbed dose to water is given as follows:-

$$k_{Q,Q_0} = \frac{(s_{w,air})_Q}{(s_{w,air})_{Q_0}} \frac{(W_{air}/e)_Q}{(W_{air}/e)_{Q_0}} \frac{p_Q}{p_{Q_0}} \qquad \text{Eqn. C.1}$$

where, $s_{w,air}$ = the mass stopping power ratio for water to air,

W_{air}/e = the average energy required to produce ion pair in dry air,

p = a chamber-specific perturbation factor,

Q = proton beam quality and

Q_0 = calibration beam quality.

Similarly, the GafChromic film should be calibrated for beam quality for proton to be used in dosimetry. Analogous to the above formula, the correction factor for GafChromic film is given by:-

$$g_{Q,Q_0} = \frac{(s_{w,film})_Q}{(s_{w,film})_{Q_0}} \frac{G_{Q_0}}{G_Q}$$ Eqn. C.2

where, $s_{w,\,film}$ = the mass stopping power for water and film active layer,

G = the yield of polymerized molecule in mol.J^{-1},

Q = proton beam quality and

Q_0 = photon and secondary electron beam quality from EGSnrc.

The study on GafChromic film was performed by a Birmingham PhD student, Daniel Kirby, whose paper has been published electronically in December 2009 [70], whilst the correction factor was obtained from the spectra of the electron fluence from the modelled Varian linac. This chapter explains briefly the research involving the GafChromic film calibration using linac head model whose dosimetry had been verified in this thesis. The whole proton dosimetry project is not discussed, as proton dosimetry is out of the scope of this thesis.

(ii) Methods

The verified 6 MV Varian linac model was used to find the electron fluence at 10 cm deep in water phantom. The DOSRZnrc code was used and the FLURZnrc option was chosen to obtain the spectrum of the electron fluence (figure C.1). The FLURZnrc user code is capable of computing fluence of various particles for instance, electron, photon, positron, etc in a cylindrical (RZ) geometry [159].

The fluence averaged over the volume calculated by FLURZnrc is equivalent to the total path length divide by the volume and is scored in different energy bins [159]. However, only the electron spectrum against energy was needed for the correction factor of the GafChromic film to be calculated.

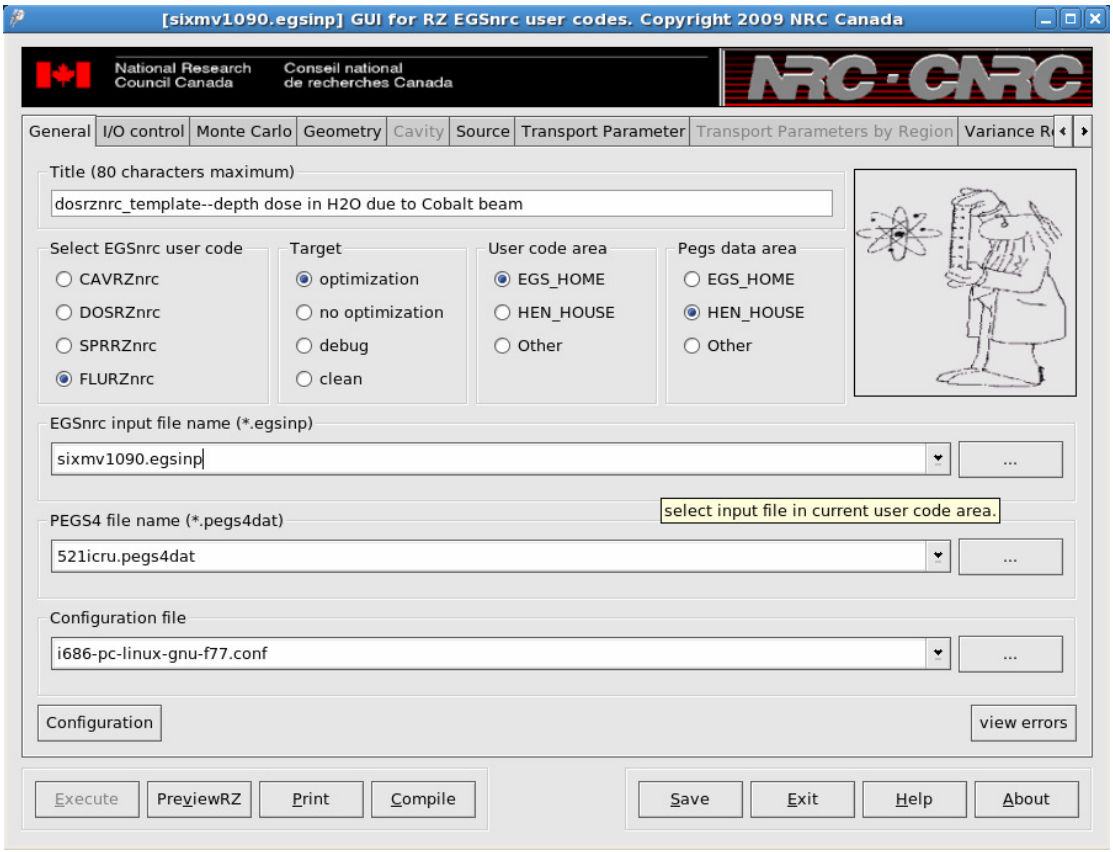

Figure C.1: FLURZnrc user code graphical user interface.

(iii) Results

The electron spectra which is the electron fluence plotted against energy is shown below in figure C.2. From here, the values were combined with the values from ICRU stopping powers (figure C.3) for each depth of measurement to obtain the average value for the film correction factor in Eqn. C.2.

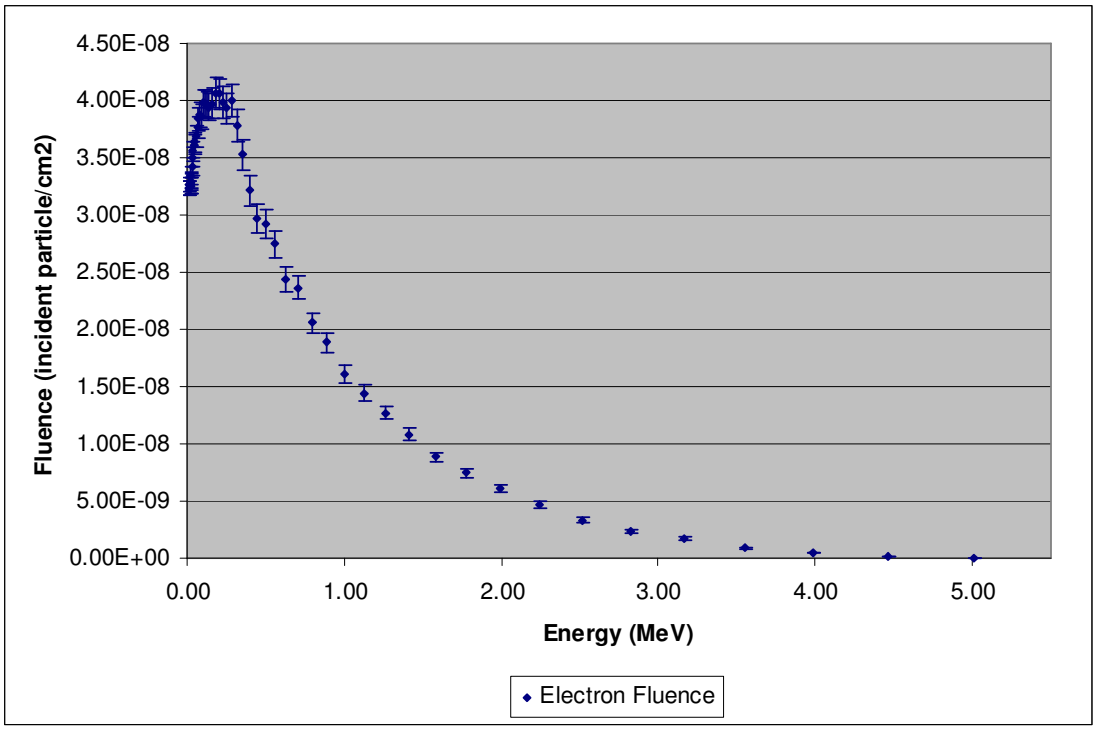

Figure C.2: The electron fluence plot using FLURZnrc for 6 MV Varian at 10 cm deep at 10 cm field width and 90 cm SSD.

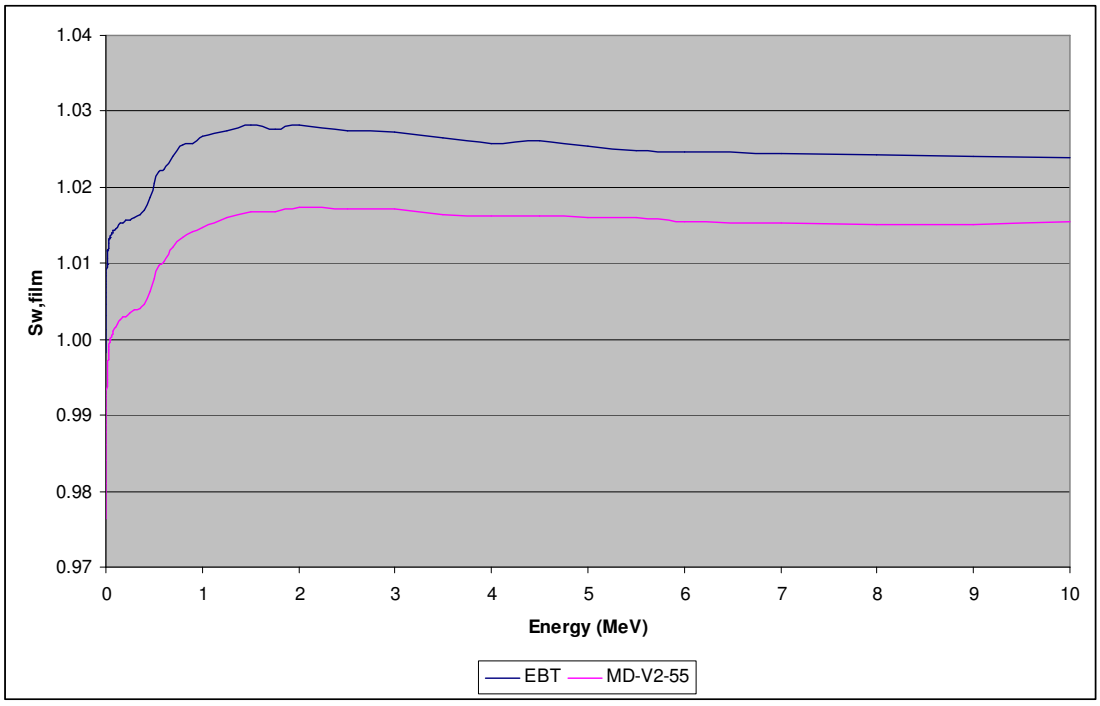

Figure C.3: Stopping power ratio for water to film for two different GafChromic films. *Courtesy of D. Kirby*.

Since this work has more to do with proton dosimetry, the final result for the correction factor was not shown here.

(iv) Discussion

The use of Monte Carlo calculations is not limited to photon dosimetry but encompasses other work such as proton therapy. It is shown here that the linac modelled was used to calibrate the beam quality of GafChromic films. In order to get the correction factor, the average mass stopping power ratio of water to film active layer is required.

This is where the role of the validated model of the 6 MV Varian linac comes into play, hence leading to the quantification of the absolute dose response with respect to proton energy. However, further discussions of the project are beyond the scope of this thesis.

Appendix D - Elekta Linac Specifications

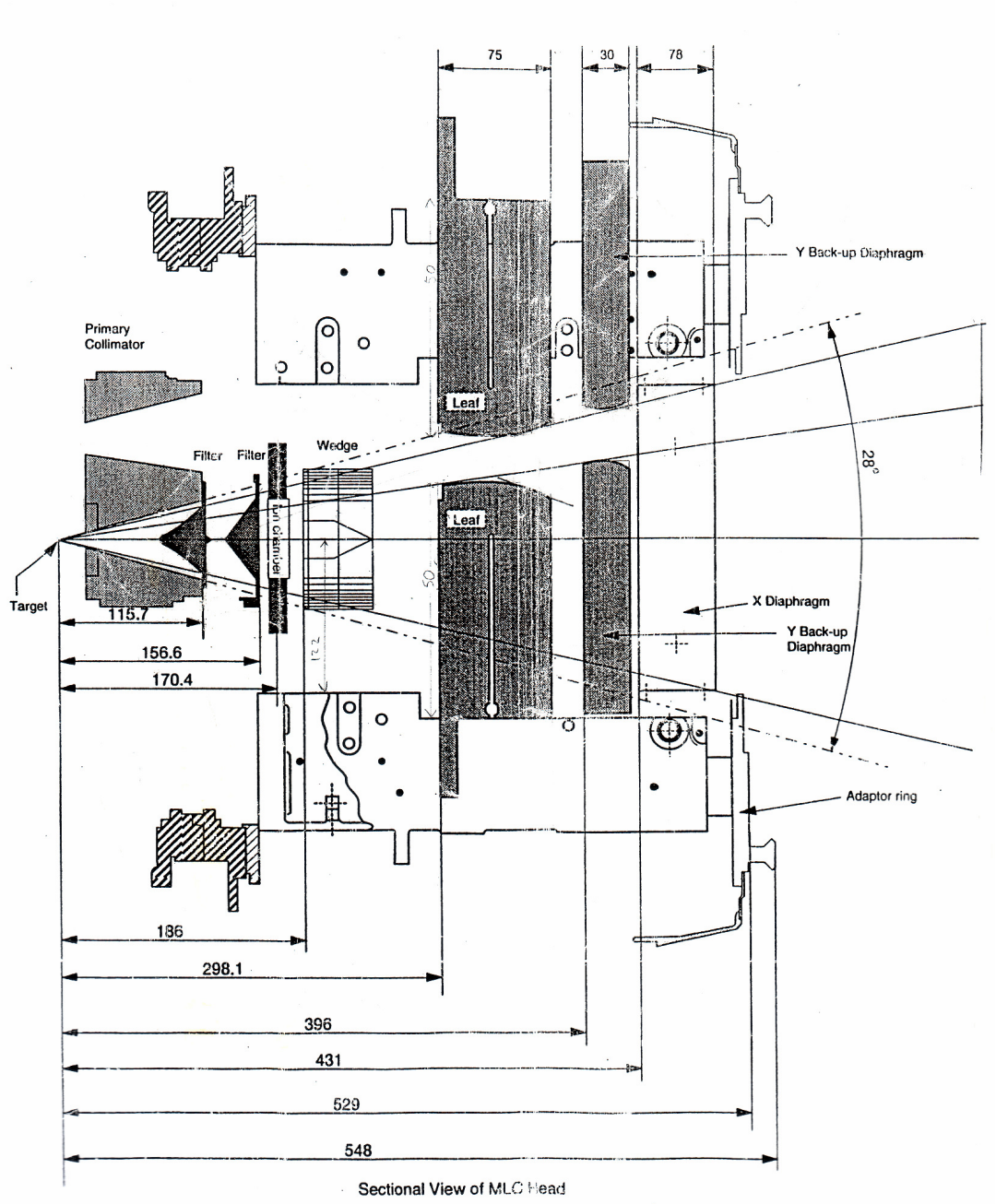

Figure D.1: Cross-sectional view of Elekta Precise treatment head. *Courtesy of Queen Elizabeth Hospital, Birmingham.*

Appendix E - Varian Linac Specifications

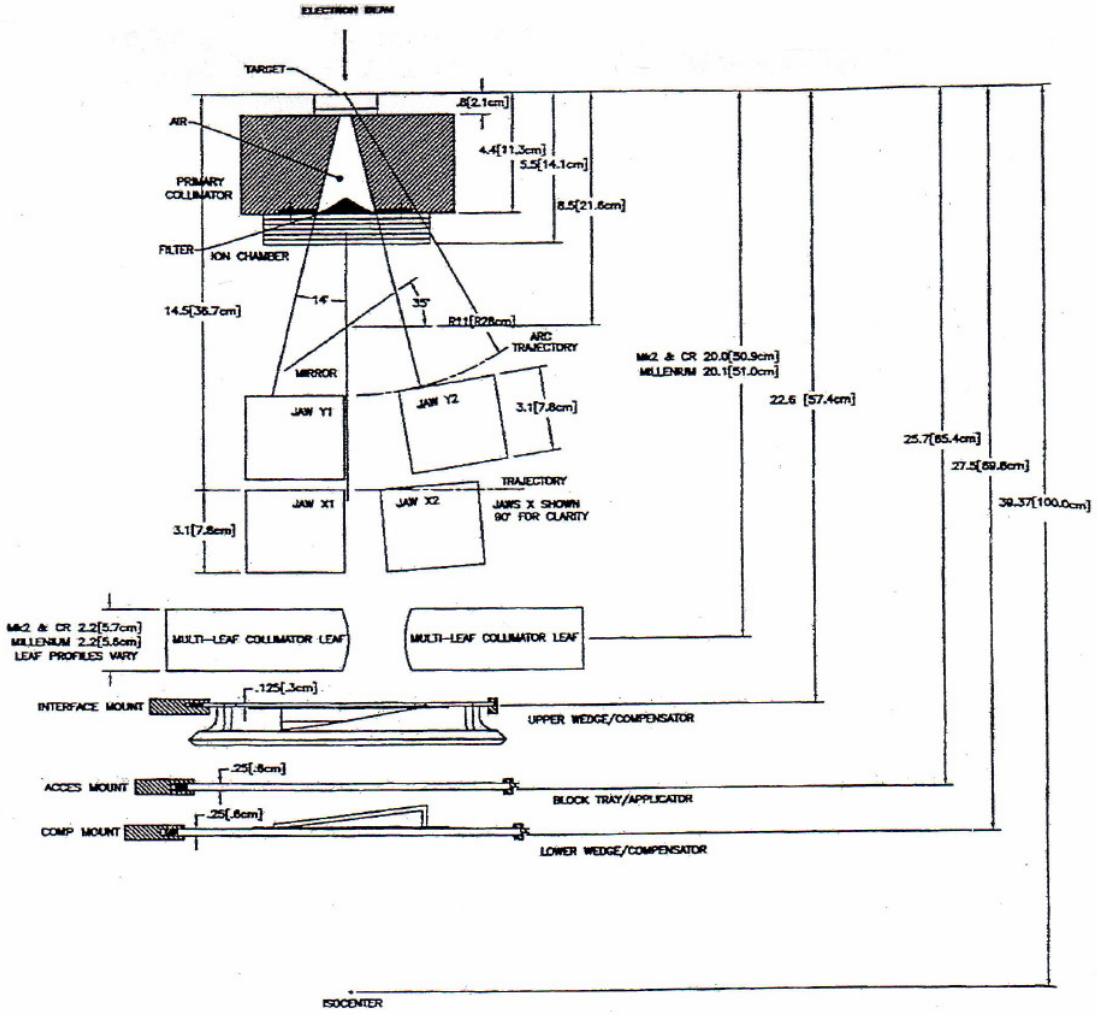

Figure E.1: Cross-sectional view of Varian 600C treatment head. *Courtesy of Queen Elizabeth Hospital, Birmingham.*

List of References

[1] Z. H. Cho, J. P. Jones and M. Singh, *Foundation of Medical Imaging* (New York: John Wiley & Sons, 1993)

[2] Z. Yin, *Solid State Detectors in Radiotherapy Dosimetry*, PhD Thesis (The University of Birmingham, 2003).

[3] F. Saeedi, *High Resolution Dosimetry in Radiation Oncology*, PhD Thesis (The University of Birmingham, 2009).

[4] http://www2.hkedcity.net/sch_files/a/tcs/tcs-phy/public_html/images/roentgen.jpg

[5] http://en.wikipedia.org/wiki/File:Roentgen-x-ray-1896-01-23.jpg

[6] http://en.wikipedia.org/wiki/Wilhelm_Conrad_R%C3%B6ntgen

[7] http://healthcare.utah.edu/radiology/images/CT-Scan-showing-lungs-and-a.jpg

[8] http://www.mgh.org/press/ct_scan_ico2.jpg

[9] http://www.healthcastle.com/radiotherapy.shtml

[10] http://en.wikipedia.org/wiki/Radiotherapy

[11] S. Falk, *Principles of cancer treatment by radiotherapy,* Surgery (Oxford) Volume 27, Issue 4, pp. 169 - 172 (April 2009).

[12] D. Greene, *Linear accelerators for radiation therapy*, Medical Physics Handbooks (IOP Publishing, Bristol, 1986).

[13] A. R. Smith, *Radiation Therapy Physics* (Springer, Berlin, 1995).

[14] S. Webb, *The Physics of Three-Dimensional Radiation Therapy: Conformal radiotherapy, Radiosurgery and Treatment Planning* (Institute of Physics Publishing, Bristol, 1993).

[15] R. P. Hugtenburg, *Medical Radiation Physics: The Physics of Radiotherapy*, Lecture Notes, University Hospital Birmingham.

[16] ICRP Publication 42, *A compilation of the major concepts and quantities in use by ICRP* (1984).

[17] ICRP publication 44, *Protection of the patient in Radiation Therapy* (1985).

[18] ICRU Report 24, *Determination of absorbed Dose in a Patient Irradiated by Beams of X or Gamma rays in Radiotherapy Procedures* (Washington, DC: ICRU Publications, 1976).

[19] M. M. Urie, M. Goiten, K. Doppke, K. G. Kutcher, T. Lo Sasso, R. Mohan, J. E. Munzenrider, M. Sontag and J. W. Wong, *The Role of Uncertainty Analysis in Treatment Planning,* Int. J. Rad. Oncol. Biol. Phys., 21, 91 - 107 (1991).

[20] D. P. Dearnaley, V. S. Khoo, A. R. Norman, L. Meyer, A. Nahum, D. Tait, J. Yarnold and A. Horwich, *Comparison of radiation side-effects of conformal and conventional radiotherapy in prostate cancer: a randomised trial*, The Lancet, 353, 267 - 272 (1999).

[21] M. W. Skwarchuk, A. Jackson, M. J. Zelefsky, E. S. Venkatraman, D. M. Cowen, S. Levegrün, C. M. Burman, Z. Fuks, S. A. Leibel and C. C. Ling, *Late rectal toxicity after conformal radiotherapy of prostate cancer (I): multivariate analysis and dose–response*. International Journal of Radiation Oncology * Biology * Physics, Volume 47, Issue 1, pp. 103 - 113 (1 April 2000).

[22] M. Hillbrand, D. Georg, H. Gadner, R. Pötter and K. Dieckmann, *Abdominal cancer during early childhood: A dosimetric comparison of proton beams to standard and advanced photon radiotherapy,* Radiotherapy and Oncology, Volume 89, Issue 2, pp. 141 - 149 (November 2008).

[23] J. L. Bedford and G. S. Shentall, *A digital method for computing target margins in radiotherapy,* Med. Phys., Volume 25, Issue 2, pp. 224 - 231 (February 1998).

[24] H. D. Kubo, R. B. Wilder and C. T. E. Pappas, *Impact of collimator leaf width on stereotactic radiosurgery and 3D conformal radiotherapy treatment plans,* International Journal of Radiation Oncology * Biology * Physics Volume 44, Issue 4, pp. 937 - 945 (1 July 1999).

[25] S. Webb, *Contemporary IMRT Developing Physics and Clinical Implementation* (Institute of Physics Publishing, 2005).

[26] Intensity Modulated Radiation Therapy Collaborative Working Group, *Intensity-modulated radiotherapy: Current status and issues of interest,* Int. J. Radiation Oncology Biol. Phys., Vol. 51, No. 4, pp. 880 - 914 (2001).

[27] S. S. Donaldson, A. L. Boyer and W. R. Hendee, *New methods for precision radiation therapy exceed biological and clinical knowledge and institutional resources needed for implementation*, Med. Phys., 27, 2477 - 2479 (2000).

[28] B. R. Paliwal, I. A. Brezovich and W. R. Hendee, *IMRT may be used to excess because of its higher reimbursement from Medicare*, Med. Phys., 31, 1 - 3 (2004).

[29] A. Boyer, *Clinical implementation of IMRT*, Med. Phys., 28, 1222 (2001).

[30] M. T. Gillin, *Socio-economic issues of IMRT in IMRT - the state of the art: AAPM Medical Physics Monograph Number 29 ed. J R Palta and T R Mackie,* pp. 829 - 841 (Madison, WI: Medical Physics Publishing, 2003).

[31] L. Potters, M. Steinberg, P. Wallner and J. Hevezi, *How one defines intensity-modulated radiation therapy*, Int. J. Radiat. Oncol. Biol. Phys., 56, 609 - 610 (2003).

[32] F. A. Vicini, M. Sharpe, L. Kestin, J. Wong, V. Remouchamps and A. Martinez, *The use of intensity modulated radiation therapy in the treatment of breast cancer: evolving definition, misdirected criticism, and untoward effects*, Int. J. Radiat. Oncol. Biol. Phys., 58, 1642 - 1644 (2004).

[33] J. A. Purdy and J. M. Michalski, *Does the evidence support the enthusiasm over 3D conformal radiation therapy and dose escalation in the treatment of prostate cancer?,* Int. J. Radiat. Oncol. Biol. Phys., 51, 867 - 870 (2001).

[34] A. Pollack, G. K. Zagars, L. G. Smith, J. Lee, A. C. von Eschenbach, J. A. Antotak, G. Starkschall and I. Rosen, *Preliminary results of a randomized radiotherapy dose escalation study comparing 70 Gy with 78 Gy for prostate cancer*, J. Clin. Oncol., 18, 3904 - 3911 (2000).

[35] A. Pollack, G. K. Zagars, G. Starkshall, J. A. Antotak, J. Lee, E. Huang, A. C. von Eschenbach, D. A. Kuban and I. Rosen, *Prostate cancer radiation dose response: results of the M D Anderson Phase-3 trial*, Int. J. Radiat. Oncol. Biol. Phys., 53, 1097 - 1105 (2002).

[36] A. Pollack and R. A. Price, *IMRT for prostate cancer In: J.R. Palta and T.R. Mackie, Editors, Intensity-modulated radiation therapy: The state of the art: AAPM Monograph No. 29*, pp. 617 - 630. (Madison, WI: Medical Physics Publishing, 2003).

[37] J. Ryu, K. Winer, J. Michalski, J. A. Purdy, A. M. Markoe, J. D. Earle, C. A. Perz, M. Roach, H. M. Sandler, A. Pollack and J. D. Cox, *Interim report of toxicity from 3D conformal radiation therapy for prostate cancer on 3DOG/RTOG 9406, Level III (79.2Gy),* International Journal of Radiation Oncology * Biology * Physics, 54, 4, pp. 1036 - 1046 (15 November 2002).

[38] S. H. Levitt and F. M. Khan, *In regard to Purdy J. A., Michalski J. M. Does the evidence support the enthusiasm over 3D conformal radiation therapy and dose escalation in the treatment of prostate cancer?* Int J Radiat Oncol Biol Phys 2001; 51: 867 - 870, Int. J. Radiat. Oncol. Biol. Phys., 53, 4, p. 1085 (2002).

[39] R. J. Schulz, J. A. Deye and W. R. Hendee, *Through the preoccupation with new technical developments, physicists have lost sight of the realities of cancer care and statistics*, Med. Phys., 28, 2185 - 2187 (2001).

[40] R. J. Schulz and A. R. Kagan, *On the role of intensity modulated radiation therapy in radiation oncology*, Med. Phys., 29, 1473 - 1480 (2002).

[41] R. J. Schulz and A. R. Kagan, *Commentry on IMRT and cancer of the prostate*, Int. J. Radiat. Oncol. Biol. Phys., 55, 851 - 852 (2003).

[42] R. J. Schulz and A. R. Kagan, *More precisely defined dose distributions are unlikely to affect cancer mortality*, Med. Phys., 30, 276 (2003).

[43] B. D. Kavanagh, *The emperor's new isodose curves*, Med. Phys., 30, 2259 - 2260 (2003).

[44] S. Manolopoulos, C. Wojnecki, R. Hugtenburg, M. A. Jaafar Sidek, G. Chalmers, G. Heyes and S. Green, *Small field measurements with a novel silicon position sensitive diode array,* Phys. Med. Biol., 54, 485 - 495 (2009).

[45] ICRU Report 35, *Radiation Dosimetry: Electron beams with energies between 1 and 50 MeV*, (ICRU, Washington D.C., 1984).

[46] G. Rikner and E. Grusell, *Effects of radiation damage on p-type silicon detectors*, Phys. Med. Biol., 28: 1261 - 1267 (1983).

[47] G. Rikner and E. Grusell, *Selective shielding of a p-Si detector for quality independence*, Acta Radiol. Oncol. 24, 65 - 69 (1985)

[48] E. Grusell and G. Rikner, *Linearity with dose rate of low resistivity p-type silicon semiconductor detectors*, Phys. Med. Biol., 38, pp. 785 - 792 (1993).

[49] S. M. Vatnitsky and H. Järvinen, *Application of a natural diamond detector for the measurement of relative dose distributions in radiotherapy,* Phys. Med. Biol., 38, pp. 172 - 184 (1993).

[50] P. W. Hoban, M. Heydarian, W. A. Beckham and A. H. Beddoe, *Dose rate dependence of a PTW diamond detector in the dosimetry of a 6 MV Photon beam*, Phys. Med. Biol., 39, pp. 1219 - 1229 (1994).

[51] W. U. Laub, T. W. Kaulich and F. Nüsslin, *Energy and dose rate dependence of a diamond detector in the dosimetry of 4-25 MV photon beams,* Med. Phys., 24, 535 - 536 (1997).

[52] W. U. Laub, T. W. Kaulich and F. Nüsslin, *A diamond detector in the dosimetry of high-energy electron and photon beams*, Phy. Med. Biol., 44, 2183 - 2192 (1999).

[53] A. Fidanzio, L. Azario, R. Miceli, A. Russo and A. Piermattei, *PTW-diamond detector: dose rate and particle type dependence,* Med. Phys., 27, pp. 2589 - 2593 (2000).

[54] C. Martens, C. De Wagter and W. De Neve, *The value of the PinPoint ion chamber for characterization of small field segments used in intensity-modulated radiotherapy*, Phys. Med. Biol., 45, 2519 - 2530 (2000).

[55] http://www.esrf.eu/events/conferences/IWORID7/FinalProgramme/redondo_1.pdf

[56] I. Redondo-Fernández, C. Buttar, S. Walsh, S. Manolopoulos, J. M. Homer, S. Young and J. Conway, *ΔOSI: a prototype microstrip dosimeter for characterisation of medical radiotherapy and radiosurgery systems,* Nuclear Instruments and Methods in Physics Research Section A, 563: 229 - 232 (2006).

[57] S. Manolopoulos, C. Buttar, M. Homer, S. Martin, I. Redondo-Fernandez, S. Walsh, S. Young and J. Conway, *ΔOSI: a prototype microstrip dosimeter for characterisation of medical radiotherapy and radiosurgery systems,* Nuclear Science Symposium Conference Record, 2005. IEEE Publication. Volume: 5, 2927 - 2930 (2005).

[58] A. L. Boyer and E. C. Mok, *In: Cunningham, J.R., Ragan, D., Van Dyk, J. (Eds.), Proceedings of the Eighth International Conference in Radiation Therapy,* p. 14 (Toronto. IEEE Computer Society, Toronto, 1984).

[59] T. R. Mackie, J. W. Scrimger and J. J. Battista, *A convolution method of calculating dose for 15-MV X-rays*, Med. Phys., 12, pp. 188 - 196 (1985).

[60] C. S. Chui, *A method for three-dimensional gamma-ray dose calculations in heterogeneous media and its applications in radiation therapy*. (Ph.D. Thesis, University of Columbia 1985).

[61] A. Ahnesjö, *Collapsed cone convolution of radiant energy for photon dose calculations in heterogeneous media*, Med. Phys., 16, pp. 577 - 592 (1989).

[62] N. Reynaert, S. C. van der Marck, D. R. Schaart, W. Van der Zee, C. Van Vliet-Vroegindeweij, M. Tomsej, J. Jansen, B. Heijmen, M. Coghe and C. De Wagter, *Monte Carlo treatment planning for photon and electron beams*, Radiation Physics and Chemistry, Volume 76, Issue 4, pp. 643 - 686 (April 2007).

[63] A. J. D. Scott, A. E. Nahum, and J. D. Fenwick, *Using a Monte Carlo model to predict dosimetric properties of small radiotherapy photon fields,* Med. Phys., 35, 4671 - 684 (2008).

[64] Z. Yin, R. P. Hugtenburg and A. H. Beddoe, *Response corrections for solid-state detectors in megavoltage photon dosimetry*, Phys. Med. Biol., 49, 3691 - 3702 (2004).

[65] M. K. Fix, P. J. Keall, K. Dawson, and J. V. Siebers, *Monte Carlo source model for photon beam radiotherapy: photon source characteristics,* Med. Phys., 31, pp. 3106 - 3121 (2004).

[66] P. Mobit, G. Sandison, *A Monte Carlo based development of a cavity theory for solid state detectors irradiated in electron beams,* Radiat. Prot. Dosimetry, 101 (1-4): 427 - 429 (2002).

[67] Z. Yin, R. P. Hugtenburg and A. H. Beddoe, *Response of silicon diode dosemeters to scattered radiation from megavoltage photon beams,* Radiation Protection Dosimetry, 101, 415 - 418 (2002).

[68] S. Stathakis, C. Esquivel, A. Gutierrez, C. R. Buckey and N. Papanikolaou, *Treatment planning and delivery of IMRT using 6 and 18 MV photon beams without flattening filter,* Appl. Radiat. Isot., 67, 1629 - 1637 (2009).

[69] W. Fu, J. Dai, Y. Hu, D. Han and Y. Song, *Delivery time comparison for intensity-modulated radiation therapy with/without flattening filter: a planning study,* Phys. Med. Biol., 49, 1535 - 1547 (2004).

[70] D. Kirby, S. Green, H. Palmans, R. Hugtenburg, C. Wojnecki and D. Parker, *LET dependence of GafChromic films and an ion chamber in low-energy proton dosimetry,* Phys. Med. Biol., 55, 417 - 433 (2010)

[71] ICRU Report 33, *Radiation Quantities and Units*, International Commission on Radiation Units and Measurements (Bethesda, Maryland, 1980).

[72] F. H. Attix, *Introduction to Radiological Physics and Radiation Dosimetry,* (Wiley, New York, 1986).

[73] G. F. Knoll, *Radiation Detection and Measurement*, John Wiley & Sons, third edition (2000).

[74] F. M. Khan, *The physics of radiation therapy*, Williams and Wilkins, Baltimore (1994).

[75] A. Konefał, A. Orlef, M. Dybek, Z. Maniakowski, K. Polaczek-Grelik and W. Zipper, *Correlation between radioactivity induced inside the treatment room and the undesirable thermal/resonance neutron radiation produced by linac*, Physica Medica, Volume 24, Issue 4, pp. 212 - 218 (December 2008).

[76] M. J. Berger and S. M. Seltzer, *Tables of Energy Losses and Ranges of Electrons and Positrons*, NASA SP - 3012, (Washington DC, 1964).

[77] E. B. Podgorsak, *Radiation Oncology Physics: A Handbook for Teachers and Students,* International Atomic Energy Agency (Vienna, 2005).

[78] H. A. Bethe and L. C. Maximon, *Theory of Bremsstrahlung and Pair Production. I. Differential Cross Section*, Phys. Rev., 93, 768 - 784 (1954).

[79] S. M. Seltzer, M. J. Berger, *Bremsstrahlung spectra from electron interactions with screened atomic nuclei and orbital electrons*, Nuclear Instruments and Methods in Physics Research Section B: Beam Interactions with Materials and Atoms, Volume 12, Issue 1, pp. 95 - 134 (August 1985).

[80] D. Baltas, L. Sakelliou and N. Zamboglou, *The Physics of Modern Brachytherapy for Oncology* (CRC Press, 2007).

[81] J. H. Hubbell, *Review of photon interaction cross section data in the medical and biological context*, Phys. Med. Biol., 44, pp. R1 - R22 (1999).

[82] J. H. Hubbell, *Photon mass attenuation and energy-absorption coefficients from 1 keV to 20 MeV*, Int. J. Appl. Radiat. Isot., 33, pp. 1269 - 1290 (1982).

[83] L. Wang and D. Jette, *Photon dose calculation based on electron multiple-scattering theory: Primary dose deposition kernels*, Med. Phys., Volume 26, Issue 8, pp. 1454 - 1465 (August 1999).

[84] R. P. Hugtenburg and M. Tiffany, *Solid-state detectors in radiotherapy: Diamond Detectors*, Lecture Notes, University Hospital Birmingham.

[85] U. Fano, *Note on the Bragg-Gray cavity principle for measuring energy dissipation*, Radiation Res. 1237 - 1240 (1954).

[86] F. Saeedi, Z. Yin and R. P. Hugtenburg, *Dosimetry in conditions of electron disequilibrium,* Radiation Physics and Chemistry, 71, 979 - 980 (2004).

[87] C-M. Ma and A. E. Nahum, *Bragg–Gray theory and ion chamber dosimetry for photon beams,* Phys. Med. Biol., 36, 413 - 428 (1991).

[88] A. E. Nahum, *Perturbation effects in dosimetry: part 1. Kilovoltage x-rays and electrons*, Phys. Med. Biol., 41, 1531 - 1580 (1996).

[89] W. H. Bragg, Consequences of the corpuscular hypothesis of the γ and x-rays, and the ranges of β rays, Phil. Mag. 20, 385 - 416 (1910).

[90] W. H. Bragg, *Studies in Radioactivity*, Mac. & Co. Ltd. (London 1912).

[91] L. H. Gray, *The Absorption of Penetrating Radiation,* Proceedings of the Royal Society of London. Series A, Containing Papers of a Mathematical and Physical Character, Vol. 122, No. 790, pp. 647 - 668 (Feb. 1, 1929).

[92] L. H. Gray, *An Ionization Method for the Absolute Measurement of γ - Ray Energy*, Proceedings of the Royal Society of London. Series A, Mathematical and Physical Sciences, Vol. 156, No. 889, pp. 578 - 596 (Sep. 1, 1936).

[93] G. C. Laurence, *The measurement of extra hard x-rays and gamma rays in roentgens,* Can. J. Res., 15, 67 (1937).

[94] F. H. Attix, W. C. Roesch, E. Tochilin, *Radiation Dosimetry.* Academic Press, II: 274 (New York, 1966).

[95] J. Borg, I. Kawrakow, D. W. O. Rogers and J. P. Seuntjens, *Monte Carlo study of correction factors for Spencer–Attix cavity theory at photon energies at or above 100 keV*, Med. Phys. Volume 27, Issue 8, pp. 1804 - 1813 (August, 2000).

[96] T. E. Burlin, *A General Theory of Cavity Ionisation*, British Journal of Radiology 39, 727 - 734 (1966).

[97] P. N. Mobit, P. Maylesy and A. E. Nahum, *The quality dependence of LiF TLD in megavoltage photon beams: Monte Carlo simulation and experiments,* Phys. Med. Biol., 41, 387 - 398 (1996).

[98] A. S. Beddar, T. M. Briere, F. A. Mourtada, O. N. Vassiliev, H. H. Liu and R. Mohan, *Monte Carlo calculations of the absorbed dose and energy dependence of plastic scintillators,* Med. Phys., 32, 5 (May 2005).

[99] K. R. Kase, B. E. Bjarngard, and F. H. Attix, *The dosimetry of ionizing radiation*, volume II (Academic Press, Ltd., London, 1987).

[100] H. O. Wyckoff and F. H. Attix, *Design of free-air ionization chambers*, Technical Report 64, 1 - 16, NBS Hanb. (U.S., 1969).

[101] http://www.atnuke.com/nuclear/INSTRUMENTATION/ptw/ionizationchambers.htm

[102] ICRU Report 37, *Stopping Powers for Electrons and Positrons,* (Washington, DC: ICRU publications, 1984).

[103] M. Boutillon, *Volume recombination parameter in ionization chambers,* Phys. Med Biol., 43: 2061 - 2072 (1998).

[104] National Bureau of Standards United States Department of Commerce, *Clinical dosimetry: recommendations of the international commission on radiological units and measurements*, handbook 87 (1962).

[105] ICRU Report 23, *Measurements of absorbed dose in a phantom irradiated by a single beam of X or Gamma rays*, (Washington, DC: ICRU publications, 1973).

[106] http://www.imagingequipment.co.uk/pdf/RO2p10.pdf

[107] http://www.harpell.ca/manufacturer/ptw/pinpoint-chamber-type-31014

[108] http://www.rpdinc.com/html/ptw_pinpoint_chamber.html

[109] E. A. Burgemeister, *Dosimetry with a diamond operating as a resistor,* Phys. Med. Biol., 26, 2, 269 - 275 (1981).

[110] R. J. Keddy, T. L. Nam and R. C. Burns, *Synthetic diamonds as ionisation chamber radiation detectors in biological environments,* Phys. Med. Biol., 32, 6, 751 - 759 (1987).

[111] J. F. Fowler, *Solid state electrical conductivity detectors in radiation dosimetry*, ed. F. H. Attix and W. C. Roesch, Radiation Dosimetry: Instrumentation, Vol 2, pp. 291 - 324 (New York: Academic, 1966).

[112] B. Planskoy, *Evaluation of diamond radiation dosemeters,* Phys. Med. Biol., 25, 3, 519 - 532 (1980).

[113] W. U. Laub, *Comparison of TG-43 dose calculations to pinpoint ion chamber and diamond detector measurements,* Phys. Med. Biol., 47, N315 - N318 (2002).

[114] T. Nakano, N. Suchowerska, M. M. Bilek, D. R. McKenzie, N. Ng and T. Kron, *High dose-rate brachytherapy source localization: positional resolution using diamond detector,* Phys. Med. Biol., 48, 2133 - 2146 (2003).

[115] M. Sakama, T. Kanai, Y. Kase, M. Komori, A. Fukumura and T. Kohno, *Responses of a diamond detector to high-LET charged particles,* Phys. Med. Biol., 50, 2275 - 2289 (2005).

[116] R. P. Hugtenburg, K. Johnston, G. J. Chalmers and A. H. Beddoe, *Application of diamond detectors to the dosimetry of 45 and 100 kVp therapy beams: comparison with a parallel-plate ionization chamber and Monte Carlo,* Phys. Med. Biol., 46, 2489 - 2501 (2001).

[117] Z. Yin, R. P. Hugtenburg, S. Green and A. H. Beddoe, *Dose responses of diamond detectors to monoenergetic x-rays*, Nuclear Instruments and Methods in Physics Research Section B: Beam Interactions with Materials and Atoms, Volume 213, pp. 646 - 649 (January, 2004).

[118] D. V. Cormack and H. E. Johns, *Spectral distribution of scattered radiation from a kilocurie cobalt 60 unit,* Br. J. Radiol., 31, 497 - 502 (1958).

[119] P. Metcalfe, T. Kron and P. Hoban, *The Physics of Radiotherapy X-rays from Linear Accelerators*, Medical Physics Publishing (Madison, WI, 1997).

[120] K. N. G. Rajan, *Advanced medical radiation dosimetry,* New Delhi: Prentice-Hall of India (1992).

[121] K. R. Kase and G. K. Svensson, *Head scatter data for several linear accelerators (4–18 MV),* Med. Phys., 13, 530 - 532 (1986).

[122] S. A. Johnsson, C. P. Ceberg, T. Knöös, and P. Nilsson, *Transmission measurements in air using the ESTRO mini-phantom,* Phys. Med. Biol., 44, 2445 - 2450 (1999).

[123] P. Huang, J. Chu and B. Bjärngard, *The effect of collimator backscatter radiation on photon output of linear accelerators,* Med. Phys., 14, 268 - 269 (1987).

[124] H. Kubo, *Telescopic measurements of backscattered radiation from secondary collimator jaws to a beam monitor chamber using a pair of slits,* Med. Phys., 16, 295 - 298 (1989).

[125] H. Kubo and K. K. Lo, *Measurement of backscattered radiation from Therac-20 collimator and trimmer jaws into beam monitor chamber,* Med. Phys., 16, 292 - 294 (1989).

[126] http://www.varian.com/media/oncology/products/clinac/images/Clinac_D-Series_DHX_Illus.jpg

[127] P. Munro and J. A. Rawlinson, *Therapy imaging: Source sizes of radiotherapy beams,* Med. Phys., 15, 517 - 524 (1988).

[128] N. Metropolis, *The beginning of the Monte Carlo method*, Los Alamos Science (1987 Special Issue dedicated to Stanislaw Ulam): pp. 125 - 130 (1987).

[129] A. F. Bielajew, *Fundamentals of the Monte Carlo method for neutral and charged particle transport* (The University of Michigan, 2001).

[130] E. Heath and J. Seuntjens, *Development and validation of BEAMnrc component module for accurate Monte Carlo modelling of Varian dynamic Millennium multileaf collimator,* Medical Physics Unit, Mcgill University, Canada (August 2003).

[131] N. Reynaert, S. C. van der Marck, D. R. Schaart, W. Van der Zee, C. Van Vliet-Vroegindeweij, M. Tomsej, J. Jansen, B. Heijmen, M. Coghe and C. De Wagter, *Review - Monte Carlo treatment planning for photon and electron beams,* Radiation Physics and Chemistry, 76, pp. 643 - 686 (2007).

[132] S. Y. Jang, O. N. Vassiliev, H. H. Liu, R. Mohan and J. V. Siebers, *Development and commissioning of a multileaf collimator model in Monte Carlo dose calculations for intensity-modulated radiation therapy,* Med. Phys., 33 (3) pp. 770 - 781 (2006).

[133] G. Jarry and F. Verhaegen, *MO-D-224A-05: In-vivo dosimetry using electronic portal imaging and monte carlo techniques,* Medical Physics, 33 (6) 2167 (2006).

[134] I. B. Mihaylov, F. A. lerma, Y. Wu and J. V. Siebers, *Analytic IMRT dose calculations utilizing Monte Carlo to predict MLC fluence modulation,* Med. Phys., 33 (4) 828 - 839 (2006).

[135] W. Abdel-Rahman, J. P. Seuntjens, F. Verhaegen, F. Deblois and E B. Podgorsak, *Validation of Monte Carlo calculated surface doses for megavoltage photon beams,* Medical Physics, 32 (1) pp. 286 - 298 (2005).

[136] W. Abdel-Rahman, J. P. Seuntjens, F. Verhaegen, F. Deblois and E. B. Podgorsak, *Radiation induced currents in parallel plate ionization chambers: Measurement and Monte Carlo simulation for megavoltage photon and electron beams,* Medical Physics, 33 (9) pp. 3094 - 3104 (2006).

[137] K. Al-Yahya, M. Schwartz, G. Shenouda, F. Verhaegen, C. Freeman and J. Seuntjens, *Energy modulated electron therapy using a few leaf electron collimator in combination with IMRT and 3D-CRT: Monte Carlo-based planning and dosimetric evaluation,* Medical Physics, 32 (9) pp. 2976 - 2986 (2005).

[138] G. Jarry, S. A. Graham, D. A. Jaffray, D. J. Moseley and F. Verhaegen, *Scatter correction for kilovoltage cone-beam computed tomography (CBCT) images using Monte Carlo simulations,* Physics of Medical Imaging, 6142, pp. 1634 - 1643 (2006).

[139] E. Poon and F. Verhaegen, *Accuracy of the photon and electron physics in GEANT4 for radiotherapy applications,* Medical Physics, 32 (6) pp. 1696 - 1711 (2005).

[140] E. Poon, J. Seuntjens and F. Verhaegen, *Consistency test of the electron transport algorithm in the GEANT4 Monte Carlo code,* Phys. Med. Biol., 50, pp. 681 - 694 (2005).

[141] J. Seco, E. Adams, M. Bidmead, M. Partridge and F. Verhaegen, *Head-and-neck IMRT treatments assessed with a Monte Carlo dose calculation engine,* Phys. Med. Biol. (50) pp. 817 - 830 (2005).

[142] D. Sheikh-Bagheri and D. W. Rogers, *Monte Carlo calculation of nine megavoltage photon beam spectra using the BEAM code,* Med. Phys., 29, 3, 391 - 402 (2002).

[143] J. V. Siebers, P. J. Keall, J. O. Kim and R. Mohan, *Comparison of EGS4 and MCNP4b Monte Carlo codes for generation of photon phase space distributions for a Varian 2100C,* Phys. Med. Biol., 44, pp. 3009 - 3026 (1999).

[144] R. Mohan, C. Chui and L. Lidofski, *Energy and angular distributions of photons from medical linear accelerators,* Med. Phys., 12, pp. 592 - 597 (1985).

[145] G. X. Ding, *Energy spectra, angular spread, fluence profiles and dose distributions of 6 and 18 MV photon beams: results of Monte Carlo simulations for a Varian 2100EX accelerator,* Phys. Med. Biol., 47, pp. 1025 - 1046 (2002).

[146] E. L. Chaney, T. J. Cullip and T. A. Gabriel, *A Monte Carlo study of accelerator head scatter,* Med. Phys., 21, pp. 1383 - 1390 (1994).

[147] D. Sheikh-Bagheri and D. W. Rogers, *Sensitivity of megavoltage photon beam Monte Carlo simulations to electron beam and other parameters,* Med. Phys., 29, pp. 379 - 390 (2002).

[148] W. van der Zee and J. Welleweerd, *Calculating photon beam characteristics with Monte Carlo techniques,* Med. Phys., 26, pp. 1883 - 1892 (1999).

[149] B. A. Faddegon, P. O'Brien and D. L. D. Mason, *The flatness of Siemens linear accelerator x-ray fields,* Med. Phys., 26, pp. 220 - 228 (1999).

[150] E. Spezi, D. G. Lewis and C. W. Smith, *Monte Carlo simulation and dosimetric verification of radiotherapy beam modifiers,* Phys. Med. Biol., 46, pp. 3007 - 3029 (2001).

[151] I. Kawrakow, E. Mainegra-Hing, D.W.O. Rogers, F. Tessier and B.R.B. Walters, *The EGSnrc Code System: Monte Carlo Simulation of Electron and Photon Transport,* Ionizing Radiation Standards NRC Canada (2009).

[152] W. van der Zee, A. Hogenbirk and S. C. van der Marck, *ORANGE: a Monte Carlo dose engine for radiotherapy,* Phys. Med. Biol., 50, pp. 625 - 641 (2005).

[153] C-M. Ma, P. J. Reckward, M. Holmes, D. W. O. Rogers and B. P. Geiser, *DOSXYZ users manual Technical Report PIRS-0509(B)* (Ottawa: National Research Council of Canada, 1995).

[154] D. W. O. Rogers, B. A. Faddegon, G. X. Ding, C-M. Ma, J. We and T. R. Mackie, *BEAM: a Monte Carlo code to simulate radiotherapy treatment units,* Med. Phys., 22, pp. 503 - 524 (1995).

[155] W. R. Nelson, H. Hirayama and D. W. O. Rogers, *The EGS4 code system Technical Report SLAC Report 265* (Stanford, CA: Stanford Linear Accelerator Center, 1985).

[156] G. Jarry and F. Verhaegen, *Electron beam treatment verification using measured and Monte Carlo predicted portal images,* Phys. Med. Biol., 50, pp. 4977 - 4994 (2005).

[157] M. S. Huq, Y. Yu, Z-P. Chen and N. Suntharalingam, *Dosimetric Characteristics of a commercial multileaf collimator,* Med Phys., 22 (2) (1995).

[158] M. S. Huq, I. J. Das, T. Steinberg and J. M. Galvin, *A dosimetric comparison of various multileaf collimators,* Phys. Med. Biol., 47, N159 - N170 (2002).

[159] D.W.O. Rogers, I. Kawrakow, J.P. Seuntjens, B.R.B. Walters and E. Mainegra-Hing, *NRC User Codes for EGSnrc,* Ionizing Radiation Standards National Research Council of Canada (2003).

[160] E. Mainegra-Hing, *User Manual for egs_inprz, a GUI for the NRC RZ user-codes,* Ionizing Radiation Standards National Research Council of Canada (2005).

[161] B. Walters, I. Kawrakow and D.W.O. Rogers, *DOSXYZnrc Users Manual,* Ionizing Radiation Standards National Research Council of Canada (2009).

[162] http://www.bear.bham.ac.uk/index.shtml

[163] D.W.O. Rogers, B. Walters and I. Kawrakow, *BEAMnrc Users Manual,* Ionizing Radiation Standards National Research Council of Canada (2009).

[164] E. Storm and H. I. Israel, *Photon cross sections from 1 keV to 100 MeV for elements Z=1 to Z=100,* Atomic Data and Nuclear Data Tables, 7, 565 - 681 (1970).

[165] M. K. Fix, P. J. Keall and J. V. Siebers, *Photon-beam subsource sensitivity to the initial electron-beam parameters,* Med. Phys., 32, pp. 1164 - 1175 (2005).

[166] D. W. O. Rogers, *Fifty years of Monte Carlo simulations for medical physics,* Phys. Med. Biol., 51, R287 - R301 (2006).

[167] H. H. Liu, T. R. Mackie and E. C. McCullough, *Modeling photon output caused by backscattered radiation into the monitor chamber from collimator jaws using a Monte Carlo technique*, Med. Phys., Volume 27, Issue 4, pp. 737 - 744 (April 2000).

[168] http://physics.nist.gov/PhysRefData/Star/Text/ESTAR.html

[169] P. N. Mobit, A. E. Nahum and P. Mayles, *An EGS4 Monte Carlo examination of general cavity theory,* Phys. Med. Biol., 42, 1319 - 1334 (1997).

[170] B. Pike, E. B. Podgorsak, T. M. Peters and C. Pla, *Dose distributions in dynamic stereotactic radiosurgery,* Med. Phys., 14, 780 - 789 (1987).

[171] W. U. Laub and T. Wong, *The volume effect of detectors in the dosimetry of small fields used in IMRT,* Med. Phys., 30, 314 - 347 (2003).

[172] M. Heydarian, P. W. Hoban and A. H. Beddoe, *A comparison of dosimetry techniques in stereotactic radiosurgery,* Phys. Med. Biol., 41, 93 - 110 (1996).

[173] R. K. Rice, J. L. Hansen, G. K. Svensson and R. L. Siddon, *Measurements of dose distributions in small beams of 6 MV x-rays,* Phys. Med. Biol., 32, 1087 - 1099 (1987).

[174] I. J. Das, G. X. Ding and A. Ahnesjö, *Small fields: nonequilibrium radiation dosimetry,* Med. Phys., 35, 206 - 215 (2008).

[175] E. Pappas, I. Seimenis, A. Angelopoulos, P. Georgolopoulou, M. Kamariotaki-Paparigopoulou, T. Maris, L. Sakelliou, P. Sandilos and L. Vlachos, *Narrow stereotactic beam profile measurements using N-vinylpyrrolidone based polymer gels and magnetic resonance imaging,* Phys. Med. Biol., 46, 783 - 797 (2001).

[176] G. Arcovito, A. Piermattei, G. D'Abramo and F. A. Bassi, *Dose measurements and calculations of small radiation fields for 9-MV x rays,* Med. Phys., 12, 779 - 784 (1985).

[177] E. B. Podgorsak, A. Oliver, M. Pla, P. Y. Lefebvre and J. Hazel, *Dynamic stereotacric radiosurgery,* Int. J. Radiat. Oncol., 14, 115 - 126 (1988).

[178] A. S. Beddar, D. J. Mason and P. F. O'Brien, *Absorbed dose perturbation caused by diodes for small field photon dosimetry,* Med. Phys., 21, 1075 - 1079 (1994).

[179] C. McKerracher and D. I. Thwaites, *Assessment of new small-field detectors against standard-field detectors for practical stereotactic beam data acquisition,* Phys. Med. Biol., 44, 2143 - 2160 (1999).

[180] P. D. Higgins, C. H. Sibata, L. Siskind and J. W. Sohn, *Deconvolution of detector size effect for small field measurement,* Med. Phys., 22, 1663 - 1666 (1995).

[181] B. E. Bjarngard, J-S. Tsai and R. K. Rice, *Doses on the central axes of narrow 6MV x-ray beams,* Med. Phys. 17, 794 - 799 (1990).

[182] S. N. Rustgi, *Evaluation of the dosimetric characteristics of a diamond detector for photon beam measurements,* Med. Phys., 22, 567 - 570 (1995).

[183] F. S. E. Norrgard, P. M. Sipila, J. A. J. Kulmala and H. R. I. Minn, *Dose characteristics of in-house-built collimators for stereotactic radiotherapy with a linear accelerator,* Phys. Med. Biol., 43, 1545 - 1556 (1998).

[184] C. M. M. Wells, T. R. Mackie, M. B. Podgorsak, M. A. Holmes, N. Papanikolaou, P. J. Reckwerdt, J. Cygler, D. W. O. Rogers, A. F. Bielajew, D. G. Schmidt and J. K. Muehlenkamp, *Measurements of the electron dose distribution near inhomogeneities using a plastic scintillation detector,* Int. J. Radiat. Oncol., 29, 1157 - 1165 (1994).

[185] D. J. Dawson, J. M. Harper and A. C. Akinradewo, *Analysis of physical parameters associated with the measurement of high energy x-ray penumbra,* Med. Phys., 11, 491 - 497 (1984).

[186] J. Cashmore, *The characterization of unflattened photon beams from a 6 MV linear accelerator,* Phys. Med. Biol., 53, 1933 - 1946 (2008).

[187] A. Mesbahi, *Dosimetric characteristics of unflattened 6 MV photon beams of a clinical linear accelerator: a Monte Carlo study,* Appl. Radiat. Isot., 65, 1029 - 1036 (2007).

[188] A. Mesbahi, P. Mehnati, A. Keshtkar and A. Farajollahi, *Dosimetric properties of a flattening filter-free 6 MV photon beam: a Monte Carlo study,* Radiation Medicine, 25, pp. 315 - 324 (2007).

[189] S. C. Sharma, J. T. Ott, J. B. Williams, and D. Dickow, *Commissioning and acceptance testing of a CyberKnife linear accelerator,* J. Appl. Clin., Med. Phys., 8, 119 - 125 (2007).

[190] U. Titt, O.N. Vassiliev, F. Ponisch, L. Dong, H. Liu and R. Mohan, *A flattening filter free photon treatment concept evaluation with Monte Carlo,* Med. Phys., 33, pp. 1595 - 1602 (2006).

[191] O. N. Vassiliev, U. Titt, S. F. Kry, F. Ponisch, M. T. Gillin and R. Mohan, *Monte Carlo study of photon fields from a flattening filter-free clinical accelerator,* Med. Phys., 33, 820 - 827 (2006).

[192] O. N. Vassiliev, U. Titt, F. Ponisch, S. F. Kry, R. Mohan and M. T. Gillin, *Dosimetric properties of photon beams from a flattening filter free clinical accelerator,* Phys. Med. Biol., 51, 1907 - 1917 (2006).

[193] O. N. Vassiliev, U. Titt, S. F. Kry, R. Mohan and M. T. Gillin, *Radiation safety survey on a flattening filter-free medical accelerator,* Radiation Protection Dosimetry, 124, 187 - 190 (2007).

[194] U. Titt, O. N. Vassiliev, F. Ponisch, S. F. Kry and R. Mohan, *Monte Carlo study of backscatter in a flattening filter free clinical accelerator,* Med. Phys, 33, 3270 - 3273 (2006).

[195] S. F. Kry, U. Titt, F. Ponisch, O. N. Vassiliev, M. Salehpour, M. Gillin and R. Mohan, *Reduced neutron production through use of a flattening-filter-free accelerator,* International Journal of Radiation Oncology, Biology, Physics, 68, 1260 - 1264 (2007).

[196] T. C. Zhu and J. R. Palta, *Electron contamination in 8 and 18 MV photon beams*, Med. Phys., 25, 1, pp. 12 -19 (1998).

[197] IAEA 2000, *Absorbed Dose Determination in External Beam Radiotherapy: An International Code of Practice for Dosimetry Based on Standards of Absorbed Dose to Water,* IAEA Technical Report 398 (Vienna: IAEA).